f-BLOCK CHEMISTRY: A STUDY OF Sm^+ AND Th^+ REACTIONS WITH SMALL MOLECULES IN THE GAS PHASE

by

Richard M Cox

A dissertation submitted to the faculty of
The University of Utah
in partial fulfillment of the requirements for the degree of

Doctor of Philosophy

Department of Chemistry

The University of Utah

December 2015

The University of Utah Graduate School

STATEMENT OF DISSERTATION APPROVAL

The dissertation of **Richard M Cox**

has been approved by the following supervisory committee members:

Peter B. Armentrout	, Chair	**August 27, 2015** Date Approved
Scott L. Anderson	, Member	**August 27, 2015** Date Approved
Michael D. Morse	, Member	**August 27, 2015** Date Approved
James Sutherland	, Member	**August 27, 2015** Date Approved
Henry S. White	, Member	**August 27, 2015** Date Approved

and by **Cynthia J. Burrows**, Chair of

the Department of **Chemistry**

and by David B. Kieda, Dean of The Graduate School.

ABSTRACT

The study of the reactions of Sm^+ and Th^+ with several small molecules using guided ion beam tandem mass spectrometry is presented. The kinetic energy dependent reaction cross sections of these reactions are modelled using a modified line-of-centers model, and thermochemical values, including bond dissociation energies (BDEs), are reported. In most cases, the experimental BDEs are compared to BDEs derived from quantum chemical calculations. Furthermore, a semiempirical model to include spin-orbit energy corrections to theoretical calculations is presented. Finally, experimental Th^+ BDEs are used to elucidate the thermochemical trends of the actinide series.

In memory of Diana Wells
She believed I could achieve before I dreamed of trying.

TABLE OF CONTENTS

ACKNOWLEDGEMENTS

Few individuals can claim to have accomplished much without the help and influence of others. I am no exception. In my case, I have had the opportunity to work with top-notch collaborators and colleagues. It seems appropriate to mention a few individuals who were key contributors to my work.

I would like to start by thanking our collaborators Dr. Albert Viggiano (Air Force Research Lab), Dr. Michael Heaven (Emory University), and Dr. Kirk Peterson (Washington State University) and their groups. Without their help and advice much of this work would not have been possible. I would also like to thank Dr. Wibe (Bert) de Jong (Lawrence Berkley National Lab), who patiently taught this confirmed "experimentalist" how to "correctly" engage in theoretical studies. While not strictly a collaborator, I must also acknowledge Dr. Michael Morse and his group from the University of Utah. In addition to being a great teacher, his group generously lent me supplies when needed.

I must also mention the help of all my fellow Armentrout group members, past and present. In particular, Dr. Murat Citir who first "showed me the ropes" in the group and patiently answered all of my questions, and Dr. Christopher Hinton and Mr. Cristopher McNary, who were always available to help. Additionally, I must thank Mr. Oscar Wheeler, who has been a true friend, and without whose encouragement I never

would have made it this far. Furthermore, I must acknowledge and thank the “admiral of my educational voyage” Dr. Peter Armentrout. He has been an exceptional mentor and teacher.

Finally, I would like to acknowledge the support of my family. In particular, Iwould like to thank my kids, Madelyn, Kylee, and Brayden, who sacrificed their time with me. Most importantly I must acknowledge and thank my wife Kimberly. Without her help and encouragement, I would have given up years ago.

CHAPTER 1

INTRODUCTION AND OVERVIEW

Introduction

Much of the interest in studying the actinides (An) is due to their application to nuclear power and national security. Most An also pose a significant health risk to humans. Consequently, the study of An chemistry is a growing field, and practical applications may include nuclear waste removal and treatment or detection methods. Nevertheless, studying An chemistry poses a significant challenge and is generally limited to dedicated radiation-controlled laboratories. However, the lanthanides (Ln) are a promising analogue to understand actinide chemistry, partly because they are much less dangerous than their An counterparts.[1]

From a fundamental standpoint, the f-block (An and Ln) represent an area of chemistry than has been studied far less frequently than the main group and transition metals: therefore, basics studies of reaction chemistry are essential to properly understand the chemistry of the *f*-block systems. Fundamental studies are best performed in the gas phase where perturbing (e.g., solvent, etc.) effects are minimized. Accordingly, the study of An and Ln reactions in the gas phase is a growing field. These studies can largely be grouped into two types: oxidation[1-13] and hydrocarbon activation.[14-24]

Another goal of studying M^+ + LR (M = Ln, An) reactions is to ascertain bond

dissociation energies (BDEs) through bond activation reactions. These values are useful basic thermochemical information that allows for the prediction of many thermochemicalprocesses. For the An^+ and Ln^+ species, most of the published BDEs are either MO^+ or MO_2^+ BDEs.[1,5] Additionally; these experimental BDEs provide reliable benchmarks to which theoretical methods can be evaluated. This is critical because working with An is typically hazardous, and theoretical study of these systems represents an alternative (and safe) method of obtaining useful information about An chemistry. However, theoretical studies of An systems is an emerging field. Many examples of apparent discrepancies between theory and experiment exist,[6,25-27] and the lack of available information makes it difficult to determine which value (experimental or theoretical) is in error.

Another interesting aspect of studying An and Ln thermochemistry is the potential insight into the chemi-ionization reactions, Eq. 1.1 and 1.2.[28]

$$M + O \rightarrow \quad MO^+ + e^- \tag{1.1}$$

$$M + O_2 \rightarrow \quad MO_2^+ + e^- \tag{1.2}$$

This reaction has primarily been studied for the Ln and An, and existing literature values[28] suggest that this is a phenomenon almost exclusively characteristic of the *f*-block species. The application of this study may include the creation of an artificial plasma. The utility of this reaction will be discussed in greater detail in Chapter 3.

Bond Activation

Studying bond activation by M^+ in the gas phase can be grouped into two broad methods: thermal methods and ion beam methods. Thermal methods include Fourier transform ion cyclotron resonance mass spectrometry (FT-ICR)[2-4,6,11-20,22]and inductively coupled plasma mass spectrometry (ICP-MS).[7-10,21] These techniques are typically performed at nominal room temperature (300 K) and are useful in studying exothermic or possibly thermo-neutral reactions. The second group, ion beam techniques, uses ion optics to collimate and manipulate an ion beam that is passed through a reaction cell containing the reaction partner. This technique often allows for the variance of the ion energy and, thereby, the study of the energy dependence of a bond activation reaction.

To date, most studies of An and Ln reactions have primarily been studied using thermal methods. For the An, Gibson and coworkers have systematically studied An^+ oxidation with various oxidants using FT-ICR across the early An series (Th – Cm).[2,12,13] Meanwhile, several others have studied Th^+ and U^+ oxidation, also with FT-ICR.[11] The oxidation reactions of the An^+ with several oxidants are summarized in Table 1.1. In general, reactivity increases moving across the An series, which, in most cases, also corresponds to the promotion energy to the lowest lying level with a configuration that contains two unpaired *6d*-electrons.[5] Likewise, Gibson and others have studied hydrocarbon activation by the An^+, and find reactivity trends similar to those of the oxidation study.[18] This is also true of studies involving sulfur ligands.[6]

Like the An^+, most Ln^+ bond activation studies have been performed using a thermal method. Oxidation reactions have been studied by Bohme and coworkers with a variety of oxidants across the entire Ln series (except Pr^+ which is not naturally

occurring) using ICP-MS.[7-10] Others have studied the reactions using FT-ICR.[11,13] A summary of the oxidation reactions of the early Ln^+ (La^+ - Gd^+) are also found in Table 1.1. Similar to the An^+, Ln^+ reactivity appears to be correlated to the promotion energy from the ground-level to the first level with two unpaired non *f*-electrons. Bohme indicates that the promotion energy, $E_p(5d6s)$ or $E_p(5d^2)$,[7] to the first available level is sufficient, while Gibson contends that the reactivity correlates better with $E_p(5d^2)$.[1] Like the An^+, hydrocarbon activation reactivity of the Ln^+ is similar to the observed reactivity of the oxidation reactions.[21,24]

Ion beam experiments have been much more limited. Prior to the work presented here, ion beam studies of the An^+ were limited to studies of the reactions of U^+ with several small molecules.[29-31] For the Ln^+, the reactions of La^+ and Lu^+ with CH_4, C_2H_6, SiH_4, and H_2 (D_2, HD)[32-34] have been studied. In all cases, the observed reactions are consistent with the analogous reactions observed using the thermal techniques, but the ability to observe the energy dependence of the reaction allowed for the determination of several BDEs such as BDEs of $D_0(U^+\text{-H}) = 2.90 \pm 0.10$ eV and $D_0(U^+\text{-N}) = 4.7 \pm 0.2$ eV from the U^+ experiments.[30]

An^+ and Ln^+ Thermochemistry

Because most studies of An^+ and Ln^+ bond activation are limited to the thermal methods, direct determination of BDEs is limited to bracketing experiments, so that the BDE is reported as a range between the BDEs of oxidants, Table 1.2, that successfully oxidize or unsuccessfully oxidize the ion of interest. This can lead to large ranges or only upper or lower limits of the BDE established (see Table 1.1). Consequently, more precise

determinations of An^+ and Ln^+ BDEs are done using the thermochemical cycle, Eq. 1.3.

$$D_0(An^+\text{-}O) + IE(An) = D_0(An\text{-}O) + IE(AnO) \quad (1.3)$$

In general, the ionization energy (IE) of most An and all the Ln are reliably known through spectroscopic methods.[35] In most cases, D_0(An-O) and D_0(Ln-O) have been determined using high-temperature methods, such as Knudsen cell effusion experiments.[36] These high-temperature methods require the use of free-energy functions to extrapolate energies to 0 K BDEs. Several have warned that the BDE is highly dependent on the free-energy function chosen, and this is a potentially significant error for this method.[36,37] This is particularly true of the An where limited experimental data is available to form the free-energy function. Ionization energies of the neutral molecule IEs have often been determined using electron impact methods at elevated temperatures. Ion beam experiments with transition metals indicate that IEs determined in this manner are usually0.2 – 0.5 eV too low[38,39] so that, in general, this method is better viewed as a lower limit to the true IE, presumably because it does not account for the population of excited-states at higher temperatures. Spectroscopic determinations of IE(ThO), IE(UO), and IE(SmO) indicate that this is true for the AnO and LnO determined using electron impact as well.[40,41] For many of the An, IE(AnO) have been determined using FT-ICR bracketing experiments with electron donor molecules.[1,2,5,12,13]This method appears to be reasonably accurate when compared to theoretical IE(AnO), but theoretical calculations indicate that at least one IE(AnO) is too small.[26] (Potentially, inefficiencies in electron transfer inhibited observation of PaO^+.)

Because AnO^+ and LnO^+ systems are the most studied, the AnO^+ and LnO^+ BDEs are the most reliable thermochemistry available for these elements. In general, most of these BDEs have been derived using Eq. 1.3 from the D_0(M-O) values reviewed by Pedley and Marshall.[36] More recently Konings et al.[42] have reviewed the AnO and LnO BDEs. Other compilations usually rely on the value of Pedley and Marshall.[5] These BDEs are summarized in Table 1.3. Table 1.3 also contains the E_p of the An^+ and Ln^+ to the first reactive state, $5f^{n-2}6d^2$ or $5f^{n-3}6d^27s$ and $4f^{n-2}5d^2$, respectively. Figure 1.1 indicates that the AnO^+ and LnO^+ BDEs correlate with the E_p. Similarly, the AnO_2^+ and LnO_2^+ are reasonably well known and have been determined using a method analogous to Eq. 1.3.[5]

Experimental Benchmarks

Because the study of An and Ln chemistry in the gas phase is an emerging field, as indicated above, experimental benchmarks are necessary to evaluate theoretical methods, basis sets, and theoretical approaches. The An and Ln are atomic centers with large atomic numbers, so these calculation must also account for relativistic effects from core electrons. This is typically accounted for by using an effective core potential (ECP) that accounts (quasi or fully) for relativistic effects, or by using full electron basis sets with an approximation of the Dirac equation, such as Douglas-Kroll-Hess Hamiltonian (DKH)[43-47] or zero-order relativistic approximation (ZORA).[48,49] Usually, theoretical methods used can be classified as density functional theory (DFT) or post self-consistent field theory (SCF), such as coupled cluster methods that include single and double excitations with triple excitations treated perturbatively (CCSD(T)), or complete active space self-consistent field (CASSCF) calculations.

Experimental benchmarks can be classified as either spectroscopic benchmarks or energetic benchmarks. The former would include molecular states and levels, molecular parameters, such as bond lengths and vibrational modes, and IEs. The latter includes BDEs and kinetic barrier heights. Recently, Heaven and coworkers have studied ThL^+ and UL^+ (L = C, N, O, F, and S) using pulsed-field ionization zero kinetic energy (PFI-ZEKE) and laser-induced fluorescence (LIF) spectroscopy.[50] Complementary calculations reproduced the observable experimental calculations reasonably well, but in some cases, such as ThF^+, it was necessary to resort to very computationally expensive levels of theory, such as coupled cluster with single, double, and triple excitations and quadruple excitations mixed in perturbatively, CCSDT(Q), and multireference configuration interaction MRCI+Q methods to reproduce the experimental ordering of the ground ($^1\Sigma^+$) and first excited-state ($^3\Delta_1$). The authors attribute this result to the accurate recovery of correlation energy.[50] Both methods included explicit treatment of spin-orbit effects. The difficulty in reproducing the experimental ground-state in this case is discouraging because AnL^+ and LnL^+ are expected to have a high density of low-lying states because of nonbinding *f*-electrons, see spectroscopic results from Chapter 3. This will likely present a considerable challenge for theoretical studies.

Another traditional experimental benchmark for theoretical calculations is the IE. A comprehensive theoretical treatment of the IE(AnO) system was performed by several post-SCF methods using an atomic natural order (ANO-RCC) basis sets of VTZP quality with the Douglas-Kroll-Hamiltonian.[26] While most calculations reproduced the experimentally observed IEs, it is difficult to fully evaluate the theoretical approach because the IE(AnO) were determined experimentally using a bracketing approach,

where the mean is the average of the range between the lower and upper limit, and the uncertainty is the range. The most notable discrepancy is between the experimental IE(PaO) = 5.9 ± 0.2 eV and the theoretical, 6.28 – 6.51 eV.[51] The bracketing determination of IE(PaO) makes it unclear which value (experimental or theoretical) is in error. With limited experimental benchmarks, determining errors in either the experimental or theoretical methods will remain challenging. BDEs are also an attractive experimental benchmark for theoretical studies. To date, most theoretical determinations have focused on AnO^+ (AnS^+) and AnO_2^+ BDEs.[6,51] Of these systems, studying the ThO_2^+ BDE is attractive because the $^2\Sigma_u^+$ ground-state that corresponds with a ThO^+ $^2\Sigma^+$ + O ^{3}P asymptote has limited spin-orbit interactions to consider. Averkiev et al. studied this system extensively with many DFT functionals and several post-SCF methods.[51] They identified several methods that reproduced the experimental value with reasonable accuracy. Of these methods, B3LYP and MPW3LYP performed well, but post-SCF methods including CCSD(T) underpredicted the experimental BDE by 0.86 eV.

Pereira et al. recently calculated the BDEs of AnO^+ and AnS^+ using B3LYP and MPW1PW91 DFT methods with a segmented basis set of at least VTZP quality and a quasirelativistic ECP (60 electrons) for An^+, a contracted 10s6p basis set for O, and a cc-pVTZP basis set for S. In the early part of the An series (Th – U), calculations overestimate the experimental AnO^+ BDE by 0.09 – 0.55 eV. Much of this error may be attributable to spin-orbit energy which was not explicitly considered; however, it is difficult to quantitate this error because of the uncertainties in the experimental values.[6] In particular, $D_0(Pa^+\text{-}O)$ = 8.29 ± 0.50 eV makes evaluation of the theoretical treatment difficult. In contrast to the early An, calculations for the latter part of the An series (Np –

Cm) underestimate the BDEs by 0.63 – 1.25 eV. Again this may be attributed to spin-orbit energy, but it is difficult to determine the extent because experimental uncertainties are 0.13 – 0.39 eV. AnS^+ calculations mirror the trends of the AnO^+ calculations; nevertheless, no evaluation of performance was made because experimental BDEs were determined in bracketing experiments.[6]

Other systems of interest for comparison of experimental results to theory are reaction coordinates. One such system is the activation of methane by Th^+. In this system, FT-ICR studies observed the dehydrogenation product, $ThCH_2^+$, but at a low efficiency (<2%).[18,22] Unfortunately, theoretical calculations proved inconclusive because one study concluded a small kinetic barrier was present,[52] while a second study concluded the inefficiency was due to a spin-crossing in the early part of the reaction.[25] While guided ion beam studies described in Chapter 4 ultimately determined experimentally that there was a kinetic barrier between the first and second intermediates, these mixed results indicate the required interplay between theory and experiment to arrive at the correct conclusion. In order to improve on previous results, reliable experimental benchmarks are necessary to improve theoretical methods and basis sets.

Chemi-Ionization Reactions

A final application of studying An and Ln thermochemistry in the gas phase is to understand the chemi-ionization reaction. Several metals have been observed to spontaneously ionize in the presence of O and O_2 as described in reactions 1.1 and 1.2. Schofield,[28] in an evaluation of current thermochemical values, determined that many of the Ln and An should undergo these reactions exothermically. Because the reaction is

exothermic, there is then a barrier to recombination so that the LnO^+ or AnO^+ ions should be long-lived, allowing for the creation of an artificial plasma.

Recently, the United States Air Force has expressed interest in using reaction 1.1 to generate an artificial plasma in the upper atmosphere, where atomic oxygen is prevalent. Such a plasma could be used to smooth natural fluctuations in the ionosphere that may hinder satellite communication. Sm was chosen as a test subject because of a relatively high volatility. Unfortunately, atmospheric studies indicated that Sm did not ionize to the extent expected from then-current thermochemistry.[53-55] A thermochemical cycle allows the determination of the enthalpy of the chemi-ionization reaction according to Eq. (1.4):

$$\Delta_r H_0° = IE(Ln) - D_0(Ln^+-O) = IE(LnO) - D_0(Ln-O) \quad (1.4)$$

GIBMS

While An^+ and Ln^+ chemistry in the gas phase is a growing field, it is still relatively unexplored. To date, multiple discrepancies between theoretical calculations and experimental results exist, such as BDEs, IEs, energy levels, and reaction coordinates in the literature.[6,25-27,52] In some cases, it is not clear which result is in error. Furthermore, the lack of experimental data is also problematic for the evaluation of theoretical methods. Guided ion beam tandem mass spectrometry is uniquely suited to study ion thermochemistry because of the ability to vary the kinetic energy of the reactant ion by 0 – 1000 eV in the laboratory frame. This allows for the study of the energy dependence of a reaction product and the determination of reaction kinetics. Furthermore, the ability to

vary the energy over a wide range of kinetic energy provides reaction thresholds so that BDEs of endothermic products can be determined. Described herein are the reactions of Sm^+ and Th^+ with several small molecules as studied by GIBMS. Additionally, complementary theoretical calculations are compared to experimental results.

Overview

Chapter 2

The GIBMS instrument, experimental methodology, and theoretical methods are outlined. The approach to correcting theoretical values for spin-orbit effects is also explained.

Chapter 3

The study of oxidation of Sm^+ by various small gasses is reported. An updated, more precise experimental SmO^+ BDE is reported, and the significance of this finding to understanding the chemi-ionization results in upper atmosphere studies is discussed.

Chapter 4

The guided ion beam and theoretical study of the activation of CH_4 by Th^+ is reported. Experimental evidence of a kinetic barrier to dehydrogenation is reported, and this barrier is reproduced in quantum calculations after including spin-orbit energy effects.

Chapter 5

The guided ion beam study of the reaction of $Th^+ + H_2$, D_2, HD is reported. Several basis sets and theoretical methods are evaluated by comparison to experimental results. Additionally, the trend of singly bound AnL^+ BDEs is predicted from existing experimental data.

Chapter 6

The guided ion beam and theoretical study of the reactions $Th^+ + O_2$, CO are presented. Basis sets and theoretical methods are further evaluated by comparison to experimental results. Additionally, AnL^+ (O and C) are predicted from measured ThL^+ BDEs.

References

(1) Gibson, J. K. *J. Phys. Chem. A* **2003**, *107*, 7891-7899.

(2) Santos, M.; Marcalo, J.; Pires, d. M. A.; Gibson, J. K.; Haire, R. G. *J. Phys. Chem. A* **2002**, *106*, 7190-7194.

(3) Santos, M.; Marcalo, J.; Leal, J. P.; Pires de Matos, A.; Gibson, J. K.; Haire, R. G. *Int. J. Mass Spectrom.* **2003**, *228*, 457-465.

(4) Gibson, J. K.; Haire, R. G. *Inorg. Chem.* **2002**, *41*, 5897-5906.

(5) Marcalo, J.; Gibson, J. K. *J. Phys. Chem. A* **2009**, *113*, 12599-12606.

(6) Pereira, C. C. L.; Marsden, C. J.; Marcalo, J.; Gibson, J. K. *Phys. Chem. Chem. Phys.* **2011**, *13*, 12940-12958.

(7) Koyanagi, G. K.; Bohme, D. K. *J. Phys. Chem. A* **2001**, *105*, 8964-8968.

(8) Cheng, P.; Koyanagi, G. K.; Bohme, D. K. *J. Phys. Chem. A* **2006**, *110*, 12832-12838.

(9) Blagojevic, V.; Flaim, E.; Jarvis, M. J. Y.; Koyanagi, G. K.; Bohme, D. K. *Int. J. Mass Spectrom.* **2006**, *249/250*, 385-391.

(10) Jarvis, M. J. Y.; Blagojevic, V.; Koyanagi, G. K.; Bohme, D. K. *Phys. Chem. Chem. Phys.* **2010**, *12*, 4852-4862.

(11) Cornehl, H. H.; Wesendrup, R.; Diefenbach, M.; Schwarz, H. *Chem. - Eur. J.* **1997**, *3*, 1083-1090.

(12) Santos, M.; Marcalo, J.; Leal, J. P.; Matos, A. P. d.; Gibson, J. K.; Haire, R. G. *Int. J. Mass Spectrom.* **2003**, *228*, 457-465.

(13) Gibson, J. K.; Haire, R. G.; Santos, M.; Pires de Matos, A.; Marcalo, J. *J. Phys. Chem. A* **2008**, *112*, 11373-11381.

(14) Gibson, J. K. *J. Am. Chem. Soc.* **1998**, *120*, 2633-2640.

(15) Gibson, J. K. *Inorg. Chem.* **1999**, *38*, 165-173.

(16) Gibson, J. K. *Radiochim. Acta* **1999**, *84*, 135-146.

(17) Gibson, J. K.; Haire, R. G. *Radiochim. Acta* **2001**, *89*, 363-369.

(18) Gibson, J. K.; Haire, R. G.; Marçalo, J.; Santos, M.; Pires de Matos, A.; Mrozik, M. K.; Pitzer, R. M.; Bursten, B. E. *Organometallics* **2007**, *26*, 3947-3956.

(19) Marcalo, J.; Santos, M.; Pires de Matos, A.; Gibson, J. K.; Haire, R. G. *J. Phys. Chem. A* **2008**, *112*, 12647-12656.

(20) Marcalo, J.; Santos, M.; Gibson, J. K. *Phys. Chem. Chem. Phys.* **2011**, *13*, 18322-18329.

(21) Shayesteh, A.; Lavrov, V. V.; Koyanagi, G. K.; Bohme, D. K. *J. Phys. Chem. A* **2009**, *113*, 5602-5611.

(22) Marçalo, J.; Leal, J. P.; Pires de Matos, A. *Int. J. Mass Spectrom. Ion Processes* **1996**, *157/158*, 265-274.

(23) Cornehl, H. H.; Heinemann, C.; Schroeder, D.; Schwarz, H. *Organometallics* **1995**, *14*, 992-999.

(24) Schilling, J. B.; Beauchamp, J. L. *J. Am. Chem. Soc.* **1988**, *110*, 15-24.

(25) de Almeida, K. J.; Duarte, H. A. *Organometallics* **2010**, *29*, 3735-3745.

(26) Infante, I.; Kovacs, A.; La, M. G.; Shahi, A. R. M.; Gibson, J. K.; Gagliardi, L. *J. Phys. Chem. A* **2010**, *114*, 6007-6015.

(27) Zhou, J.; Schlegel, H. B. *J Phys Chem A* **2010**, *114*, 8613-8617.

(28) Schofield, K. *J. Phys. Chem. A* **2006**, *110*, 6938-6947.

(29) Armentrout, P. B.; Beauchamp, J. L. *Chem. Phys.* **1980**, *50*, 27-36.

(30) Armentrout, P. B.; Hodges, R. V.; Beauchamp, J. L. *J. Chem. Phys.* **1977**, *66*, 4683-4688.

(31) Armentrout, P. B.; Beauchamp, J. L. *Chem. Phys.* **1980**, *50*, 21-25.

(32) Kickel, B. L.; Armentrout, P. B. *J. Am. Chem. Soc.* **1995**, *117*, 4057-4070.

(33) Sunderlin, L. S.; Armentrout, P. B. *J. Am. Chem. Soc.* **1989**, *111*, 3845-3855.

(34) Elkind, J. L.; Sunderlin, L. S.; Armentrout, P. B. *J. Phys. Chem.* **1989**, *93*, 3151-3158.

(35) Sansonetti, J. E.; Martin, W. C. *J. Phys. Chem. Ref. Data* **2005**, *34*, 1559-2259.

(36) Pedley, J. B.; Marshall, E. M. *J. Phys. Chem. Ref. Data* **1983**, *12*, 967-1031.

(37) Hildenbrand, D. L.; Murad, E. *J. Chem. Phys.* **1974**, *61*, 1232-1237.

(38) Hinton, C. S.; Li, F.; Armentrout, P. B. *Int. J. Mass Spectrom.* **2009**, *280*, 226-234.

(39) Sievers, M. R.; Chen, Y.-M.; Armentrout, P. B. *J. Chem. Phys.* **1996**, *105*, 6322-6333.

(40) Goncharov, V.; Heaven, M. C. *J. Chem. Phys.* **2006**, *124*, 064312.

(41) Cox, R. M.; Kim, J. S.; Armentrout, P. B.; Bartlett, J.; Van Gundy, R. A.; Heaven, M. C.; Ard, S. G.; Melko, J. J.; Shuman, N. S.; Viggiano, A. A. *J. Chem. Phys.* **2015**, *142*, 134307.

(42) Konings, R. J. M.; Benes, O.; Kovacs, A.; Manara, D.; Sedmidubsky, D.; Gorokhov, L.; Iorish, V. S.; Yungman, V.; Shenyavskaya, E.; Osina, E. *J. Phys. Chem. Ref. Data* **2014**, *43*, 013101.

(43) Hess, B. A. *Phys. Rev. A* **1985**, *32*, 756-763.

(44) Hess, B. A. *Phys. Rev. A: Gen. Phys.* **1986**, *33*, 3742-3748.

(45) Jansen, G.; Hess, B. A. *Phys. Rev. A* **1989**, *39*, 6016-6017.

(46) de Jong, W. A.; Harrison, R. J.; Dixon, D. A. *J. Chem. Phys.* **2001**, *114*, 48-53.

(47) Barysz, M.; Sadlej, A. J. *J. Mol. Struct.: THEOCHEM* **2001**, *573*, 181-200.

(48) van Lenthe, E.; Baerends, E. J.; Snijders, J. G. *J. Chem. Phys.* **1994**, *101*, 9783-9792.

(49) van Lenthe, E.; Snijders, J. G.; Baerends, E. J. *J. Chem. Phys.* **1996**, *105*, 6505-6516.

(50) Heaven, M. C.; Barker, B. J.; Antonov, I. O. *J. Phys. Chem. A* **2014**, *118*, 10867-10881.

(51) Averkiev, B. B.; Mantina, M.; Valero, R.; Infante, I.; Kovacs, A.; Truhlar, D. G.; Gagliardi, L. *Theor. Chem. Acc.* **2011**, *129*, 657-666.

(52) di Santo, E.; Michelini, M. d. C.; Russo, N. *Organometallics* **2009**, *28*, 3716-3726.

(53) Shuman, N. S.; Hunton, D. E.; Viggiano, A. A. *Chem. Rev.* **2015**, in press.

(54) Caton, R. G.; Pederson, T. R.; Paris, R. T.; Groves, K. M.; Bernhardt, P. A.; Cannon, P. S. 2013.

(55) Groves, K. M.; Caton, R. G.; Pederson, T. R.; Paris, R. T.; Su, Y.; Cannon, P. S.; Jackson-Booth, N. K.; Angling, M. J.; Retterer, J. M. In *American Geophysical Union, Fall Meeting* 2013.

(56) *NIST Computational Chemistry Comparison and Benchmark Database NIST Standard Reference Database Number 101 Release 16a*; Johnson III, R. D., Ed., August 2013.

(57) Demireva, M.; Kim, J.; Kaffle, A.; Armentrout, P. B. *unpublished*.

(58) Blaise, J.; Wyart, J.-F. In *Interantional Tables of Selected Constants* Paris, 1992; Vol. 20.

Table 1.1. Reaction efficiencies of $Ln^+/An^+ + RO$.

$Ln^+ + RO \rightarrow$	La^+	Ce^+	Pr^+	Nd^+	Pm^+	Sm^+	Eu^+	Gd^+
$LnO^+ + N_2$[b]	0.82	0.72	0.39	0.40	NA	0.19	0.097	0.75
		1.03[c]		0.47[c]		0.18[d]		0.46[e]
$LnO^+ + O$[b]	0.75	0.88	0.75	0.57	NA	0.78	NR	0.86
		1.05[c]		0.80[c]		0.49[d]		0.61[e]
						1.0[f]		
$LnO^+ + CO$[g]	0.64	0.66	0.23	0.054	NA	NR	NR	0.50
		0.70[c]		0.08[c]		NR		0.22[e]
$LnO^+ + N$[h]	0.40	0.89	0.32	0.06	NA	NR	NR	0.41
						NR[d]		0.16[e]
$LnO^+ + CH_2$[e]	NA	NA	NA	NA	NA	NA	NA	0.088
$An^+ + RO \rightarrow$	Ac^+	Th^+	Pa^+	U^+	Np^+	Pu^+	Am^+	Cm^+
$AnO^+ + N_2$[i]	NA	0.68	0.49[j]	0.47	0.48	0.02	0.004[k]	0.17[e]
		1.02[c]		1.25[c]				
$AnO^+ + O$[i]	NA	0.86	0.66[j]	0.72	0.68	0.27	0.32[k]	0.37[e]
		1.12[c]		1.17[c]				
		1.20[l]						
$AnO^+ + CO$[i]	NA	0.35	0.38[j]	0.29	0.30	0.003	0.001[k]	0.08[e]
		0.95[c]		1.02[c]				
$AnO^+ + N$[i]	NA	0.49	0.51[j]	0.46	0.45	0.17	NR[k]	0.013[e]
$AnO^+ + CH_2$[i]	NA	0.61	0.48[j]	0.53	0.28	NR	NA	NR[e]

Table 1.1 Continued

[a] Reaction efficiency k/k_{col} where k_{col} is defined as the Su-Chesnavich semiclassical trajectory rate constant. NA = no reported measurement. NR = No observed reaction.
[b] FT-MS measurement Ref. 7, unless noted otherwise, uncertainty ±30%.
[c] FT-ICR measurement Ref. 11, uncertainty ±30%.
[d] FT-MS measurement, Chapter 3, uncertainty ±25%.
[e] FT-ICR measurement Ref.13, uncertainty ±50%.
[f] GIBMS measurement, Chapter 3, uncertainty ±20%.
[g] FT-MS measurement Ref. 8, unless noted otherwise, uncertainty ±30%.
[h] FT-MS measurement Ref. 9, unless noted otherwise, uncertainty ±30%.
[i] FT-ICR measurement Ref. 2, unless noted otherwise, uncertainty ±50%.
[j] FT-ICR measurement Ref., unless noted otherwise, uncertainty ±50%.
[k] FT-ICR measurement Ref. 12, unless noted otherwise, uncertainty ±50%.
[l] GIBMS measurement, Chapter 6, uncertainty ±20%.

Table 1.2. Neutral RO BDEs (in eV)[a]

Neutral Reactant	N_2O	O_2	CO_2	NO	CH_2O
D_0(R-O)	1.667 ± 0.001	5.117 ± 0.001	5.453 ± 0.002	6.500 ± 0.004	7.964 ± 0.017

[a] Values calculated from Ref. 56.

Table 1.3. Comparison of LnO^+/AnO^+ BDEs to E_p to the reactive state.

Lanthanide	La^+	Ce^+	Pr^+	Nd^+	Pm^+	Sm^+	Eu^+	Gd^+
config.[a]	$5d^2$	$4f5d^{2+}$	$4f^36s$	$4f^46s$	$4f^56s$	$4f^66s$	$4f^76s$	$4f^75d6s$
$E_p(5d^2)$[b]	0.00	0.00	0.72	1.14	1.18	2.35	4.54	0.50
$D_0(Ln^+\text{-}O)$[c]	8.78 ± 0.16	8.80 ± 0.16	8.21 ± 0.16	7.76 ± 0.16	NA[d]	5.72 ± 0.07[e]	4.03 ± 0.16	7.63 ± 0.12[f]
Actinide	Ac^+	Th^+	Pa^+	U^+	Np^+	Pu^+	Am^+	Cm^+
config.[a]	$7s^2$	$6d^27s$	$5f^27s^2$	$5f^37s^2$	$5f^46d7s$	$5f^67s$	$5f^77s$	$5f^77s^2$
$E_p(6d^2)$[g]	1.64	0.00	0.59	0.57	0.9 ± 0.4[h]	2.14	3.6 ± 0.2[h]	1.84
$D_0(An^+\text{-}O)$[i]	NA[d]	8.51 ± 0.16[j]	8.29 ± 0.50	8.02 ± 0.13	7.88 ± 0.10	6.75 ± 0.20	5.80 ± 0.29	6.94 ± 0.39

[a] Configuration of the ground-level.
[b] Difference in energy between the ground-level and the first level with an appropriate configuration, $4f^{n-2}5d^2$, see Ref. 35 and refs. therein. For An^+ $5f^{n-2}6d^2$ or $5f^{n-3}6d^27s$.
[c] Unless noted otherwise, from Ref. 1.
[d] No experimental data available.
[e] See Chapter 3.
[f] Ref. 57.
[g] Unless noted otherwise, from Ref. 58.
[h] Ref. 5.
[i] Unless noted otherwise, from Ref. 5.
[j] See chapter 6.

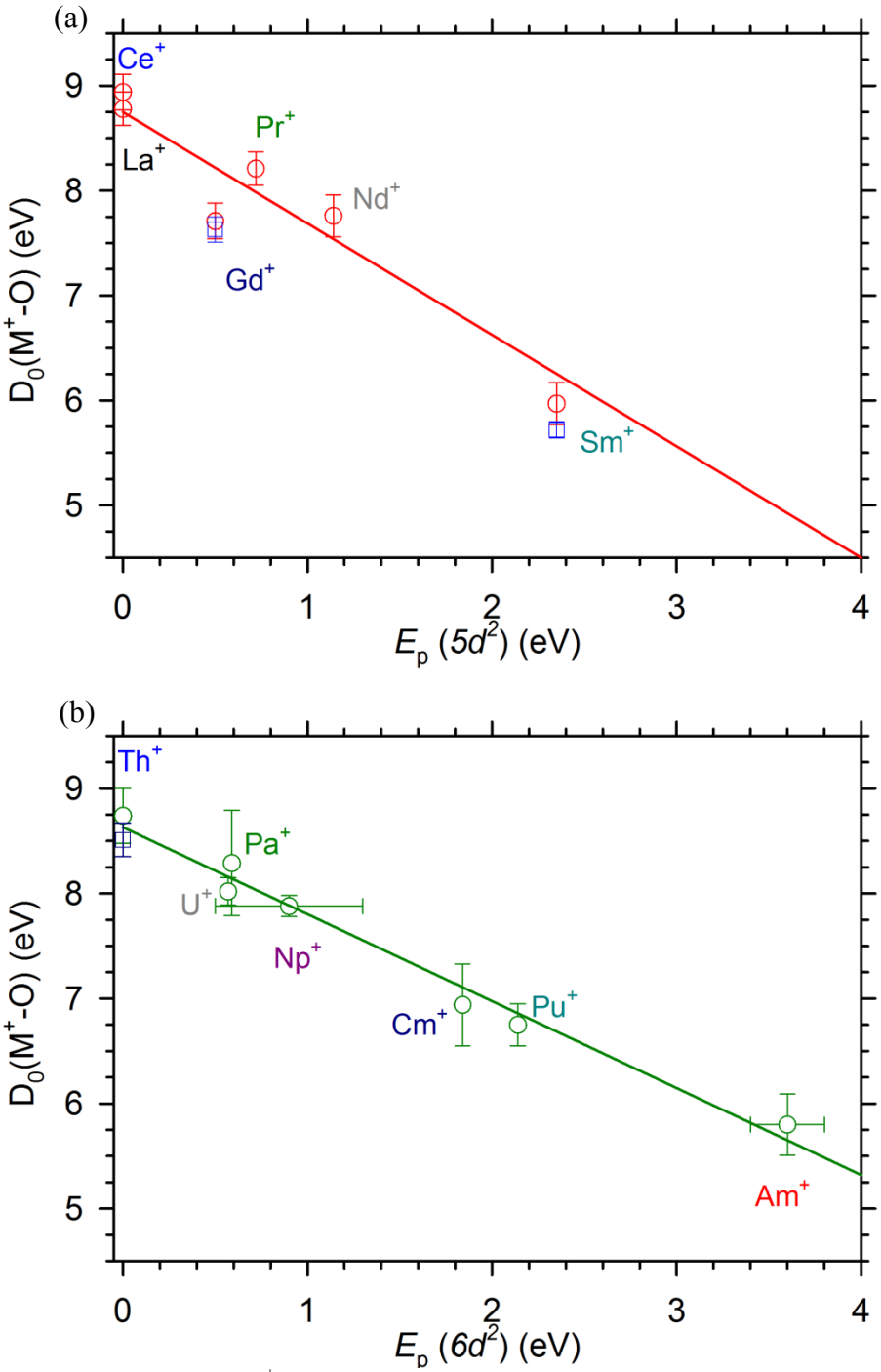

Figure 1.1. Comparison of MO^+ BDEs (M = Ln, An) to the promotion energy to the reactive state. Solid line represents the linear least-square trend line. Ln/An congeners labeled in same color. Values in blue squares represent GIBMS values. See Table 1.3. (a) LnO^+ BDEs vs. $E_p(5d^2)$. EuO^+ not shown, but included in trend line fit. (b) AnO^+ BDEs vs. $E_p(6d^2)$.

CHAPTER 2

EXPERIMENTAL AND THEORETICAL TECHNIQUES

Instrument

Overview

The guided ion beam tandem mass spectrometer, pictured in Figure 2.1, has been described in detail previously.[1] Briefly, ions are created in a direct current/flow tube source (DC/FT) that is described in greater detail below.[2] Ions are then focused into a magnetic momentum analyzer, where the reactant ion beam is mass selected. Upon mass selection, the ion beam is decelerated to a well-defined kinetic energy and passed into the radio frequency (rf) octopole ion guide,[3-5] described in greater detail below, where the ions are trapped radially. The octopole passes through a reaction cell that contains the neutral reactant gas of interest. Pressures in the reaction cell are kept low, 0.05 – 0.40 mTorr for the present work, to ensure that the probability of multiple collisions is sufficiently small, and all reaction cross sections are verified to be pressure independent. For the present work, pressure-dependent cross sections are only observed in sequential reactions. Resulting product and remaining reactant ions drift to the end of the octopole, where they are focused through a quadrupole mass filter and counted at a Daly detector.[6] Ion intensities are corrected for background counts and converted to an energy-dependent

absolute cross section.[5]

Lab frame energies are converted to the center-of-mass (CM) frame using Eq. 2.1:

$$E_{CM} = E_{Lab} \times m/m+M \quad (2.1)$$

where m and M are the mass of the neutral gas and ion, respectively. The ion energy distribution (fwhm) and absolute energy zero are measured by using the octopole as a retarding potential analyzer after directing neutral gas flow into the chamber as described previously.[5] Typical fwhms for these experiments are 0.4 – 0.9 eV (Lab). Several factors are known to broaden the reactant energy distribution; these include the thermal motion of the neutral gas (Doppler broadening).[7] The absolute uncertainty in kinetic energy is 0.05 eV (Lab).

DC/FT Source

The DC/FT source consists of a cathode that contains the sample (Sm foil or Th powder) held at 1.2 or 2.5 kV. A 90:10 He/Ar mix flows over the sample at a total pressure of 0.3 – 0.5 Torr. In the resulting electric field, Ar ionizes and collides with the cathode, sputtering off sample cations that are swept by the carrier gas into a ~1 m long flow tube. In the flow tube ions thermalize under ~ 10^5 collisions. Molecular ions are created by leaking a reactive gas into the flow tube 19 cm from the source using a variable leak valve.

Previous work with transition metals indicates that the DC/FT source creates ions with an internal temperature distribution of 300 – 1100 K.[8-12] Population analyses of Sm^+

and Th^+ indicate 67.8%and 99.9% of ions, respectively, are found in their ground-levels at 300 K.[13,14] At 1100 K, 21.1% and 76.4% of Sm^+ and Th^+ ions are found in their ground-levels.[13,14] Conservatively, we estimate the internal temperature as 700 ± 400 K, so that the average internal energy is 0.06 ± 0.05 and 0.02 ± 0.03 eV for Sm^+ and Th^+,[13,14] respectively. Average internal energies are incorporated into all reported BDEs. In most reactions studied, no evidence of excited-states is observed in the cross sections; however, in select cases (see Chapter 3), when evidence of excited-states is present in the observed cross section, a quenching gas (the reactant gas) is introduced through the leak valve, described above, to selectively remove reactive states. Molecular ions are presumed to be thermalized, with no evidence of excited-state ions observed.

Octopole Ion Guide

The effective trapping potential (U_{eff}) of the octopole is described by Eq. 2.2:

$$U_{eff} = [\, 4q^2V_0^2/m\omega^2r_0^2][r^6/r_0^6] \qquad (2.2)$$

where q and m are the ion charge and mass, V_0 and ω are the rms voltage and rf frequency, r_0 is the inner radius of the octopole, and r is the ion distance from the central axis. The octopole trapping field has a broad flat potential that steeply rises at the edges so that translational energy is relatively unperturbed while transverse energy is effectively trapped. Ideally, reaction products are trapped and transmitted with unit efficiency. In practice, small ion losses can occur (particularly at high kinetic energies), but the octopole effectively reduces ion loss so that absolute errors in the reaction cross

section are minimized. Another advantage of the octopole ion guide is that ions near the axis are relatively unaffected by the rf field, so that the kinetic energy of the reactant ions is well defined. This advantage leads to more reliable thermochemical values.

Data Reduction and Analysis

Raw ion counts are converted to absolute cross sections using Eqs. 2.3 and 2.4:

$$\ln(I_0/I) = \sigma_{tot} n l \tag{2.3}$$

$$\sigma_p = \sigma_{tot}(I_p/\Sigma I_p) \tag{2.4}$$

where I_0 is the initial reactant ion intensity, I is the transmitted reactant ion intensity, σ_{tot} is the total product cross section, n is the number density of the neutral reactant, l is the effective gas-cell path length, and σ_p is an individual product cross section having transmitted intensity I_p. Because trapping is efficient in the octopole, it is assumed that $I_0 = I + \Sigma I_p$. The absolute uncertainty in the cross section is estimated to be ±20%, and relative uncertainties are ±5%.

Kinetic energy dependent absolute cross sections are modelled using a modified line-of-centers model, Eq. 2.5:[4,15,16]

$$\sigma(E) = \sigma_0 \Sigma\, g_i\, (E + E_i - E_0)^n/E \tag{2.5}$$

where σ_0 is an empirical scaling parameter, E_i is the internal energy of the reactants summed over g_i states ($\Sigma g_i = 1$), n is an empirical fitting parameter, and E_0 is the

threshold. Eq. 2.5 is first convoluted over the internal and kinetic energy distributions and a nonlinear least-squares method is used to find a fit that best reproduces the experimental cross section.[5,16,17] Because the model explicitly accounts for reactant internal energy distributions, the E_0 represents the 0 K threshold. Uncertainty in E_0 is derived from fits over multiple independent data sets and over a range of acceptable values of n. For exchange reactions E_0 can be used to establish bond dissociation energies (BDEs) of ML^+ according to the relationship in Eq. 2.6:

$$D_0(M^+\text{-}L) = D_0(L\text{-}R) - E_0 \tag{2.6}$$

where the neutral reactant BDE, D_0(L-R), is calculated from Ref. 18, unless stated otherwise. Eq. 2.6 is valid, assuming that no barrier in excess of the reaction endothermicity exists, which is typical for most ion-molecule reactions. Otherwise, Eq. 2.6 represents the lower limit to the true BDE. For collision-induced dissociation reactions, $E_0 = D_0(M^+\text{-}L)$, given that no inefficiencies in energy transfer occur. Such inefficiencies may be observed in strongly bound molecules (MO^+ etc.), and in this case E_0 represents an upper limit to the BDE.[19-21]

Several factors may influence E_0 that are not explicitly included in Eq. 2.5.[4] The first factor is competition with another product. This is common for products that share a common intermediate, where the threshold for higher energy processes may be delayed (see Chapter 3). One such way to account for this effect is to compare the BDE measured from a competitive reaction using Eq. 2.6 to a BDE derived from a reaction that precludes competition (i.e., L_2). The E_0 measured from the competitive reaction (and

products with very similar energetics) is shifted by the difference between the two BDEs.[22] Alternatively, a model that utilizes transition state molecular parameters that explicitly accounts for competition such as phase space theory (PST)[23,24] can be used. PST is described in more detail in Appendix A. Another possible influence on the reaction threshold is caused by dissociation periods that exceed the experimental timeframe (10^{-4} s). This may be common in large molecular ions that contain many internal modes. The kinetic shift in E_0 can be accounted for by using a variation of Eq. 2.5, described elsewhere,[4] that incorporates Rice-Ramsperger-Kassel-Marcus theory (RRKM).[25,26] The systems in the present work are sufficiently small that kinetic shift does play an important role. Finally, pressure dependent cross sections may display a shift in the apparent threshold towards lower energies due to multiple collisions.[4] This shift is more evident in CID reactions of large molecular ions that have many internal nodes to store energy from nonreactive collisions with the CID gas. Cross sections that are observed to be pressure-dependent are extrapolated to rigorous single collision conditions (~0 mTorr).

Theoretical Calculations

Most theoretical calculations were performed using the Gaussian 09 suite of programs.[27] Other programs used are described in the applicable chapter where used. No calculations for SmL^+ systems are detailed in this work. Density functional theory (DFT) calculations are performed using the B3LYP,[28,29] B3PW91,[30] BHandHLYP (BHLYP),[31] M06,[32] and PBE0[30,33] functionals. In a theoretical study of actinide dioxide cation BDEs, B3LYP and M06 performed particularly well.[34] B3PW91 has been shown by others to

perform reasonably well in several actinide systems.[35,36] BHLYP has been shown to perform well for singly bound systems;[37] however, it performs poorly for higher-bond order-systems.[38,39] BHLYP also performs well calculating excitation energies for the Th^+ and ThL^+ systems studied here. PBE0 calculations yield optimized structures very similar to B3LYP structures (Appendix A). In addition to the DFT methods, single-point energy calculations are performed using the coupled cluster method that includes single and double excitations and triple excitations perturbatively (CCSD(T))[40-43] of the B3LYP optimized structures. For CCSD(T) correlation energy calculations, the Th^+ *5s* and *5p* and the C or O *1s* electrons are frozen. For full electron basis sets, an equivalent number of electrons are frozen. All calculations are performed using an unrestricted open-shell method.

Basis Sets

Several basis sets for Th^+ were employed in the studies presented here. A detailed description of each basis set can be found in Table 2.1. Basis sets are identified by their name-quality-effective core potential (ECP). ECPs used are the Stuttgart-Dresden (SDD) qausirelativistic (MWB)[44] and a fully relativistic (MDF)[45] small core (60 electrons) ECPs. The MWB ECP is used with the SDD basis set,[44] an atomic natural orbital (ANO),[46] and a segmented (Seg. SDD)[46] basis sets that are double-ζ (VDZ), quadruple-ζ (VQZ), and quadruple-ζ in quality, respectively. The MDF basis set is used with an ANO basis set[45] similar to the ANO-VQZ-MWB basis set, the correlation consistent cc-pVXZ-PP (X = T, Q) basis sets, and polarized core correlation consistent cc-pwCVXZ-PP basis sets published by K. A. Peterson.[47] Additionally, full electron variations of the cc-pVXZ

and cc-pwCVXZ basis sets[47] are used with the second-order Douglas-Kroll-Hess (DKH) Hamiltonian.[48-52] Some error is expected in the use of the cc-pVXZ-DK3 and cc-pwCVXZ-DK3 basis sets because these basis sets were designed explicitly to be used with the third-order DKH (DK3);[47] however, the error is expected to be minimal, and DK3 calculations are impractical at present. For the neutral atoms (H, C, O) Pople 6-311++G(d,p) and 6-311++G(3df,3p) basis sets,[55-57] cc-pVXZ (X = T, Q), cc-pwCVXZ, aug-cc- pVQZ, and aug-cc-pwCVQZ basis sets are used. Extrapolation to the complete basis set limit (CBS) for the cc-pVXZ and cc-pwCVXZ basis sets is performed using the Karton-Martin method,[58] Eq. 2.7, proposed for HF energies (T = 3, Q = 4):

$$E_X = E_{CBS} + A(X + 1)e^{-6.57\sqrt{X}} \tag{2.7}$$

For CCSD(T) calculations, Eq. 2.8 is used to extrapolate the correlation energy:[59]

$$E_X = E_{CBS} + B(X + ½)^{-4} \tag{2.8}$$

Spin-Orbit Corrections

Because it is a heavy metal, spin-orbit effects for ThL^+ systems are large; however, energies from typical theoretical calculations do not explicitly account for spin-orbit energy, but are an average of all spin-orbit levels. Furthermore, explicit spin-orbit calculations are computationally expensive. A simple semiempirical model to estimate spin-orbit splitting is used here. This model has been used to successfully estimate spin-orbit splitting in several third-row transition metal systems.[60-63] It is also validated in

Chapter 5 for ThH^+ using explicit spin-orbit calculations. The approach to correcting theoretical BDEs is displayed in Figure 2.2, where the diabatic BDE potential energy surface (PES) corresponding to the Th^+ (^4F) + L is represented by the solid black line, and the diabatic BDE PES corresponding to the Th^+ (^2D) + L asymptote is represented by the solid green line. (Here, diabatic is used to indicate that the orbital occupation remains constant throughout the PES.) In most cases, the reactive state (i.e., the state with the required electronic configuration to form the covalent bonds in ground-state ThL^+) of Th^+ is ^4F; however, the ground-state of Th^+ is ^2D (when averaged over all spin-orbit levels, see Chapter 4 and Appendix A), so the theoretical adiabatic BDE is ThL^+ referenced to the Th^+ (^2D) + L asymptote without considering spin-orbit effects. To better approximate the experimental BDE (red energy gap), the Th^+ (^2D) + L asymptote is corrected by the energy difference (dark red double-headed arrow) between the ^2D ground-state (averaged over all spin-orbit levels) and theground-level Th^+ ($^4F_{3/2}$) + L asymptote (red line). (The spin-orbit energy of L from the Th^+ + L asymptote is considered negligible.) When spin-orbit splitting occurs in ThL^+, the BDE is also increased by the energy difference (dark blue double-headed arrow) between the ground-state and the ground-level ThL^+. (Individual levels of a triplet ThL^+ state are represented by the red dotted surfaces.) Note that the approach used here is a first-order approximation of the spin-orbit effects and does not include second-order interactions between states (configuration interaction). Second-order effects are presumed inconsequential because the excitation energy between potential interactive states is large. Possible exceptions are noted in Chapters 4 and 5.

A peculiar aspect of Th^+ is that it has a ^2D ground-state, but a J = 3/2 level

ground-level where the major component is $^4F_{3/2}$.[13] (For comparison to theoretical calculations, we identify this level as $^4F_{3/2}$, see Appendix A.) When correcting for the Th^+ spin-orbit energy, there are two possible approaches. The first approach is to evaluate the BDEs relative to the ^4F (reactive) state and then lower the BDE by the average, empirical excitation energy of the ^4F state, 0.46 eV. The second approach is to correct the BDE from the ^2D ground-state, by lowering the BDE by the empirical difference in energy between the ^2D state averaged over all spin-orbit levels and the $^4F_{3/2}$ ground-level, 0.40 eV. The latter method appears to perform slightly better compared to experimental values and is the approach used.[22] The spin-orbit energy of ThL^+ is estimated using Eq. 2.9:[22,60,61,63]

$$E^{SO} = \Lambda \, M_S \, A \tag{2.9}$$

where A is the spin-orbit splitting constant, Λ is the orbital angular momentum quantum number, and M_S is the spin quantum number associated with a particular level $\Omega = \Lambda + M_S$. E^{SO} is also equal to $\Sigma \, a_i \, \ell_i \bullet s_i$, where $\ell_i \bullet s_i$ is the dot product of the orbital angular momentum and the spin of electron i and a_i is the spin-orbit parameter,[64] which can be represented by the atomic spin-orbit parameter for the *6d* electrons of thorium $\zeta_{6d}(Th) = 1458$ cm^{-1}. Appendix A contains a detailed explanation of the values used to calculate $\zeta_{6d}(Th)$.

References

(1) Loh, S. K.; Hales, D. A.; Li, L.; Armentrout, P. B. *J. Chem. Phys.* **1989**, *90*, 5466-5485.

(2) Schultz, R. H.; Armentrout, P. B. *Int. J. Mass Spectrom. Ion Processes* **1991**, *107*, 29-48.

(3) Gerlich, D. *Adv. Chem. Phys.* **1992**, *82*, 1-176.

(4) Armentrout, P. B. *Int. J. Mass Spectrom.* **2000**, *200*, 219-241.

(5) Ervin, K. M.; Armentrout, P. B. *J. Chem. Phys.* **1985**, *83*, 166-189.

(6) Daly, N. R. *Rev. Sci. Instrum.* **1960**, *31*, 264-267.

(7) Chantry, P. J. *J. Chem. Phys.* **1971**, *55*, 2746-2759.

(8) Haynes, C. L.; Armentrout, P. B. *Organometallics* **1994**, *13*, 3480-3490.

(9) Clemmer, D. E.; Chen, Y.-M.; Khan, F. A.; Armentrout, P. B. *J. Phys. Chem.* **1994**, *98*, 6522-6529.

(10) Kickel, B. L.; Armentrout, P. B. *J. Am. Chem. Soc.* **1995**, *117*, 764-773.

(11) Kickel, B. L.; Armentrout, P. B. *J. Am. Chem. Soc.* **1995**, *117*, 4057-4070.

(12) Sievers, M. R.; Chen, Y.-M.; Elkind, J. L.; Armentrout, P. B. *J. Phys. Chem.* **1996**, *100*, 54-62.

(13) Blaise, J.; Wyart, J.-F. In *Interantional Tables of Selected Constants* Paris, 1992; Vol. 20.

(14) Sansonetti, J. E.; Martin, W. C. *J. Phys. Chem. Ref. Data* **2005**, *34*, 1559-2259.

(15) Chesnavich, W. J.; Bowers, M. T. *J. Phys. Chem.* **1979**, *83*, 900-905.

(16) Muntean, F.; Armentrout, P. B. *J. Chem. Phys.* **2001**, *115*, 1213-1228.

(17) Aristov, N.; Armentrout, P. B. *J. Am. Chem. Soc.* **1986**, *108*, 1806-1819.

(18) *NIST Computational Chemistry Comparison and Benchmark Database NIST Standard Reference Database Number 101 Release 16a*; Johnson III, R. D., Ed., August 2013.

(19) Fisher, E. R.; Kickel, B. L.; Armentrout, P. B. *J. Chem. Phys.* **1992**, *97*, 4859-4870.

(20) Sievers, M. R.; Chen, Y.-M.; Armentrout, P. B. *J. Chem. Phys.* **1996**, *105*, 6322-6333.

(21) Zhang, X.-G.; Armentrout, P. B. *J. Phys. Chem. A* **2003**, *107*, 8904-8914.

(22) Cox, R. M.; Armentrout, P. B.; de Jong, W. A. *Inorg. Chem.* **2015**, *54*, 3584-3599.

(23) Chesnavich, W. J.; Bowers, M. T. *J. Chem. Phys.* **1977**, *66*, 2306-2315.

(24) Ervin, K. M.; Armentrout, P. B. *J. Chem. Phys.* **1986**, *84*, 6750-6760.

(25) Gilbert, R. G.; Smith, S. C. *Theory of Unimolecular and Recombination Reactions*; Blackwell Scientific: Oxford, 1990.

(26) Holbrook, K. A.; Pilling, M. J.; Robertson, S. H. *Unimolecular Reactions*; Wiley: New York, 1996.

(27) Frisch, M. J.; Trucks, G. W.; Schlegel, H. B.; Scuseria, G. E.; Robb, M. A.; Cheeseman, J. R.; Scalmani, G.; Barone, V.; Mennucci, B.; Petersson, G. A.; Nakatsuji, H.; Caricato, M.; Li, X.; Hratchian, H. P.; Izmaylov, A. F.; Bloino, J.; Zheng, G.; Sonnenberg, J. L.; Hada, M.; Ehara, M.; Toyota, K.; Fukuda, R.; Hasegawa, J.; Ishida, M.; Nakajima, T.; Honda, Y.; Kitao, O.; Nakai, H.; Vreven, T.; Montgomery, J. A., Jr.; Peralta, J. E.; Ogliaro, F.; Bearpark, M.; Heyd, J. J.; Brothers, E.; Kudin, K. N.; Staroverov, V. N.; Kobayashi, R.; Normand, J.; Raghavachari, K.; Rendell, A.; Burant, J. C.; Iyengar, S. S.; Tomasi, J.; Cossi, M.; Rega, N.; Millam, N. J.; Klene, M.; Knox, J. E.; Cross, J. B.; Bakken, V.; Adamo, C.; Jaramillo, J.; Gomperts, R.; Stratmann, R. E.; Yazyev, O.; Austin, A. J.; Cammi, R.; Pomelli, C.; Ochterski, J. W.; Martin, R. L.; Morokuma, K.; Zakrzewski, V. G.; Voth, G. A.; Salvador, P.; Dannenberg, J. J.; Dapprich, S.; Daniels, A. D.; Farkas, Ö.; Foresman, J. B.; Ortiz, J. V.; Cioslowski, J.; Fox, D. J.; Gaussian, Inc: Wallingford CT, 2009.

(28) Lee, C.; Yang, W.; Parr, R. G. *Phys. Rev. B: Condens. Matter* **1988**, *37*, 785-789.

(29) Becke, A. D. *J. Chem. Phys.* **1993**, *98*, 5648-5652.

(30) Perdew, J. P.; Burke, K.; Wang, Y. *Phys. Rev. B: Condens. Matter* **1996**, *54*, 16533-16539.

(31) Becke, A. D. *J. Chem. Phys.* **1993**, *98*, 1372-1377.

(32) Zhao, Y.; Truhlar, D. G. *Theor. Chem. Acc.* **2008**, *120*, 215-241.

(33) Adamo, C.; Barone, V. *J. Chem. Phys.* **1999**, *110*, 6158-6170.

(34) Averkiev, B. B.; Mantina, M.; Valero, R.; Infante, I.; Kovacs, A.; Truhlar, D. G.; Gagliardi, L. *Theor. Chem. Acc.* **2011**, *129*, 657-666.

(35) Goncharov, V.; Heaven, M. C. *J. Chem. Phys.* **2006**, *124*, 064312.

(36) de Almeida, K. J.; Duarte, H. A. *Organometallics* **2010**, *29*, 3735-3745.

(37) Holthausen, M. C.; Heinemann, C.; Cornehl, H. H.; Koch, W.; Schwarz, H. *J. Chem. Phys.* **1995**, *102*, 4931-4941.

(38) Hinton, C. S.; Armentrout, P. B. *J. Chem. Phys.* **2010**, *133*, 124307.

(39) Hinton, C. S.; Citir, M.; Armentrout, P. B. *J. Chem. Phys.* **2011**, *135*, 234302.

(40) Pople, J. A.; Head-Gordon, M.; Raghavachari, K. *J. Chem. Phys.* **1987**, *87*, 5968-5975.

(41) Cizek, J. In *Advances in Chemical Physics*; Hariharan, P. C., Ed.; Wiley Interscience: New York, 1969; Vol. 14, p 35.

(42) Purvis, G. D., III; Bartlett, R. J. *J. Chem. Phys.* **1982**, *76*, 1910-1918.

(43) Scuseria, G. E.; Janssen, C. L.; Schaefer, H. F., III *J. Chem. Phys.* **1988**, *89*, 7382-7387.

(44) Kuechle, W.; Dolg, M.; Stoll, H.; Preuss, H. *J. Chem. Phys.* **1994**, *100*, 7535-7542.

(45) Weigand, A.; Cao, X.; Hangele, T.; Dolg, M. *J. Phys. Chem. A* **2014**, *118*, 2519-2530.

(46) Cao, X.; Dolg, M.; Stoll, H. *J. Chem. Phys.* **2003**, *118*, 487-496.

(47) Peterson, K. A. *J. Chem. Phys.* **2015**, *142*, 074105.

(48) Hess, B. A. *Phys. Rev. A* **1985**, *32*, 756-763.

(49) Hess, B. A. *Phys. Rev. A: Gen. Phys.* **1986**, *33*, 3742-3748.

(50) Jansen, G.; Hess, B. A. *Phys. Rev. A* **1989**, *39*, 6016-6017.

(51) de Jong, W. A.; Harrison, R. J.; Dixon, D. A. *J. Chem. Phys.* **2001**, *114*, 48-53.

(52) Barysz, M.; Sadlej, A. J. *J. Mol. Struct.: THEOCHEM* **2001**, *573*, 181-200.

(53) Feller, D. *J. Comput. Chem.* **1996**, *17*, 1571-1586.

(54) Schuchardt, K. L.; Didier, B. T.; Elsethagen, T.; Sun, L.; Gurumoorthi, V.; Chase, J.; Li, J.; Windus, T. L. *J. Chem. Inf. Model.* **2007**, *47*, 1045-1052.

(55) Krishnan, R.; Binkley, J. S.; Seeger, R.; Pople, J. A. *J. Chem. Phys.* **1980**, *72*, 650-654.

(56) Frisch, M. J.; Pople, J. A.; Binkley, J. S. *J. Chem. Phys.* **1984**, *80*, 3265-3269.

(57) Clark, T.; Chandrasekhar, J.; Spitznagel, G. W.; Schleyer, P. v. R. *J. Comput. Chem.* **1983**, *4*, 294-301.

(58) Karton, A.; Martin, J. M. L. *Theor. Chem. Acc.* **2006**, *115*, 330-333.

(59) Martin, J. M. L. *Chem. Phys. Lett.* **1996**, *259*, 669-678.

(60) Armentrout, P. B. *J. Chem. Phys.* **2013**, *139*, 084305.

(61) Armentrout, P. B.; Li, F.-X. *J. Phys. Chem. A* **2013**, *117*, 7754-7766.

(62) Armentrout, P. B.; Parke, L.; Hinton, C.; Citir, M. *ChemPlusChem* **2013**, *78*, 1157-1173.

(63) Garcia, M. A.; Morse, M. D. *J. Chem. Phys.* **2011**, *135*, 114304.

(64) Lefebvre-Brion, H.; Field, R. W. *The Spectra And Dynamics of Diatomic Molecules*; Elsevier: Amsterdam, 2004.

Table 2.1. Description of basis sets used in Th^+ theoretical calculations

Basis Set	ECP	Functions
SDD-VDZ[a]	MWB[a]	(12s11p10d8f)/[8s7p6d4f]
Seg. SDD-VQZ[b]	MWB	(14s13p10d8f6g)/[10s9p5d4f3g]
ANO-VQZ[b]	MWB	(14s13p10d8f6g)/[6s6p5d4f3g]
ANO-VQZ[c]	MDF[d]	(14s13p10d8f6g)/[6s6p5d4f3g]
cc-pVTZ-PP[d]	MDF	(17s16p11d10f3g1h)/[6s6p5d4f3g1h]
cc-pVQZ-PP[d,e]	MDF	(20s17p12d11f5g3h1i)/[7s7p6d5f5g3h1i]
cc-pwCVTZ-PP[d]	MDF	(17s16p11d10f4g1h)/[8s8p7d6f4g1h]
cc-pwCVQZ-PP[d]	MDF	(20s17p12d11f7g4h1i)/[9s9p8d8f7g4h1i]
cc-pVTZ[d]	DK3[f]	(33s29p20d13f3g1h)/[10s9p7d5f3g1h]
cc-pVQZ[d]	DK3	(37s34p24d15f5g3h1i)/[11s10p8d6f5g3h1i]
cc-pwCVTZ[d]	DK3	(33s29p20d13f4g1h)/[12s11p9d7f4g1h]
cc-pwCVQZ[d]	DK3	(37s34p24d15f7g4h1i)/[13s12p10d9f7g4h1i]

[a] Ref. 44. Available on the EMSL Basis Set Exchange.[53,54]
[b] Ref. 46.
[c] Ref. 45.
[d] Ref. 47.
[e] Also called KAP in Chapter 4.
[f] Full electron basis sets that utilize the Douglas-Kroll-Hess Hamiltonian.

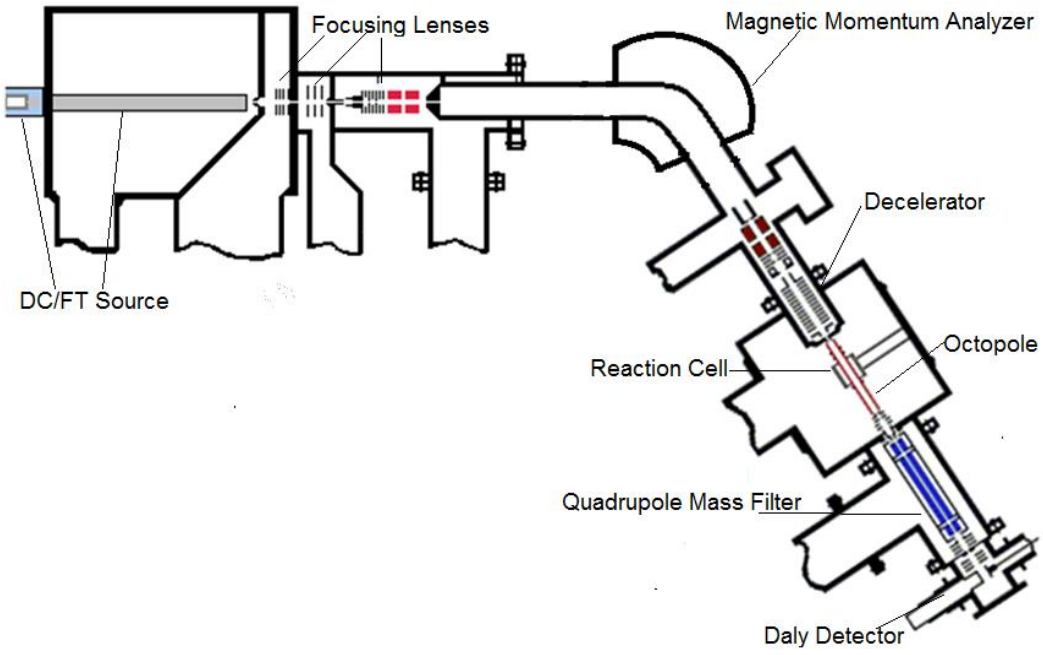

Figure 2.1. The guided ion beam tandem mass spectrometer (GIBMS).

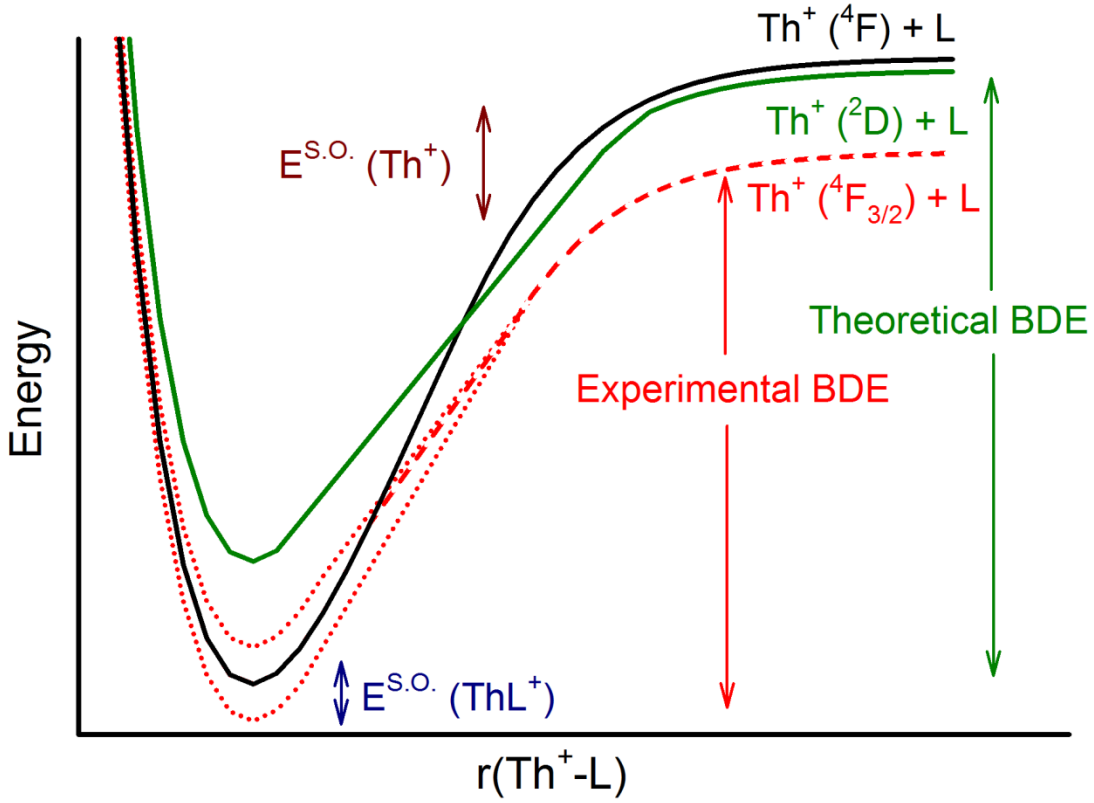

Figure 2.2 Schematic representation of the semiempirical spin-orbit energy correction applied to theoretical bond dissociation energies.

CHAPTER 3

EVALUATION OF THE EXOTHERMICITY OF THE CHEMI-IONIZATION REACTION Sm + O → $SmO^+ + e^-$

Cox, R. M; Kim, J.; Armentrout, P. B.; Bartlett, J.;

VanGundy, R. A.; Heaven, M. C.; Ard, S. G.;

Melko, J. J.; Shuman, N. S.; Viggiano, A. A.

J. Chem. Phys. 2015, 142, 134307.

Abstract

The exothermicity of the chemi-ionization reaction Sm + O → $SmO^+ + e^-$ has been re-evaluated through the combination of several experimental methods. The thermal reactivity (300 – 650 K) of Sm^+ and SmO^+ with a range of species measured using a selected ion flow tube apparatus (SIFT-MS) is reported and provides limits for the bond strength of SmO^+, 5.661 eV ≤ $D_0(Sm^+\text{-}O)$ ≤ 6.500 eV. A more precise value is measured to be 5.73 ± 0.07 eV, bracketed by the observed reactivity of Sm^+ and SmO^+ with several species using a guided ion beam tandem mass spectrometer (GIBMS). Combined with

the established Sm ionization energy, this value indicates an exothermicity of the title reaction of 0.08 ± 0.07 eV, ~0.2 eV smaller than previous determinations. In addition, the ionization energy of SmO has been measured by resonantly enhanced two-photonionization (REMPI) and pulsed-field ionization zero kinetic energy (PFI-ZEKE) photoelectron spectroscopy to be 5.7427 ± 0.0006 eV, significantly higher than the literature value. Combined with literature bond energies of SmO, this value indicates an exothermicity of the title reaction of 0.14 ± 0.17 eV, independent from and in agreement with the GIBMS result presented here. The evaluated thermochemistry also suggests that $D_0(SmO)$ = 5.83 ± 0.07 eV, consistent with but more precise than literature values. Implications of these results for interpretation of chemical release experiments in the thermosphere are discussed.

Introduction

There has long been an interest in small-scale chemical releases to alter the electron density in local regions of the atmosphere.[1] Recently, the Air Force Research Laboratory (AFRL) has conducted two releases of samarium from sounding rockets intended to artificially generate local electron density and conductivity enhancements in order to provide regional suppression of naturally occurring ionospheric scintillation. The chemistry involved starts with the reaction of the released Sm and ambient atomic oxygen to create ionization,

$$Sm + O \rightarrow SmO^+ + e^-. \qquad (3.1)$$

The experiments took place at the Reagan Test Site, Kwajalein Atoll in May 2013. Two sounding rockets were launched that reached altitudes of 170 km and 180 km.[2,3] Each rocket had canisters with 5 kg of samarium vapor released by heating with a thermite explosion, as developed by General Sciences Inc. Creation of the cloud was confirmed by observations from a host of ground-based sensors from five locations on four separate atolls in the Republic of the Marshall Islands. Models based on laboratory data of the chemi-ionization, or associative ionization, reaction (3.1) and subsequent processes predicted a higher level of ionization than was observed. The present work aims to help understand these unexpected results by reexamining the thermochemistry of reaction (3.1).

A small number of elements, primarily a subset of the lanthanides and actinides, form monoxides having ionization energies (IE) smaller than their bond dissociation enthalpies (BDE).[4] This property dictates that reactions analogous to (3.1) are exothermic and may proceed efficiently at thermal energies. In turn, this places those monoxide cations into the exclusive group of molecular cations that are stable to dissociative recombination, i.e., the reverse of reaction (3.1). Any of the species in this group are potentially effective at producing elevated electron densities at altitudes above ~100 km, where atomic oxygen is a dominant atmospheric species.

With interest in the atmospheric effects of chemistry of this type, several experiments were undertaken in the 1970s to evaluate both the kinetics and the thermochemistry of these systems. Fite et al. measured cross-sections of chemi-ionization processes by crossing beams of several atomic metals with beams of neutral O, O_2, and O_3 and monitoring the ionized products using a quadrupole mass spectrometer.[5-9] These

results, summarized in a technical report[10] to the Air Force Geophysics Laboratory (now AFRL), indicated cross sections for reactions analogous to (3.1) of between ~10^{-17} to 10^{-15} cm^2, equivalent to room temperature rate constants of ~10^{-12} to 10^{-10} cm^3 s^{-1}. Although the reported kinetics of Sm + O were slow, lying towards the lower end of those ranges, Sm was chosen for chemical release experiments because of its relatively high vapor pressure and the subsequently expected ease of vaporizing the metal during the release. Interestingly, the magnitude of the reported rate constants for these chemi-ionization reactions are highly correlated with the exothermicity of the reactions.

Thermochemical cycles demand that the exothermicity of reaction (3.1) is equal to either of two differences: 1) as stated above, the IE and the BDE of SmO and 2) the BDE of SmO^+ and the IE of Sm. This is illustrated in Figure 3.1, which shows a schematic representation of these energy levels. Of these four quantities, the IE of Sm is by far the most well-determined, evaluated as IE(Sm) = 5.6437 ± 0.0006 eV.[11,12] The ionization energy of SmO has been reported as IE(SmO) = 5.55 ± 0.1 eV, derived from linear extrapolation of the ionization efficiency curve of SmO^+ produced by electron impact of SmO at 2300 K.[13] This value is in agreement with a coarse determination made from the appearance energy of SmO^+ (here, the value cited of 5.5 eV also equaled the value measured for atomic Sm, indicating it is likely too low).[14] The earliest work concerning the 0 K BDE of SmO was reported by Ames et al.,[15] who found a value of 5.94 ± 0.04 eV from the vaporization of Sm_2O_3 and a third-law determination of 6.31 eV from an equilibrium of Sm-YO. Brewer and Rosenblatt later reevaluated these data, reporting BDEs of 5.72 and 5.81 eV, respectively, assigning 5.77 ± 0.35 eV as the recommended value,[16] a value also adopted by Ackermann, Rauh, and Thorn.[13]

Subsequently, Hildenbrand reported the SmO BDE as D_0(Sm-O) = 5.90 ± 0.09 eV, derived from measured equilibrium constants of the exchange reactions of Sm with several metal oxides (i.e., the third-law method).[14] (Specific values obtained were 5.86 ± 0.12 eV with AlO, 5.91 ± 0.13 eV with TiO, and 5.94 ± 0.15 eV for EuO.) This value is quite close to a lower limit of 5.88 ± 0.03 eV, established by measurement of the chemiluminescent spectrum of the reaction of Sm with NO_2.[17] In a subsequent review utilizing updated thermochemistry, Pedley and Marshall suggested a value of D_0(Sm-O) = 5.88 ± 0.17 eV[18] on the basis of data from Hildenbrand,[14] Ames et al.,[15] and Dickson et al.[17] In another review, Chandrasekharaiah and Gingerich[19] adopted the value of Hildenbrand and adjusted the uncertainty, 5.90 ± 0.10 eV, a value later cited by Gibson.[20] The GIANT (Gas-phase Ion And Neutral Thermochemistry) Tables compilation adopts the 298 K heat of formation for SmO suggested by Pedley and Marshall but adjusts the heat of formation to 0 K differently, such that D_0(Sm-O) = 6.04 ± 0.13 eV is calculated from the 0 K heats of formation provided.[21] More recently, Konings et al. relied primarily on the Sm-AlO equilibrium values from Hildenbrand[14] (ignoring the Sm-TiO and Sm-EuO equilibria for reasons left unstated) and assign the SmO BDE as D_0(Sm-O) = 5.76 ± 0.08 eV.[22] Adopting the more inclusive and conservative value from Pedley and Marshall,[18] the difference between the SmO IE and BDE yields $\Delta_r H_0^o$ for reaction (3.1) of -0.33 ± 0.20 eV.

For the cationic species, a value of $D_0(Sm^+\text{-}O)$ = 5.97 ± 0.20 eV may be derived from the adopted literature values above. This is essentially equivalent to the value cited by Murad and Hildenbrand, 5.98 ± 0.13 eV, who used an earlier spectroscopic value for IE(Sm) = 5.63 eV.[23] Ackermann et al.[13] cited 5.80 ± 0.10 eV using their IE values for

both Sm (5.58 eV) and SmO along with the Brewer and Rosenblatt neutral BDE. Chandrasekharaiah and Gingerich[19] (whose value is also adopted by Gibson)[20] reported $D_0(Sm^+\text{-}O) = 5.86 \pm 0.16$ eV, but the 0 K heats of formation for Sm, Sm^+, SmO, and SmO^+ provided in this reference indicate IE(Sm) = 3.49 eV and IE(SmO) = 3.55 eV, which are clearly incorrect. (Neither the specific IE values used nor their origins are provided in this work.) Finally, heats of formation given in the GIANT Tables suggest $D_0(Sm^+\text{-}O) = 6.14 \pm 0.16$ eV.[12] This literature thermochemistry is largely supported by CASSCF *ab initio* calculations, differing significantly only in that the calculations produce a lower BDE for SmO^+ of 5.74 eV.[24] These calculations also indicate $D_0(Sm\text{-}O)$ = 5.92 eV, IE(SmO) = 5.58 eV, and IE(Sm) = 5.69 eV. However, the authors do not address the discrepancy that the sum of the theoretically calculated IE(SmO) and BDE of SmO^+ is 0.29 eV less than the sum of the calculated SmO BDE and IE(Sm) (see Fig. 3.1).

The lower-than-expected electron density observed in the Sm release experiments raises questions about the seemingly established thermochemistry of the reaction. That the chemi-ionization reaction involving Sm was observed in the experiment by Fite et al.[10] strongly suggests that the reaction is exothermic. Later efforts by Cockett et al.[25] report an upper bound to the reaction exothermicity of reaction (3.1) as 0.27 ± 0.08 eV (on the basis of the maximum electron kinetic energy observed) that is in good agreement with the accepted literature value reported above. However, this reported exothermicity may be influenced by excited-states as Sm samples were vaporized at 800 K. A population analysis indicates that at 800 K Sm has an average internal electronic energy of 0.07 eV with significant populations at the $^7F_2$ (25%), $^7F_3$ (10%), and $^7F_4$ (3%) levels that have energies lying 0.10, 0.18, and 0.28 eV, respectively, above the ground $^7F_0$

level.[26] As discussed below, the magnitude of the exothermicity could have large effects on the efficiency of the chemical release efforts. Here, the exothermicity of the title reaction is re-evaluated through two independent determinations: measurement of $D_0(Sm^+\text{-}O)$ and measurement of IE(SmO). Additionally, the thermal reactivity of Sm^+ and SmO^+ with a number of species is investigated.

Experimental and Theoretical Methods

Selected Ion Flow Tube (SIFT) Apparatus

The Air Force Research Laboratory's variable temperature selected ion flow tube instrument (VT-SIFT) has been described in detail elsewhere.[27] Sm^+ and SmO^+ ions are created in a newly implemented electrospray ion source.[28] An approximately 1mM solution of samarium iodide in methanol flows at 150 μL hr^{-1} through a fused silica capillary biased to approximately 4000 V in open atmosphere. The spray enters vacuum through a dielectric capillary heated to 100 °C for increased desolvation. The ions formed are focused by an ion funnel and lenses, then transported by a rectilinear ion guide and ion bender to a quadrupole mass filter where either the Sm^+ or SmO^+ ions are isolated.

The ions are focused before introduction to a laminar flow tube via a Venturi inlet, where ~10^4 to 10^5 collisions with a He buffer gas act to thermalize the ions and carry them downstream. Operating pressures of 0.4 Torr of He are typical; however, for several of the reactions observed, the operating pressure in the flow tube was varied up to 0.8 Torr in order to identify termolecular processes. The neutral reagent (O_2, N_2O, NO_2, NO, CO_2, SO_2) is added 59 cm upstream of the end of the flow tube, with typical reaction times on the order of 4 ms, dependent upon flow tube pressure and temperature. After

traveling the length of the flow tube, the core of the flow is sampled through a truncated nose-cone with a 2 mm aperture. The remainder of the flow is pumped away by a roots pump through a throttled gate valve that acts to maintain the desired pressure within the flow tube. After the nose-cone, the primary ions and product ions are guided by a lens stack to a quadrupole mass filter for analysis, and are subsequently detected using an electron multiplier operated in counting mode. Rate constants are derived by monitoring the decay of the primary ion as a function of the neutral reagent flow. Measurements were made from approximately 300 K to 650 K and temperature dependences of the rate coefficients were determined. Uncertainties in the rate coefficients are estimated to be ±25% absolute and ±15% relative to each other.[27]

Guided Ion Beam Tandem Mass Spectrometer

The guided ion beam tandem mass spectrometer (GIBMS) at the University of Utah used in these studies has been described previously.[29] Briefly, Sm^+ and SmO^+ ions are created in a direct current discharge flow tube (DC/FT) source described in detail elsewhere.[30] Sm^+ ions are created when Ar ionized by a dc electric field (1.2 – 1.4 kV) collides with a cathode holding the samarium foil sample. Ions typically thermalize under ~10^5 collisions with the He/Ar carrier gasses in a 9:1 mixture in a 1 m flow tube held at a total pressure of 0.5 Torr. To further ensure thermalization, O_2 or SO_2 gas is introduced to the flow tube 15 cm downstream from the ion source to quench any excited-state ions. SmO^+ ions are created by introducing O_2 gas through the same inlet. Previous work in our laboratory has indicated that the DC/FT source produces atomic metal cations with an internal electronic energy of 300 – 1100 K.[31-35] At 300 K, 67.8% of Sm^+ ions are found in

the $^8F_{1/2}$ ground-level. At 1100 K, 21.1% of ions are found in the $^8F_{1/2}$ ground-level.[26] Conservatively, we estimate that the average internal temperature of the Sm^+ ions is 700 ± 400 K, for an average internal energy of 0.06 ± 0.05 eV that is incorporated in all reported BDEs. The internal energies of SmO^+ ions are presumed to be at 300 K.

Ions are extracted from the source and focused through a magnetic momentum analyzer, where the reactant ion is mass selected. To ensure efficient mass separation between the several abundant isotopes of Sm, the second most abundant and heaviest isotope, ^{154}Sm (22.7% abundance), was chosen because it is separated from the next closest isotope by 2 amu. These ions are subsequently decelerated to a well-defined kinetic energy and passed into a radiofrequency (rf) octopole ion beam guide,[36-38] where the ions are trapped radially. The octopole passes through a static gas cell that contains the neutral reactant gas at pressures of 0.10 - 0.40 mTorr. Pressures are low to ensure that the probability of more than one collision occurring between the reactants is small, and it was verified that the measured cross sections reported below do not vary with neutral reactant pressure. After the collision cell, remaining reactant and product ions drift to the end of the octopole, are focused through a quadrupole mass filter for mass analysis, and counted using a Daly detector.[39] Reaction cross sections are calculated, as described previously, from product ion intensities relative to reactant ion intensities after correcting for product ion intensities with the neutral gas no longer directed to the gas cell. Uncertainties in the measured absolute cross sections are estimated to be ±20%, with relative uncertainties of ±5%.

Laboratory ion energies (lab) are converted to the center-of-mass frame (CM) using the relationship $E_{CM} = E_{lab} \times m/(m + M)$ where m and M are the masses of the

neutral and ionic reactants, respectively. The absolute zero of energy and the full width at half-maximum (FWHM) of the ion beam are determined by using the octopole guide as a retarding potential analyzer.[37] Typical FWHMs of the energy distribution for these experiments were 0.4 - 0.6 eV (lab). Uncertainties in the absolute energy scale are 0.1 eV (lab). All energies reported below are in the CM frame.

GIBMS Data Analysis

The kinetic energy dependence of endothermic reactions observed using the GIBMS is modeled using Eq. (3.2),[38,40,41]

$$\sigma(E) = \sigma_0 \Sigma\, g_i\,(E + E_i - E_0)^n/E \qquad (3.2)$$

where σ_0 is an energy-independent scaling factor, E is the relative kinetic energy of the reactants, E_i is the internal energy of the reactants' electronic, vibrational, and rotational states having populations g_i ($\Sigma g_i = 1$), n is an adjustable parameter, and E_0 is the 0 K reaction threshold. Before comparison to the data, Eq. (3.2) is convoluted over the kinetic energy distributions of the reactants.[37,42,43] The σ_0, n, and E_0 parameters are then optimized using a nonlinear least-squares method to best reproduce the experimental cross section. Uncertainties in E_0 are calculated from the threshold values for several independent data sets over a range of n values combined with the absolute uncertainties in the kinetic energy scale and internal energies of reactant ions. For exchange reactions, calculated thresholds are then used to determine BDEs, $D_0(Sm^+\text{-}R)$, using relationship (3.3):

$$D_0(Sm^+\text{-}R) = D_0(L\text{-}R) - E_0 \quad (3.3)$$

This equation assumes that there are no barriers in excess of the endothermicity of the reaction. When evidence of a barrier exists, Eq. (3.3) provides a lower limit to the true BDE. Neutral BDEs, D_0(L-R), were taken from thermochemistry found in the NIST webBook.[44]

REMPI and PFI-ZEKE

The ionization energy (IE) of SmO was determined by means of resonantly enhanced two-photon ionization measurements. The experiments were performed at Emory University using an apparatus that has been described in previous publications.[45] Gas phase SmO was produced using pulsed laser vaporization (1064 nm) of a pure Sm rod (ESPI Metals, natural isotopic composition). The metal vapor was entrained in a pulse of He that contained 1% O_2. The products from the ablation source were cooled by supersonic expansion. The vacuum chamber that housed the ablation source was equipped for interrogation of the products using laser-induced fluorescence (LIF). A pulsed tunable dye laser (Lambda Physik, Scan-Mate Pro, 0.15 cm^{-1} linewidth, 10 ns pulse duration) was used as the excitation source. The absolute wavenumber calibration of this laser was established by recording previously characterized bands of SmO.[46,47]

For photo-ionization measurements, the core of the supersonic expansion was sampled, via a conical skimmer, into a second vacuum chamber. This was equipped with a Wiley-McLaren time-of-flight mass spectrometer and a separate set of microchannel plates for photoelectron detection.[45] The Scan-Mate Pro dye laser was used for the first

excitation step. Ionization was achieved using pulses from a second Nd/YAG pumped dye laser (Continuum ND6000, 0.1 cm^{-1} linewidth, 10 ns pulse duration). Wavelengths in the 300 - 330 nm range were generated by frequency doubling, and the absolute wavenumber calibration for the ND6000 was obtained by using the fundamental to record the B-X spectrum of I_2.[48]

Photo-ionization efficiency (PIE) curves were recorded with the first laser tuned to an established electronic transition of SmO, and the wavelength of the second laser was swept to locate the ionization threshold. For these scans, the mass spectrometer was used to monitor the signals resulting from the most abundant isotopologs ($^{152}SmO^+$ and $^{154}SmO^+$). The threshold energy was then refined by means of pulsed-field ionization zero kinetic energy (PFI-ZEKE) photoelectron spectroscopy.

Experimental Results

SIFT Results

The reactions of Sm^+ with several common oxygen-donating molecules are shown in Table 3.1. The LO bond energy is also shown as a guide to the expected reaction exothermicity, which is simply the difference between the BDEs of LO and SmO^+. The room temperature rate constants for the reactions with N_2O, O_2, and NO_2 agree very well with those in the literature.[49-51] The previously reported formation of SmO^+ from reaction with NO was not observed, which is consistent with similar differences in NO reactivity that have been reported previously for other metals.[52-55] Table 3.1 shows that the efficiencies of these reactions show no clear correlation with the LO bond energy, and therefore the reaction exothermicity. The temperature dependences are typical for

exothermic reactions such as these. The reaction with SO_2 serves to provide a rigorous lower limit to the bond strength of SmO^+ of 5.661 ± 0.014 eV, whereas the null reaction with NO serves as a tentative upper limit of 6.500 eV. This limit is tentative because kinetic barriers may be present in the reaction path. Indeed such barriers seem likely in the null reaction observed for CO_2,[56,57] which has a lower LO bond energy than SO_2 such that the $Sm^+ + CO_2 \rightarrow SmO^+ + CO$ reaction must be exothermic. GIBMS experiments verify the presence of these kinetic barriers in both cases.[57]

The lower limit of 5.661 ± 0.014 eV for $D_0(SmO^+)$ combined with IE(Sm) dissociative recombination reaction is endothermic. Given this conclusion, we considered the possibility of continued oxidation of the SmO^+ cation. Reactions of SmO^+ with each of the oxygen donating neutrals, other than NO, were then studied and are shown in Table 3.2. In all cases, these reactions led only to cluster formation, with no bimolecular reactions being observed. Termolecular rate constants are derived from measured effective two-body rate constants over pressure ranges of 0.4 – 2 Torr; however, the likely small bond energies of these clusters suggest thermal or electric field excitation may result in cluster dissociation prior to detection, resulting in potentially large error. As expected, clustering to each of the triatomic species was significantly faster than for O_2, which was too slow for a rate to be established. Clustering with SO_2 and NO_2 was an order of magnitude faster than for N_2O and CO_2, implying larger bond energies for these species.

In regards to the lower-than-expected electron density observed by the recent chemical release, the SIFT work has several important findings. The reaction of Sm^+ with SO_2 firmly establishes that reaction (3.1) is exothermic. A more precise magnitude of this

exothermicity is pursued using the GIBMS and REMPI studies reported below. The reaction of Sm^+ with O_2 shows that any Sm^+ formed by either thermal or photo-ionization will quickly react to form SmO^+, as opposed to species where dissociative recombination may play a larger role in limiting the electron density. Furthermore, it was found that SmO^+ will not further oxidize, which would result in electron sinks via dissociative recombination of the larger product ions. The only observed reactions with SmO^+, clustering, will have little to no impact for these results, given the low atmospheric densities at these altitudes.

GIBMS Results

$Sm^+ + LO$ (L = O, SO, C)

A key feature of the GIBMS is the ability to study the kinetic energy dependence of a reaction over a large range of energies. This feature allows for the direct determination of a BDE from an endothermic process. Given the scope of this project, reactions of Sm^+ with N_2O and NO_2 were not studied using GIBMS because the BDE of these O donors are much smaller than the expected SmO^+ BDE (Table 3.1), and therefore, are not expected to yield much additional information beyond the SIFT experiments. Reactions of Sm^+ with CO_2 and NO were studied using GIBMS, and the failure of both reactions to yield SmO^+ at thermal energies found in the SIFT studies was confirmed (Table 3.1). In both cases, these reactions have interesting kinetic features that are beyond the scope of this text and will be published elsewhere.[57]

The kinetic energy dependent cross sections from the reaction of Sm^+ and O_2 are found in Fig. 3.2. In this reaction, two products were observed according to reactions

(3.4) and (3.5).

$$Sm^+ + O_2 \rightarrow SmO^+ + O \quad (3.4)$$

$$Sm^+ + 2\,O_2 \rightarrow SmO_2^+ + 2\,O \quad (3.5)$$

The cross section of SmO^+ from reaction (3.4) is consistent with an exothermic and barrierless process as the cross section declines with increasing energy. Reaction (3.4) is observed to occur with unit efficiency, $k/k_{col} = 1.0 \pm 0.2$, where k_{col} is defined as the Su-Chesnavich semiclassical trajectory rate constant.[58] The cross section of reaction (3.5) is observed to be dependent on the pressure of the O_2 reactant partner, indicating that it is the product of sequential reactions, i.e., $SmO^+ + O_2$. The observation that this reaction exhibits a substantial barrier is consistent with the failure of the SIFT studies to observe this reaction at thermal energies.

The efficiency of reaction (3.4), observed using GIBMS, is significantly larger than that observed in SIFT experiments, where the present work observes an efficiency of $k/k_{col} = 0.49 \pm 0.15$ and previous work by Koyanagi and Bohme[50] observed an efficiency of $k/k_{col} = 0.48 \pm 0.14$. To ensure that the efficiency of reaction (3.4), observed using GIBMS, is not a result of excited-state ions, the reaction was repeated while leaking O_2 into the source flow tube region. This approach selectively removes ions with excessive internal energy; however, no effect on the overall efficiency of reaction (3.4) was observed. We therefore have no explanation for this discrepancy, the cause of which may be interesting. Fortunately, the difference is of no consequence to the primary purpose of this paper, i.e., the thermodynamics of reaction (3.1).

The kinetic energy dependent cross sections from the reaction of Sm^+ and SO_2 are found in Fig. 3.3 and are in accord with the SIFT results. At all energies, the dominant product is SmO^+ formed according to reaction (3.6):

$$Sm^+ + SO_2 \rightarrow SmO^+ + SO \quad (3.6)$$

The SmO^+ cross section declines with an energy dependence similar to the Su-Chesnavich cross section until ~ 1 eV, where the cross section levels off. A secondary feature with an apparent threshold near 1.5 eV and a peak at 5.5 eV is also observed. The energy of the peak corresponds nicely to $D_0(OS\text{-}O) = 5.66$ eV, indicating that the SmO^+ cross section declines because the $Sm^+ + O + SO$ channel becomes available at this energy. The efficiency of reaction (3.6) is $k/k_{col} = 0.22 \pm 0.04$, which is similar to the 0.29 ± 0.09 observed in the SIFT experiments here.

Samarium ions react with SO_2 to form additional products according to reactions (3.7) – (3.9).

$$Sm^+ + SO_2 \rightarrow SmSO_2^+ \quad (3.7)$$

$$\rightarrow SmSO^+ + O \quad (3.8)$$

$$\rightarrow SmO_2^+ + S \quad (3.9)$$

Reaction (3.7) is observed at the lowest energies with a cross section that is consistent with an exothermic, barrierless reaction. Furthermore, no pressure dependence for the cross section was observed, indicating that this species is not collisionally stabilized. The

observation of the $SmSO_2^+$ adduct as a long-lived intermediate is likely a result of the large dipole moment (1.63 D)[44] and polarizability (3.22 $Å^3$)[44] of the SO_2 gas. The threshold of reaction (3.8) has an apparent onset near 3.5 eV and peaks at ~ 5.7 eV, again corresponding to D_0(OS-O). Reaction (3.9) has an apparent threshold of ~ 4.5 eV and peaks near ~ 6 eV. A secondary feature with an apparent onset near 8 eV is also observed. The product from reaction (3.9) is identified as SmO_2^+ (rather than the isobaric $^{154}Sm^{32}S^+$) because no reaction product with a mass consistent with $^{154}Sm^{34}S^+$ was observed. In addition, the SmO_2^+ cross section showed no discernable pressure dependence, indicating that this product is formed in a single ion-molecule interaction rather than a sequential reaction, such as reaction (3.5). Finally, the apparent threshold is similar to the expected threshold for reaction (3.9) given the thermochemistry reported below.

The kinetic energy dependent cross sections from the reaction of Sm^+ and CO is found in Fig. 3.4. SmO^+ and SmC^+ were observed according to reactions (3.10) and (3.11).

$$Sm^+ + CO \rightarrow SmO^+ + C \quad (3.10)$$

$$\rightarrow SmC^+ + O \quad (3.11)$$

The cross section for reaction (3.10) has an apparent threshold of ~5.5 eV and rises with increasing energy. The cross section peaks near the BDE of CO, 11.109 ± 0.005 eV,[44] where enough energy is available for SmO^+ to dissociate to Sm^+ and O. Reaction (3.11) has an apparent threshold near 8.5 eV and rises with increasing energy until peaking

again near $D_0(CO)$. Note that the apparent threshold is consistent with a BDE for SmO^+ in the vicinity of 5.6 eV, close to that expected from the literature thermochemistry. A precise determination of this threshold and the resultant $D_0(SmO^+)$ is discussed below.

$\underline{SmO^+ + Xe/O_2}$

Reactions of SmO^+ with Xe and O_2 were also performed. The cross section from the collision-induced dissociation (CID) reaction (3.12),

$$SmO^+ + Xe \rightarrow Sm^+ + O + Xe \qquad (3.12)$$

is found in Fig. 3.5. This reaction has an apparent threshold of ~ 6 eV, again roughly consistent with the literature thermochemistry. Although not obvious from the logarithmic scale of Fig. 3.5, the CID cross section rises rather slowly and reaches a relatively small magnitude of only 0.15×10^{-16} cm^2 at 15 eV, consistent with the need to break a relatively strong diatomic bond. The kinetic energy dependent cross sections for the reaction of SmO^+ and O_2 are found in Fig. 3.6. Products are observed according to reactions (3.13) and (3.14).

$$SmO^+ + O_2 \rightarrow SmO_2^+ + O \qquad (3.13)$$

$$\rightarrow Sm^+ + O + O_2 \qquad (3.14)$$

Reaction (3.13) has an apparent threshold of 3.5 eV and rises in intensity until ~ 6 eV, where it begins to decline. Reaction (3.14) has an apparent threshold similar to that

observed for reaction (3.12), substantiating the CID mechanism listed in reaction (3.14), as opposed to concomitant formation of ozone, discussed further below. Notably, this CID cross section rises more rapidly than that of reaction (3.12), which suggests that determination of the threshold energy from this reaction is more reliable.

REMPI and PFI-ZEKE Results

LIF spectra for SmO were recorded to locate a suitable transition for the first excitation step and to characterize the internal temperature of the jet-cooled ablation products. The origin band of the [16.6]1-X0$^-$ transition proved to be suitable for this purpose. Because of the large number of Sm isotopes, the spectrum was not rotationally resolved. However, the P/Q/R branch structure was easily recognizable, as can be seen in Fig. 3.7. The lower trace in Fig. 3.7 is a simulation of the rotational band contour, performed using the molecular constants for ^{152}SmO and ^{154}SmO from Bujin and Linton,[47] the program PGOPHER,[59] and a rotational temperature of about 10 K. Note that the difference between the simulation and the LIF spectrum in the region between the P- and Q-branch contours is a result of neglecting the less abundant isotopes of Sm, for which spectroscopic constants were not reported. (^{152}Sm and ^{154}Sm have natural abundances of 26.75 and 22.75%, respectively). At a rotational temperature of 10 K, the Q-branch was heavily overlapped, and by far the most intense part of the band contour. Consequently, the photo-ionization measurements were carried out with the first laser tuned to the maximum of the Q-branch (16585.5 cm^{-1}).

The ablation products were further characterized by recording the mass spectrum. To probe the widest range of species, one color non-resonant two-photon excitation at

310 nm was employed. The resulting mass spectrum contained only the Sm^+ and SmO^+ signals, with relative Sm isotopic peak intensities that were consistent with the natural abundances. Larger molecular species did not appear to be formed under the jet expansion conditions used.

A two-color PIE scan for SmO is presented in Fig. 3.8. Here it can be seen that the threshold for SmO^+ ion production was located at a two-photon energy of 46226 ± 10 cm^{-1}. This trace was recorded with the ionization lasers positioned between the repeller plate and the draw-out grid of the mass spectrometer, where the local field was F= 250 V cm^{-1}. This field depresses the IE by an energy of $\Delta E\left(cm^{-1}\right) = 6.12\sqrt{F(V\ cm^{-1})}$, which is 97 cm^{-1} in this instance. Correcting for this effect yields an initial estimate for the IE of SmO of 46323 ± 10 cm^{-1}. Care was needed to ensure that the threshold observed was a two-color resonance, as features arising from two-photon excitation by the second laser alone were commonly encountered. The density of electronically excited-states of SmO in the near uv spectral range is high, which is easily appreciated given that the ground-state has the electronic configuration $Sm^{2+}(4f^5 6s)O^{2-}$. The signal-to-noise ratios of the PIE trace, and the PFI-ZEKE scan shown in Fig. 3.8 (see below), were low because the laser intensities were attenuated to suppress one-color multiphoton processes.

A PFI-ZEKE spectrum was recorded with the first laser tuned to the Q-branch feature noted above. The most populated rotational level within this feature was J=3, so levels of the intermediate state with J=1-4 were significantly populated. Fig. 3.9 shows the PFI-ZEKE spectrum. The PFI-ZEKE measurement relies on the fact that the high-n Rydberg states that are just below the ionization threshold are long-lived. SmO was excited to the Rydberg states under field-free conditions. After a delay of 2 ms, a 0.36 V

cm^{-1} field was applied to remove electrons from the Rydberg states and accelerate them to the microchannel plate detector. The time delay is used to suppress the signal from any process that causes direct ionization. Hence, the blue-edge of the PFI-ZEKE feature corresponds to the convergence limit of the Rydberg-series, and thereby defines the IE. It is helpful to contrast the fact that the PFI-ZEKE scan shows the energy levels immediately below the ionization threshold, whereas the PIE curve shows the continuum and auto-ionizing states above the threshold. After local field corrections, it is expected that the red threshold of the PIE curve and the blue-edge of the PFI-ZEKE spectrum will coincide with the IE. The data shown in Fig. 3.9 yielded an IE of 46318 ± 5 cm^{-1} (5.7427 ± 0.0006 eV), in good agreement with the less accurate value from the PIE scan.

Tests were conducted to ensure that the observed PFI-ZEKE threshold corresponded to the intended sequential excitation process that passed through the [16.6]1, v'=0 state. The peak in Fig. 3.9 was only observed when the first laser was tuned to the more intense regions of the [16.6]1-$X0^-$ rotational contour.

Thermochemical Results

SmO^+

In SIFT-MS experiments, SmO^+ was observed in reactions with N_2O, NO_2, O_2 and SO_2, but was not observed in reactions with CO_2 and NO. The results of all these reactions, with the exception of CO_2, are consistent with the literature BDE for SmO^+ of 5.97 ± 0.20 eV. Previous SIFT-MS experiments observed the formation of $Sm^+(CO_2)_{1-3}$, indicating that the anomalous results from the CO_2 reaction can be attributed to a barrier to the reaction in excess of thermal energies.[56] In GIBMS experiments that will be

reported elsewhere, we confirm the presence of this barrier.[57] The results of the SIFT-MS experiments indicate that $D_0(Sm^+\text{-}O) \geq D_0(OS\text{-}O) = 5.661 \pm 0.014$ eV, and probably that $D_0(Sm^+\text{-}O) < D_0(N\text{-}O) = 6.500 \pm 0.004$ eV .

In GIBMS experiments, SmO^+ was observed to form exothermically in reactions (3.4) and (6) in direct agreement with the SIFT-MS experiments. Modeling of the SmO^+ cross section for reaction (3.10) using Eq. (3.2) indicates a threshold, $E_0 = 5.49 \pm 0.12$ eV. Parameters used in Eq. (3.2) for this and all other modelled reactions can be found in Table 3.3. Using Eq. (3.3) and $D_0(C\text{-}O) = 11.109 \pm 0.005$ eV,[44] this yields $D_0(Sm^+\text{-}O) = 5.62 \pm 0.15$ eV. This value is consistent with the results from reaction (3.6) and within experimental uncertainties of the literature values.

Additionally, $D_0(Sm^+\text{-}O)$ was measured in CID reactions with Xe and O_2 used as the collision gas with thresholds of 5.67 ± 0.16 eV and 5.78 ± 0.09 eV, respectively, which in both cases are direct measures of the desired BDE. In this instance, the slow onset in the cross section for reaction (3.12) leads to the larger uncertainty. By contrast, the sharp rise in the threshold for the cross section of reaction (3.14) suggests that the value $D_0(Sm^+\text{-}O) = 5.78 \pm 0.09$ eV is more reliable. The agreement in the threshold energies for these two CID processes also provides support that reaction (3.14) rather than (3.15) is responsible for the Sm^+ product.

$$SmO^+ + O_2 \rightarrow Sm^+ + O_3 \qquad (3.15)$$

The threshold for reaction (3.15) is lower than that for (3.14) by $D_0(O_2\text{-}O) = 1.05 \pm 0.02$ eV,[44] a result that is clearly inconsistent with the results from modeling with Eq. (3.2) as

listed in Table 3.3. In some cases, the threshold measured in CID reactions of strongly bound molecules like SmO^+ is conservatively reported as an upper limit to the true BDE because of inefficiencies in the energy transfer needed to dissociate the reactant.[60-62] In the present case, however, the excellent agreement between BDEs derived from the CID values, from reaction (3.10), and the literature suggest that this is a good measure of the SmO^+ BDE.

The $D_0(Sm^+\text{-}O)$ values measured from reactions (3.10), 5.62 ± 0.15 eV, (3.13), 5.67 ± 0.16 eV, and (3.14), 5.78 ± 0.09 eV are within experimental uncertainty of each other. A weighted average of all three values yields $D_0(Sm^+\text{-}O) = 5.72_5 \pm 0.07$ eV (one standard deviation). This value agrees with the literature values within experimental uncertainties and is in good agreement with theoretical work, $D_0(Sm^+\text{-}O) = 5.74$ eV.[24] Combined with IE(Sm) = 5.6437 eV, our BDE indicates that the chemi-ionization reaction (3.1) is exothermic by only -0.08 ± 0.07 eV, substantially less than originally thought. Combined with IE(SmO) = 5.7427 eV, the SmO^+ BDE indicates that $D_0(SmO) = 5.83 \pm 0.07$ eV, in good agreement with the previously recommended experimental values of 5.88 ± 0.17 eV[18] and 5.76 ± 0.08 eV,[22] and reasonable agreement with theoretical work, $D_0(Sm\text{-}O) = 5.92$ eV.[24]

Other Thermochemical Results

In the course of the present work, several other Sm^+ species were observed in the GIBMS studies in addition to SmO^+. With the exception of SmO_2^+, which was previously observed in laser ablation spectroscopic studies in Ar matrices by Willson and Andrews,[63] these species have not been previously reported. They report a linear structure

but no energetics associated with its formation. The formation of SmO_2^+ was observed here in reactions (3.5), (3.9), and (3.13). Reaction (3.5) is pressure-dependent and is a subsequent reaction of SmO^+ formed in reaction with another O_2, i.e. reaction (3.13), to form SmO_2^+. The threshold measured using Eq. (3.2) for reaction (3.13) is E_0 = 3.98 ± 0.15 eV. Using Eq. (3.3) with D_0(O-O) = 5.117 ± 0.001 eV, this indicates that $D_0(OSm^+\text{-}O)$ = 1.14 ± 0.15 eV. When this value is combined with $D_0(Sm^+\text{-}O)$ derived above, $D_0(Sm^+\text{-}O_2)$ = 1.76 ± 0.17 eV can be determined using Eq. (3.16).

$$D_0(Sm^+\text{-}O_2) = D_0(OSm^+\text{-}O) + D_0(Sm^+\text{-}O) - D_0(O\text{-}O) \qquad (3.16)$$

This bond energy can be combined with $D_0(S\text{-}O_2)$ = 5.897 ± 0.003 eV[44] to determine an expected threshold for reaction (3.9) of E_0 = 4.14 ± 0.17 eV. This is consistent with the apparent threshold for this reaction as observed in Fig. 3.3; however, this cross section was not modelled using Eq. (3.2) because of the low signal intensity.

The BDEs of $SmSO^+$ and SmC^+ were also determined by modelling the cross sections for reactions (3.8) and (3.11), respectively, using Eq. (3.2) and then using Eq. (3.3) to convert the E_0 threshold energies listed in Table 3.3 to BDEs. For reaction (3.8), E_0 = 3.86 ± 0.08 eV, indicating that $D_0(Sm^+\text{-}SO)$ = 1.80 ± 0.08 eV given D_0(O-SO) = 5.661 ± 0.014 eV. For reaction (3.11), E_0 = 8.95 ± 0.07 eV, indicating that $D_0(Sm^+\text{-}C)$ = 2.16 ± 0.07 eV, given D_0(C-O) = 11.109 ± 0.005 eV.[44]

Discussion

Chemi-ionization Reaction

At the time of the chemical release, reaction (3.1) was assumed to be exothermic by 0.33 ± 0.20 eV on the basis of $D_0(SmO) = 5.88 \pm 0.17$ eV evaluated by Pedley and Marshall[18] along with IE(SmO) = 5.55 ± 0.10 eV reported by Rauh and Ackermann.[13] (The subsequent evaluation by Konings et al.[22] suggests a smaller exothermicity of 0.21 ± 0.08 eV.) Both values are within experimental uncertainty of the value measured directly by Cockett et al., 0.28 ± 0.07 eV;[25] however, these data may be unduly influenced by excited-states, as discussed above. The present PFI-ZEKE results show that the electron impact ionization energy of SmO is too low by ~0.2 eV and greatly improves the precision of this value. Combined with the neutral bond energies, IE(SmO) = 5.7427 ± 0.0006 eV indicates that the exothermicity of reaction (3.1) decreases by 0.19 eV to 0.14 ± 0.17 or 0.02 ± 0.08 eV, depending on the adopted $D_0(SmO)$. These values are independently verified by combining $D_0(Sm^+\text{-}O) = 5.72_5 \pm 0.07$ eV from the present GIBMS results with IE(Sm) = 5.6437 ± 0.0006 eV. Doing so yields an exothermicity of 0.08 ± 0.07 eV, within experimental uncertainty of any of the IE(SmO) – $D_0(SmO)$ values and midway between the values derived from the updated and evaluated recommendations for $D_0(SmO)$. Conversely, combining our $D_0(Sm^+\text{-}O)$ and IE(SmO) values provides $D_0(SmO) = 5.83 \pm 0.07$ eV, consistent with but more precise than any literature evaluation.

The revised thermochemistry for this reaction may play a vital part in the lower than expected electron density observed in the recent Sm release. (It should be noted that this release occurred in sunlight, where photoionization could yield significant quantities

of Sm^+, which would be long-lived with respect to recombination. However, the present SIFT and GIBMS results indicate that such ions would rapidly convert to SmO^+ via the reaction with O_2, reaction (3.4).) Although the chemi-ionization reaction (3.1) remains exothermic, and thus the reverse dissociative recombination reaction endothermic, the exothermicity is far less than previously believed. At the altitude of the release, ~200 km, the electron energy distribution is reasonably described by a temperature of ~1000 K, Fig. 3.10. A significantly larger fraction of this electron distribution has enough energy to overcome the updated 0.08 eV barrier to recombination (Fig. 3.10), potentially leading to an equilibrium preventing full ionization of the released samarium and leading to the observed low electron density. The equilibrium constant of reaction (3.1) may be roughly estimated from the exothermicity reported here and calculation of $\Delta_r S^\circ_{1000}$= -66 J mol^{-1} K^{-1} [64,65] to be ~10^{-3} at 1000 K. Taking the forward chemi-ionization rate constant[4] to be 10^{-11} cm^3 s^{-1} yields a reverse dissociative recombination rate constant of ~10^{-8} cm^3 s^{-1}. Employing a typical ambient O atom density at 200 km to be 10^{10} cm^3, an ambient electron density of 10^5 cm^{-3}, and a density of released Sm of 10^7 cm^{-3}, a simple, zero-dimensional model suggests incomplete ionization of the Sm, with an equilibrium at about 60% ionization, the same order of magnitude as that observed. (Assuming an exothermicity for reaction (3.1) of 0.33 eV, or even 0.21 eV, would suggest complete ionization.) This estimation is crude, but sufficient to justify further study. Although dissociative recombination kinetics have been studied for a wide range of systems[66] and are almost universally rapid ($k > 10^{-7}$ cm^3 s^{-1}), no measurement has been made for any near-endothermic or thermoneutral reaction such as the reverse of reaction (3.1). Measurement of the dissociative recombination cross-section for SmO^+, or for any of the

systems with similar energetics (e.g., the much lower mass TiO^+ may be more amenable to study in a magnetic ion storage ring), would be informative.

Conclusion

We have reevaluated the exothermicity of the title reaction, $Sm + O \rightarrow SmO^+ + e^-$. The bond strength of SmO^+ has been measured as $5.72_5 \pm 0.07$ eV, using a GIBMS apparatus. Combined with the firmly established ionization energy of Sm, this gives an exothermicity of the reaction (3.1) of 0.08 ± 0.07 eV. Furthermore, we have remeasured the ionization energy of SmO using REMPI/PFI-ZEKE, finding a value of 5.7427 ± 0.0006 eV, higher than the previously reported value of 5.55 ± 0.1 eV. Combining this IE with literature values for the SmO bond strength gives exothermicities of either 0.14 ± 0.17 or 0.02 ± 0.08 eV for the reaction (3.1), independent of and in agreement with the IE(Sm) - $D_0(SmO^+)$ value, lending great confidence to the latter determination. Adopting this value suggests $D_0(SmO) = 5.83 \pm 0.07$ eV.

The exothermicity of the chemi-ionization reaction is far smaller than had been believed when the reaction was exploited to produce a local region of artificially high electron density by releasing Sm at ~200 km from a sounding rocket. This may explain the unexpectedly low electron yield observed in that release experiment, a result of incomplete ionization caused by equilibrium between the chemi-ionization reaction and the reverse dissociative recombination reaction. A significant unknown remaining in that analysis is the dissociative recombination cross-section of SmO^+ or of any other system with similar energetics (i.e., slightly endothermic to dissociative recombination).

Acknowledgements

This material is based upon work supported by the Air Force Office of Scientific Research under AFOSR Award No. FA9550-14-1-0357 (P.B.A.), FA9550-13-1-0006 (M.C.H.), and AFOSR-2303EP (A.A.V.). S.G.A. acknowledges the support of Boston College Institute of Scientific Research.

References

[1]N. S. Shuman, D. E. Hunton, and A. A. Viggiano, Chemical Reviews, in press (2015).

[2]R. G. Caton, T. R. Pederson, R. T. Paris, K. M. Groves, P. A. Bernhardt, and P. S. Cannon, 2013).

[3]K. M. Groves, R. G. Caton, T. R. Pederson, R. T. Paris, Y. Su, P. S. Cannon, N. K. Jackson-Booth, M. J. Angling, and J. M. Retterer, in *American Geophysical Union, Fall Meeting*2013).

[4]K. Schofield, J. Phys. Chem. A **110**, 6938 (2006).

[5]H. H. Lo, and W. L. Fite, Chem. Phys. Lett. **29**, 39 (1974).

[6]W. L. Fite, H. H. Lo, and P. Irving, J. Chem. Phys. **60**, 1236 (1974).

[7]P. Vasu, H. H. Lo, and W. L. Fite, Chem. Phys. Lett. **54**, 89 (1978).

[8]T. A. Patterson, M. W. Siegel, and W. L. Fite, J. Chem. Phys. **69**, 2163 (1978).

[9]J. C. Halle, H. H. Lo, and W. L. Fite, J. Chem. Phys. **73**, 5681 (1980).

[10]W. L. Fite, T. A. Patterson, and M. W. Siegeal, (Air Force Geophysics Laboratory, 1977).

[11]T. Jayasekharan, M. A. N. Razvi, and G. L. Bhale, J. Phys. B: At., Mol. Opt. Phys. **33**, 3123 (2000).

[12]S. G. Lias, and J. E. Bartmess, (National Institute of Standards and Technology, Gaithersburg MD, 20899 (http://webbook.nist.gov). 2000).

[13]R. J. Ackermann, E. G. Rauh, and R. J. Thorn, J. Chem. Phys. **65**, 1027 (1976).

[14]D. L. Hildenbrand, Chem. Phys. Lett. **48**, 340 (1977).

[15]L. L. Ames, P. N. Walsh, and D. White, J. Phys. Chem. **71**, 2707 (1967).

[16]L. Brewer, and G. M. Rosenblatt, in *Adv. High Temp. Chem.*, edited by L. Eyring (Academic, New York, 1969), pp. 1.

[17]C. R. Dickson, and R. N. Zare, Chem. Phys. **7**, 361 (1975).

[18]J. B. Pedley, and E. M. Marshall, J. Phys. Chem. Ref. Data **12**, 967 (1983).

[19]M. S. Chandrasekharaiah, and K. A. Gingerich, in *Handbook on the Physics and Chemistry of Rare Earths*, edited by K. A. Gschniedner, and L. Eryring Jr. (Elsevier, Amsterdam, 1989).

[20]J. K. Gibson, J. Phys. Chem. A **107**, 7891 (2003).

[21]S. G. Lias, J. E. Bartmess, J. F. Liebman, J. L. Holmes, R. D. Levin, and W. G. Mallard, J. Phys. Chem. Ref. Data, Suppl. **17**, 1 (1988).

[22]R. J. M. Konings, O. Benes, A. Kovacs, D. Manara, D. Sedmidubsky, L. Gorokhov, V. S. Iorish, V. Yungman, E. Shenyavskaya, and E. Osina, J. Phys. Chem. Ref. Data **43**, 013101/1 (2014).

[23]E. Murad, and D. L. Hildenbrand, J. Chem. Phys. **73**, 4005 (1980).

[24]J. Paulovic, L. Gagliardi, J. M. Dyke, and K. Hirao, J. Chem. Phys. **120**, 9998 (2004).

[25]M. C. R. Cockett, L. Nyulaszi, T. Veszpremi, T. G. Wright, and J. M. Dyke, J. Electron Spectrosc. Relat. Phenom. **57**, 373 (1991).

[26]J. E. Sansonetti, and W. C. Martin, J. Phys. Chem. Ref. Data **34**, 1559 (2005).

[27]A. A. Viggiano, R. A. Morris, F. Dale, J. F. Paulson, K. Giles, D. Smith, and T. Su, J. Chem. Phys. **93**, 1149 (1990).

[28]J. J. Melko, S. G. Ard, N. S. Shuman, R. E. Pedder, C. R. Taormina, and A. A. Viggiano, manuscript in preparation.

[29]S. K. Loh, D. A. Hales, L. Li, and P. B. Armentrout, J. Chem. Phys. **90**, 5466 (1989).

[30]R. H. Schultz, and P. B. Armentrout, Int. J. Mass Spectrom. Ion Processes **107**, 29 (1991).

[31]C. L. Haynes, and P. B. Armentrout, Organometallics **13**, 3480 (1994).

[32]D. E. Clemmer, Y.-M. Chen, F. A. Khan, and P. B. Armentrout, J. Phys. Chem. **98**, 6522 (1994).

[33]B. L. Kickel, and P. B. Armentrout, J. Am. Chem. Soc. **117**, 764 (1995).

[34]B. L. Kickel, and P. B. Armentrout, J. Am. Chem. Soc. **117**, 4057 (1995).

[35]M. R. Sievers, Y.-M. Chen, J. L. Elkind, and P. B. Armentrout, J. Phys. Chem. **100**, 54 (1996).

[36]D. Gerlich, Adv. Chem. Phys. **82**, 1 (1992).

[37]K. M. Ervin, and P. B. Armentrout, J. Chem. Phys. **83**, 166 (1985).

[38]P. B. Armentrout, Int. J. Mass Spectrom. **200**, 219 (2000).

[39]N. R. Daly, Rev. Sci. Instrum. **31**, 264 (1960).

[40]W. J. Chesnavich, and M. T. Bowers, J. Phys. Chem. **83**, 900 (1979).

[41]F. Muntean, and P. B. Armentrout, J. Chem. Phys. **115**, 1213 (2001).

[42]N. Aristov, and P. B. Armentrout, J. Am. Chem. Soc. **108**, 1806 (1986).

[43]P. B. Armentrout, in *Adv. Gas Phase Ion Chem.*, edited by N. Adams, and L. M. Babcock (JAI Press, Greenwich, Connecticut, 1992), pp. 83.

[44]R. D. Johnson III, *NIST Computational Chemistry Comparison and Benchmark Database NIST Standard Reference Database Number 101 Release 16a* August 2013).

[45]M. C. Heaven, B. J. Barker, and I. O. Antonov, J. Phys. Chem. A **118**, 10867 (2014).

[46]G. Bujin, and C. Linton, J. Mol. Spectrosc. **137**, 114 (1989).

[47]G. Bujin, and C. Linton, J. Mol. Spectrosc. **147**, 120 (1991).

[48]H. Salami, and A. J. Ross, J. Mol. Spectrosc. **233**, 157 (2005).

[49]E. Murad, Int. J. Mass Spectrom. Ion Processes **58**, 159 (1984).

[50]G. K. Koyanagi, and D. K. Bohme, J. Phys. Chem. A **105**, 8964 (2001).

[51]M. J. Y. Jarvis, V. Blagojevic, G. K. Koyanagi, and D. K. Bohme, Phys. Chem. Chem. Phys. **12**, 4852 (2010).

[52]J. J. Melko, S. G. Ard, J. A. Fournier, N. S. Shuman, J. Troe, and A. A. Viggiano, J. Phys. Chem. A **116**, 11500 (2012).

[53]J. J. Melko, S. G. Ard, J. A. Fournier, N. S. Shuman, J. Troe, and A. A. Viggiano, J. Phys. Chem. A **117**, 9108 (2013).

[54]V. Blagojevic, E. Flaim, M. J. Y. Jarvis, G. K. Koyanagi, and D. K. Bohme, Int. J. Mass Spectrom. **249/250**, 385 (2006).

[55]V. Blagojevic, M. J. Y. Jarvis, G. K. Koyanagi, and D. K. Bohme, J. Phys. Chem. A **117**, 3786 (2013).

[56]P. Cheng, G. K. Koyanagi, and D. K. Bohme, J. Phys. Chem. A **110**, 12832 (2006).

[57]R. M. Cox, J. Kim, and P. B. Armentrout, manuscript in preparation.

[58]T. Su, and W. J. Chesnavich, J. Chem. Phys. **76**, 5183 (1982).

[59]C. M. Western, *PGOPHER, A Program for Simulating Rotational Structure* University of Bristol, 2007.

[60]E. R. Fisher, B. L. Kickel, and P. B. Armentrout, J. Chem. Phys. **97**, 4859 (1992).

[61]M. R. Sievers, Y.-M. Chen, and P. B. Armentrout, J. Chem. Phys. **105**, 6322 (1996).

[62]X.-G. Zhang, and P. B. Armentrout, J. Phys. Chem. A **107**, 8915 (2003).

[63]S. P. Willson, and L. Andrews, J. Phys. Chem. A **103**, 3171 (1999).

[64]M. W. Chase, Jr., C. A. Davies, J. R. Downey, Jr., D. J. Frurip, R. A. McDonald, and A. N. Syverud, J. Phys. Chem. Ref. Data, Suppl. **14**, 927 (1985).

[65]A. Kramida, Y. Ralchenko, and J. Reader, NIST Atomic Spectra Database (ver 5.2), [Online]: Available: http;//physics.nist.gov/asd National Institute of Standards and Technology: Gaithersburg, MD, (2014).

[66]M. Larsson, and A. E. Orel, *Dissociative Recombination of Molecular Ions* (Cambridge University Press, Cambridge, 2008).

Table 3.1. Reaction rate constants, efficiencies, and temperature dependence for reactions of Sm^+ with N_2O, O_2, NO_2, CO_2, SO_2 and NO measured using the VT-SIFT apparatus.

$Sm^+ + LO \rightarrow SmO^+ + L$	D_0(L-O)[a]	k_{300}[b]	k/k_{col}[c]	Literature k/k_{col}	T dep.
LO = N_2O	1.677 ± 0.001	1.3 ± 0.3	0.18 ± 0.05	0.19 ± 0.06[d]	$T^{-0.4}$
LO = NO_2	3.116 ± 0.001	6.3 ± 1.6	0.84 ± 0.21	1.0 ± 0.3[e]	$T^{-0.6}$
LO = O_2	5.117 ± 0.001	2.8 ± 0.9	0.49 ± 0.15 (1.0 ± 0.2)	0.48 ± 0.14[d]	$T^{-0.1}$
LO = CO_2	5.453 ± 0.002	NR		NR[f]	
LO = SO_2	5.661 ± 0.014	4.0 ± 1.2	0.29 ± 0.09 (0.22 ± 0.04)		$T^{-0.6}$
LO = NO	6.500 ± 0.004	NR		NR[g]	

[a] BDEs (eV) calculated from thermochemical data found in Ref. 44.
[b] Rate at 300 K (in units of 10^{-10} cm^3s^{-1}). NR = no reaction observed.
[c] Reaction efficiency where k_{col} is defined as the Su-Chesnavich semiclassical ion trajectory rate.58 Values in parentheses are measured using the GIBMS.
[d] Ref. 50.
[e] Ref. 51.
[f] Ref. 56.
[g] Reported as a secondary reaction in Ref. 54. See also text and Refs. 52,53 and 55.

Table 3.2. Apparent termolecular rate constants for reactions of SmO^+ with O_2, NO_2, N_2O, SO_2, and CO_2.

Reaction	$k_{termolecular}$(300 K) (x 10^{-27} cm^6s^{-1})[a]
$SmO^+ + O_2 + He \rightarrow SmO(O_2)^+ + He$	observed
$SmO^+ + CO_2 + He \rightarrow SmO(CO_2)^+ + He$	0.1
$SmO^+ + N_2O + He \rightarrow SmO(N_2O)^+ + He$	0.1
$SmO^+ + SO_2 + He \rightarrow SmO(SO_2)^+ + He$	1.2
$SmO^+ + NO_2 + He \rightarrow SmO(NO_2)^+ + He$	2.1

[a] See text for a discussion of uncertainty.

Table 3.3. Fitting parameters of Eq. (3.2) for the indicated reaction cross section.

Reaction	σ_0	n	E_0 (eV)
$Sm^+ + CO \rightarrow SmO^+ + C$	0.5 ± 0.2	2.3 ± 0.2	5.49 ± 0.15
$\rightarrow SmC^+ + O$	1.1 ± 0.1	1.7 ± 0.2	8.95 ± 0.07
$Sm^+ + SO_2 \rightarrow SmSO^+ + O$	1.3 ± 0.2	1.8 ± 0.2	3.86 ± 0.08
$SmO^+ + Xe \rightarrow Sm^+ + O + Xe$	0.1 ± 0.1	2.0 ± 0.2	5.67 ± 0.16
$SmO^+ + O_2 \rightarrow SmO_2^+ + O$	1.1 ± 0.2	1.0 ± 0.2	3.98 ± 0.15
$\rightarrow Sm^+ + O + O_2$	0.3 ± 0.1	1.2 ± 0.1	5.78 ± 0.09

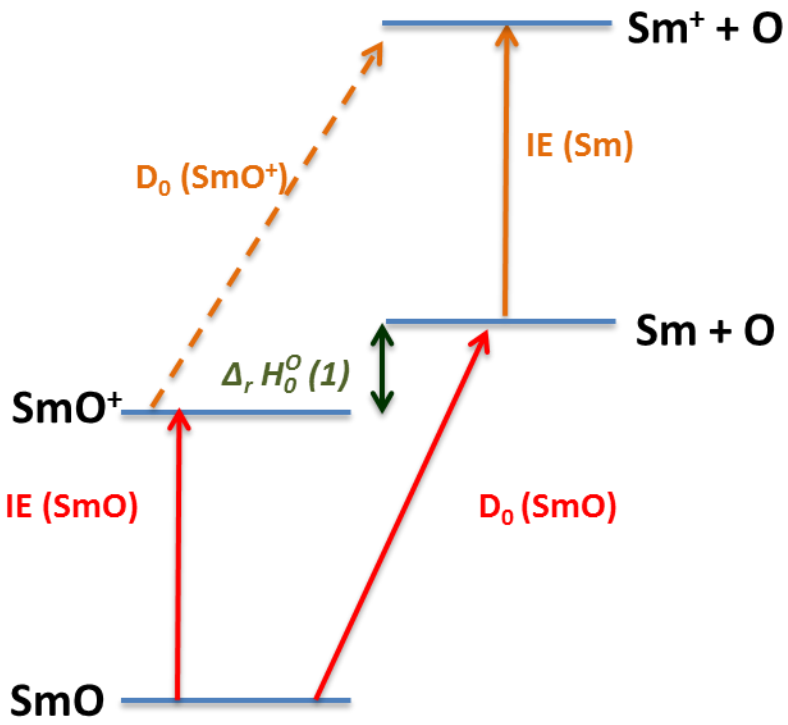

Figure 3.1 Energy schematic of values employed for the determination of $\Delta_r H_0°$ for reaction (3.1).

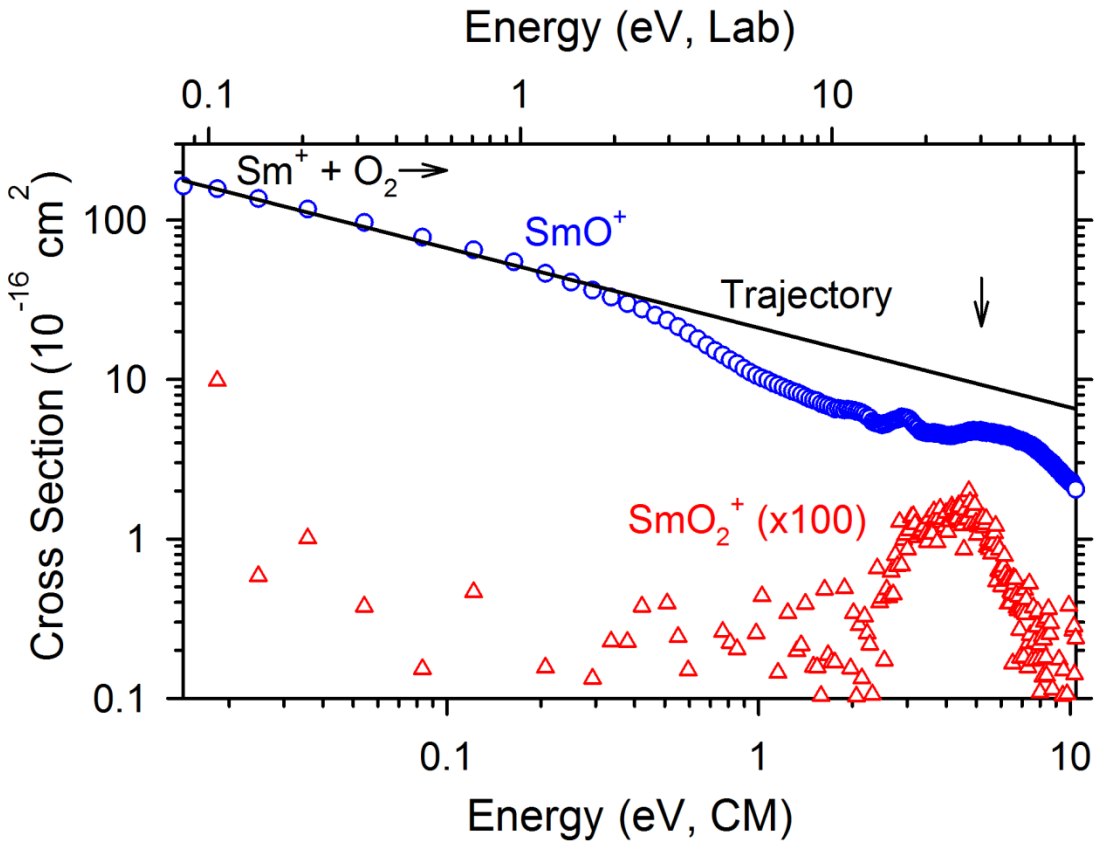

Figure 3.2. Cross sections for the reaction between Sm^+ and O_2 as a function of energy in the center-of-mass (lower x-axis) and laboratory (upper x-axis) frames. The arrow indicates the bond energy of O_2. The line is the calculated semiclassical trajectory collision cross section.

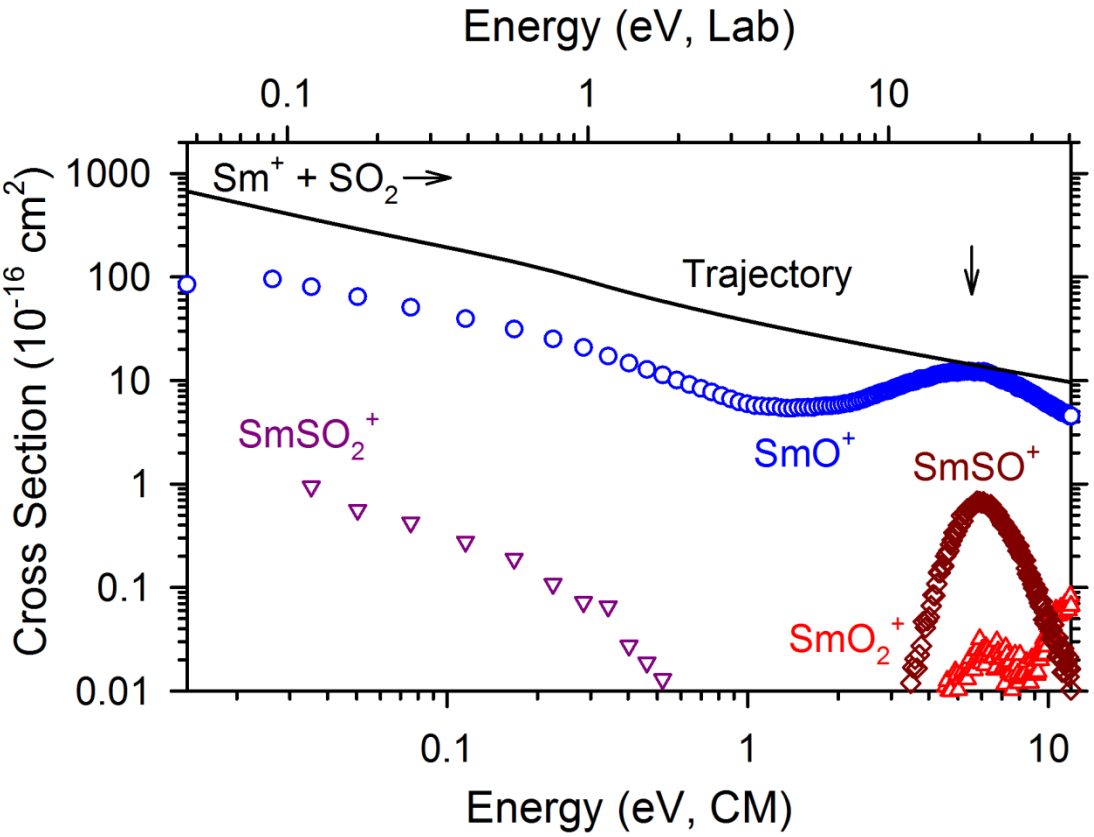

Figure 3.3. Cross sections for the reaction between Sm^+ and SO_2 as a function of energy in the center-of-mass (lower x-axis) and laboratory (upper x-axis) frames. The arrow indicates the bond energy of OS-O. The line is the calculated semiclassical trajectory collision cross section.

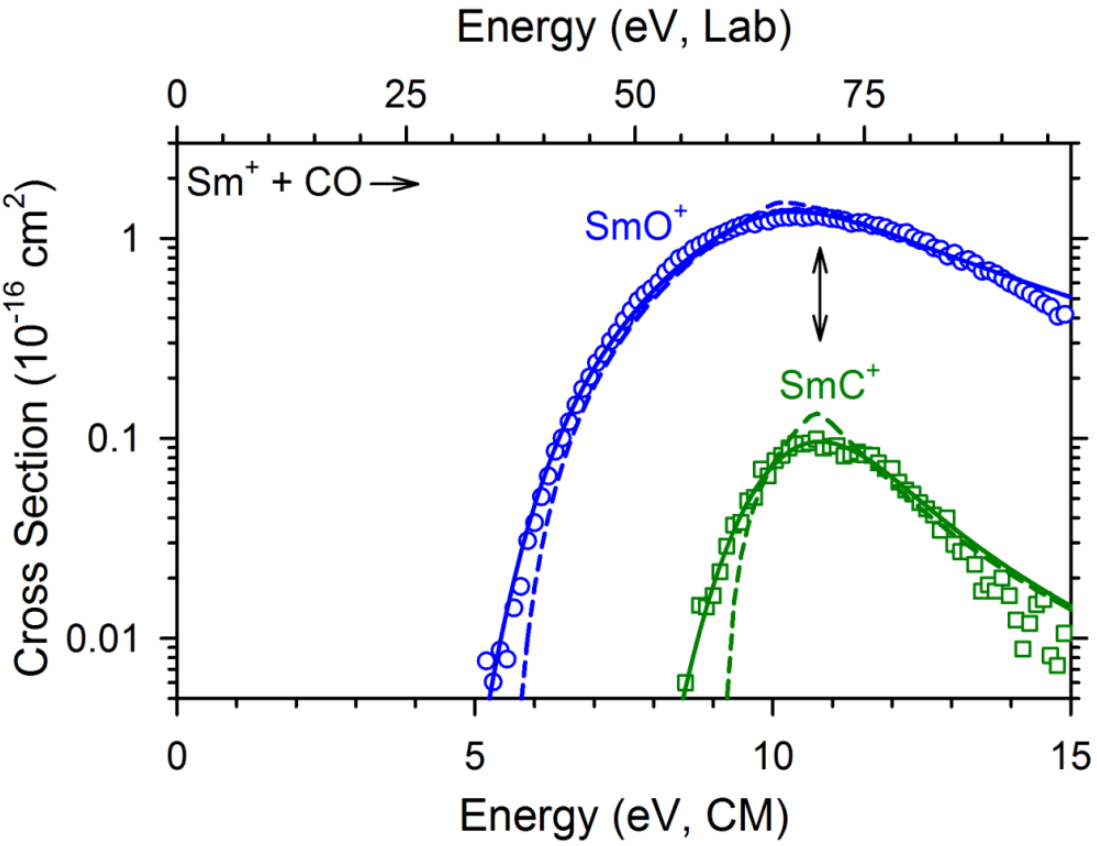

Figure 3.4. Cross sections for the reaction between Sm^+ and CO as a function of energy in the center-of-mass (lower x-axis) and laboratory (upper x-axis) frames. The arrow indicates D_0(C-O). The dashed lines show the model cross section given by Eq. (3.2). Solid lines are convoluted over the experimental energy distributions.

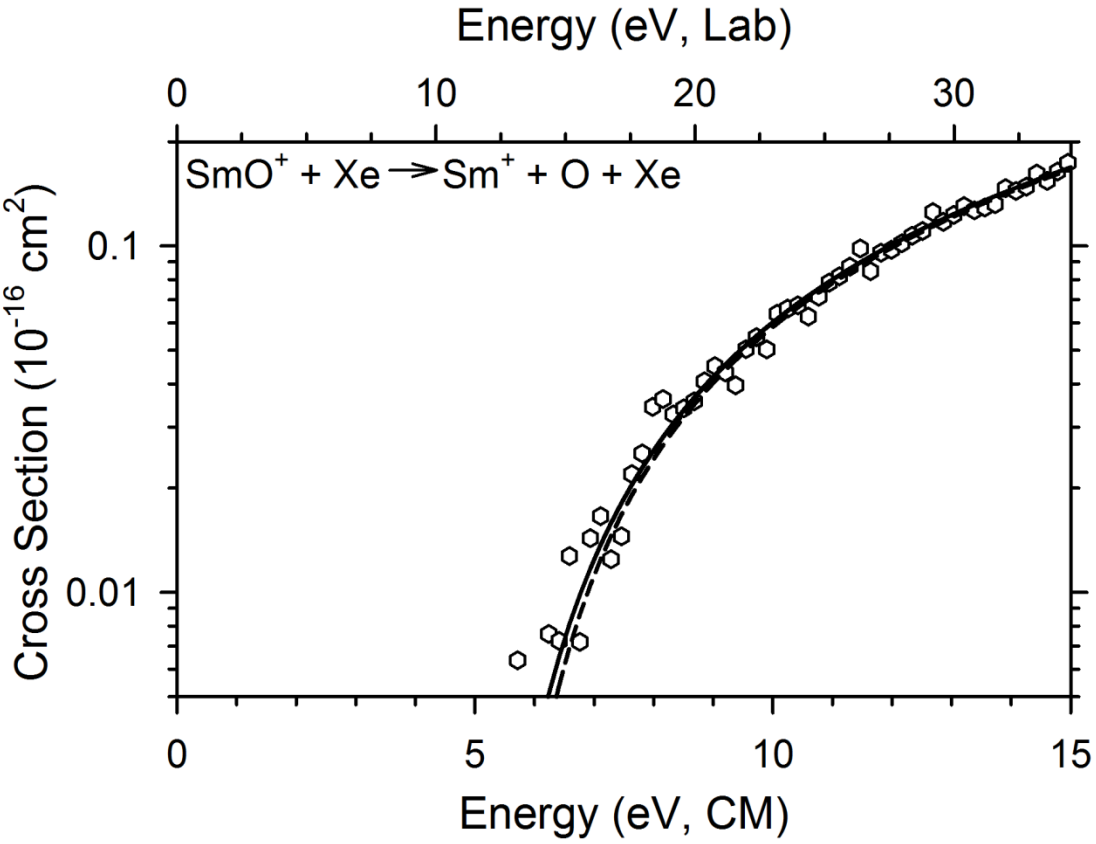

Figure 3.5. Cross section for the collision-induced dissociation reaction between SmO^+ and Xe as a function of energy in the center-of-mass (lower x-axis) and laboratory (upper x-axis) frames. The dashed line represents the model cross section given by Eq. (3.2). Solid lines are convoluted over the experimental energy distributions.

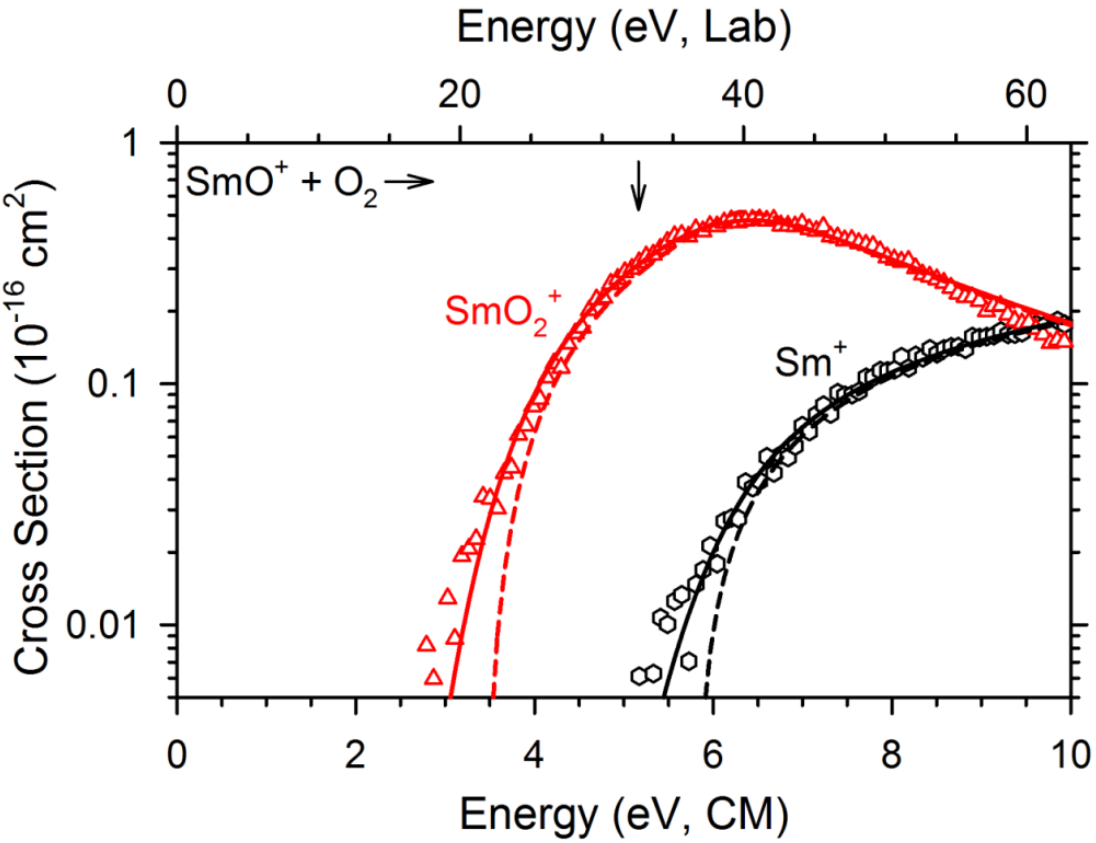

Figure 3.6. Cross sections for the reaction between SmO^+ and O_2 as a function of energy in the center-of-mass (lower x-axis) and laboratory (upper x-axis) frames. The arrow indicates D_0(O-O). The dashed lines show the model cross section given by Eq. (3.2). Solid lines are convoluted over the experimental energy distributions.

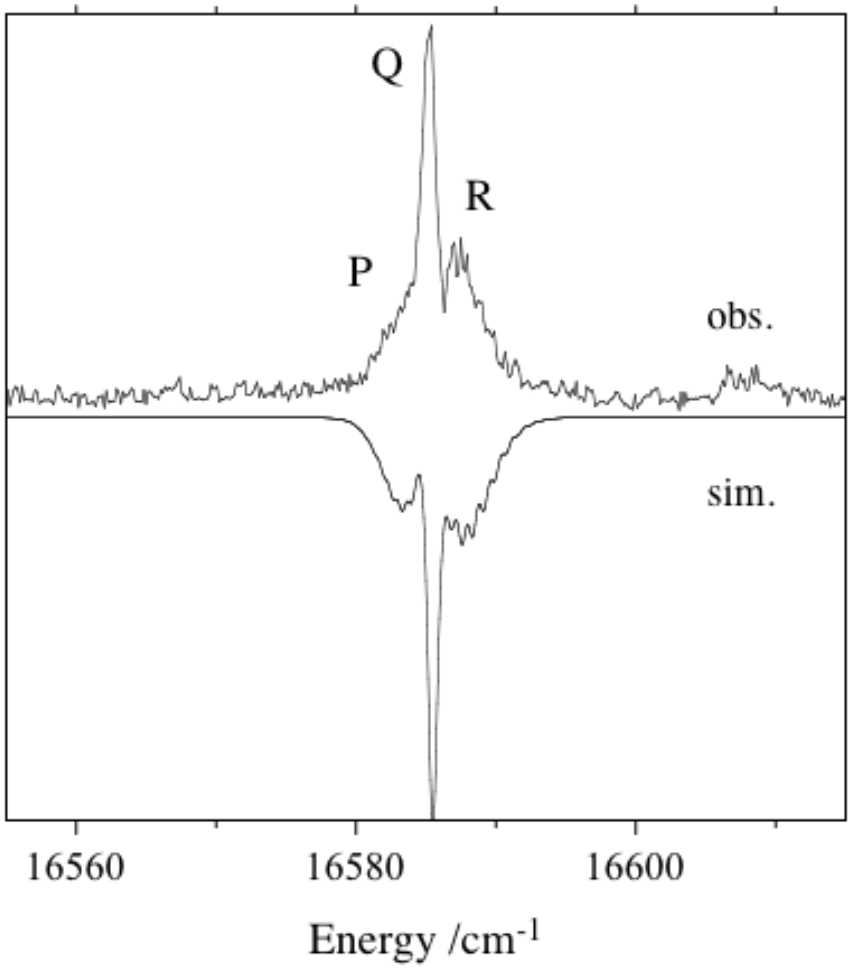

Figure 3.7. Section of the SmO LIF spectrum showing the [16.6]1-X0⁻ origin band (upper trace). The downward-going trace is a simulation of the rotational contour using the two most abundant isotopologs (^{152}SmO and ^{154}SmO). The rotational temperature for the simulation was 10 K.

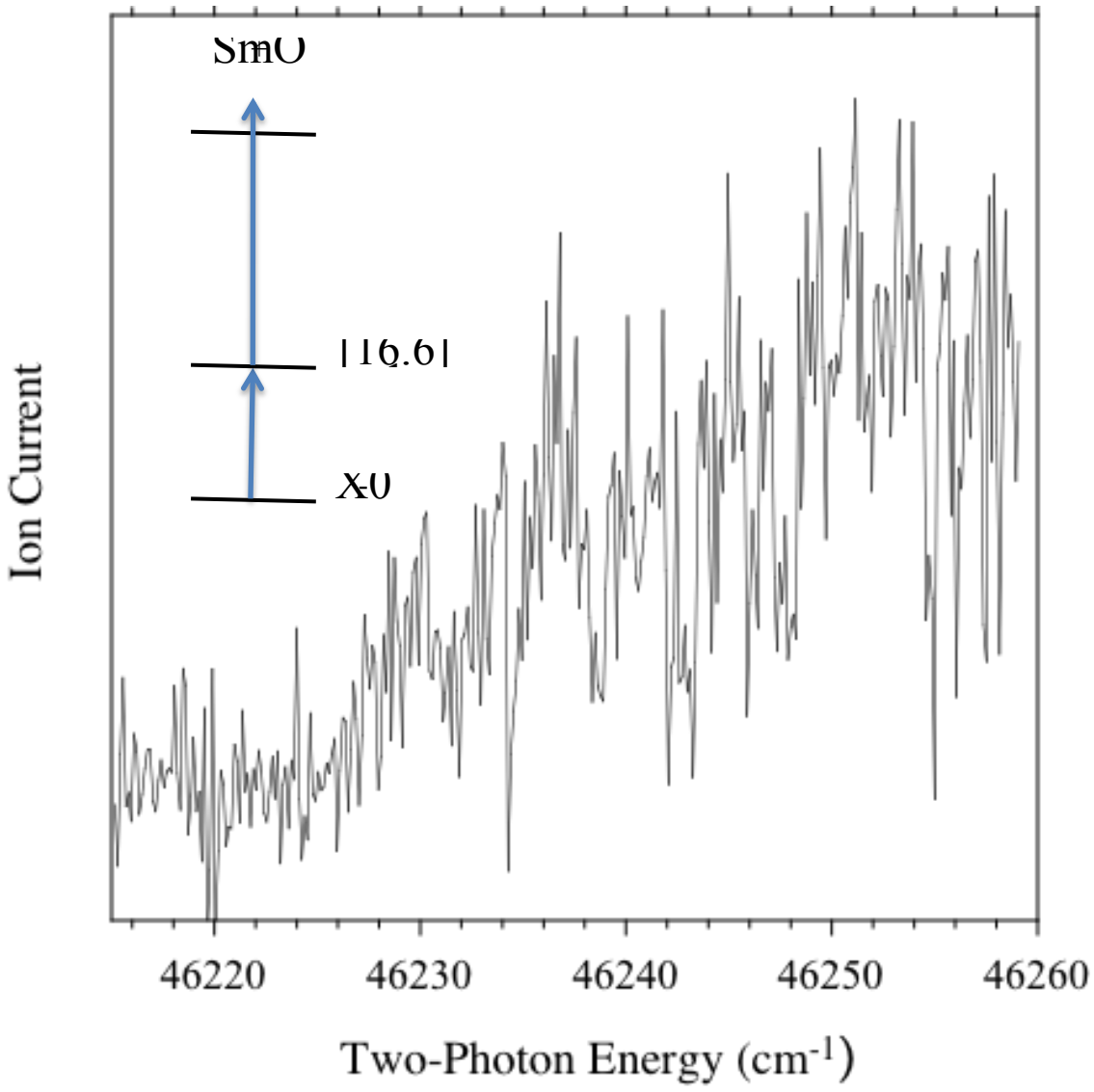

Figure 3.8. Photoionization efficiency curve for ionization of SmO via the [16.6]1 state. This trace was recorded with the first laser tuned to the Q-branch feature of the spectrum shown in FIG. 3.7. The abscissa is the energy sum of the two photons. The local electric field for this measurement was 250 V cm^{-1}.

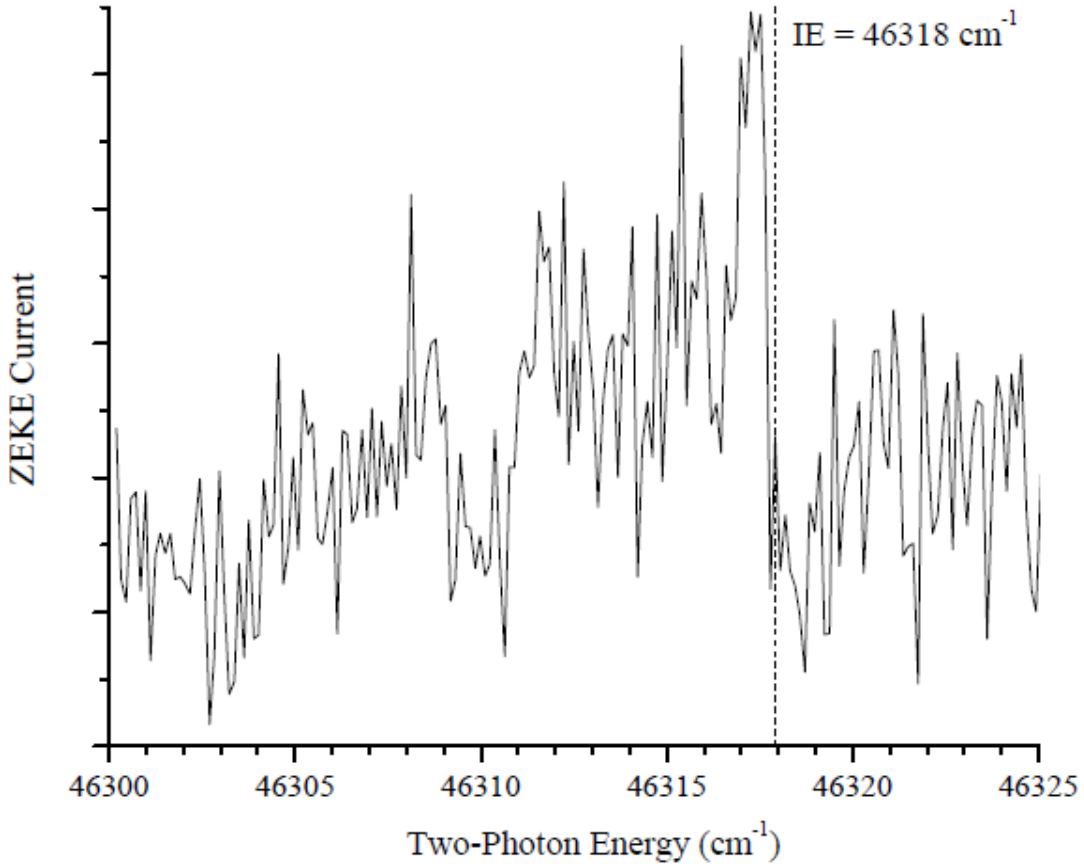

Figure 3.9. A PFI-ZEKE spectrum for SmO recorded using first photon excitation of the Q-branch of the [16.6]1-X0$^-$ origin band. The vertical broken line indicates the blue-edge of the high-n Ryberg series that converges on the zero-point level of SmO^+.

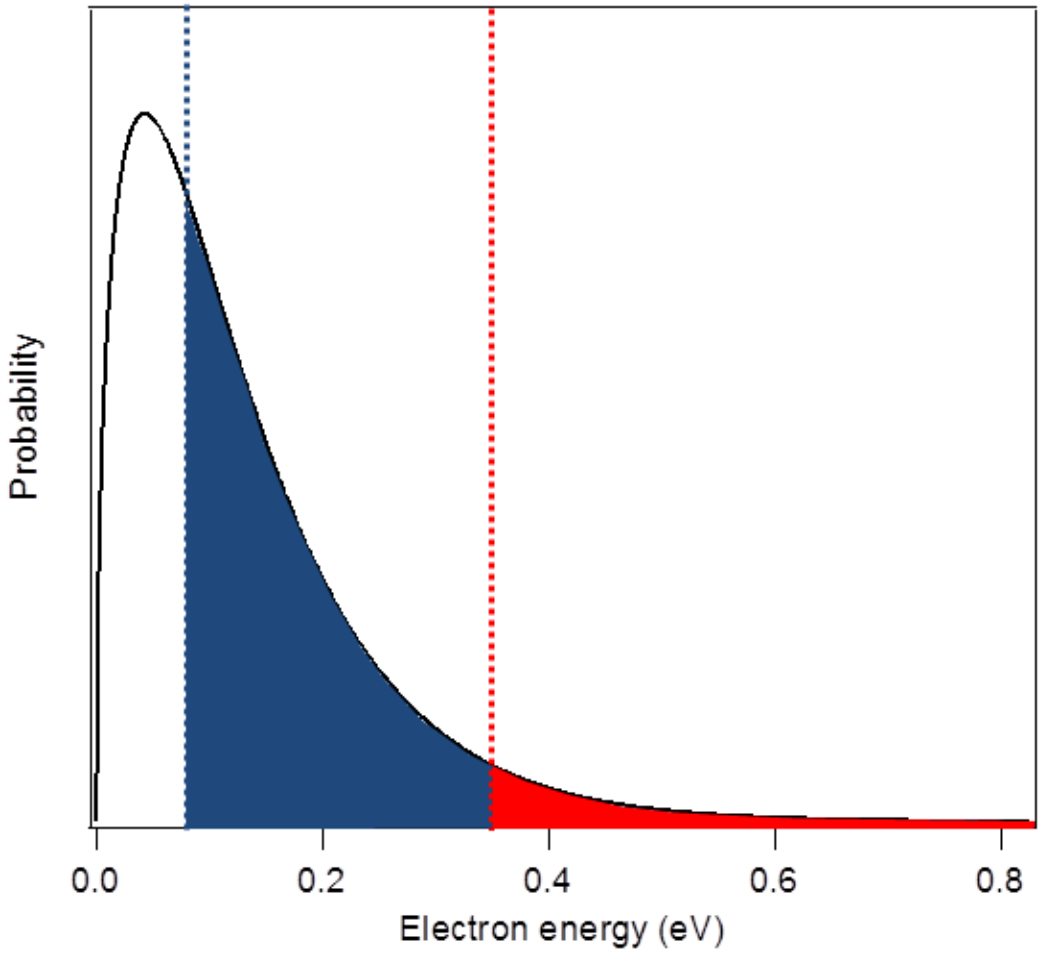

Figure 3.10. Electron energy distribution for $T_{electron}$ = 1000 K. The red shaded region highlights electrons energetic enough to overcome the barrier to the reverse of reaction (3.1) from previously reported thermochemistry. The blue shaded region highlights the electrons meeting this requirement with the newly derived value.

CHAPTER 4

ACTIVATION OF CH_4 BY Th^+ AS STUDIED BY GUIDED ION BEAM MASS SPECTROMETRY AND QUANTUM CHEMISTRY

Cox, R. M; Armentrout, P. B.; de Jong, W. A.

Inorg. Chem. 2015, 54, 3584 - 3599.

Abstract

The reaction of atomic thorium cations with CH_4 (CD_4) and the collision-induced dissociation (CID) of $ThCH_4^+$ with Xe are studied using guided ion beam tandem mass spectrometry. In the methane reactions at low energies, $ThCH_2^+$ ($ThCD_2^+$) is the only product; however, the energy dependence of the cross section is inconsistent with a barrierless exothermic reaction as previously assumed on the basis of ion cyclotron resonance mass spectrometry results. The dominant product at higher energies is ThH^+ (ThD^+), with $ThCH_3^+$ ($ThCD_3^+$) having a similar threshold energy. The latter product subsequently decomposes at still higher energies to $ThCH^+$ ($ThCD^+$). CID of $ThCH_4^+$ yields atomic Th^+ as the exclusive product. The cross sections of all product ions are

modeled to provide 0 K bond dissociation energies (in eV) of $D_0(Th^+\text{-}H) \geq 2.25 \pm 0.18$, $D_0(Th^+\text{-}CH) = 6.19 \pm 0.16$, $D_0(Th^+\text{-}CH_2) \geq 4.54 \pm 0.09$, $D_0(Th^+\text{-}CH_3) = 2.60 \pm 0.30$, and $D_0(Th^+\text{-}CH_4) = 0.47 \pm 0.05$. Quantum chemical calculations at several levels of theory are used to explore the potential energy surfaces for activation of methane by Th^+ and the effects of spin-orbit coupling are carefully considered. When spin-orbit coupling is explicitly considered, a barrier for C-H bond activation that is consistent with the threshold measured for $ThCH_2^+$ formation (0.17 ± 0.02 eV) is found at all levels of theory, whereas this barrier is only observed at BHLYP and CCSD(T) levels otherwise. The observation that CID of the $ThCH_4^+$ complex produces Th^+ as the only product with a threshold of 0.47 eV indicates that this species has a $Th^+(CH_4)$ structure, which is also consistent with a barrier for C-H bond activation. This barrier is thought to exist as a result of the mixed (^4F,^2D) electronic character of the Th^+ J = 3/2 ground-level combined with extensive spin-orbit effects.

Introduction

The activation of methane by metals is an active area of research.[1-3] This interest is motivated in part by the desire to find more efficient or selective catalysts as well as to gain insight into the physical aspects involved in the C-H bond activation process at metal centers. Such insight would be useful because methane is relatively inert but a plentiful feedstock in the synthesis of more complex hydrocarbons.[2,4] To this end, several groups, including our own, have looked at the reactions of methane with the atomic first-,[1,5-12] second-,[1,7,13-19] and third-row[1,7,20-30] transition metal cations. Others have investigated the same reaction for lanthanide[1,2,31-33] and actinide cations.[34-36]

The latter actinide studies were conducted using Fourier transform ion cyclotron resonance mass spectrometry (FT-ICR MS). This instrumentation has also been used to examine oxidation reactions of actinide cations, with thorium being established as the most reactive of the actinide series.[37,38] Actinide reactivity has been inversely correlated to the promotion energy from the ground-level to the first level with two *6d* electrons ($5f^{n-3}6d^27s$ or $5f^{n-2}6d^2$ configurations).[39] In these studies, the ground-state of Th^+ was reported to have a $6d^27s$ (^{4}F) configuration, thus requiring no promotion.

Similar to the oxidation studies, thorium was also observed to be the most reactive of the actinides with several hydrocarbons studied using FT-ICR.[36] It is the only actinide to dehydrogenate methane at thermal energies, albeit with low efficiency, $k/k_{col} = 0.009 \pm 0.005$[36] and $k/k_{col} = 0.02 \pm 0.01$,[35] where the collision rate limit (k_{col}) is the rate derived from modified variational transition-state/classical trajectory theory.[40] Both studies interpreted their observations to indicate an exothermic reaction, which suggested that $D_0(Th^+\text{-}CH_2) \geq D_0(H_2C\text{-}H_2) = 457 \pm 1$ kJ/mol.[36]

The reaction of thorium cation with methane has also been studied theoretically.[41,42] Two competing explanations for the low efficiency of the dehydrogenation pathway have emerged. In a reaction coordinate presented by di Santo et al.,[41] the reaction proceeds exclusively on the doublet spin surface, originating from a ^{2}F Th^+ ground-state, with a small barrier of 4 kJ/mol at the transition state between the first two intermediates: $Th^+(CH_4)$, the association complex of the ion and methane formed through electrostatic interactions, and $HThCH_3^+$, the inserted species. These calculations used B3LYP in combination with a Stuttgart-Dresden effective core potential and basis set (SDD) for Th^+ and a 6-311++G(d,p) basis set for C and H. Such a barrier

would indicate that only a small population of the reactants would have the necessary energy to react, consistent with the experimentally observed low efficiency. Another recent study[42] used the same Pople basis set for C and H and an unpublished double-ζ quality basis set in combination with the Stuttgart-Dresden ECP and the B3PW91 functional. Here no barrier along the lowest energy pathway was observed, but a crossing was found between the quartet (the ground-state of the Th^+ reactant in this study) and doublet (needed to form the ground-state of $HThCH_3^+$) surfaces near the first intermediate. They concluded that the inefficiency at this crossing point hindered the crossover to the doublet surface on which the reaction evolves to products. In this study, the electronic state of the Th^+ reactant was not identified beyond its spin.

Despite these efforts, actinide chemistry (particularly in the gas phase) is largely unexplored. This is attributable, in part, to safety concerns, as all actinides except thorium and uranium are highly radioactive. This limits the ability to study most actinides to dedicated laboratories or theoretical studies. In order for theoretical methods to be accurate, reliable experimental benchmarks are critically needed. Here we present a study of the activation of methane and its deuterated analogue by atomic thorium cations using guided ion beam tandem mass spectrometry (GIBMS). A key feature of GIBMS is the ability to control the kinetic energy of the reactant ion over three or more orders of magnitude in the laboratory frame. This allows for the determination of the energy dependence of the dehydrogenation reaction as well as the study of higher energy reaction pathways. To more fully explore this reaction surface experimentally, we also examine the collision-induced dissociation (CID) of the $ThCH_4^+$ cation. This experimental work is complemented by quantum chemical calculations performed here at

several levels of theory and a careful quantitative evaluation of spin-orbit effects. A key objective of the present study is the determination of experimental bond dissociation energies (BDEs) from which theoretical methods can be evaluated more completely.

Experimental and Theoretical Methods

Instrument

The guided ion beam tandem mass spectrometer used in these studies has been described previously.[43] Briefly, Th^+ (^{232}Th 100% abundance) and $ThCH_4^+$ ions are created in a direct current discharge flow tube (DC/FT) source described further below.[44] Ions are extracted from the source, focused through a magnetic momentum analyzer where the reactant ion is mass selected, and subsequently decelerated to a well-defined kinetic energy. These ions are passed into a radiofrequency (rf) octopole ion beam guide[45-47] where the ions are radially trapped. The octopole passes through a static gas cell that contains the neutral reactant gas at pressures of 0.05 - 0.40 mTorr. Pressures are low to ensure that the probability of more than one collision occurring between the reactants is small. It is verified that the measured cross sections reported below do not vary with neutral reactant pressure. After the collision cell, remaining reactant and product ions drift to the end of the octopole, are focused through a quadrupole mass filter for mass analysis, and counted using a Daly detector.[48] Reaction cross sections are calculated, as described previously, from product ion intensities relative to reactant ion intensities after correcting for ion intensities with the neutral gas no longer directed to the gas cell.[47] Uncertainties in the measured absolute cross sections are estimated to be ±20 %, with relative uncertainties of ±5%.

Laboratory ion energies (lab) are converted to the center-of-mass frame (CM) using the relationship $E_{CM} = E_{lab} \times m/(m + M)$ where m and M are the masses of the neutral and ionic reactants, respectively. The absolute zero of energy and the full width at half-maximum (FWHM) of the ion beam are determined by using the octopole guide as a retarding potential analyzer.[47] Typical FWHMs of the energy distribution for these experiments were 0.4 - 0.6 eV (lab). Uncertainties in the absolute energy scale are 0.1 eV (lab). All energies reported below are in the CM frame.

Ion Source

The DC/FT source is described in detail elsewhere.[44] Th^+ ions are created when Ar ionized by a dc electric field (2.5 kV) collides with a cathode holding the thorium powder sample. Ions typically thermalize under ~10^5 collisions with the He/Ar carrier gasses in a 9:1 mixture in a 1 m long flow tube. Total pressure in the flow tube is 0.2 – 0.5 Torr. $ThCH_4^+$ is created by leaking methane into the flow tube 15 cm downstream of the discharge through a variable leak valve. Previous experiments have indicated that atomic metal ions generated in the DC/FT source generally have internal electronic temperatures between 300 and 1100 K.[49-53] At 300 K, 99.99% of Th^+ is in its J = 3/2 ground-level.[54,55] At 1100 K, 76% of Th^+ is in the ground-level with an average electronic energy of only 0.05 eV (see Table A.1). For the $ThCH_4^+$ complex, the ions are expected to have an internal temperature of 300 K.

Data Analysis

The kinetic energy dependence of endothermic reactions is modeled using Eq. 4.1,[46,56,57]

$$\sigma(E) = \sigma_0 \Sigma\, g_i\, (E + E_i - E_0)^n / E \qquad (4.1)$$

where σ_0 is an energy-independent scaling factor, E is the relative kinetic energy of the reactants, E_i is the internal energy of the reactants' electronic, vibrational, and rotational states having populations g_i ($\Sigma g_i = 1$), n is an adjustable parameter, and E_0 is the 0 K reaction threshold. Before comparison to the data, Eq. 4.1 is convoluted over the kinetic energy distributions of the reactants.[47,58,59] The σ_0, n, and E_0 parameters are then optimized using a nonlinear least-squares method to best reproduce the experimental cross section. Uncertainties in E_0 are calculated from the threshold values for several independent data sets over a range of n values combined with the absolute uncertainties in the kinetic energy scale and internal energies of reactant ions. Calculated thresholds are then used to determine bond dissociation energies (BDEs), $D_0(Th^+\text{-}R)$, using relationship 4.2.

$$D_0(Th^+\text{-}L) = D_0(L\text{-}R) - E_0 \qquad (4.2)$$

This equation assumes that there are no barriers in excess of the endothermicity of the reaction. When evidence of a barrier exists, Eq. 4.2 provides a lower limit to the true BDE. Neutral BDEs, $D_0(L\text{-}R)$, were taken from thermochemistry found in the NIST

webBook[60] or previous compilation.[22] Thermodynamic values used to determine neutral BDEs are listed in Table A.2 of the Supporting Information.

Theoretical Calculations

Most of the quantum chemical calculations were performed using the Gaussian 09 suite of programs.[61] Geometries of all intermediates and transition states were optimized using the B3LYP[62,63] functional with a Stuttgart-Dresden small core (60 electron) relativistic effective core potential (ECP) and accompanying basis set (SDD)[64] for Th^+ and the Pople basis set[65] 6-311++G(d,p) for C and H. This SDD basis set is the 1997 revision made by the Stuttgart/Dresden groups and can be obtained from the EMSL basis set exchange.[66,67] Single-point energies were then calculated using several density functional theory (DFT) approaches, B3LYP, B3PW91, and BHandHLYP (BHLYP) functionals with the SDD basis set for Th^+ and a 6-311++G(3df,3p) basis set for C and H that has been shown to be reasonably accurate in studies of third-row transition metal-methane systems by our group.[25,28,29,68-70] Additional single-point calculations using the B3LYP/SDD/6-311++G(d,p) structures were performed using a (14s13p10d8f6g)/[6s6p5d4f3g] atomic natural orbital basis set of quadruple-ζ quality with the SDD small core ECP (ANO) and a (14s13p10d8f6g)/[10s9p5d4f3g] segmented basis set of quadruple-ζ quality with the SDD small core ECP (Seg. SDD) for Th along with a 6-311++G(3df,3p) basis set for C and H.[71] Unless noted otherwise, all theoretical energies reported below are calculated using Seg. SDD/6-311++G(3df,3p) basis sets for Th^+/C and H. Other groups have indicated that the B3PW91 has performed well in the study of other actinide systems.[42] Holthausen et al.[72] previously have considered the

appropriate choice of level of theory to study first- and third-row transition metal methyl cation species, and concluded that BHLYP performed well for singly bound species. This conclusion has been confirmed in subsequent use by our group that BHLYP performs well for several third-row transition metal hydride systems; however, BHLYP is not accurate for species having more than a single covalent bond.[69,70] Additionally, single-point energies were calculated using the coupled cluster method that mixes in single and double excitations and perturbative triple excitations with the Th^+ (*5s,5p*) and the C (*1s*) orbitals frozen for electron correlation, CCSD(T).[65,73-75] For all open-shell calculations, unrestricted open-shell wave functions were utilized throughout. With a few exceptions that are explicitly noted, spin contamination is insignificant. All single-point energies were zero-point energy-corrected using the frequencies of the optimized structures after scaling by 0.989.[76] Transition states were found by employing a Synchronous Transit-Guided Quasi-Newton (STQN) method[77,78] to approach the quadratic region around the transition state. Transition states were checked to ensure that there was only one imaginary frequency, which led to the appropriate intermediates or products. BDEs of the reaction products were also calculated from these various single-point energies.

Additional calculations were performed using the NWChem computational chemistry software.[79] Here the geometries were optimized using the PBE0 functional using the latest Stuttgart-Cologne ECP[80] with a newly developed correlation consistent type basis set for Th (20s17p12d11f5g3h1i)/[7s7p6d5f5g3h1i] developed by K.A. Peterson (KAP).[81] For C and H, the cc-pVTZ basis sets[82] were used. All geometries used in NWChem were optimized using the PBE functional.[83] The Nudged Elastic Band method[84] was used to locate transition states, and saddle point optimizations and

frequency calculations were used to ensure a transition state with one imaginary frequency was found. It should be noted that although different basis sets and functionals were used in the Gaussian and NWChem calculations, the resulting structures were found to be very similar (as detailed in Table A.6 of the Supporting Information). Single-point energies were calculated using the CCSD(T) method. As with the Gaussian calculations, the Th^+ (*5s,5p*) and the C (*1s*) orbitals were frozen. For CCSD(T), a spin-restricted open-shell wave function was used as a reference for the correlated calculations based on an unrestricted formulation.

Experimental Results

$Th^+ + CH_4$ (CD_4)

The reaction of Th^+ with methane yields products formed in reactions 4.3 – 4.6.

$$Th^+ + CH_4 \rightarrow ThCH_2^+ + H_2 \quad (4.3)$$

$$\rightarrow ThH^+ + CH_3 \quad (4.4)$$

$$\rightarrow ThCH_3^+ + H \quad (4.5)$$

$$\rightarrow ThCH^+ + H + H_2 \quad (4.6)$$

The cross sections for these reactions are shown in Figure A.1 in the Supporting Information and are very similar to the analogous methane-d_4 reaction cross sections shown in Figure 4.1. Mass overlap for the $ThCH_3^+$ and $ThCH^+$ products with the more intense $ThCH_2^+$ product was observed. In both cases, cross sections were corrected to remove overlap from adjacent mass peaks, a procedure that was straightforward and

unambiguous because of the different energy dependences of the products in question. The reactions with methane-d_4 showed much less mass overlap. In all cases, the cross sections produced in reactions 4.3 – 4.6 for both methane and methane-d_4 are similar in energy dependence and magnitude.

At low energy, reaction 4.3 dominates with a cross section that initially rises with increasing energy. The energy dependence of reaction 4.3 is inconsistent with that of a barrierless exothermic reaction, as was concluded from the FT-ICR studies.[35,36] A plot of our experimental data for reaction 4.3 converted to a rate coefficient as a function of kinetic energy according to a method outlined elsewhere[47] is presented in Figure 4.2. For CH_4, it can be seen that at the lowest energies in the present experiment (0.07 ± 0.02 eV, equivalent to a temperature of 500 ± 150 K), we do observe a small amount of product with a rate constant of $0.02 \pm 0.01 \times 10^{-10}$ cm^3/s and a reaction efficiency of $k/k_{col} = 0.002 \pm 0.001$, where the collision limit is defined by the Su-Chesnavich variational transition-state/classical trajectory theory rate constant.[40] Likewise, the rate coefficient for reaction 4.3 with CD_4 is $0.03 \pm 0.02 \times 10^{-10}$ cm^3/s at our lowest energies (0.09 ± 0.04 eV, equivalent to an average temperature of 700 ± 300 K). At this same temperature, the rate coefficient for reaction 4.3 with CH_4 is $0.04 \pm 0.03 \times 10^{-10}$ cm^3/s. The slight differences between the rates observed in reaction 4.3 using CH_4 and CD_4 can be explained by two effects. The first takes into account that the collisional rate coefficient depends inversely on the square root of the reduced mass of the reactants, 15.00 u for CH_4 and 18.46 u for CD_4, such that the CD_4 collision rate is 90% of that for CH_4. The second relates to the differences in zero-point-energy (ZPE) between the two reactants. As a result, $D_0(D_2C\text{-}D_2)$ is slightly stronger than $D_0(H_2C\text{-}H_2)$ so that the threshold for reaction 4.3 with CD_4 is

higher than with CH_4.

Previously, Marcalo et al.[35] and Gibson et al.[36] observed that Th^+ reacts with CH_4 with rates of $0.20 \pm 0.10 \times 10^{-10}$ cm^3/s for an efficiency of $k/k_{col} = 0.02 \pm 0.01$ and $0.10 \pm 0.05 \times 10^{-10}$ cm^3/s for an efficiency of $k/k_{col} = 0.009 \pm 0.005$, respectively, in ICR experiments at nominally room temperature. Both ICR rates are larger than that measured here, but of similar magnitude and nearly within the combined uncertainties, Figure 4.2. It seems plausible that the ICR rates are somewhat elevated because the reactants have an effective temperature (electronic or translational) above 300 K.

The $ThCH_2^+$ ($ThCD_2^+$) cross section rises until ~2 eV, where it begins to fall off, Figures A.1 and 4.1. This decline corresponds with the apparent thresholds for ThH^+ (ThD^+) and $ThCH_3^+$ ($ThCD_3^+$). Because decomposition of $ThCH_2^+$ ($ThCD_2^+$) to ThH^+ (ThD^+) cannot occur until much higher energies, this decline can only be explained by a shared common intermediate between the three channels. In addition, the peak in the magnitude of the $ThCH_3^+$ ($ThCD_3^+$) cross section corresponds to the rise of the $ThCH^+$ ($ThCD^+$) cross section, indicating that this latter product is formed by the dehydrogenation of $ThCH_3^+$ ($ThCD_3^+$). Finally, the $ThCH_3^+$ ($ThCD_3^+$) product can decompose by H (D) atom loss, which can be seen as the faster decline in the $ThCH_3^+$ ($ThCD_3^+$) cross section starting near 6 eV and the plateau in the $ThCH_2^+$ ($ThCD_2^+$) cross section starting at the same energy. The potential product, ThC^+, was also explicitly looked for but not observed.

The parameters used in Eq. 4.1 to model the experimental cross sections are found in Table 4.1. Each channel was modeled independently. Because Eq. 4.1 explicitly includes the rotational, vibrational, and translational energy distributions of the reactants,

the E_0 threshold energies determined correspond to 0 K values. Therefore, all BDEs determined below using Eq. 4.2 are 0 K dissociation energies.

$$ThCH_4^+ + Xe$$

The CID reaction of the $ThCH_4^+$ complex yields a single product, the atomic thorium cation, reaction 4.7, as shown in Figure 4.3.

$$ThCH_4^+ + Xe \rightarrow Th^+ + CH_4 + Xe \quad (4.7)$$

Other products explicitly looked for but not observed were ThH^+, $ThCH_3^+$, and $ThCH_2^+$, species that would indicate a structure of $HThCH_3^+$ or $H_2ThCH_2^+$. As discussed in more detail below, the $HThCH_3^+$ structure is the global minimum along the methane activation reaction pathway. In previous work,[22] the CID of $PtCH_4^+$ yielded both Pt^+ and PtH^+ products, indicating that the reactant had a $HPtCH_3^+$ structure (again the global minimum structure). Because the CID products expected from this inserted structure are not observed in the thorium system, the present CID results suggest that this species has a $Th^+(CH_4)$ structure. This is also confirmed by the comparison of the threshold energy obtained from analysis of this cross section, Table 4.1, with theoretical values for the two possible structures. The evidence for this structural identification is discussed further below.

Thermochemical and Theoretical Results

Th^+ Ground-state

Some ambiguity surrounds the ground-state of Th^+ because there is considerable interaction between the $^2D(6d7s^2)$ and $^4F(6d^27s)$ states. The J = 3/2 ground-level is identified as having mixed character, 43% $^4F(6d^27s)$ and 27% $^2D(6d7s^2)$.[54] A detailed list of the levels, including energies and character, chosen as representative of each state listed in Table 4.2, can be found in Table A.1 in the Supporting Information. For the purpose of comparing the theoretical energies of each state, which are averaged over all spin-orbit levels, to the experimental results, the ground-level is assigned as $^4F_{3/2}$. Despite the assignment of the ground-level as part of the ^4F state, after averaging over all spin-orbit levels, the experimental ground-state is ^2D. Experimental energies, averaged over properly weighted spin-orbit levels, for each low-lying state are listed in Table 4.2, as are theoretical energies of these states. Both BHLYP and CCSD(T) correctly identify the ground-state as a ^2D ($6d7s^2$), whereas B3LYP and B3PW91 prefer the ^2F ($5f^27s$) state. At all levels of theory, considerable spin contamination, s(s+1) ~ 1.5, is observed for the ^2D state, consistent with mixing in ^4F character. Overall, the BHLYP and CCSD(T) calculations do a particularly good job of reproducing the experimental values. When using the SDD and ANO basis sets, results are similar to those observed using the Seg. SDD basis set and can be found in Table A.3. The use of the larger basis sets does significantly improve the results of the CCSD(T) calculations compared to experiment. Notably, the largest basis set, KAP, correctly predicts the order of the ^2D and ^4F states and yields the best agreement with experiment, Table 4.2. Given that the ^2D ($6d7s^2$) state is the calculated ground-state for Th^+ using CCSD(T) and BHLYP, all theoretical BDEs

are determined here relative to this ^2D state in the next several sections. Consideration of spin-orbit interactions is needed to properly reference these BDEs to the $^4F_{3/2}$ ground-level and is discussed later.

$ThCH_2^+$

The threshold measured for reaction 4.3 is 0.17 ± 0.02 eV, Table 4.1. Combined with $D_0(H_2C\text{-}H_2)$ = 4.74 ± 0.02 eV,[60] this would yield a BDE of $D_0(Th^+\text{-}CH_2)$ = 4.57 ± 0.06 eV if the threshold corresponds to the product asymptote. Similarly, the threshold for the deuterated system is 0.28 ± 0.03 eV, which would lead to $D_0(Th^+\text{-}CD_2)$ = 4.54 ± 0.06 eV. After accounting for the explained below, we report $D_0(Th^+\text{-}CH_2) \geq 4.54 \pm 0.09$ eV as a lower limit to the true BDE zero-point energy differences of 0.03 eV, the weighted average is $D_0(Th^+\text{-}CH_2)$ = 4.54 ± 0.09 eV, where the uncertainty is two standard deviations of the mean. This result is significantly different than the lower limit, $D_0(Th^+\text{-}CH_2) \geq 4.74$ eV,[60] reported by Marcalo et al.[35] and Gibson et al.,[36] who assume that reaction 4.3 is barrierless and exothermic. This assumption is inconsistent with the cross section for reaction 4.3 in Figure 4.1 (and the rate coefficients in Figure 4.2), which increase with increasing kinetic energy. Because of experimental and theoretical results explained below, we report $D_0(Th^+\text{-}CH_2) \geq 4.54 \pm 0.09$ eV as a lower limit to the true BDE.

The calculated ground-state of $ThCH_2^+$ is $^2A'$ with a metal carbene geometry that has an agostic structure where one H is tilted towards the metal, essentially donating electron density from this CH bond into an empty d orbital on the metal. This agostic structure has been found to be characteristic of the early transition metals.[25,28,30,85]

Geometrical parameters found here are similar to the structures reported by di Santo et al.[41] and de Almeida and Duarte,[42] who also find a $^2A'$ ground-state. The CH_2 wagging motion passes through the symmetric $^2A_1$ state (a transition state having C_{2v} symmetry) lying only 0.05 eV higher in energy. A $^2A''$ state is found 0.6 eV higher in energy, where the radical electron is moved from the a′-orbital composed primarily of the *7s*-orbital to a *6d* δ-like a″-orbital, and a $^4A''$ state is 1.3 eV above the ground-state. All other isomers, such as $HThCH^+$ and H_2ThC^+, are at least 1.3 eV above the ground-state and can be found in Table A.4 in the Supporting Information.

BDEs derived from the seg. SDD theoretical calculations are listed in Table 4.3 and predict bond energies of 4.82 – 5.44 eV, not accounting yet for the spin-orbit contribution as discussed in the next section. CCSD(T)/KAP calculations indicate a BDE of 5.34 eV. The SDD and ANO basis sets yield similar results and can be found in Table A.5. All levels of theory investigated here indicate that reaction 4.3 is exothermic when the associated theoretical value for $D_0(CH_2\text{-}H_2)$ is used. The range calculated here encompasses the theoretical value reported by di Santos et al.[41] of 5.08 eV calculated at the B3LYP/SDD/6-311++G(d,p) level. They also report a theoretical value of 5.98 eV using PW91PW91/TZ2P employing a zero-order regular approximation (PW91/ZORA), but other BDEs determined using this method appear to overestimate bond strengths. All theoretical BDEs are consistent with the experimental lower limit, and thus this comparison provides no definite quantitative information that allows evaluation of any theoretical method.

ThH^+

The threshold for reaction 4.4 is measured to be 2.38 ± 0.16 eV. Given $D_0(H_3C\text{-}H)$ = 4.48 ± 0.01 eV,[60] this suggests $D_0(Th^+\text{-}H)$ = 2.10 ± 0.16 eV. A similar result is obtained for the deuterated system, $D_0(Th^+\text{-}D)$ = 2.33 ± 0.11 eV. After accounting for zero-point energy differences (0.03 eV), the weighted average BDE is $D_0(Th^+\text{-}H)$ = 2.25 ± 0.18 eV. To the best of our knowledge, this represents the first experimental report of this bond energy.

For transition metal cations studied in our lab, BDEs measured using H_2 are 0.10 – 0.43 eV greater than those determined using CH_4 as a reactant.[22,23,25,27,28,30,53,69,70,86] In all cases, the difference is attributed to competition with the formation of the metal carbene because of a shared, common intermediate. Because reactions of M^+ with H_2 produce only one product, no competition exists that may delay the onset of reaction. For this reason, BDEs for metal hydrides measured using H_2 as the reaction partner are considered more reliable. Unpublished results[87] for the reaction of Th^+ with H_2 and D_2 determine that $D_0(Th^+\text{-}H)$ = 2.46 ± 0.07 eV, indicating that the average threshold for reaction 4.4 is delayed by 0.21 ± 0.19 eV. This observation is further substantiated by a phase space theory modeling of the competition between reactions 4.3 and 4.4, as described in greater detail in the Supporting Information and depicted in Figure A.2. This model, which explicitly considers angular momentum effects, indicates that the threshold for reaction 4.4 is shifted by ~0.3 eV, consistent with the more quantitative comparison above.

Di Santo and co-workers[41] calculated a $^3\Delta$ ground-state for ThH^+ with a $^1\Sigma^+$ state very close in energy (0.02 eV) using B3LYP/SDD/6-311+G(p). Using a larger basis set

for Th^+, we calculate similar results with a $^3\Delta$ ground-state and low-lying excited-states of $^1\Sigma^+$ (0.30 eV) and $^3\Pi$ (0.18 eV) at the B3LYP level of theory. CCSD(T) calculations reverse the order by placing the $^1\Sigma^+$ state 0.07 eV lower in energy than the $^3\Delta$ state and also indicate that the $^3\Pi$ is 0.37 eV higher in energy than the $^1\Sigma^+$. CCSD(T)/KAP calculations yield similar results with the $^1\Sigma^+$ state 0.04 eV lower in energy than the $^3\Delta$ state. Bonding in ThH^+ occurs by combining the Th^+ (*6d*) and H (*1s*) electrons. The $^3\Delta$ correlates with the ^{4}F ($6d^27s$) state where the unpaired electrons are found in essentially $6d\delta$ and *7s* atomic orbitals on the metal. Conversely, the $^1\Sigma^+$ state forms from the ^{2}D ($6d7s^2$) state of Th^+ with the *7s* orbital filled. Given the mixed nature of the Th^+ ground-level, formation of either state should be possible directly from the J = 3/2 ground-level. The $^3\Pi$, which places the *6d* electron in a π orbital rather than a δ, should also form directly from the ground-level.

Compared to experiment, Table 4.3, all levels of theory overbind ThH^+ by 0.3 – 0.5 eV, with the BHLYP value closest to the experimental value. Di Santo et al. report a similar BDE of 2.98 eV determined at the B3LYP/SDD/6-311++G(d,p) level and 3.49 eV using PW91/ZORA.[41] As for $ThCH_2^+$, the latter method appears to overestimate the bond strength significantly. Differences between the theoretical and experimental values for $D_0(Th^+\text{-}H)$ are attributable in part to spin-orbit splitting effects, as discussed in a following section.

$ThCH_3^+$

Because the $ThCH_3^+$ product dissociates readily to $ThCH^+$ at slightly higher energies, we determined the threshold for $ThCH_3^+$ production by analyzing the sum of

these two product cross sections. Using this procedure, the threshold for reaction 4.5 is 2.11 ± 0.15 eV, which corresponds to a bond energy for $D_0(Th^+\text{-}CH_3)$ of 2.37 ± 0.18 eV. Results from the CD_4 reaction lead to $D_0(Th^+\text{-}CD_3)$ = 2.44 ± 0.14 eV. After accounting for zero-point energy differences (0.04 eV), the weighted average BDE is $D_0(Th^+\text{-}CH_3)$ = 2.39 ± 0.22 eV. This value is likely a lower limit, because like ThH^+, $ThCH_3^+$ competes with reaction 4.3 through a shared intermediate such that the reaction 4.5 threshold may be delayed. Given that both experimental data and theoretical models (see Table 4.3) indicate that the BDEs for $ThCH_3^+$ and ThH^+ are similar, the delay in threshold onset for reaction 5 should be equivalent to the delay observed in reaction 4.4, 0.21 ± 0.19 eV. This conclusion is substantiated by the phase space theory modelling described in the Supporting Information, Figure A.2. This model indicates that thresholds for both reactions 4.4 and 4.5 are shifted by comparable amounts that are consistent with a shift of 0.21 ± 0.19 eV. Therefore, a better estimate of the $ThCH_3^+$ BDE is $D_0(Th^+\text{-}CH_3)$ = 2.60 ± 0.30 eV. Previously, no theoretical or experimental report of the BDE for $ThCH_3^+$ has been made.

Similar to results for ThH^+, the DFT methods indicate that $ThCH_3^+$ has a ground-state of ^3E with the unpaired electrons found in the *7s* and *6d* atomic orbitals and a low-lying level, $^1A_1$, only 0.06 eV above the ^3E for B3LYP. Additionally, a structural isomer, $HThCH_2^+$ ($^1A'$), is found nearly isoenergetic to the ^3E. CCSD(T) calculations place the $^1A_1$ and $^1A'$ states 0.22 and 0.01 eV, respectively, below the ^3E. CCSD(T)/KAP calculations place the $^1A_1$ and $^1A'$ states 0.18 and 0.19 eV lower in energy, respectively. Other structures and states investigated are listed in Table A.4, but are found to be at least 2 eV higher in energy than $ThCH_3^+$ (^3E).

Theoretical BDEs listed in Table 4.3 for both the ^3E and $^1A_1$ states indicate that $D_0(Th^+\text{-}CH_3)$ and $D_0(Th^+\text{-}H)$ have similar magnitudes, with the former being stronger by 0.23 – 0.67 eV. Similar results are obtained using the SDD and ANO basis sets, Table A.5. A direct comparison of the thresholds from reaction 4.4 and 4.5 in Table 4.1 suggests that $D_0(Th^+\text{-}CH_3)$ is 0.27 ± 0.22 eV larger than $D_0(Th^+\text{-}H)$ and that $D_0(Th^+\text{-}CD_3)$ is 0.12 ± 0.14 eV larger than $D_0(Th^+\text{-}D)$, with a weighted average (after ZPE corrections) of 0.15 ± 0.12 eV. This is comparable to results for the transition metal congeners, Zr^+,[15,53] and Hf^+,[25,69] where MCH_3^+ and MH^+ BDEs are similar in strength, and to Ti^+,[88] where the BDE for $TiCH_3^+$ is stronger than that for TiH^+ by 0.2 ± 0.2 eV. Similar to the results for ThH^+, theory overbinds by 0.4 – 0.9 eV, again in part because of spin-orbit effects discussed below.

$ThCH^+$

The threshold for reaction 4.6 is 3.08 ± 0.17 eV and 2.98 ± 0.06 eV for the deuterated analogue, Table 4.1. The correlation between the decline in the cross section for $ThCH_3^+$ at the apparent onset for the formation of $ThCH^+$ indicates that this product is formed by the dehydrogenation of $ThCH_3^+$. Thus, we combine these thresholds with $D_0(H_2C\text{-}H_2) + D_0(HC\text{-}H) = 9.07 \pm 0.02$ eV[60] and the value of its deuterated counterpart to obtain BDEs of $D_0(Th^+\text{-}CH) = 5.99 \pm 0.20$ eV and $D_0(Th^+\text{-}CD) = 6.27 \pm 0.09$ eV. After accounting for differences in the zero-point energy (0.03 eV), the weighted average is $D_0(Th^+\text{-}CH) = 6.19 \pm 0.16$ eV.

The ground-state structure of $ThCH^+$ identified by theory is a linear methylidyne having a $^1\Sigma^+$ ground-state. Several geometries including bent and linear insertion

($HThC^+$) geometries were also investigated, but these are all found to be at least 2.2 eV higher in energy, as detailed in Table A.4.

Theoretical predictions of $D_0(Th^+\text{-}CH)$ range from 0.4 eV too high (B3PW91) to 0.6 eV too low in energy (BHLYP) with the values derived from B3LYP and CCSD(T) (seg. SDD and KAP) within experimental uncertainty. Benchmark studies by Zhang and Schwarz[89] indicate that although BHLYP performs well for MCH_3^+ species, it performs poorly for other MCH_x^+ systems. Studies from our group have also observed similar poor performance by BHLYP for studies involving higher bond order thirdrow transition metal species,[23,25-28,30] indicating that BHLYP is an inappropriate choice of level of theory for the study of species with bond orders higher than 1.

$ThCH_4^+$

The threshold for reaction 4.7 obtained using Eq. 4.1 is 0.46 ± 0.05 eV, which should equal $D_0(Th^+\text{-}CH_4)$, as discussed below. Previous work[90,91] in our lab has indicated that collisionally excited association complexes may have a sufficiently long lifetime such that dissociation does not occur within the experimental time frame of 1×10^{-4} s. In such cases, the apparent threshold is higher than the true bond energy because of a kinetic shift in the threshold.[91,92] Therefore, the cross section for reaction 4.7 was also modeled using a modified version of Eq. 4.1 that incorporates RRKM rate theory[93,94] to account for any possible kinetic shift. This model, which has been thoroughly explained elsewhere,[91,92] yields a threshold of 0.47 ± 0.05 eV, indicating there is no significant kinetic shift, consistent with the simplicity of this system.

The ground-state of $Th^+(CH_4)$ is ^2A with a calculated structure that is

nonsymmetrical as Th^+ binds to CH_4 such that the bond lengths r(Th-H) of the three closest H atoms are 2.71, 2.70, and 2.66 Å. The methane is largely unperturbed, consistent with the formation of an electrostatic bond. Both di Santo et al.[41] and de Almeida and Duarte[42] also report a ^2A structure for the ground-state of $Th^+(CH_4)$. A more symmetrical $^2A'$ state is also found 0.1 – 0.2 eV higher in energy. A $^4A''$ state lies 0.06 – 0.22 eV higher in energy than the ^2A state, Table A.4.

The theoretical BDEs of the $Th^+(CH_4)$ (^2A) state relative to Th^+ (^2D,$6d7s^2$) + CH_4 range from 0.33 - 0.64 eV, Table 4.3, where B3LYP and B3PW91 overestimate the bond strength and BHLYP and CCSD(T) are too low in energy. Results using the SDD and ANO basis sets are similar with the exception of the BHLYP/SDD and CCSD(T)/SDD values, which underestimate the bond strength by ~0.2 eV, Table A.5. CCSD(T)/KAP results place the BDE slightly outside of experimental uncertainty. Di Santo et al.[41] report theoretical BDEs of 0.32 and 1.05 eV using B3LYP/SDD/6-311++G(d,p) and PW91/ZORA, respectively. Again PW91/ZORA appears to significantly overestimate the BDE, and the B3LYP value is somewhat low. Theoretical BDEs of 0.47 and 0.44 eV calculated by B3PW91/DZP/6-311++G(d,p) and B3LYP/DZP/6-311++G(d,p), respectively, can also be inferred from de Almeida and Duarte's potential energy surface for reaction 4.3.[42] These latter values are in good agreement with the experimental and theoretical values determined here.

As discussed more thoroughly below, the lowest energy structure for $ThCH_4^+$ is not $Th^+(CH_4)$ but rather the inserted $HThCH_3^+$. Theoretical BDEs for this inserted species losing CH_4 range from 1.47 – 2.00 eV, well above the experimental value. Given the agreement between theoretical and experimental BDEs for $Th^+(CH_4)$, it can be concluded

that $ThCH_4^+$ complex formed in our experiment is $Th^+(CH_4)$. By extension, the failure to generate $HThCH_3^+$ in the flow tube source suggests that there must be a barrier in excess of thermal energies when Th^+ interacts with methane. The presence of this barrier will be explored in greater detail below.

Doublet Potential Energy Surface for $Th^+ + CH_4$ Reaction

The potential energy surfaces for reactions 4.3, 4.4, and 4.5 were calculated using several basis sets for Th^+. The PES at the CCSD(T)/Seg. SDD/6-311++G(3df,3p)//B3LYP/SDD/6-311++G(d,p) level of theory appears to reproduce the experimental data most accurately and is presented in Figure 4.4 with structures in Figure 4.5. Geometrical parameters can be found in Table A.6 in the Supporting Information section. The energies of each intermediate and transition state (TS) as well as values from additional levels of theory are in Table 4.4. Energies from the SDD and ANO basis sets are listed in Table A.7 in the Supporting Information. Most energies in Figure 4.4 and Table 4.4 are relative to the Th^+ (^{2}D, $6d7s^2$) + CH_4 reactants, except where explicitly noted otherwise. As discussed in detail below, accounting for spin-orbit interactions is critical when comparing the PESs to experimentally measured values. Thus, the solid lines in Figure 4.4 denote surfaces with spin-orbit energy explicitly accounted for and the dotted lines represent the uncorrected surfaces. Geometries and electronic states of all the intermediates and transition states are similar to those reported by di Santo et al. (B3LYP)[41] and de Almeida and Duarte (B3PW91),[42] and their calculated values are included in Table 4.4. (Note these are referenced to different ground-state reactants.) When compared to the present calculations using the same level of theory and the same

reactant state, the mean absolute deviations in all energies are about 11 and 12 kJ/mol, respectively. Similar to the reaction coordinate published by di Santo et al.,[41] before spin-orbit interactions are included, the reaction appears to evolve entirely along the doublet surface. This contrasts with B3PW91 calculations of de Almeida and Duarte where they observe a crossing between the reactants' ground quartet surface and the doublet surface near the first intermediate because their calculations place Th^+ (^{4}F) below Th^+ (^{2}D).[42] No such crossing point was observed at any level of theory studied here, although the doublet and quartet thorium-methane adducts are close in energy at the B3PW91, BHLYP, and CCSD(T) levels of theory, Table 4.4.

The first intermediate (^{2}**1**) is the association complex, $Th^+(CH_4)$, where the methane is largely unperturbed. ^{2}**1** (^{2}A) lies 31 – 62 kJ/mol lower in energy than the ground-state reactants, which is consistent with the CID threshold of 45.3 ± 4.8 kJ/mol in reaction 4.7 (Figure 4.3). It is worth noting that ^{2}**1** is the only intermediate that shows spin contamination, s(s+1) = 1.35 – 1.69 in the present calculations, of a similar magnitude to that of the Th^+ separated atom. This spin contamination probably arises from the proximity (in energy) of the quartet intermediate. This intermediate has similar geometric properties to the doublet analogue and is only 6 – 22 kJ/mol higher in energy.

The first transition state (^{2}**TS1/2**) connects ^{2}**1** with the global minimum ^{2}**2**, $HThCH_3^+$, the thorium hydrido methyl cation intermediate. The r(Th^+-C) bond decreases from 2.78 Å in ^{2}**1** to 2.29 Å in ^{2}**TS1/2**, a single C-H bond elongates from 1.10 to 1.37 Å, and the H moves closer to the metal center. ^{2}**TS1/2** (^{2}A) lies 6 and 26 kJ/mol above the reactants according to CCSD(T) and BHLYP calculations, respectively, whereas B3LYP and B3PW91 indicate ^{2}**TS1/2** lies below the reactants by 17 and 35 kJ/mol, all referenced

to the Th^+ (^2D) + CH_4 asymptote. Di Santo and coworkers previously reported the presence of a 5 kJ/mol barrier in similar B3LYP calculations;[41] however, their reported potential energy surface was referenced to the Th^+ (^2F, $5f7s^2$) state that is the ground-state for B3LYP and B3PW91 calculations but is 18 – 56 kJ/mol (Table 4.2) higher in energy for the other levels of theory and 42 kJ/mol higher experimentally. The use of the ^2F state as the reference in our surface would lead to a barrier of 2 kJ/mol for the surface calculated using B3LYP/Seg. SDD/6-311++G(3df,3p), similar to the result of di Santo and coworkers. No barrier is observed in the results of de Almeida and Duarte, who place the ^{2}TS1/2 transition state 7 – 25 kJ/mol below the ^2D asymptote and 15 – 18 kJ/mol below the ^4F ground asymptote.[42]

The ground-state of $HThCH_3^+$, ^{2}**2**, where the metal is inserted into one of the C-H bonds, lies 162 – 202 kJ/mol below ground-state reactants. It has a $^2A'$ ground-state with r(Th-H) = 2.00 Å and r(Th-CH_3) = 2.32 Å bond lengths. These are comparable to r(Th-H) for ThH^+ of 1.99 Å and r(Th-CH_3) for $ThCH_3^+$ of 2.31 Å, consistent with the formation of single covalent bonds between the Th cation (having three valence electrons) and both ligands, which necessitates having the doublet low-spin. (Thus, the quartet state of this species can no longer form two covalent bonds, leading to the much higher energy.)

^{2}**TS2/3** has a ^2A ground-state and lies 26 – 101 kJ/mol below the reactants in energy. ^{2}**TS2/3** is a four-centered transition state in which another C-H bond elongates from 1.10 to 1.71 Å as this second H is transferred from the C to the H ligand. Thus, the Th^+-H bond in ^{2}**2** lengthens, consistent with the Th^+-H covalent bond beginning to break as the H-H bond forms. This leads to ^{2}**3** (^2A), a thorium carbene cation-dihydrogen association complex, $(H_2)ThCH_2^+$, which lies 35 – 98 kJ/mol lower than the reactants.

Loss of H_2 from ^{2}**3** requires only 13 – 21 kJ/mol and leads to the $ThCH_2^+$ ($^2A'$) + H_2 products. Overall, the dehydrogenation reaction is calculated to be exothermic by 22 – 77 kJ/mol along the doublet surface.

An alternative pathway for dehydrogenation is to proceed through ^{2}**TS2/4**, which forms when a second hydrogen is transferred to the metal center to form ^{2}**4**, a dihydride carbene cation, $H_2ThCH_2^+$. In this case, both r(Th-H) bonds have lengths of 2.01 Å, consistent with covalent bonds, and the ∠HThH angle (100.7°) is much larger than ∠HThH (25.3°) in ^{2}**TS2/3**. Furthermore, r(Th-C) = 2.32 Å in ^{2}**4** is longer than r(Th-C) = 2.11 Å in ^{2}**TS2/3**, considerably longer than r(Th-C) = 2.04 Å in the $ThCH_2^+$ product, and equivalent to r(Th-C) = 2.31 Å in $ThCH_3^+$, showing that the Th-C bond in ^{2}**4** no longer has double bond character. ^{2}**4** has a ^{2}A' ground-state that converts to ^{2}**3** through ^{2}**TS4/3** (^{2}A) by rotating the hydrogens located on the Th^+ together. As this pathway is considerably higher in energy (by 85 – 116 kJ/mol) than passing through ^{2}**TS2/3**, it is unlikely to be influential experimentally.

Quartet Potential Energy Surface for $Th^+ + CH_4$ Reaction

The quartet surface presented here is energetically less favorable than the doublet surface at all points along the surface for all levels of theory investigated, Table 4.4. The structures of all intermediates and transition states are similar to their analogous doublet structures and are pictured in Figure A.3 in the Supporting Information. The surface originates from Th^+ (^{4}F, $6d^27s$) + CH_4, which is 2 – 18 kJ/mol higher in energy than Th^+ (^{2}D, $6d7s^2$) + CH_4. The $Th^+(CH_4)$ association complex of CH_4 with Th^+, where the methane is largely unperturbed. ^{4}**1** is 6 – 22 kJ/mol higher in energy than ^{2}**1** with r(Th-C)

increased by 0.12 Å. The surface is repulsive as it moves through ^{4}**TS1/2** to ^{4}**2** and r(Th-C) decreases from 2.90 to 2.86 Å. ^{4}**TS1/2** lies 59 – 95 kJ/mol higher in energy than ^{2}**TS1/2** and ^{4}**2** lies 245 – 259 kJ/mol higher in energy than ^{2}**2** with r(Th-H) and r(Th-C) being 0.05 and 0.37 Å longer, respectively. Thus, the higher spin state means that the HTh-CH_3 bond is no longer a covalent single bond, greatly increasing the energy of this species. ^{4}**2** is connected to ^{4}**3** by ^{4}**TS2/3**, which is 169 – 196 kJ/mol higher in energy than ^{2}**TS2/3**. ^{4}**3** is a thorium carbene cation – dihydrogen association complex that is 100 – 134 kJ/mol higher in energy than ^{2}**3**. Similar to the doublet complex, loss of H_2 requires only 9 – 17 kJ/mol to dissociate to the products, $ThCH_2^+$ (^{4}A") + H_2. Overall, the dehydrogenation reaction along this pathway is 39 – 79 kJ/mol endothermic compared to the ^{2}D ground-state reactants and 96 – 130 kJ/mol above the $ThCH_2^+$ (^{2}A') + H_2 products. Notably, r(Th-C) of $ThCH_2^+$ (^{4}A") is 2.32 Å, 0.27 Å longer than $ThCH_2^+$ (^{2}A'), and similar to $ThCH_3^+$ where r(Th-C) = 2.31 Å. Thus, the high-spin state of $ThCH_2^+$ (^{4}A") no longer allows a Th-C covalent double bond.

Discussion

Spin-Orbit Corrections to Theoretical BDEs

The present theoretical calculations correspond to the average energy over all spin-orbit levels in a given state; however, the experimental results presented here should correspond to the energies of the lowest spin-orbit states. For Th^+, this effect is quite large, thereby accounting for much of the deviation between theoretical and experimental BDEs. In order to make a better comparison between theory and experiment, it is necessary to explicitly estimate the spin-orbit energies. For dissociation of Th^+-L bonds,

the experimental asymptote for $Th^+ + L$ lies below the theoretical asymptote such that the theoretical BDE should be lowered by the average excitation energy of Th^+ and the ligands (where the spin-orbit correction for the latter is negligible here) and raised by the spin-orbit splitting of the ground-state of ThL^+. Th^+ is an interesting case where the ground-state averaged over all spin-orbit levels is ^2D, but the ground-level is $^4F_{3/2}$. The estimation of the spin-orbit effects of the asymptote can be done in two ways. The first is to consider that the spin state and bonding of the molecules listed in Table 4.3 (except ThH^+ ($^1\Sigma^+$), $ThCH_3^+$ ($^1A_1$), and $ThCH_4^+$ (^2A)) necessitate that the molecules are diabatically associated with the Th^+ (^4F) + L asymptote. Thus, to include the spin-orbit effects of the $Th^+ + L$ asymptote, the theoretically calculated BDE for dissociation to Th^+ (^4F) + L (rather than for dissociation to the ^2D state as listed in Table 4.3) is corrected to the Th^+ ($^4F_{3/2}$) + L asymptote by the empirical difference in energy of the ^4F state averaged over all spin-orbit levels and the $^4F_{3/2}$ level, 3729.960 cm^{-1} = -0.46 eV, Table A.1. When necessary, the BDE is also corrected by the spin-orbit splitting of the respective ThL^+ molecule, as estimated below. Utilizing this method yields mean absolute deviations (MADs) of 0.31 – 0.41 eV compared to experimental values excluding $ThCH_2^+$. The second method is to correct directly from the Th^+ (^2D) + L asymptote to the Th^+ ($^4F_{3/2}$) + L asymptote by the difference between the $^4F_{3/2}$ level and the ^2D state averaged over all spin-orbit states. Empirically, the $^4F_{3/2}$ lies 3211.991 cm^{-1} = 0.40 eV below the ^2D state, Table A.1. Utilizing this method yields MADs of 0.27 – 0.38 eV, Table 4.3, indicating that this method provides slightly more reliable predictions, which is why the latter method is used here.

It should be noted that this semiempirical approach to estimating spin-orbit effects

is only a first-order approximation, as second-order effects associated with coupling with other states is possible in some instances (mentioned specifically below). An estimation of these effects is beyond the scope of the present approach, such that we assume such second-order perturbations are negligible, which may lead to (potentially significant) errors in the estimated stabilization energies. We also note that rigorous theoretical methods designed to treat spin-orbit interactions tend to underestimate the experimentally observed couplings.[95]

$ThCH_2^+$ has a $^2A'$ ground-state and hence has no spin-orbit splitting. Second-order interactions of this state with the $^2A''$ and $^4A''$ states may occur, but these interactions are assumed to be negligible because these states are much higher in energy, Table A.4. Thus, spin-orbit corrections to $D_0(Th^+\text{-}CH_2)$ involve only the average excitation energy of -0.40 eV from the $Th^+(^2D) + CH_2$ asymptote. After including this spin-orbit energy correction, the theoretical BDEs for $ThCH_2^+$ are 4.42 (BHLYP) and 4.74 – 5.04 eV, Table 4.3, such that reaction 4.3 is endothermic by 0.17 for BHLYP, whereas the other levels predict the reaction will be exothermic by 0.13 – 0.40 eV (Table 4.4). Note that the BHLYP result (which is suspect for this multiply bonded species) is potentially consistent with the threshold experimentally measured for reaction 4.3; however, at all levels of theory, the barrier at ^{2}**TS1/2** in the reaction coordinate (Figure 4.4) lies 42 – 58 kJ/mol above the product asymptote. Thus, theory indicates that the threshold must correspond to the barrier at ^{2}**TS1/2**. Therefore, our experimental value of $D_0(Th^+\text{-}CH_2)$ can only be reported as a lower limit to the true BDE, although CCSD(T), B3LYP, and B3PW91 levels all indicate the bond is not that much stronger. Nevertheless, comparison of experimental and theoretical results with and without explicitly accounting for spin-orbit

effects is inexact.

$ThCH^+$ has a $^1\Sigma^+$ ground-state, which has no spin-orbit splitting, so like $ThCH_2^+$, the only spin-orbit correction to the BDE needed is that from the Th^+ (^2D) + CH asymptote. Here, second-order spin-orbit interactions are assumed to be negligible because the appropriate excited-states with which the $^1\Sigma^+$ ground-state can interact are much higher in energy, Table A.4. When this spin-orbit correction is included, the theoretical BDEs are 5.17 (BHLYP) and 5.64 – 6.21 eV, Table 4.3, where the latter values are in reasonable agreement with the experimental value of 6.19 ± 0.16 eV. BHLYP underestimates the BDE by the most (~1 eV), which as noted above, is typical of BHLYP calculations for multiply bonded species. Excluding the BHLYP results, the average deviation between theory and experiment when spin-orbit corrections are included is 0.32 ± 0.27 eV, which is comparable to the average deviation without including spin-orbit corrections (0.19 ± 0.20 eV). Thus, the applied correction does little to improve (or harm) the theoretical BDEs in this case. CCSD(T)/KAP calculations are similar with both the uncorrected and corrected BDEs being slightly outside of experimental uncertainty.

Previous work has successfully estimated the spin-orbit splitting for third-row transition metal molecules[30,96-98] by using:

$$E^{SO} = \Lambda M_S A \tag{4.8}$$

where A is the spin-orbit splitting constant, Λ is the orbital angular momentum quantum number, and M_S is the spin quantum number associated with a particular level $\Omega = \Lambda +$

M_S.[99] E^{SO} is also equal to the summation $\Sigma\, a_i\, \ell_i \bullet s_i$, where $\ell_i \bullet s_i$ is the dot product of the orbital angular momentum and the spin of electron i and a_i is the spin-orbit parameter, which can be represented by the atomic spin-orbit parameter for the *6d* electrons of thorium ζ_{6d}(Th). To the best of our knowledge, this constant has not been determined experimentally, but we estimate that ζ_{6d}(Th) = 1458 cm^{-1} as explained in the Supporting Information.

The $^3\Delta$ state of ThH^+ splits into $^3\Delta_1$, $^3\Delta_2$, and $^3\Delta_3$ levels where $^3\Delta_1$, with $\Lambda = 2$ and $M_S = -1$, is the ground-level. Using Eq. 4.8 and our estimated value of ζ_{6d}(Th), this ground-level lies relative to the spin-orbit average value by $E^{SO} = 2\ (-1)\ A = -\zeta_{6d}(Th)$ = -1458 cm^{-1} = -0.18 eV so that A = 729 cm^{-1}. The splitting for $^3\Delta_2$ is $E^{SO} = 2\ (0)\ A = 0.0$ eV, and the $^3\Delta_3$ level is destabilized by $E^{SO} = 2\ (1)\ A = 0.18$ eV from the unperturbed state. Thus, the theoretical BDEs for ThH^+ ($^3\Delta$) relative to Th^+ (^{2}D) should be decreased by 0.40 eV, the difference between the average ^{2}D and $^4F_{3/2}$ level for Th^+, and increased by 0.18 eV to account for the splitting in the $^3\Delta_1$ state. Doing so yields BDEs of 2.57 – 2.96 eV for the ThH^+ ($^3\Delta_1$) state, Table 4.3. In general, inclusion of spin-orbit corrections improves the agreement between the theoretical BDEs for ThH^+ and the experimental value, with the BHLYP result within experimental uncertainty, CCSD(T)/seg. SDD nearly so, and the other methods slightly higher.

The $^1\Sigma^+$ state of ThH^+ has no spin-orbit splitting, so BDEs need only be corrected by the difference in energy between the average ^{2}D state and the $^4F_{3/2}$ level. Applying this correction, BDEs for the $^1\Sigma^+$ state are 2.26 – 2.47 eV and 2.55 eV for CCSD(T)/KAP. As noted above, the predicted ground-state for ThH^+ is $^3\Delta$ for all methods except CCSD(T), such that these BDEs should not correspond to the experimentally measured value. In the

CCSD(T) case, a $^1\Sigma^+$ ground-state lying 0.07 eV below the $^3\Delta$ is predicted, but after including spin-orbit effects, the $^3\Delta_1$ lies 0.11 eV below the $^1\Sigma^+$. CCSD(T)/KAP calculations indicate that the $^3\Delta_1$ lies 0.14 eV below the $^1\Sigma^+$. Additionally, Eq. 8 indicates that the stabilization of the $^3\Pi_0$ level is only 0.09 eV such that the $^3\Delta_1$ is predicted to be the ground-level at all levels of theory. The results using the ANO basis set are similar, whereas the SDD basis set indicates that the $^1\Sigma^+$ and $^3\Delta_1$ are isoenergetic, Table A.5. Further complicating the assignment of the ground-level is the second-order spin-orbit interaction of the $^3\Delta_1$ level with the $^3\Pi_1$ and of the $^1\Sigma^+$ with the $^3\Pi_0$ level. In these cases, the interactions should stabilize both the $^3\Delta_1$ and $^1\Sigma^+$ levels, but we make no attempt to quantify this effect. Because both the $^3\Delta$ and $^1\Sigma^+$ states can be formed directly from the (^{4}F,^{2}D) mixed ground-level of Th^+, the mixed results here preclude a confident determination of the true ThH^+ ground electronic state.

The calculated ground-state of $ThCH_3^+$ is ^{3}E (DFT) or $^1A_1$ (CCSD(T)). Like ThH^+ ($^3\Delta$), the unpaired electrons in the triplet state are d^1s^1, where the *d*-electron is found in a δ-like orbital. As an approximation to the spin-orbit splitting for the ^{3}E state, we assume that the splitting is similar to that for ThH^+ ($^3\Delta$). The $^1A_1$ state has no spin-orbit corrections. Unlike ThH^+, after inclusion of spin-orbit effects, the $^1A_1$ still lies below the ^{3}E for CCSD(T) and the states are isoenergetic for CCSD(T)/KAP. After applying the spin-orbit corrections, the theoretical BDEs are 2.76 – 3.32 eV for the ^{3}E and 2.56 – 3.00 eV for the $^1A_1$ (3.22 eV for CCSD(T)/KAP), Table 4.3, improving the agreement with the experimental value of $D_0(Th^+\text{-}CH_3) = 2.60 \pm 0.30$ eV. Here, the BHLYP value for the ^{3}E is within experimental uncertainty of the experimental BDE, and the CCSD(T)/seg. SDD value for the $^1A_1$ is just outside the experimental range.

The calculated ground-state of $Th^+(CH_4)$ is ^2A where the CH_4 is loosely bound and largely unperturbed. Because bonding results from electrostatic interactions between Th^+ and CH_4, a zero-order approximation of the spin-orbit splitting of this molecule assumes it is very similar to that found on the atomic metal center when unperturbed. Thus, we make no spin-orbit corrections to the theoretical BDEs for this species; however, because the $^4F_{3/2}$ level lies 0.23 eV (1859.938 cm^{-1}) below the $^2D_{3/2}$ level (Table A.1) and the calculated BDEs for ^{2}1 and ^{4}1 are comparable (within 0.13 eV, Table 4.4), the ground-state of $Th^+(CH_4)$ becomes the $^4A''$ at all levels of theory. The theoretical BDEs for this state are 0.43 – 0.57 eV and 0.51 eV for CCSD(T)/KAP, in very good agreement with the experimental value, Table 4.3.

This first-order approximation to the true spin-orbit interaction in $Th^+(CH_4)$ cannot be rigorously correct because the degenerate *d*-orbitals of the nonperturbed Th^+ will be split by interaction with CH_4, which can be thought about in terms of a simple donor-acceptor model. When CH_4 is brought into close proximity, it donates electron density into the d_{z2}-orbital. This interaction of the σ-like orbitals of the Th^+ and CH_4 leads to a pair of bonding and antibonding orbitals, such that the d_{z2}-orbital is pushed up in energy. Simultaneously, the δ–like orbitals on Th^+ are largely noninteractive with CH_4, whereas the π-like *d*-orbitals interact with antibonding orbitals on CH_4 stabilizing these orbitals. This analysis agrees with the results of our calculations on $Th^+(CH_4)$ (^2A), where the unpaired electron is located in a π-like *6d*-orbital located on Th^+ and with those for $Th^+(CH_4)$ ($^4A''$) where the unpaired electrons are in the *7s*–orbital and two π-like *6d*-orbitals. Thus, to a first approximation, the theoretical results naturally account for the orbital occupation preference, but a quantitative account of how these interactions change

the first-order spin-orbit correction applied above is not attempted here. The approximation made here should be reasonable as long as the splitting of the degenerate *6d*-orbital energies resulting from the ligand is smaller than the spin-orbit splitting of the free ion. This assumption appears reasonable because of a favorable comparison to the experimental value for the $Th^+(CH_4)$ well depth.

Bonding in $ThCH_x^+$

Figure 4.6 shows a comparison of the $D_0(Th^+\text{-}CH_x)$ values with their organic analogues $D_0(H_xC\text{-}CH_x)$. Such a plot is a useful means of experimentally determining bond order and has proven useful for many transition metal systems.[15,22,25,28,30] The solid line represents the least-squares linear regression constrained to pass through the origin. In order to ascertain a more accurate trend, $D_0(Th^+\text{-}H) = 2.46 \pm 0.07$ eV from the reaction of Th^+ with H_2 and the adjusted value for $D_0(Th^+\text{-}CH_3)$ are used.[87] Notably, there is no meaningful change in the trend line when $D_0(Th^+\text{-}CH_2)$, which is a lower limit, is excluded from the fit. This suggests that the true value of $D_0(Th^+\text{-}CH_2)$ is unlikely to be much higher than the limit, consistent with theory. The good correlation of the plot clearly indicates that $Th^+\text{-}H$ and $Th^+\text{-}CH_3$ are single bonds, $Th^+{=}CH_2$ is a double bond, and $Th^+{\equiv}CH$ is a triple bond. These assignments are fully consistent with the quantum chemical calculations described above.

It is also interesting to compare these BDEs with those of several related metals. Unfortunately, comparable experimental data for other actinides do not exist, with the exception of $D_0(U^+\text{-}H) = 2.9 \pm 0.1$ eV.[34] However, because Th^+ does not occupy the *5f* orbitals in its ground-state, a better comparison might be to transition metals with three

valence electrons: Hf^+ (^{2}D, $5d6s^2$), Zr^+ (^{4}F, $4d^25s$), and Ti^+ (^{4}F, $3d^24s$). In this regard, it is worth noting the similarities of Th^+ with Hf^+, where experiment and theory both assign a ^{2}D ($5d6s^2$) ground-state.[25,55,69] In calculations of the Hf^+ (^{2}D) state, the observed spin contamination, s(s+1) ~ 1.2, is comparable to that of the Th^+ system.[25] The BDEs for these metals are compared to those for Th^+ in Table 4.5 and Figure 4.6. The slope of the trend line for Th^+, m = 0.62, is very similar to that of Zr^+, m = 0.60, and systematically higher than those observed for Hf^+, m = 0.53, and Ti^+, m = 0.54. Thus, the relative BDEs are $Ti^+ \approx Hf^+ < Zr^+ \approx Th^+$. Typically BDEs increase moving down the periodic table because of the lanthanide contraction,[22,23,26,27,89] leading to an expected trend in BDEs of $Ti^+ < Zr^+ < Hf^+ < Th^+$. The lower BDEs of Hf^+ (^{2}D, $5d6s^2$) have previously been explained by the filled *6s* orbital, which inhibits bond formation,[25] compared to the open *d*-shell configurations of Ti^+ (^{4}F, $3d^24s$) and Zr^+ (^{4}F, $4d^25s$). Likewise, the partial ^{2}D character of the ground J = 3/2 level may suppress the BDEs of Th^+ somewhat.

The individual trends for each bond type indicate that for the singly bonded M^+-H and M^+-CH_3, the BDE trend is $Hf^+ < Zr^+ < Ti^+ < Th^+$, whereas the multiply bonded species, M^+-CH_2 and M^+-CH, have bonds that follow the order $Ti^+ < Hf^+ < Zr^+ \approx Th^+$ and $Hf^+ < Ti^+ < Zr^+ < Th^+$, respectively. Presumably, some of these variations are associated with the strength of the π-bonds, which can vary through the periodic table because of overlap differences as the size of the *d* orbitals on the metal changes. Despite some deviation from the expected trend for the smaller metal cations, Th^+ BDEs are consistently higher than the other metal cation BDEs considered here, with the possible exception of $D_0(Th^+$-$CH_2)$, which is only a lower limit. For the other BDEs, the Th^+ BDEs average 0.24 ± 0.16 eV higher in energy than the Zr^+ BDEs. Assuming that the

trend between Th^+ and Zr^+ BDEs holds true for MCH_2^+, then $D_0(Th^+\text{-}CH_2) = 4.86 \pm 0.17$ eV can be estimated. This value is in reasonable agreement with BDEs obtained using the seg. SDD basis set at the B3LYP (4.92 eV), B3PW91 (5.04 eV), and CCSD(T) (4.74 eV) levels as well as CCSD(T)/KAP (4.94 eV).

Spin-Orbit Corrected Potential Energy Surface

The kinetic energy dependent cross section of reaction 4.3, Figure 4.1, clearly has an energy dependence inconsistent with a barrierless, simple exothermic reaction, as previously concluded on the basis of the FT-ICR experiments.[35,36] Thus, this reaction is either endothermic, or a barrier in excess of the reactant energies is present. As noted above, before spin-orbit corrections, all levels of theory here, Table 4.4, and previous theoretical work[41,42] indicate that reaction 4.3 is exothermic overall; however, a valid comparison between experiment and theory requires consideration of a correction to account for spin-orbit interactions. (Ideally, this could be accomplished using either a two-component approach or a perturbative approach where matrix elements of the SOC Hamiltonian are computed between states that are low in energy. Here, we use a simpler first-order approximation to all spin-orbit corrections.) With the exception of intermediate **1**, all intermediates and transition states along the potential energy surface in Figure 4.4 are A states (including the $ThCH_2^+$ products discussed above) and as such should experience no first-order spin-orbit splitting. Furthermore, the quartet surface for this part of the potential energy surface is well above the doublet surface, such that spin-orbit interactions between these surfaces should also be relatively small. For intermediate **1**, an electrostatic interaction of Th^+ and CH_4, we expect a similar spin-orbit splitting as

the unbound Th^+, which does exhibit spin-orbit interaction. As discussed above, this approximation leads to a calculated well depth for **1** relative to its respective asymptote remaining constant. To approximately correct the PES in Figure 4.4, we identify the true J = 3/2 reactant asymptote as lying 38.4 kJ/mol (3211.991 cm^{-1}) lower in energy than the ^2D ($6d7s^2$) theoretical value, which is an average over all spin-orbit states of Th^+ (^2D). Likewise, the $^2D_{3/2}$ asymptote lies 16.2 kJ/mol (1352.053 cm^{-1}) below the ^2D. Referencing the PES to the $^4F_{3/2}$ asymptote pushes the energy of all intermediates (except **1**), transition states, and products up by 38.4 kJ/mol relative to Th^+ ($^4F_{3/2}$) + CH_4, as indicated by the solid line in Figure 4.4. Note that by using experimental spin-orbit splittings, we effectively include the mixing of the ^4F state into the reactants and intermediate **1** complex. Table 4.4 lists the explicit values of all species along the spin-orbit corrected PES at the CCSD(T) level shown in Figure 4.4, with results for other levels of theory in Table A.7. Making this correction, B3LYP, B3PW91, and CCSD(T) levels predict that reaction 4.3 is exothermic by 13 – 39 kJ/mol, Table 4.4. (BHLYP predicts the reaction is endothermic by 16 kJ/mol, although as noted above, BHLYP is not expected to be accurate for the multiply bound $ThCH_2^+$ product.)

A second corollary of the spin-orbit corrections is that a crossing between the quartet and doublet surfaces is observed between **1** and **^{2}TS1/2** at all levels of theory. De Almeida and Duarte also reported a crossing along their B3PW91 surface, Table 4.4, although it occurs between the $Th^+ + CH_4$ reactants and **1** and is a consequence of finding a Th^+ (^4F) ground-state.[42] For the spin-orbit corrected surface shown in Figure 4.4, it can be realized that the "surface crossing" is an artifact of imposing the construct of a spin state on the reaction surface, whereas only the total spin-orbit quantum state is likely to

be a good quantum number for such a heavy element. As a consequence, calculations designed to locate the crossing point would not be useful as there is no crossing between doublet and quartet surfaces before including spin-orbit corrections. In addition, experimentally, the J = 3/2 ground-level is a mixture of the ^{4}F and ^{2}D states so that ^{2}**1** and ^{4}**1** are both conceivably accessible directly from the ground-level asymptote without a surface crossing.

The presence of a barrier in excess of reactant energies is established experimentally by the CID of $ThCH_4^+$, Figure 4.3, which yields $Th^+ + CH_4$ exclusively. This result shows that the $ThCH_4^+$ adduct is trapped as the association intermediate **1**, $Th^+(CH_4)$. In previous work of the related platinum system, reaction of $Pt^+ + CH_4$ leads to dehydrogenation in a barrierless exothermic reaction and CID of $PtCH_4^+$ with Xe yielded $Pt^+ + CH_4$ and $PtH^+ + CH_3$ products, consistent with a $HPtCH_3^+$ structure.[22] Furthermore, the threshold measured for the $Pt^+ + CH_4$ products in the CID reaction, $E_0 = 1.72 \pm 0.05$ eV, is consistent with this inserted structure and much greater than would be expected for $Pt^+(CH_4)$, where theory predicts a threshold of $E_0 = 0.9$ eV. In the Th^+ system, if the barrier at ^{2}**TS1/2** were not present, the formation of ^{2}**2**, $HThCH_3^+$, would be expected as this is the most stable species on the reaction surface. Then, like the Pt^+ system, the CID products $ThCH_2^+ + H_2$ or $ThH^+ + CH_3$ should be observed at higher energies if $HThCH_3^+$ were present. Both of these products were explicitly looked for but not observed. Additionally, the threshold for forming the $Th^+ + CH_4$ products from **2** would be expected to be ~ 1 eV higher in energy than observed, Table 4.4.

When the PES is corrected for spin-orbit effects (ignoring any potential second-order effects), all levels of theory predict a barrier for reaction 4.3 of 4.4 – 65 kJ/mol. The

B3LYP and B3PW91 results indicate that the barrier results from spin-orbit effects. This is further substantiated by CCSD(T)/KAP calculations where no barrier is observed absent spin-orbit effects, but when spin-orbit effects are included a barrier in excellent agreement with the threshold from reaction 4.3 is observed, Table 4.6. Furthermore, the difference in the computed barrier height at ^{2}**TS1/2** in the CH_4 and CD_4 systems is 5.7 kJ/mol, similar to the observed difference in the thresholds measured for reaction 3, 10.6 ± 3.5 kJ/mol. Given that the only product observed from the CID reaction is the loss of methane and that there is reasonable agreement between the theoretical barrier height and the experimental threshold, the threshold for reaction 4.3 is assigned to the barrier located at ^{2}**TS1/2**.

The presence of this barrier can be understood using a simple donor-acceptor model that predicts σ-bond activation requires an orbital on the thorium cation that can accept the electrons from the bond on the ligand to be broken. Furthermore, π-electrons on the metal backdonate into the antibonding orbital of the bond to be broken.[100] On the calculated potential surface for Th^+ (^{2}D, $6d7s^2$), the *7s* acceptor orbital is doubly occupied, leading to the repulsive interaction at **TS1/2**. By contrast, the ^{4}F ($6d^27s$) has less electron density along the bond axis so that the interaction is less repulsive. The argument can be extended to a mixed electronic character J = 3/2 (^{4}F, ^{2}D) ground-level of the ion where the ^{2}D character increases the electron density in the *7s* acceptor orbital such that a repulsive interaction still occurs.

To further understand the repulsive nature of the Th^+ (J = 3/2) ground-level interacting with CH_4, it is instructive to compare the potential energy surfaces of methane reacting with Zr^+,[15] Hf^+,[25] and Th^+. At the B3LYP/HW/6-311++G(3df,3p) and

B3LYP/HW$^+$/6-311++G(3df,3p) levels of theory, the barrier height at **TS1/2** is 0 kJ/mol and 8 kJ/mol relative to the reactants for Zr^{+}[15] and Hf^{+}.[25] When spin-orbit corrections of 9 kJ/mol for Zr^+ and 21 kJ/mol for Hf^+ are made,[55] these barriers are 9 and 29 kJ/mol, respectively. The high barrier of Hf^+ has been ascribed to the filled *6s* orbital of its ^{2}D (*5d6s^2*) ground-state.[25] Zr^+ has a ^{4}F (*4d^{2}5s*) ground-state and does not experience the same repulsive forces because of the half-filled *5s* orbital.[15] The barrier height at **TS1/2** calculated using B3LYP for Th^+ is 18 kJ/mol, when using the similarly sized SDD basis set after accounting for spin-orbit energy. The observation that the **TS1/2** barrier for Th^+ lies in between those for Zr^+ and Hf^+ is consistent with the mixed electronic character of the Th^+ (^{4}F, ^{2}D) ground-level.

Basis Set Comparison

Theoretical calculations were performed using several basis sets for Th^+. The smallest of these basis sets, SDD, is double-ζ in quality and does not include polarization functions. Additionally, ANO and Seg. SDD basis sets from Cao et al.[71] that are quadruple-ζ in quality and include polarization *g*-functions and the KAP basis set that includes *g*-, *h*-, and *i*-functions were utilized. The results for the DFT calculations for the SDD, ANO and Seg. SDD were similar for both the BDEs and PES calculated here, Tables A.5 and A.7, suggesting that there is little advantage in using the large basis set. For CCSD(T) calculations, the MADs found in Table A.5 suggest that the SDD basis set performs the worst for BDEs, but that there is little difference between the three larger basis sets. There is some indication that the larger basis sets perform better than SDD for the multiply bound species and worse than SDD for singly and electrostatically bound

species for both DFT and CCSD(T) calculations.

In contrast to the DFT results, significant differences with basis set were observed in CCSD(T) calculations for the PES. A comparison of the energies from the CCSD(T) calculations using SDD, ANO, Seg. SDD, and KAP basis sets to the thresholds measured in reactions 4.3 and 4.7 can be found in Table 4.6. BDEs and full PESs with estimated spin-orbit corrections from the SDD, ANO, and Seg. SDD basis sets can be found in Tables A.5 and A.7 in the Supporting Information. As seen in Table 4.6, CCSD(T)/SDD calculations identify the ^{2}D ($6d7s^2$) (after averaging over all spin-orbit states) as the ground-state in agreement with the experimentally determined ground-state, but overestimate the difference between the ^{2}D and ^{4}F ($6d^27s$) states by 23 kJ/mol. When spin-orbit corrections are applied, this level of theory incorrectly predicts the ground-level as $^2D_{3/2}$. The use of the larger basis sets improves the agreement between theory and experiment, where deviations between theoretical and experimental spacing between the ^{2}D and ^{4}F states are 11, 12, and 6 kJ/mol for the ANO, Seg. SDD, and KAP basis sets, respectively. Furthermore, when spin-orbit effects are included, all three extended basis sets predict a $^4F_{3/2}$ ground-level.

For the first intermediate, **1**, the CCSD(T) result when using the SDD basis set is within experimental uncertainty after including spin-orbit corrections. When the larger basis sets are used, ANO overestimates the well depth by 13 kJ/mol and the Seg. SDD and KAP are also within experimental uncertainty. However, although the SDD basis set performs reasonably well for **1**, it overestimates the barrier height at **TS1/2** by 49 kJ/mol. When using the larger basis sets, agreement with the threshold from reaction 3 improves to deviations of 10, 28, and 1 for ANO, Seg. SDD, and KAP, respectively. SDD also

indicates that reaction 4.3 is endothermic by 16 kJ/mol, whereas ANO, Seg. SDD, and KAP indicate that the reaction is exothermic by 30, 13, and 25 kJ/mol, respectively. Table 4.6 lists MADs for the CCSD(T) results using each basis set. These demonstrate that correcting for spin-orbit interactions generally improves agreement with the experimental results. This is most notable for the results obtained using the SDD and KAP basis sets. There is also significant improvement in agreement with the experimental results as the larger basis sets get larger, with MADs improving from 18 kJ/mol (SDD) to 8 and 11 kJ/mol for ANO and Seg. SDD, respectively, and the KAP basis set is in excellent agreement with all experimental values. As previously noted for Hf^+, the lack of polarization functions in CCSD(T) calculations leads to improper electron correlation calculations.[69] Thus, the inclusion of the polarization *g*-functions in the Seg. SDD and ANO basis sets and of additional polarizing *g*-, *h*-, and *i*-functions in the KAP basis set significantly improves accuracy compared to experiment.

High Energy Mechanisms

The cross section for $ThCH_2^+$ in Figure 4.1 peaks at 2 eV and begins to fall off as the cross sections for $ThCH_3^+$ and ThH^+ rise. Above 4 eV, ThH^+ dominates all other products. This is consistent with a common intermediate between the three species, which the calculations indicate is ^{2}**2**, $HThCH_3^+$. At high energies, it is kinetically more favorable to simply cleave a bond (loose transition state) as opposed to following the pathway through ^{2}**TS2/3** (tight transition state). Although $ThCH_3^+$ formation is slightly more favorable thermodynamically, the ThH^+ product dominates because angular momentum constraints necessitate that small impact parameters are required for $ThCH_3^+$ + H

formation, whereas much larger impact parameters permit $ThH^+ + CH_3$ formation.[25] This constraint has been observed previously and explained thoroughly elsewhere.[14,88,101]

As noted above, reaction 4.6 occurs as the subsequent dehydrogenation of $ThCH_3^+$ produced from reaction 4.5. Other possible mechanisms are reactions 4.9 and 4.10.

$$Th^+ + CH_4 \rightarrow ThCH^+ + 3\,H \quad (4.9)$$

$$\rightarrow ThCH_2^+ + H_2 \rightarrow ThCH^+ + H + H_2 \quad (4.10)$$

Of these possible mechanisms, reaction 4.9 cannot occur until much higher energies, and reaction 4.10 is unlikely because reaction 4.4 is kinetically more favorable (see Figure 4.1) at energies near the reaction 4.6 threshold. The mechanism for the dehydrogenation of $ThCH_3^+$, reaction 4.6, is expected to be similar to the mechanism for reaction 4.3 observed in Figure 4.4, where H atoms from the CH_3 ligand are sequentially transferred to the metal to form an electrostatically bound $(H_2)ThCH^+$ complex that subsequently dissociates to products. According to this model, the first intermediate would be $HThCH_2^+$ ($^1A'$), which is only 1.0 kJ/mol higher in energy than the $ThCH_3^+$ (^3E) ground-state (Table A.4) according to B3LYP/SDD/6-311++G(d,p). This also necessitates a crossing seam between the triplet and singlet reaction surfaces in order to form ground-state $ThCH^+$ ($^1\Sigma^+$), although it seems unlikely that this would be restrictive given the extensive spin-orbit coupling in Th^+. Also according to CCSD(T) theory, the ground-state of $ThCH_3^+$ is actually $^1A_1$, which could dehydrogenate in a spin-allowed process. Note that both states of $ThCH_3^+$ can be formed in spin-allowed processes from the $HThCH_3^+$

(^{2}A′) intermediate, Figure 4.4.

Conclusion

The reaction of methane with thorium cation produces several products over a wide energy range. The dominant product at low energies is the thorium carbene cation; however, the energy dependence of this product is inconsistent with that of a barrierless exothermic reaction. Theory coupled with careful examination of spin-orbit interactions suggests that the threshold of this reaction corresponds to a barrier found in the first transition state associated with C-H bond activation. This is further substantiated by the CID reaction of the thorium-methane adduct, which dissociates exclusively to form the atomic Th^+ ion and methane. The barrier likely exists because the ground J = 3/2 level has mixed electronic character in which the closed $7s^2$ shell character of the ^{2}D ($6d7s^2$) hinders bond activation. Importantly, the barrier disappears at most levels of theory when spin-orbit interactions are not included, such that spin-orbit effects are critical to understanding the observed experimental behavior.

At higher energies, the thorium hydride cation product dominates, although the thorium methyl product has a similar threshold. These products are kinetically favored once the endothermicity is overcome, because they require a simple bond cleavage of the hydrido-methyl thorium cation as opposed to the molecular rearrangement needed for dehydrogenation. Meanwhile, the ThH^+ channel is favored over the $ThCH_3^+$ channel because of angular momentum constraints.[14,88,101]

Thorium's electronic structure is unique among the actinides because the *f*-orbitals are unoccupied for the neutral and singly charged cation. By all accounts, Th^+ is

more comparable to Ti^+, Zr^+, and Hf^+, which also have three valence electrons. Th^+ BDEs are typically stronger than the BDEs of its congeners, consistent with the assumption that BDEs increase moving down the periodic table because of a lanthanide contraction effect.[22,23,26,27,89] This indicates that although the mixed character ground-level of the Th^+ plays a significant role in the $Th^+ + CH_4$ reaction surface (i.e., the barrier at **TS1/2**), it hampers Th^+ bonding only slightly.

Supporting Information Available: Ion electronic population analysis, neutral BDEs of CH_4 and CD_4, reaction cross section as a function of kinetic energy of $Th^+ + CH_4$, evaluation of $\zeta_{6d}(Th)$, comparison of Th^+ theoretical energies with several additional basis sets, theoretical energies of all calculated structures, $ThCH_x^+$ BDEs with several additional basis sets. This material is available free of charge via the Internet at http://pubs.acs.org.

Acknowledgements

This work is supported by the Heavy Element Chemistry Program, Office of Basic Energy Sciences, U. S. Department of Energy, Grant No. DE-SC0012249. We thank the Center for High Performance Computing at the University of Utah for the generous allocation of computer time. This research used resources of the Oak Ridge Leadership Computing Facility, which is a DOE Office of Science User Facility supported under Contract DE-AC05-00OR22725. An award of computer time was provided by the Innovative and Novel Computational Impact on Theory and Experiment (INCITE) program. Professor Michael Morse is thanked for several useful conversations regarding the estimation of spin-orbit corrections.

References

(1) Shayesteh, A.; Lavrov, V. V.; Koyanagi, G. K.; Bohme, D. K. *J. Phys. Chem. A* **2009**, *113*, 5602-5611.

(2) Roithová, J.; Schröder, D. *Chem. Rev.* **2010**, *110*, 1170–1211.

(3) Schwarz, H. *Angew. Chem. Int. Ed.* **2011**, *50*, 10096-10115.

(4) Haggin, J. *Chem. Eng. News* **1993**, *71*, 22-23.

(5) Halle, L. F.; Armentrout, P. B.; Beauchamp, J. L. *J. Am. Chem. Soc.* **1981**, *103*, 962-963.

(6) Sunderlin, L. S.; Armentrout, P. B. *J. Phys. Chem.* **1988**, *92*, 1209-1219.

(7) Sunderlin, L. S.; Armentrout, P. B. *J. Am. Chem. Soc.* **1989**, *111*, 3845-3855.

(8) Schröder, D.; Schwarz, H.; Clemmer, D. E.; Chen, Y.; Armentrout, P. B.; Baranov, V. I.; Bohme, D. K. *Int. J. Mass Spectrom. Ion Process.* **1997**, *161*, 175-191.

(9) Aristov, N.; Armentrout, P. B. *J. Phys. Chem.* **1987**, *91*, 6178-6188.

(10) Georgiadis, R.; Armentrout, P. B. *J. Phys. Chem.* **1988**, *92*, 7067-7074.

(11) Haynes, C. L.; Chen, Y.-M.; Armentrout, P. B. *J. Phys. Chem.* **1995**, *99*, 9110-9117.

(12) Liu, F.; Zhang, X.-G.; Armentrout, P. B. *Phys. Chem. Chem. Phys.* **2005**, *7*, 1054-1064.

(13) Mandich, M. L.; Halle, L. F.; Beauchamp, J. L. *J. Am. Chem. Soc.* **1984**, *106*, 4403-4411.

(14) Chen, Y.-M.; Armentrout, P. B. *J. Phys. Chem.* **1995**, *99*, 10775-10779.

(15) Armentrout, P. B.; Sievers, M. R. *J. Phys. Chem. A* **2003**, *107*, 4396-4406.

(16) Armentrout, P. B. *J. Phys. Chem. A* **2006**, *110*, 8327-8338.

(17) Schultz, R. H.; Elkind, J. L.; Armentrout, P. B. *J. Am. Chem. Soc.* **1988**, *110*, 411-423.

(18) Chen, Y.-M.; Sievers, M. R.; Armentrout, P. B. *Int. J. Mass Spectrom. Ion Processes* **1997**, *167/168*, 195-212.

(19) Sievers, M. R.; Chen, Y.-M.; Haynes, C. L.; Armentrout, P. B. *Int. J. Mass Spectrom.* **2000**, *195/196*, 149-170.

(20) Irikura, K. K.; Beauchamp, J. L. *J. Phys. Chem.* **1991**, *95*, 8344-8351.

(21) Irikura, K. K.; Beauchamp, J. L. *J. Am. Chem. Soc.* **1991**, *113*, 2769-2770.

(22) Zhang, X.-G.; Liyanage, R.; Armentrout, P. B. *J. Am. Chem. Soc.* **2001**, *123*, 5563-5575.

(23) Armentrout, M. M.; Li, F.-X.; Armentrout, P. B. *J. Phys. Chem. A* **2004**, *108*, 9660-9672.

(24) Li, F.-X.; Armentrout, P. B. *J. Chem. Phys.* **2006**, *125*, 133114

(25) Parke, L. G.; Hinton, C. S.; Armentrout, P. B. *Int. J. Mass Spectrom.* **2006**, *254*, 168-182.

(26) Armentrout, P. B.; Shin, S.; Liyanage, R. *J. Phys. Chem. A* **2006**, *110*, 1242-1260.

(27) Li, F.-X.; Zhang, X.-G.; Armentrout, P. B. *Int. J. Mass Spectrom.* **2006**, *255-256*, 279-300.

(28) Parke, L. G.; Hinton, C. S.; Armentrout, P. B. *J. Phys. Chem. C* **2007**, *111*, 17773-17787.

(29) Parke, L. G.; Hinton, C. S.; Armentrout, P. B. *J. Phys. Chem. A* **2008**, *112*, 10469-10480.

(30) Armentrout, P. B.; Parke, L.; Hinton, C.; Citir, M. *ChemPlusChem* **2013**, *78*, 1157-1173.

(31) Schilling, J. B.; Beauchamp, J. L. *J. Am. Chem. Soc.* **1988**, *110*, 15-24.

(32) Cornehl, H. H.; Heinemann, C.; Schroeder, D.; Schwarz, H. *Organometallics* **1995**, *14*, 992-999.

(33) Marcalo, J.; Santos, M.; Pires, d. M. A.; Gibson, J. K.; Haire, R. G. *J. Phys. Chem. A* **2008**, *112*, 12647-12656.

(34) Armentrout, P. B.; Hodges, R. V.; Beauchamp, J. L. *J. Chem. Phys.* **1977**, *66*, 4683-4688.

(35) Marçalo, J.; Leal, J. P.; Pires de Matos, A. *Int. J. Mass Spectrom. Ion Processes* **1996**, *157/158*, 265-274.

(36) Gibson, J. K.; Haire, R. G.; Marçalo, J.; Santos, M.; Pires de Matos, A.; Mrozik, M. K.; Pitzer, R. M.; Bursten, B. E. *Organometallics* **2007**, *26*, 3947-3956.

(37) Cornehl, H. H.; Wesendrup, R.; Diefenbach, M.; Schwarz, H. *Chem.--Eur. J.* **1997**, *3*, 1083-1090.

(38) Gibson, J. K.; Haire, R. G. *Inorg. Chem.* **2002**, *41*, 5897-5906.

(39) Marcalo, J.; Gibson, J. K. *J. Phys. Chem. A* **2009**, *113*, 12599-12606.

(40) Su, T.; Chesnavich, W. J. *J. Chem. Phys.* **1982**, *76*, 5183-5185.

(41) Di Santo, E.; Michelini, M. d. C.; Russo, N. *Organometallics* **2009**, *28*, 3716-3726.

(42) de Almeida, K. J.; Duarte, H. A. *Organometallics* **2010**, *29*, 3735-3745.

(43) Loh, S. K.; Hales, D. A.; Li, L.; Armentrout, P. B. *J. Chem. Phys.* **1989**, *90*, 5466-5485.

(44) Schultz, R. H.; Armentrout, P. B. *Int. J. Mass Spectrom. Ion Processes* **1991**, *107*, 29-48.

(45) Gerlich, D. *Adv. Chem. Phys.* **1992**, *82*, 1-176.

(46) Armentrout, P. B. *Int. J. Mass Spectrom.* **2000**, *200*, 219-241.

(47) Ervin, K. M.; Armentrout, P. B. *J. Chem. Phys.* **1985**, *83*, 166-189.

(48) Daly, N. R. *Rev. Sci. Instrum.* **1960**, *31*, 264-267.

(49) Haynes, C. L.; Armentrout, P. B. *Organometallics* **1994**, *13*, 3480-3490.

(50) Clemmer, D. E.; Chen, Y.-M.; Khan, F. A.; Armentrout, P. B. *J. Phys. Chem.* **1994**, *98*, 6522-6529.

(51) Kickel, B. L.; Armentrout, P. B. *J. Am. Chem. Soc.* **1995**, *117*, 764-773.

(52) Kickel, B. L.; Armentrout, P. B. *J. Am. Chem. Soc.* **1995**, *117*, 4057-4070.

(53) Sievers, M. R.; Chen, Y.-M.; Elkind, J. L.; Armentrout, P. B. *J. Phys. Chem.* **1996**, *100*, 54-62.

(54) Blaise, J.; Wyart, J.-F. Selected Constants, Energy Levels, and Atomic Spectra of Actinides. http://web2.lac.u-psud.fr/lac/Database/Contents.html.

(55) Sansonetti, J. E.; Martin, W. C. *J. Phys. Chem. Ref. Data* **2005**, *34*, 1559-2259.

(56) Chesnavich, W. J.; Bowers, M. T. *J. Phys. Chem.* **1979**, *83*, 900-905.

(57) Muntean, F.; Armentrout, P. B. *J. Chem. Phys.* **2001**, *115*, 1213-1228.

(58) Aristov, N.; Armentrout, P. B. *J. Am. Chem. Soc.* **1986**, *108*, 1806-1819.

(59) Armentrout, P. B. In *Adv. Gas Phase Ion Chem.*; Adams, N., Babcock, L. M., Eds.; JAI Press: Greenwich, Connecticut, 1992; Vol. 1, p 83-119.

(60) *NIST Computational Chemistry Comparison and Benchmark Database NIST Standard Reference Database Number 101 Release 16a*; Johnson III, R. D., Ed., August 2013.

(61) Frisch, M. J.; Trucks, G. W.; Schlegel, H. B.; Scuseria, G. E.; Robb, M. A.; Cheeseman, J. R.; Scalmani, G.; Barone, V.; Mennucci, B.; Petersson, G. A.; Nakatsuji, H.; Caricato, M.; Li, X.; Hratchian, H. P.; Izmaylov, A. F.; Bloino, J.; Zheng, G.; Sonnenberg, J. L.; Hada, M.; Ehara, M.; Toyota, K.; Fukuda, R.; Hasegawa, J.; Ishida, M.; Nakajima, T.; Honda, Y.; Kitao, O.; Nakai, H.; Vreven, T.; Montgomery, J. A., Jr.; Peralta, J. E.; Ogliaro, F.; Bearpark, M.; Heyd, J. J.; Brothers, E.; Kudin, K. N.; Staroverov, V. N.; Kobayashi, R.; Normand, J.; Raghavachari, K.; Rendell, A.; Burant, J. C.; Iyengar, S. S.; Tomasi, J.; Cossi, M.; Rega, N.; Millam, N. J.; Klene, M.; Knox, J. E.; Cross, J. B.; Bakken, V.; Adamo, C.; Jaramillo, J.; Gomperts, R.; Stratmann, R. E.; Yazyev, O.; Austin, A. J.; Cammi, R.; Pomelli, C.; Ochterski, J. W.; Martin, R. L.; Morokuma, K.; Zakrzewski, V. G.; Voth, G. A.; Salvador, P.; Dannenberg, J. J.; Dapprich, S.; Daniels, A. D.; Farkas, Ö.; Foresman, J. B.; Ortiz, J. V.; Cioslowski, J.; Fox, D. J.; Gaussian, Inc: Wallingford CT, 2009.

(62) Lee, C.; Yang, W.; Parr, R. G. *Phys. Rev. B: Condens. Matter* **1988**, *37*, 785-789.

(63) Becke, A. D. *J. Chem. Phys.* **1993**, *98*, 5648-5652.

(64) Kuechle, W.; Dolg, M.; Stoll, H.; Preuss, H. *J. Chem. Phys.* **1994**, *100*, 7535-7542.

(65) Pople, J. A.; Head-Gordon, M.; Raghavachari, K. *J. Chem. Phys.* **1987**, *87*, 5968-5975.

(66) Feller, D. *J. Comput. Chem.* **1996**, *17*, 1571-1586.

(67) Schuchardt, K. L.; Didier, B. T.; Elsethagen, T.; Sun, L.; Gurumoorthi, V.; Chase, J.; Li, J.; Windus, T. L. *J. Chem. Inf. Model.* **2007**, *47*, 1045-1052.

(68) Hinton, C. S.; Li, F.; Armentrout, P. B. *Int. J. Mass Spectrom.* **2009**, *280*, 226-234.

(69) Hinton, C. S.; Armentrout, P. B. *J. Chem. Phys.* **2010**, *133*, 124307.

(70) Hinton, C. S.; Citir, M.; Armentrout, P. B. *J. Chem. Phys.* **2011**, *135*, 234302.

(71) Cao, X.; Dolg, M.; Stoll, H. *J. Chem. Phys.* **2003**, *118*, 487-496.

(72) Holthausen, M. C.; Heinemann, C.; Cornehl, H. H.; Koch, W.; Schwarz, H. *J. Chem. Phys.* **1995**, *102*, 4931-4941.

(73) Cizek, J. In *Advances in Chemical Physics*; Hariharan, P. C., Ed.; Wiley Interscience: New York, 1969; Vol. 14, p 35.

(74) Purvis, G. D., III; Bartlett, R. J. *J. Chem. Phys.* **1982**, *76*, 1910-1918.

(75) Scuseria, G. E.; Janssen, C. L.; Schaefer, H. F., III *J. Chem. Phys.* **1988**, *89*, 7382-7387.

(76) Foresman, J. B.; Frisch, A. E. *Exploring Chemistry with Electronic Structure Methods*; 2nd ed.; Gaussian, Inc.: Pittsburgh, PA, 1996.

(77) Peng, C.; Schlegel, H. B. *Isr. J. Chem.* **1994**, *33*, 449-454.

(78) Peng, C.; Ayala, P.; Schlegel, H. B.; Frisch, M. J. *J. Comput. Chem.* **1996**, *17*, 49-56.

(79) Valiev, M.; Bylaska, E. J.; Govind, N.; Kowalski, K.; Straatsma, T. P.; Van Dam, H. J. J.; Wang, D.; Nieplocha, J.; Apra, E.; Windus, T. L.; de Jong, W. A. *Comput. Phys. Commun.* **2010**, *181*, 1477-1489.

(80) Weigand, A.; Cao, X.; Hangele, T.; Dolg, M. *J. Phys. Chem. A* **2014**, *118*, 2519-2530.

(81) Peterson, K. A. *to be published*.

(82) Dunning, T. H. *J. Chem. Phys.* **1989**, *90*, 1007.

(83) Adamo, C.; Barone, V. *J. Chem. Phys.* **1999**, *110*, 6158-6170.

(84) Jonsson, H.; Mills, G.; Jacobsen, K. W. In *Classical and Quantum Dynamics in Condensed Phase Simulations*; Berne, B. J., Ciccotti, G., Coker, D. F., Eds.; World Scientific: 1998, p 385.

(85) Lapoutre, V. J. F.; Redlich, B.; van, d. M. A. F. G.; Oomens, J.; Bakker, J. M.; Sweeney, A.; Mookherjee, A.; Armentrout, P. B. *J. Phys. Chem. A* **2013**, *117*, 4115-4126.

(86) Armentrout, P. B.; Li, F.-X. *J. Chem. Phys.* **2004**, *121*, 248-256.

(87) Cox, R.; Armentrout, P. B. *manuscript in preparation*.

(88) Sunderlin, L. S.; Armentrout, P. B. *J. Phys. Chem.* **1988**, *92*, 1209-1219.

(89) Zhang, X.; Schwarz, H. *Chem. Eur. J.* **2010**, *16*, 5882 – 5888.

(90) Rodgers, M. T.; Armentrout, P. B. *J. Chem. Phys.* **1998**, *109*, 1787-1800.

(91) Armentrout, P. B.; Ervin, K. M.; Rodgers, M. T. *J. Phys. Chem. A* **2008**, *112*, 10071-10085.

(92) Rodgers, M. T.; Ervin, K. M.; Armentrout, P. B. *J. Chem. Phys.* **1997**, *106*, 4499-4508.

(93) Gilbert, R. G.; Smith, S. C. *Theory of Unimolecular and Recombination Reactions*; Blackwell Scientific: Oxford, 1990.

(94) Holbrook, K. A.; Pilling, M. J.; Robertson, S. H. *Unimolecular Reactions*; Wiley: New York, 1996.

(95) Heaven, M. C.; Barker, B. J.; Antonov, I. O. *J. Phys. Chem. A* **2014**, *118*, 10867-10881.

(96) Garcia, M. A.; Morse, M. D. *J. Chem. Phys.* **2011**, *135*, 114304.

(97) Armentrout, P. B. *J. Chem. Phys.* **2013**, *139*, 084305.

(98) Armentrout, P. B.; Li, F.-X. *J. Phys. Chem. A* **2013**, *117*, 7754-7766.

(99) Lefebvre-Brion, H.; Field, R. W. *The Spectra And Dynamics of Diatomic Molecules*; Elsevier: Amsterdam, 2004.

(100) Armentrout, P. B. In *Topics in Organometallic Chemistry*; Brown, J. M., Hofmann, P., Eds.; Springer-Verlag: Berlin, 1999; Vol. 4, p 1-45.

(101) Armentrout, P. B.; Kickel, B. L. In *Organometallic Ion Chemistry*; Freiser, B. S., Ed.; Kluwer: Dordrecht, The Netherlands, 1996, p 1-45.

Table 4.1. Fitting parameters of Eq. 4.1 for the indicated reaction cross section.

Reaction[a]	σ_0	n	E_0 (eV)
$Th^+ + CH_4 \rightarrow ThH^+ + CH_3$	11 ± 3	1.2 ± 0.1	2.38 ± 0.16
	(7.0 ± 0.8)	(1.4 ± 0.2)	(2.25 ± 0.08)
$Th^+ + CH_4 \rightarrow ThCH^+ + H_2 + H$	2.1 ± 0.1	0.8 ± 0.2	3.08 ± 0.17
	(2.3 ± 0.2)	(1.8 ± 0.1)	(2.98 ± 0.06)
$Th^+ + CH_4 \rightarrow ThCH_2^+ + H_2$	6.6 ± 0.3	1.5 ± 0.1	0.17 ± 0.02
	(6.6 ± 0.1)	(1.4 ± 0.1)	(0.28 ± 0.03)
$Th^+ + CH_4 \rightarrow ThCH_3^+ + H$	0.9 ± 0.3	1.6 ± 0.4	2.11 ± 0.15
	(1.2 ± 0.4)	(2.0± 0.4)	(2.13 ± 0.11)
$ThCH_4^+ + Xe \rightarrow Th^+ + CH_4$[b]	3.0 ± 0.3	1.8 ± 0.2	0.46 ± 0.05
	[3.1 ± 0.4]	[1.7 ± 0.2]	[0.47 ± 0.05]

[a] Values in parentheses are for the analogous reaction with CD_4. Uncertainties are one standard deviation of the mean.
[b] Values in brackets include lifetime effects by incorporating RRKM theory.[91,92]

Table 4.2. Comparison of theoretically computed excited-state energies (eV) to spin-orbit averaged experimental values.

State	Experimental[a]	CCSD(T)[b]	B3LYP[b]	B3PW91[b]	BHLYP[b]
^{2}D ($6d7s^2$)	0.00	**0.00 (0.00)**	0.20	0.004	**0.00**
^{4}F ($6d^27s$)	0.06	0.19 (0.12)	0.38	0.02	0.18
^{2}F ($5f^27s$)	0.43	0.58	**0.00**	**0.00**	0.19
^{4}H ($5f6d7s$)	0.67	1.26	0.46	0.15	0.60
^{4}F ($6d^3$)	0.81	1.08	1.12	0.66	0.88

[a] Spin-orbit averaged values.[54,55] The choice of levels used for each state is explained in the Supporting Information.

[b] Calculated using (14s13p10d8f6g)/[10s9p5d4f3g] segmented basis set with SDD ECP. Values in parentheses calculated using (20s17p12d11f5g3h1i)/[7s7p6d5f5g3h1i] basis with Stuttgart-Cologne ECP (KAP).

Table 4.3. Comparison of experimental and theoretical bond dissociation energies (eV) without and (with) spin-orbit corrections.

		Experimental		Theoretical[a]				
Bond	State	This Work	Literature	CCSD(T) [b]	CCSD(T) [c]	B3LYP	B3PW91	BHLYP
Th^+-H [d]	$^3\Delta$ [e]	≥2.25 ± 0.18	2.46 ± 0.07[f]	2.91 (**2.69**)	2.79 (**2.57**)	**3.16 (2.94)**	**3.18 (2.96)**	**2.99 (2.77)**
	$^1\Sigma^+$			**2.95** (2.55)	**2.87** (2.47)	2.86 (2.46)	2.66 (2.26)	2.71 (2.31)
Th^+-CH [d]	$^1\Sigma^+$	6.19 ± 0.16		6.38 (5.98)	6.04 (5.64)	6.20 (5.80)	6.61 (6.21)	5.57 (5.17)
Th^+-CH_2 [d]	$^2A'$	≥4.54 ± 0.09	≥4.74 ± 0.02[g]	5.34 (4.94)	5.14 (4.74)	5.32 (4.92)	5.44 (5.04)	4.82 (4.42)
Th^+-CH_3 [d]	^3E [e]	≥2.39 ± 0.22		3.44 (**3.22**)	3.17 (2.95)	**3.35 (3.13)**	**3.54 (3.32)**	**2.98 (2.76)**
		2.60 ± 0.30[h]						
	$^1A_1$			**3.62** (**3.22**)	**3.40 (3.00)**	3.29 (2.89)	3.25 (2.85)	2.96 (2.56)
Th^+-CH_4 [i]	$^2A/(^4A'')$	0.47 ± 0.05		0.41 (0.51)	0.36 (0.49)	0.56 (0.51)	0.64 (0.57)	0.33 (0.43)
MAD[j]				0.44 (0.28)	0.37 (0.27)	0.39 (0.36)	0.56 (0.34)	0.42 (0.38)

Table 4.3 Continued

[a] Values are relative to Th^+ (^2D, $6d7s^2$). Values in parentheses are relative to Th^+ ($^4F_{3/2}$,$6d^27s$) and include estimated spin-orbit corrections. Structures optimized (except CCSD(T)) at the indicated level of theory using seg. SDD for Th^+ and a 6-311++G(3df,3p) for C and H See text. For ThH^+ and $ThCH_3^+$, the calculated ground-state is in bold.

[b] CCSD(T)/KAP/cc-pVTZ single-point calculations using PBE0/KAP/cc-pVTZ optimized structures..

[c] CCSD(T)/Seg. SDD/6-311++G(3d,3p) single-point calculations using B3LYP/Seg. SDD/6-311++G(3df,3p) optimized structures.

[d] Spin-orbit correction of -0.40 eV, the empirical difference between the ^2D state averaged over all spin-orbit levels and the ground $^4F_{3/2}$ level.

[e] Spin-orbit correction of 0.18 eV for stabilization of $^3\Delta_1$ state. See text.

[f] Ref. 87.

[g] Result based on FT-ICR results.[35,36] Utilizes updated $D_0(H_2C\text{-}H_2) = 4.74 \pm 0.02$ eV.[60]

[h] Includes correction for competition. See text.

[i] Value in parentheses corresponds to the $^4A''$ ground-state after including spin-orbit effects. See text and Figure 4.4.

[j] Mean absolute deviation of ground-state theoretical BDEs from the experimental values excluding $ThCH_2^+$. Values in parentheses correspond to MADs after inclusion of spin-orbit estimates.

Table 4.4. Single-point energies (kJ/mol) relative to the $Th^+ + CH_4$ reactants without and (with) spin-orbit corrections.[a]

Species	State	This work				Literature	
		CCSD(T)	B3LYP	B3PW91	BHLYP	B3LYP[b]	B3PW91[c]
$Th^+ + CH_4$	$^2D + {}^1A_{1g}$	0.0 (22.2)	0.0 (22.2)	0.0 (22.2)	0.0 (22.2)	0.0 (^2F)	6.8
	$^4F + {}^1A_{1g}$	18.3 (0.0)	17.4 (0.0)	1.0 (0.0)	17.4 (0.0)	24.4	0.0
$Th^+(CH_4)$ (1)	^2A	-35.2 (-13.0)	-53.7 (-31.5)	-61.7 (-39.5)	-31.5 (-9.3)	-30.9	-45.0
	$^4A''$	-29.4 (-47.5)	-32.0 (-49.4)	-54.1 (-55.4)	-24.4 (-41.8)	-10.1	-27.7
TS1/2[d]	^2A	6.2 (44.8)	-17.1 (21.5)	-35.0 (3.6)	26.4 (65.0)	4.8	-18.3
	^4A	101.2 (139.8)	72.2	58.8	85.2	97.8	94.6
$HThCH_3^+$ (2)	$^2A'$	-161.8 (-123.2)	-188.7	-202.3	-163.7	-168.0	-186.0
	$^4A'$	97.2 (135.8)	61.1	48.9	81.2	79.3	62.1
TS2/3	^2A	-55.5 (-16.9)	-75.3	-101.2	-25.6	-52.7	-81.4
	^4A	140.1 (178.7)	109.5	82.5	143.3		101.5
TS2/4	^2A	-26.2 (12.4)	-64.0	-79.4	-27.0	-43.1	-62.1
$H_2ThCH_2^+$ (4)	$^2A'$	-46.0 (-7.4)	-84.4	-94.8	-61.7	-62.7	
TS4/3	^2A	60.8 (99.4)	9.4	-12.8	61.0	30.4	6.0
$(H_2)ThCH_2^+$ (3)	^2A	-65.4 (-26.8)	-79.0	-98.4	-35.5	-57.3	-81.8
	^4A	68.5 (107.1)	41.2	21.8	65.0	62.6	39.4
$ThCH_2^+ + H_2$	$^2A' + {}^1\Sigma_g^+$	-51.6 (-13.0)	-63.9 (-25.3)	-77.2 (-38.6)	-22.2 (16.4)	-42.4	-59.8
	$^4A'' + {}^1\Sigma_g^+$	78.6 (117.2)	53.4	39.2	74.0	68.9	58.6

Table 4.4 Continued

[a] Structures optimized and vibrational frequencies calculated using B3LYP/SDD/6-311++G(d,p). Single-point energies calculated at the respective level of theory with Seg. SDD/6-311++G(3df,3p) and zero point corrected (scaled by 0.989). Values in parentheses are relative to Th^+ ($^4F_{3/2}$) + CH_4 and corrected by the empirical difference between the ^2D state averaged over all spin-orbit levels and the $^4F_{3/2}$ level, 38.6 kJ/mol except for **1** where the well depth remains constant relative to its asymptote, see text. Note that the spin-orbit corrected reactant asymptotes are fixed at their empirical energy difference.
[b] Ref. 41.
[c] Ref. 42.

Table 4.5. Comparison of BDEs (eV) for Th^+ and transition metal congeners.

Metal	Slope[a]	$D_0(M^+-CH_3)$	$D_0(M^+-H)$	$D_0(M^+-CH_2)$	$D_0(M^+-CH)$
Ti[b]	0.54	2.49 ± 0.12	2.31 ± 0.11	4.05 ± 0.15	5.25 ± 0.17
Zr	0.60	2.30 ± 0.24[c]	2.26 ± 0.08[d]	4.62 ± 0.07[c]	5.96 ± 0.22[c]
Hf	0.53	2.12 ± 0.27[e]	2.11 ± 0.08[f]	4.37 ± 0.07[e]	5.10 ± 0.15[e]
Th	0.62	2.60 ± 0.30	2.46 ± 0.07[g]	≥ 4.54 ± 0.09	6.19 ± 0.16
U			2.9 ± 0.1[h]		

[a] Slope of linear least square trend line of $D_0(M^+-L)$ versus $D_0(L-L)$, Figure 4.6, forced to pass through the origin.
[b] Ref. 6.
[c] Ref. 15.
[d] Ref. 53.
[e] Ref. 25.
[f] Ref. 69.
[g] Ref. 87.
[h] Ref. 34.

Table 4.6. Comparison of CCSD(T) theoretical results using several basis sets for Th^+ to experimentally measured values (kJ/mol) along the potential energy surface for reaction 4.3.[a]

	Experimental	SDD[b]	ANO[c]	Seg. SDD[d]	KAP[e]
Th^+ ($^4F_{3/2}$) + CH_4[f]	0.0	0.0	0.0	0.0	0.0
Th^+ (^4F) + CH_4[g]	(5.8)	(28.9)	(16.4)	(18.3)	(11.6)
Th^+ ($^2D_{3/2}$) + CH_4[f]	22.2	-0.9	11.6	9.7	16.4
Th^+ (^2D) + CH_4[g]	(0.0)	(0.0)	(0.0)	(0.0)	(0.0)
^{4}1 ($^4A''$)	-45.3 ± 4.8	-46.9	-57.6	-47.5	-49.4
^{2}1 (^2A)		(-26.0)	(-53.6)	(-35.2)	(-39.6)
^{2}TS1/2 (^2A)[h]	16.4 ± 1.9	65.7	26.4	44.8	17.4
		(27.1)	(-12.2)	(6.2)	(-15.4)
$ThCH_2^+$ ($^2A'$) + H_2		15.9	-30.2	-13.0	-24.9
		(-22.7)	(-68.8)	(-51.6)	(-63.5)
MAD		19	8	11	3
		(22)	(12)	(11)	(11)

Table 4.6 Continued

[a] Structures optimized using B3LYP/SDD/6-311++G(d,p). Energies include estimated spin-orbit corrections and are relative to Th^+ ($^4F_{3/2}$, $6d^27s$) + CH_4. See text. Values in parentheses are relative to Th^+ (^2D, $6d7s^2$) + CH_4 and do not include estimated spin-orbit corrections.
[b] Single-point energy using SDD/6-311++G(3df,3p).
[c] Single-point energy using (14s13p10d8f6g)/[6s6p5d4f3g] /6-311++G(3df,3p).
[d] Single-point energies using (14s13p10d8f6g)/[10s9p5d4f3g]/6-311++G(3df,3p).
[e] Structures optimized at PBE0/(20s17p12d11f5g3h1i)/[7s7p6d5f5g3h1i]/cc-pVTZ. Single-point energies performed with CCSD(T) utilizing the same basis sets.
[f] Theoretical prediction of the lowest level in each state. Corrected from theoretical energy of each state by the empirical average excitation energy of that state, -44.4 kJ/mol for ^4F and -16.4 kJ/mol for ^2D.
[g] Values in parentheses are averaged over all spin-orbit levels.[54,55]
[h] Corrected by the empirical difference between ^2D averaged over all spin-orbit states and the $^4F_{3/2}$ level, 38.6 kJ/mol.

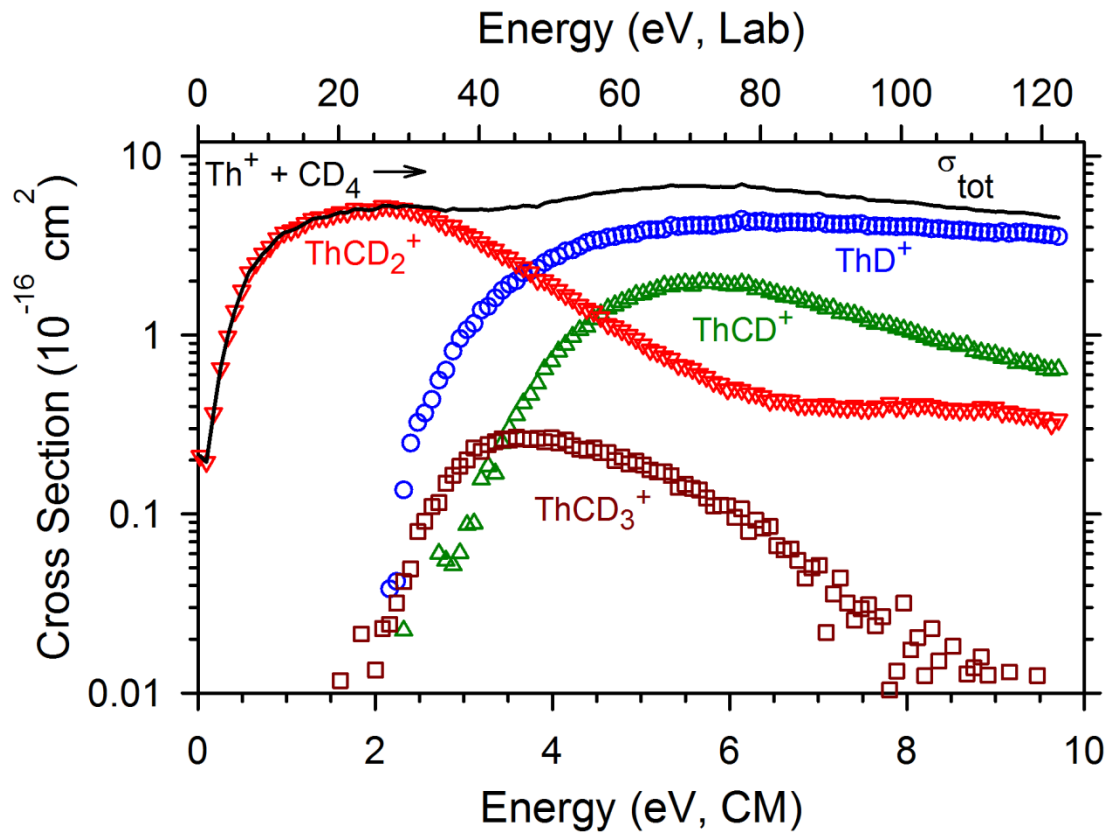

Figure 4.1. Cross sections for the reaction between Th^+ and CD_4 as a function of energy in the CM (lower x-axis) and Lab (upper x-axis) frames.

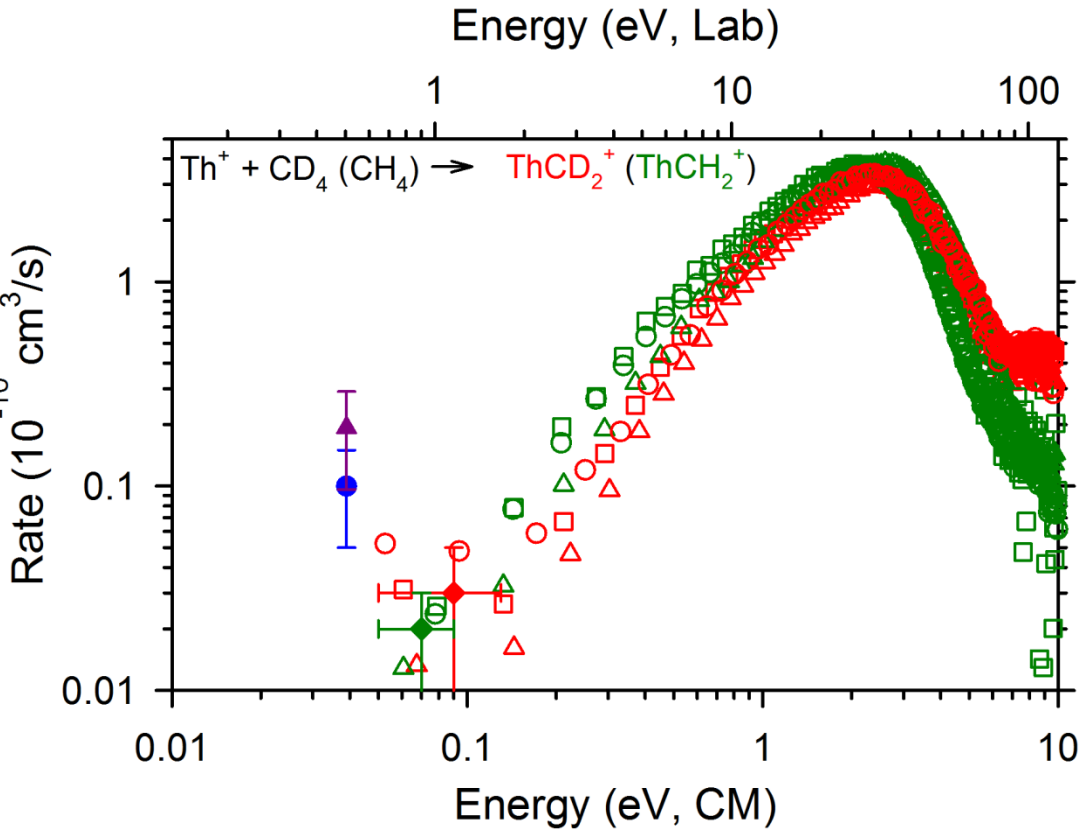

Figure 4.2. Reaction rate for $Th^+ + CD_4$ (CH_4) → $ThCD_2^+$ ($ThCH_2^+$) + D_2 (H_2) plotted as a function of kinetic energy. Present work in red ($ThCD_2^+$) and green ($ThCH_4^+$). Average rates at 700 ± 300 K for $ThCD_2^+$ (red diamond) and 500 ± 150 K for $ThCH_2^+$ (green diamond). FT-ICR results from Gibson et al.[36] (blue circle) and Marcalo et al.[35] (purple triangle). Lab frame shown corresponds to the CD_4 reaction.

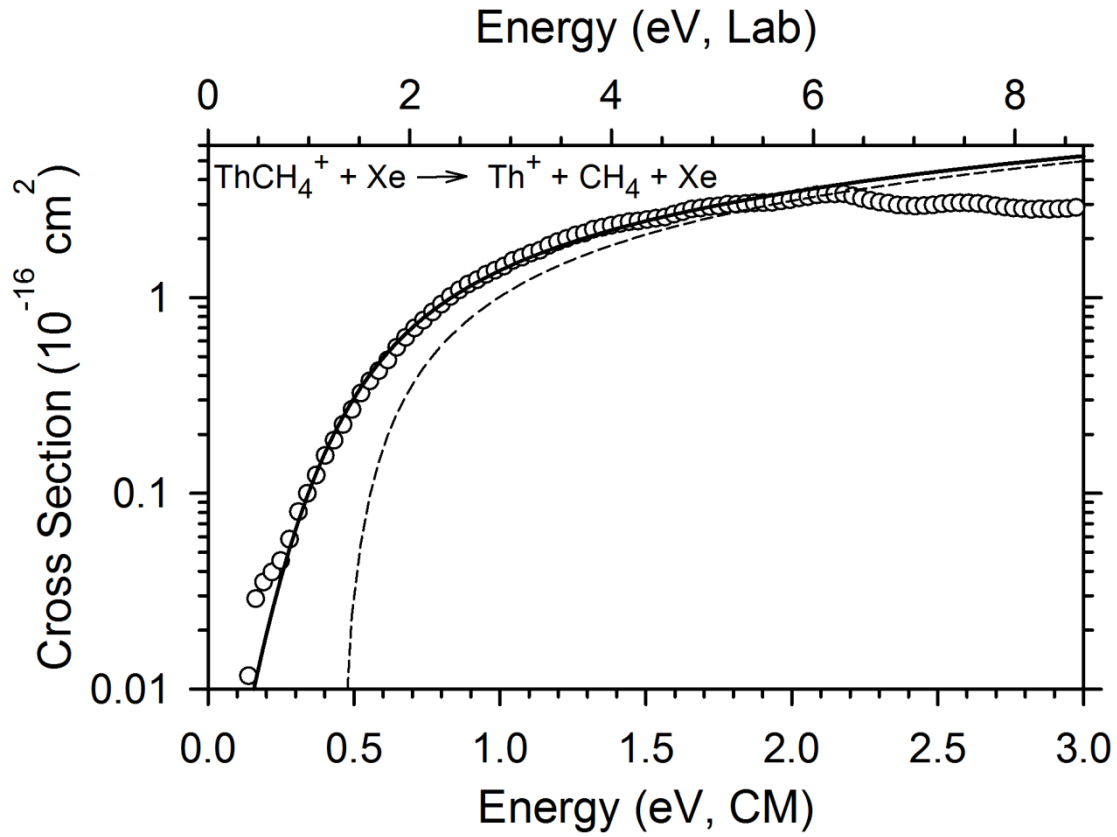

Figure 4.3. Cross section for the collision-induced dissociation reaction of $ThCH_4^+$ with Xe. The best model of the data using parameters of Eq. 4.1 found in Table 4.1 is shown as a dashed line. The solid line shows this model convoluted over the kinetic and internal energy distributions of reactants at 300 K.

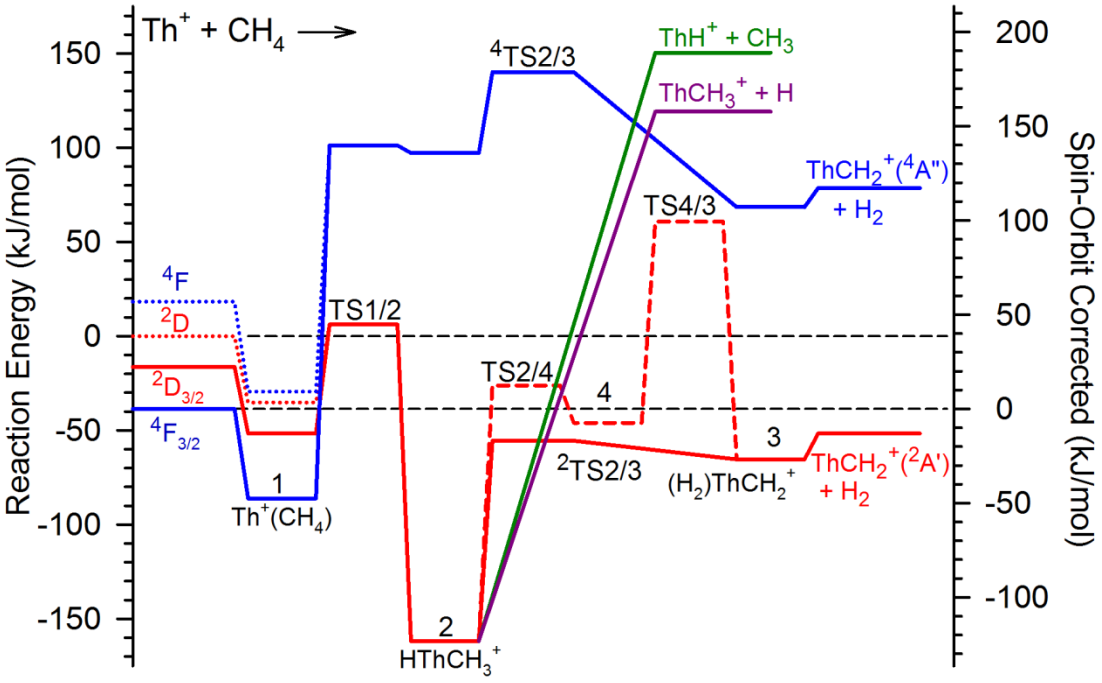

Figure 4.4. The potential energy surface for the reaction of methane with thorium cation calculated at the CCSD(T)/Seg. SDD/6-311++G(3df,3p)//B3LYP/SDD/6-311++G(d,p) level of theory. The full lines show spin-orbit corrected surfaces relative to Th^+ ($^4F_{3/2}$) + CH_4 and indicated by the axis on the right. Dotted lines and full line past TS1/2 show uncorrected surfaces relative to Th^+ (^2D) + CH_4 and indicated by the axis on the left. Doublet surface in red and quartet in blue.

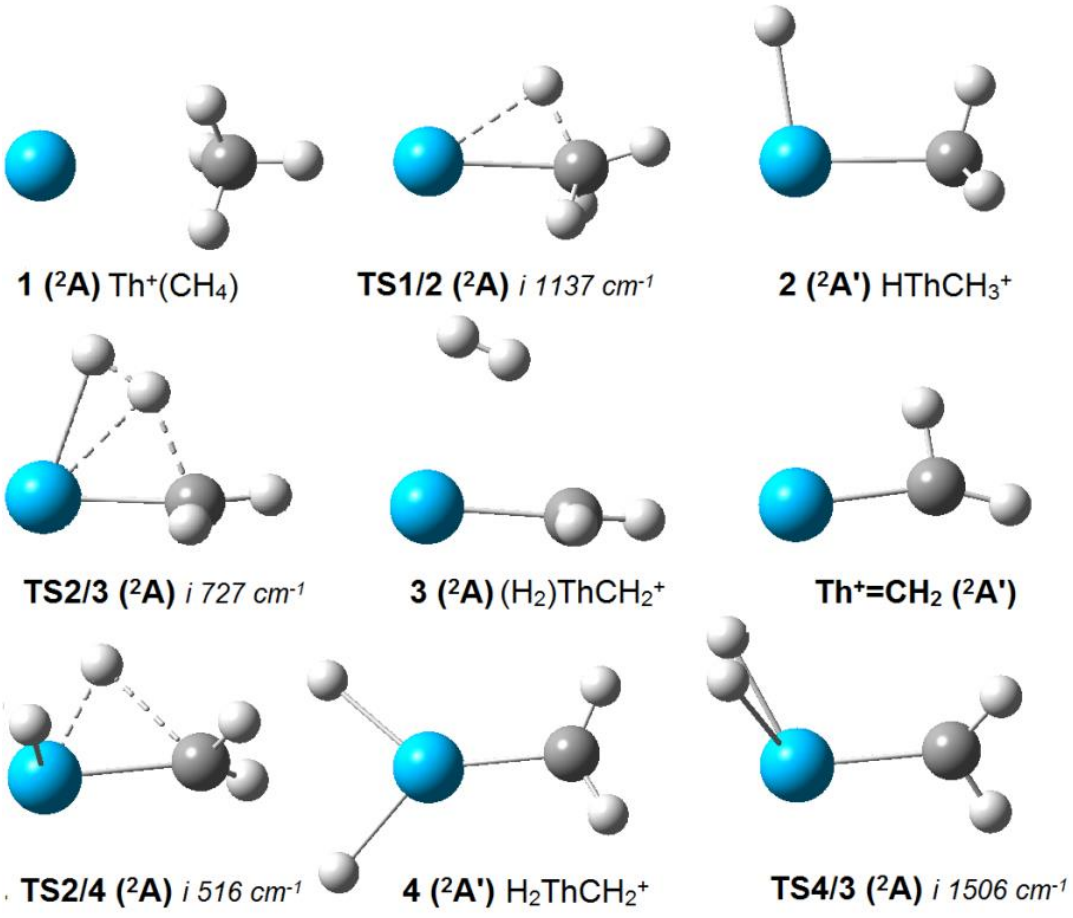

Figure 4.5. Geometrical structures of each doublet spin intermediate and transition state in Figure 4.4. All structures optimized using the B3LYP/SDD/6-311++G(d,p) approach.

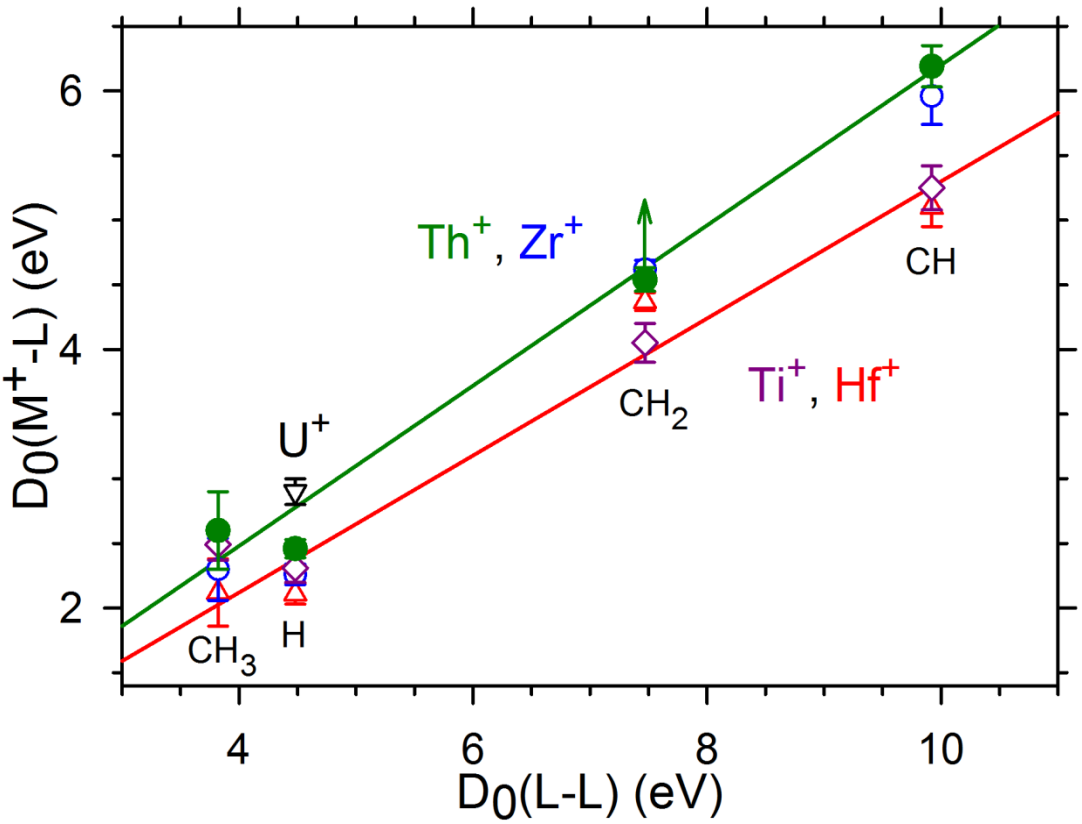

Figure 4.6. Bond energy-bond order comparison of M^+-L for M = Th^+ (green), Zr^+ (blue), Hf^+ (red), Ti^+ (purple), U^+ (black) by plotting $D_0(M^+\text{-}L)$ versus $D_0(L\text{-}L)$.

CHAPTER 5

REACTIONS OF $Th^+ + H_2$, D_2, AND HD STUDIED BY GUIDED ION BEAM TANDEM MASS SPECTROMETRY AND QUANTUM CHEMICAL CALCULATIONS

Cox, R. M; Armentrout, P. B.; De Jong, W. A.

J. Phys. Chem. B 2015, SUBMITTED.

Abstract

Kinetic energy dependent reactions of Th^+ with H_2, D_2, and HD were studied using a guided ion beam tandem mass spectrometer. Formation of ThH^+ and ThD^+ is endothermic in all cases with similar thresholds. Branching ratio results for the reaction with HD indicate that Th^+ reacts via a statistical mechanism, similar to Hf^+. The kinetic energy dependent cross sections for formation of ThH^+ and ThD^+ were evaluated to determine a 0 K bond dissociation energy (BDE) of $D_0(Th^+\text{-}H) = 2.45 \pm 0.07$ eV. This value is in good agreement with a previous result obtained from analysis of the $Th^+ +$

CH_4 reaction. $D_0(Th^+-H)$ is observed to be larger than its transition metal congeners, TiH^+, ZrH^+, and HfH^+, believed to be a result of lanthanide contraction. The reactions with H_2 were also explored using quantum chemical calculations that include a semiempirical estimation and explicit calculation of spin-orbit contributions. These calculations agree nicely and indicate that ThH^+ most likely has a $^3\Delta_1$ ground-level with a low-lying $^1\Sigma^+$ excited-state. Theory also provides the reaction potential energy surfaces and BDEs that are in reasonable agreement with experiment.

Introduction

There is considerable interest in actinide chemistry, although the radioactivity of most actinides (except Th and U) has limited their study to dedicated laboratories. As a consequence, actinide chemistry in the gas phase, in particular, where fundamental actinide chemistry can be studied absent solvent effects, is still largely in its infancy. To date, most experimental work has dealt with oxidation[1-9] and hydrocarbon activation reactions.[10-18] The dearth of experimental work has led to increased theoretical studies of actinides in the gas phase.[17, 19-29] Although the use of theoretical methods to study actinide systems mitigates safety concerns, the limited experimental data leaves few benchmarks to which theoretical methods can be compared. Several examples of discrepancies (real or apparent) between experimental results and theoretical methods can be found in the literature.[24-26, 30] Some of these discrepancies can be traced to errors in the experimental work,[26] others appear to be method- or basis set- related.[24-25, 30]

In order to provide experimental benchmarks for comparison to theoretical work, Heaven and collaborators have recently studied several simple Th and U molecules

spectroscopically, as summarized in Ref. 31. In our group, we have used guided ion beam tandem mass spectrometry to study the reaction of $Th^+ + CH_4$, which leads to thermodynamic bond dissociation energies (BDEs) for several species.[30] A simple actinide system that can be studied in detail both experimentally and theoretically is the reaction with H_2 and its isotopic analogues. This system is of interest, in part, because it provides the simplest example of covalent bond activation by metal cations and deuterium labeling provides experimental insight into the reaction mechanism. Periodic trends in this chemistry are also of interest as the $M^+ + H_2$ reaction has been extensively studied for first-row,[32-39] second-row,[36, 39-41] and third-row[42-46] transition metals.

Because all the lanthanides (Ln) can be studied without radioactivity concerns, they can be considered model systems to shed light on the analogous actinide systems. Of the lanthanides and actinides, only the reactions of La^+, Yb^+, $Lu^+ + H_2$, and $U^+ + D_2$ have been studied experimentally.[10, 39, 47-48] LnH^+ formation has also been observed in reactions of many Ln^{2+} with alkanes and alkenes, as studied using ion cyclotron resonance (ICR) mass spectrometry.[49] Additionally, LaH^+ and LuH^+ have been observed as products in reactions of La^+ and Lu^+ with methane and ethane in guided ion beam experiments.[39, 48] For the actinides, AnH^+ (An = U, Np, Pu, Am, Cm) has been observed as a product of An^{2+} reacting with alkanes and alkenes in ICR experiments, but ThH^+ was not observed in analogous experiments.[17-18] Recently, we have observed ThH^+ in a guided ion beam study of the $Th^+ + CH_4$ reaction.[30] Here we report the absolute cross sections as a function of kinetic energy for the reactions of H_2, D_2, and HD with Th^+. Analysis of these cross sections allows determination of $D_0(Th^+\text{-}H)$. Theoretical calculations of ThH^+ and ThH_2^+ are also performed to assign electronic states and explore

possible reaction mechanisms.

Experimental and Theoretical Methods

Instrument

The guided ion beam tandem mass spectrometer used in this study has been described in detail previously.[50] Briefly, thorium ions are created using a direct current discharge/flow tube source (DC/FT)[51] described in further detail below. Ions are extracted and focused through a magnetic momentum analyzer, where the $^{232}Th^+$ beam is mass selected before being decelerated to a well-defined kinetic energy. The Th^+ beam is then focused into a radio frequency (rf) octopole guide that traps ions radially.[52-53] This octopole passes through a static pressure gas cell that contains the neutral gas reactant. To ensure that the probability of multiple collisions is sufficiently small, pressures are kept low (0.05 – 0.40 mTorr). Reactions were repeated at several pressures to ensure that the reported cross sections are independent of neutral gas pressure. After the collision cell, product ions and remaining reactant ions drift to the end of the octopole where they are extracted, focused through a quadrupole mass filter for mass analysis, and counted using a Daly detector.[54] Reaction cross sections are calculated from product ion intensities relative to reactant ion intensities after correcting for background ion intensities after the neutral gas is no longer directed into the gas cell.[55] Uncertainties in the calculated absolute cross section are estimated to be ± 20 %, with relative uncertainties of ± 5%.

Laboratory ion energies (lab) are converted to the center-of-mass frame (CM) using the relationship $E_{CM} = E_{lab} \times m/(m + M)$ where m and M are the masses of the neutral and ionic reactants, respectively. Cross sections are known to be broadened by the

kinetic energy distribution of the reactant ions and the thermal (300 K) motion of the neutral reactant.[56] The absolute zero of energy and the full width at half-maximum (fwhm) of the ion beam are determined by using the octopole guide as a retarding potential analyzer.[55] Typical fwhms of the energy distribution for these experiments were 0.4 - 0.8 eV (lab). Uncertainties in the absolute energy scale are 0.1 eV (lab). All energies reported below are in the CM frame.

Ion Source

The DC/FT source is described in detail elsewhere.[51] A cathode, held at 2.5 kV and containing a thorium powder sample, creates an electric field that ionizes Ar from the carrier gas. Ar cations collide with the thorium sample such that Th^+ sputters off the cathode. Ions are swept into a 1 m long flow tube by a 9:1 mixture of He/Ar at a total pressure of 0.2 – 0.5 Torr. The ions undergo ~10^5 collisions with the flow gases, which should thermalize them. No evidence of excited-states is evident in the reaction cross sections presented below nor in our previous work on $Th^+ + CH_4$.[30] Previous experiments have indicated that atomic ions generated in the DC/FT may have internal electronic temperatures between 300 and 1100 K.[41, 57-60] A population analysis at 300 K indicates that 99.89% of Th^+ is in its ground-level ($^4F_{3/2}$, $6d^27s$), whereas at 1100 K, 76 % is in the ground-level.[30] Conservatively, we estimate the internal temperature distribution of Th^+ as 700 ± 400 K, such that the internal energy of the reactant ions is 0.02 ± 0.03 eV.

Data Analysis

The kinetic energy dependence of endothermic reactions is modeled using eq 5.1,[61-63]

$$\sigma(E) = \sigma_0 \Sigma\, g_i\, (E + E_i - E_0)^n/E \qquad (5.1)$$

where σ_0 is an energy-independent scaling factor, E is the relative kinetic energy of the reactants, E_i is the internal energy of the reactant states (electronic for Th^+ and rotational for H_2, D_2, and HD) having populations g_i ($\Sigma g_i = 1$), n is an adjustable parameter, and E_0 is the 0 K reaction threshold. Before comparison to the data, eq 5.1 is convoluted over the kinetic energy distributions of the reactants, and the σ_0, n, and E_0 parameters are optimized using a nonlinear least-squares method to best reproduce the experimental cross section. Uncertainties in E_0 are calculated from the threshold values from several independent data sets (minimum of two for each system) and combined with the absolute uncertainties in the kinetic energy scale (<0.002 eV) and internal energies of reactant ions (0.02 ± 0.03 eV). Thresholds are used to determine the bond dissociation energy (BDE), $D_0(Th^+\text{-H})$, using eq 5.2 and its isotopic analogues.

$$D_0(Th^+\text{-H}) = D_0(\text{H-H}) - E_0 \qquad (5.2)$$

Equation 5.2 assumes that there are no barriers in excess of the endothermicity of the reaction. No experimental or theoretical evidence was found to suggest that such a barrier is present.

Theoretical Approaches

Most quantum chemical calculations are performed using the Gaussian 09 suite of programs.[64] Unless otherwise noted, a correlation consistent polarized core (20s17p12d11f7g4h1i)/[9s9p8d8f7g4h1i] basis set (cc-pwCVQZ-PP-MDF) developed by K.A. Peterson [65] that utilizes the Stuttgart-Cologne (MDF) fully relativistic small core (60 electron) ECP[66] is used for Th along with the aug-cc-pVQZ[67] basis set for H. For calculating bond dissociation energies, several additional basis sets are used for Th^+ and H. For Th^+, these include the Stuttgart Dresden basis set (SDD-VDZ-MWB) with its accompanying small-core quasirelativistic ECP (MWB) available on the EMSL basis set exchange,[68-69] a segmented basis set (Seg. SDD-VQZ-MWB) that utilizes the MWB ECP,[70] atomic natural orbital basis sets designed for use with the MWB (ANO-VQZ-MWB)[70] and MDF (ANO-VQZ-MDF)[66] ECPs, correlation consistent cc-pVTZ-PP-MDF, cc-pVQZ-PP-MDF, and cc-pwCVTZ-PP-MDF (which includes core-valence correlation) basis sets[65] with the MDF ECP. Pople 6-311+G(3p), cc-pVTZ, and cc-pVQZ basis sets[67] are also used for H. Additionally, BDEs are calculated using single-point energies utilizing the all-electron variants of cc-pVXZ (cc-pVXZ-DK3) and cc-pwCVXZ (cc-pwCVXZ-DK3) basis sets[65] (where X = T or Q) and B3LYP/cc-pwCVQZ-PP-MDF/aug-cc-pVQZ optimized structures. These latter calculations are performed using the second-order Douglas-Kroll-Hess Hamiltonian (DK2).[71-76] Of note is that the all-electron basis sets were formulated for use with a third order Douglas-Kroll-Hess Hamiltonian (DK3), but the DK3 calculations cannot be performed presently in the current setup. Use of the DK2 may lead to errors, but we anticipate that these errors should be small.[77] Extrapolation to the complete basis set limit (CBS) is performed using the Karton-Martin

method,[65, 78] eq 5.3, proposed for the HF energies with the TZ (X = 3) and QZ (X = 4) energies:

$$E_X = E_{CBS} + A(X + 1)e^{-6.57\sqrt{X}} \quad (5.3)$$

For CCSD(T) calculations, eq 5.4[65, 79-80] is used to extrapolate the correlation energy:

$$E_X = E_{CBS} + B(X + ½)^{-4} \quad (5.4)$$

The calculations utilize the density functional theory (DFT) methods B3LYP, B3PW91, BHandHLYP (BHLYP), M06, and PBE0. Of these functionals, B3LYP has been shown to perform well in similar systems.[28, 30] B3PW91 has been shown by us[30] and others[24] to perform reasonably well in other actinide systems. BHLYP has been shown to perform well in singly bound metal ligand systems.[44-45, 81] M06 recently performed well in a theoretical evaluation of several DFT methods by comparison to the experimental $D_0(OTh^+-O)$.[28] PBE0 has previously yielded similar geometrical structures to B3LYP in our previous Th^+ study.[30] Additionally, a coupled cluster method that mixes single and double excitations with perturbative triple excitations (CCSD(T)) was used for single-point calculations using the B3LYP optimized structures. For CCSD(T) electron correlation calculations, the *5s* and *5p* electrons are frozen. All energies discussed below are corrected by the zero-point energy using the frequencies generated for their respective optimized structure after scaling by 0.989.[82]

Experimental Results

$Th^+ + H_2$ and D_2

The reactions of Th^+ with H_2 and D_2 yield products according to reactions 5.5 and 5.6.

$$Th^+ + H_2 \rightarrow ThH^+ + H \quad (5.5)$$

$$Th^+ + D_2 \rightarrow ThD^+ + D \quad (5.6)$$

The kinetic energy dependent cross section for reaction 5.5 can be found in Figure 5.1, with the analogous deuterium cross section in Figure 5.2. Reactions 5.5 and 5.6 have apparent thresholds near 2 eV, with the cross sections peaking near D_0(H-H) = 4.478 eV and D_0(D-D) = 4.556 eV.[83] Above these energies, the cross sections decrease because the ThH^+ and ThD^+ products can dissociate, leading to Th^+ + 2 H (2 D).

The mass resolution settings in the quadrupole for both the H_2 and D_2 (as well as HD) reactions were constant. Resolution was held as low as possible to ensure efficient product collection, such that the product ion peaks overlap with the reactant ion peak, with the overlap being worse for ThH^+ than ThD^+, which explains why the H_2 data is somewhat noisier. In the present case, the magnitude at the maximum ThH^+ cross section, Figure 5.1, is 1.2 times that for ThD^+, Figure 5.2. This is within the estimated absolute cross section uncertainty (±20%), indicating that the resolution settings are adequate for accurately measuring the product ion intensities.

$Th^+ + HD$

Reaction of Th^+ with HD yields products according to reactions 5.7 and 5.8.

$$Th^+ + HD \rightarrow ThH^+ + D \quad (5.7)$$

$$\rightarrow ThD^+ + H \quad (5.8)$$

The cross sections measured for these reactions are shown in Figure 5.3. Reactions 5.7 and 5.8 have similar apparent thresholds as reactions 5.5 and 5.6 and peak near D_0(H-D) = 4.514 eV.[83] At energies somewhat above the apparent thresholds, ThH^+ is found to be the dominant product by a 2:1 ratio. The magnitude of the total cross section, Figure 5.3, is 0.8 times the magnitude of the cross section for reaction 5.6, Figure 5.2, also within experimental uncertainty.

Thermochemical Results

The fitting parameters from eq 5.1 used to model the cross sections in reactions 5.5 – 5.8 can be found in Table 5.1. The models for reactions 5.5 and 5.6 are included in Figures 5.1 and 5.2 and can be seen to reproduce the data throughout the energy range examined. Above the neutral reactant bond energy, product ions can have enough internal energy to dissociate. To account for this effect, eq 5.1 is augmented with a simple model for dissociation, detailed elsewhere.[63, 84] Because the model of eq 5.1 explicitly accounts for the internal energy of all reactants, the E_0 values reported in Table 5.1 are 0 K thresholds. It can be seen that the thresholds for all four reactions are similar. Given D_0(H-H) = 4.478 ± 0.001 eV and D_0(D-D) = 4.556 ± 0.001 eV[83] in eq 5.2, the thresholds

measured for reactions 5.5 and 5.6 indicate that $D_0(Th^+-H) = 2.30 \pm 0.12$ eV and $D_0(Th^+-D) = 2.54 \pm 0.05$ eV. Using eq 5.2 and $D_0(H-D) = 4.514 \pm 0.001$ eV[83] leads to $D_0(Th^+-H) = 2.36 \pm 0.06$ eV and $D_0(Th^+-D) = 2.38 \pm 0.19$ eV. After correcting for zero-point energy differences of 0.03 eV, the weighted average of these four measurements is $D_0(Th^+-H) = 2.45 \pm 0.07$ eV, where the uncertainty is two standard deviations of the mean.

This result is in good agreement with the value, $D_0(Th^+-H) \geq 2.25 \pm 0.20$ eV, measured in the reaction of Th^+ with CH_4.[30] The present value is considered more reliable because there are no competing products, unlike in the methane reaction where the $ThH^+ + CH_3$ channel competes with the thermodynamically more favored dehydrogenation channel, $ThCH_2^+ + H_2$. In that study, a phase space theory (PST) model of the cross sections of products that share a common intermediate ($ThCH_2^+$, $ThCH_3^+$, and ThH^+) was used to account for this competition. This model explicitly accounts for angular momentum conservation and statistical factors by utilizing the theoretically calculated molecular parameters (vibrational and rotational) of all products and reactants. The PST analysis yielded a threshold energy for ThH^+ formation of $E_0 = 2.05$ eV indicating $D_0(Th^+-H) = 2.45$ eV,[30] in excellent agreement with the present value.

Reaction Mechanism

Previous work with transition metals has shown that the $M^+ + HD$ branching ratio is very sensitive to the reaction mechanism.[40-41, 85] Three guidelines have been established to predict the reaction mechanism: (1) If M^+ has an electronic configuration with empty *s* and $d\sigma$ orbitals, such as a d^n configuration where $n < 5$, the reaction proceeds efficiently by an insertion mechanism. These processes are consistent with the statistical behavior of

a long-lived intermediate and have branching ratios ($\sigma_{MH^+}/\sigma_{Tot}$) near 0.5. (2) If M^+ has an electronic configuration with occupied valence *s* or *dσ* orbitals and is low-spin, such as for d^n where $n > 5$ or low-spin coupled $d^{n-1}s^1$ configurations, the reaction proceeds efficiently via a direct mechanism. These processes are consistent with arguments that conserve angular momentum and favor MH^+ by factors of two – four, such that $\sigma_{MH^+}/\sigma_{Tot}$ is typically between 0.66 and 0.80.[32, 48, 86-87] (3) If M^+ has an electronic configuration with occupied valence *s* or *dσ* orbitals and has the highest possible spin state, such as a high-spin coupled $d^{n-1}s^1$ configuration, the reaction proceeds by an impulsive mechanism and is not efficient. Such processes favor $MD^+ + H$ by a large factor. However, these rules are only appropriate for strictly diabatic behavior where the M^+ electronic configuration is essentially static through the course of the reaction.

Figure 5.4 compares the branching ratio, $\sigma_{MH^+}/\sigma_{Tot}$, for Th^+ with the group 4 transition metal cations. Given that both Ti^+ and Zr^+ have ^4F (d^2s) ground-states, an impulsive mechanism according to category 3 is expected. However, Figure 5.4 clearly indicates a statistical (category 1) reaction for Ti^+. This can be explained by coupling with the low-lying ^4F ($4d^3$) state, which is then expected to react according to the first guideline. Zr^+ has a reactivity consistent with a direct mechanism (category 2). This is explained by the coupling of the high-spin surfaces evolving from ground-state Zr^+ (^4F, $4d^25s$) + H_2 with the low-spin surfaces that lead to the intermediates and products.[41] For Hf^+, the ground-state is ^2D ($5d6s^2$), indicating that an impulsive mechanism is expected. However, the $HHfH^+$ PES indicates that coupling occurs between low-spin surfaces originating from the ground-state reactants and a $^2A_1$ surface that leads to a long-lived $HHfH^+$ intermediate, which can evolve directly to products.[44] This is substantiated by the

results in Figure 5.4.

Interestingly, for Th^+, the $\sigma_{MH}^+/\sigma_{Tot}$ ratio is between that of Hf^+ and Zr^+, Figure 5.4. The Th^+ ground-state is enigmatic because the ground-level is a mixture of the $^4F_{3/2}$ ($6d^27s$) and $^2D_{3/2}$ ($6d7s^2$). Like Zr^+ and Hf^+, it appears that the $Th^+ + H_2$ ground-state reactants evolve along surfaces starting from the mixed character of the J = 3/2 ground-level and coupling with low-spin surfaces leading to a long-lived $HThH^+$ intermediate (category 1).

For all metals, the branching ratio increasingly favors $ThH^+ + D$ formation at energies above D_0(H-D) = 4.57 eV. This trend has been explained previously,[32] and is a consequence of the heavier D atom's ability to carry away more energy than the lighter H atom.

Theoretical Results

Energy Levels of Th^+

One way to gauge the accuracy of a theoretical method is to compare predicted low-lying states to those observed experimentally. Previously, this has been done for the atomic Th^+ cation[20-21,24,30] using several basis sets at various levels of theory. A comparison of the theoretically predicted low-lying states calculated using the cc-pwCVQZ-PP-MDF basis set to those experimentally observed is listed in Table 5.2. For comparison to the theoretical values, the experimental levels were averaged over all spin-orbit levels of each state.[88-89] For Th^+, this is not straightforward because of considerable interaction between the ^4F ($6d^27s$) and ^2D ($6d7s^2$) states. A detailed explanation of the choice of each level has been given previously in the Supporting Information section of

Ref. 30.

With the exception of M06 and B3LYP, which prefer the ^{2}F state, all levels of theory correctly predict a ^{2}D ground-state. Furthermore, BHLYP, B3PW91, and PBE0 correctly predict the ordering of all states. However, for these approaches, the spacing between states is smaller than that observed experimentally (particularly so for B3PW91). Although CCSD(T) incorrectly places the ^{4}H (*5f6d7s*) higher in energy than the ^{4}F ($6d^3$), it otherwise correctly orders the states. CCSD(T) reproduces the correct spacing between the states, deviating from the excited experimental states by only 0.10 – 0.17 eV when excluding the ^{4}H. Additionally, the relative energies of the ^{2}D and ^{4}F states were calculated using the all-electron cc-pwCVQZ-DK3 basis set for Th^+ and are also listed in Table 5.2. (M06 calculations did not converge and are not included here.) These results are similar to cc-pwCVQZ-PP-MDF values.

Spin-Orbit Energy Corrections

Typically theoretical BDEs correspond to a value that has been averaged over all spin-orbit states, whereas experimental 0 K BDEs correspond to dissociation from the lowest levels of the molecule to its fragments. In order to make a more valid comparison between experimental and theoretical values, spin-orbit effects, which are quite large for Th^+, must be explicitly accounted for. Here we employ a semiempirical approach to estimate the spin-orbit effects in the ThH^+ system. This approach has been used successfully to estimate spin-orbit effects in third-row transition metal systems and another Th^+ system.[30, 90-93] These corrections require that the Th^+ + H asymptote be lowered by the empirical difference between the ground-level of Th^+ and the ground-state

energy averaged over all spin-orbit levels. A nuance of the Th^+ system is that the experimental ground-state is ^2D ($6d7s^2$), whereas the ground-level is $^4F_{3/2}$ ($6d^27s$).[30] This allows two possible approaches for correcting BDEs. The first is to assume that the theoretical BDE is robust along the diabatic dissociation surface. This necessitates that the BDE must be referenced to its diabatic asymptote and corrected by the empirical difference in energy between the $^4F_{3/2}$ ground-level and the average energy of the respective state, 0.46 eV for ^4F and 0.40 eV for ^2D. The second approach corrects directly from the ^2D ground-state to the $^4F_{3/2}$ ground-level by the empirical difference (0.40 eV). Previously, the latter method yielded slightly better results and, as such, is the method used here.[30]

In addition to the spin-orbit correction to the asymptote, the BDE should also be corrected for the spin-orbit splitting of ThH^+ when applicable.[30, 90-93] To do so, we assume that the spin-orbit splitting energy is given by eq 5.9:

$$E^{SO} = \Lambda \, M_S \, A \tag{5.9}$$

where A is the spin-orbit splitting constant, Λ is the orbital angular momentum quantum number, and M_S is the spin quantum number associated with a particular level $\Omega = \Lambda + M_S$.[94] E^{SO} is also equal to the summation $\Sigma \, a_i \, \ell_i \bullet s_i$, where $\ell_i \bullet s_i$ is the dot product of the orbital angular momentum and the spin of electron i and a_i is the spin-orbit parameter, which can be represented by the atomic spin-orbit parameter for the *6d* electrons of thorium ζ_{6d}(Th). We have previously estimated ζ_{6d}(Th) as 1458 cm^{-1} (0.18 eV).[30]

Spin-Orbit Energy Corrections for ThH^+

Previously di Santo et al. have reported a $^3\Delta$ ground-state with a $^1\Sigma^+$ state 0.02 eV higher in energy in B3LYP/SDD-VDZ-MWB/6-311+G(p) calculations.[21] We also reported similar results using B3LYP/Seg. SDD-VQZ-MWB/6-311+G(3p), where we observed a $^3\Delta$ ground-state with excited-states at 0.18 ($^3\Pi$) and 0.30 eV ($^1\Sigma^+$).[30] CCSD(T)/Seg. SDD-VQZ-MWB/6-311+G(3p) results reverse the order placing the $^1\Sigma^+$ 0.07 eV below the $^3\Delta$, and CCSD(T)/cc-pVQZ-PP-MDF/cc-pVTZ calculations place the $^1\Sigma^+$ only 0.04 eV below the $^3\Delta$.[30] These results do not include corrections for spin-orbit energy. When spin-orbit effects were included, the ground-level was $^3\Delta_1$ at all levels of theory studied.[30]

The present work finds similar results to the previous reports. In order to compare theoretical results more readily to experimental values, spin-orbit effects are estimated using eq 5.9. These results are summarized in Table 5.3. The $^1\Sigma^+$ and $^3\Sigma^-$ states have no first-order spin-orbit corrections, whereas the $^3\Delta$ splits into Ω = 1, 2, 3, $^3\Pi$ splits into Ω = 0, 1, 2, and $^3\Phi$ splits into Ω = 2, 3, 4. For $^3\Delta$, where Λ = 2 and M_S = -1, 0, and +1, eq 5.9 shows that A = 729 cm^{-1} and E^{SO} = -0.18, 0, and 0.18 eV for $^3\Delta_1$, $^3\Delta_2$, $^3\Delta_3$, respectively. For $^3\Pi$ (Λ = 1 and M_S = -1, 0, 1), E^{SO} = -0.09, 0, and 0.09 eV for $^3\Pi_0$, $^3\Pi_1$, and $^3\Pi_2$, respectively. For $^3\Phi$, (Λ = 3 and M_S = -1, 0, 1), E^{SO} = -0.27, 0, 0.27 eV for $^3\Phi_2$, $^3\Phi_3$, $^3\Phi_4$, respectively. Once these spin-orbit corrections have been applied, the ground-level is predicted to be $^3\Delta_1$ (by 0.13 – 0.69 eV) for all levels of theory except M06, which predicts that the $^1\Sigma^+$ is 0.10 eV lower in energy. This trend is also reflected in the calculations using additional basis sets, Table B.1 in the Supporting Information.

The $^3\Delta$ state has a $1\sigma^2 2\sigma 1\delta$ electron configuration. A natural bond orbital analysis

(NBO) performed using CCSD(T) indicates that the 1σ bonding orbital comprises the H *1s*-orbital and a *sd*-hybridized orbital that also contains some *f*-character (70% 6*d*, 20% 7*s*, 10% 5*f*). The nonbonding 2σ-orbital comprises mostly the Th^+ *7s*-orbital (75%) with some *6d*-character (20%). The nonbonding 1δ-orbital is composed entirely of the Th^+ *6dδ*-orbital. The $^1\Sigma^+$ state has a $1\sigma^2 2\sigma^2$ electron configuration. These orbitals are similar to those for the $^3\Delta$ with an NBO analysis using CCSD(T), indicating that the 1σ bonding interaction occurs between the H *1s* and an orbital on Th^+ having 75% 6*d*, 15% 7*s*, and 10% 5*f* character, whereas the nonbonding 2σ-orbital has 85% 7*s* and 15% 6*d*. For the higher energy states, the $^3\Pi$ state has a $1\sigma^2 2\sigma 1\pi$ electron configuration, where the 1δ-electron in the $^3\Delta$ state is moved to a π-orbital that is the Th^+ *6dπ*-orbital, and the $^3\Phi$ has a $1\sigma^2 1\delta 1\pi$ electron configuration. For the two $^3\Sigma^-$ states, the two nonbonding electrons are placed in either the Th^+ *6dδ* or *6dπ*-orbitals.

The $^3\Delta$ and $^3\Pi$ states can originate from the Th^+ (^{4}F, $6d^2 7s$) + H (^{2}S) and possibly the ^{2}D ($6d7s^2$) + H (^{2}S) asymptotes, whereas the $^1\Sigma^+$ can originate only from the Th^+ (^{2}D, $6d7s^2$) + H (^{2}S) asymptote, and the $^3\Phi$ and $^3\Sigma^-$ states likely come from the Th^+ (^{4}F, $6d^3$) + H (^{2}S) asymptote. Here, Th^+ is an interesting case because the assigned ground-level is $^4F_{3/2}$; however, the J = 3/2 ground-level is actually a mixture of the $^4F_{3/2}$ and $^2D_{3/2}$ levels indicating that all states of ThH^+ presumably can be formed directly from the Th^+ ground-level. The $^3\Sigma^-$ states can also form from the ground-level or from the Th^+ (^{4}F, $6d^3$) state. In this regard, it can be noted that the excitation energies of the $^3\Sigma^-$ states are similar to the difference (0.83 eV) between the ground $^4F_{3/2}$ ($6d^2 7s$) and $^4F_{3/2}$ ($6d^3$) levels of Th^+.

Bond lengths, r(Th^+-H), and vibrational frequencies (scaled by 0.989)[82] calculated

for the various states of ThH^+ using B3LYP/cc-pwCVQZ-PP-MDF/aug-cc-pVQZ are listed in Table 5.3. To the best of our knowledge, neither experimental nor theoretical molecular parameters have been reported previously for ThH^+. Bond lengths vary from r(Th^+-H) = 1.946 ($^1\Sigma^+$) – 2.032 ($^3\Phi$) Å with r(Th^+-H) = 1.996 Å for the $^3\Delta$. Vibrational frequencies range from 1491 ($^3\Phi$) – 1653 ($^3\Delta$) with ν = 1592 cm^{-1} for $^1\Sigma^+$. Parameters calculated at other levels of theory are listed in Tables B2 and B3 in the Supporting Information section.

Table 5.4 lists the theoretical BDEs of ground-level ThH^+ at various levels of theory and basis set combinations. The ground-state is $^3\Delta_1$ after accounting for spin-orbit energy for all levels of theory except M06, which find a $^1\Sigma^+$ ground-state. However, because of the close proximity in energy of the $^1\Sigma^+$ and $^3\Delta_1$ states, a definitive determination of the true ground-state is difficult. Consequently, the calculated BDEs of both states can be found in Table B.4 in the Supporting Information. (Table B.4 also contains values uncorrected for spin-orbit splitting and for additional basis sets.) In general, the ground-state BDEs overestimate the experimental bond strength by 0.2 – 0.5 eV with CCSD(T) (2.71 eV), BHLYP (2.75 eV), and M06 (2.73 eV) values being in closest agreement to experiment when using the cc-pwCVQZ-PP-MDF/aug-cc-pVQZ basis sets. Notably, spin-orbit corrections yield better results in all cases, Table B.4.

The DFT cc-pwCVQZ-PP-MDF/aug-cc-pVQZ results listed in Table 5.4 are typical of the DFT results regardless of the basis set combination; however, CCSD(T) calculations vary appreciably. Among the basis sets that utilize an ECP, the smallest basis set, CCSD(T)/SDD-VDZ-MWB/6-311+G(3p), reproduces $D_0(Th^+$-H) within experimental uncertainty, and the larger CCSD(T)/Seg. SDD-VQZ-MWB/6-311+G(3p)

and CCSD(T)/ANO-VQZ-MWB/6-311+G(3p) results are just outside of experimental uncertainty. Meanwhile the use of a similarly sized CCSD(T)/ANO-VQZ-MDF/6-311+G(3p) basis set with the fully relativistic basis set (MDF) leads to results that overestimate the bond strength considerably for both states. This substantial deviation is not understood but suggests that this basis set may not be well optimized for Th^+. An extrapolation to the complete basis set limit using the cc-pwCVXZ-PP-MDF (X= T, Q) basis sets leads to CCSD(T)/CBS-cc-pwCVXZ-PP-MDF results similar to CCSD(T)/cc-pwCVQZ-PP-MDF/aug-cc-pVQZ results. The BDEs of the CBS limit for the all-electron basis sets (CBS-cc-pwCVXZ-DK3) are 0 – 0.11 eV lower than their counterparts that utilize the MDF ECP (CBS-cc-pwCVXZ-DK3).

Fully Relativistic Calculations on ThH^+

To investigate the role of second-order spin-orbit effects on the ordering of the $^3\Delta_1$ and $^1\Sigma^+$, fully relativistic Dirac Hartree-Fock calculations are performed, where the spin-orbitals are generated using the average-of-configuration SCF approach, and all states are projected out with a full CI in this spin-orbital space. These calculations are performed with the DIRAC14 code[95] using an uncontracted Dyall basis set for thorium[96] and an uncontracted Dunning basis set for hydrogen.[67] The standard finite nucleus model of the DIRAC14 code is used and all two-electron integrals including the Gaunt interaction[97] responsible for the spin-other-orbit interaction are included in the calculations. Two different orbital configuration spaces are utilized, one large space representing the Th 5f, 6d, 7s and H 1s and a second small space with 8 spin-orbitals that describe 17 spin-orbit split states including the lowest levels for $^3\Delta$, $^1\Sigma^+$, $^3\Pi$, and $^3\Phi$. The

calculated $^3\Delta$ spin-orbit splitting constants of 0.17 and 0.16 eV for the large and small space, respectively, are slightly smaller than the 0.18 eV estimated from the atomic thorium *6d* splitting. Relative energies for the $^3\Delta_1$, $^3\Delta_2$, and $^3\Delta_3$ states obtained from these calculations are -0.14, 0.00 and 0.20 eV for the large configuration space and -0.13, 0.00 and 0.19 eV for the small space, respectively. Here the $^3\Delta_2$ is defined as zero to allow for a direct comparison with the results obtained from eq 5.9. The relative energies show that the second-order effects are relatively small, on the order of 0.02 – 0.03 eV. In both configuration spaces used, the $^3\Delta_1$ state is the ground-state with the $^1\Sigma^+$ state 0.03 and 0.10 eV higher in energy for the large and small space, respectively. The relative energy differences between the $^3\Delta_1$ and $^1\Sigma^+$ states obtained in the fully relativistic calculations are similar, although somewhat smaller, as compared to the CCSD(T) calculations combined with eq 5.9, suggesting the model is a reasonable approach to estimate the effect of spin-orbit splitting in these systems.

$HThH^+$

Calculated ground and excited-states of $HThH^+$ are listed in Table 5.5. The ground-state, $^2A_1$, has bond distances, r(Th^+-H), of 1.995 Å and a bond angle, ∠HThH, of 102.3° (B3LYP/cc-pwcVQZ-PP-MDF/aug-cc-pVQZ). The $^2B_1$, $^2A_2$, and $^2B_2$ states lie 0.11 – 0.35, 0.18 – 0.48, and 0.43 – 1.30 eV higher in energy, respectively. A series of quartet states were also located at both small and large ∠HThH bond angles and lie at least 1.18 eV above the $^2A_1$ ground-state. Linear variants of $HThH^+$ were also calculated but were all found to have one negative vibrational frequency, indicating that these are transition states. Similar results were observed for linear $ThHH^+$ variants. Theory predicts

that the $^2A_1$ state has a BDE, $D_0(Th^+\text{-}H_2)$, relative to $Th^+(^4F_{3/2})$ + H of 1.07 – 1.32 eV with $D_0(HTh^+\text{-}H)$ = 2.73 – 2.96 eV. Note that the second hydride bond energy is comparable to the first, consistent with covalent coupling of H to one of the unpaired electrons in ThH^+ ($^3\Delta$).

The $^2A_1$ state has a $(1a_1)^2(1b_2)^2(2a_1)^1$ electron configuration where the lone electron is found in an orbital ($2a_1$) composed primarily of the Th^+ (*7s*). The $1a_1$ bonding orbital is a *sd* hybridized orbital interacting with the H (*1s*) orbitals, and the $1b_2$ orbital is a bonding interaction of the $6d_{yz}$ (where the z axis is defined as the C_2 symmetry axis and the molecule lies in the yz-plane) and the H (*1s*) orbitals. For the $^2B_1$ state, the lone electron is moved into the $6d_{xz}$ orbital, and for the $^2A_2$ state, the electron is moved into the $6d_{xy}$ orbital. The $^2B_2$ state places the lone electron in the antibonding $2b_2$ orbital, leading to its higher energy.

For the quartet states, one of the bonding electrons must be moved to a nonbonding or antibonding orbital, such that these states lie considerably higher in energy. In the large angle variants, all with ∠HThH near 170°, this also leads to slightly longer Th^+-H bond lengths, ~2.1 Å. For each of these states, minima are also observed at small ∠HThH angles, Table 5.5, corresponding to $Th^+(H_2)$ association complexes. In general, the geometries of these intermediates are characterized by ∠HThH of ~20° with r(H-H) of approximately 0.8 Å, similar to r(H-H) = 0.739 – 0.744 Å calculated for free H_2. Additionally, $r(Th^+\text{-}H)$ = 2.30 – 2.35 Å are observed, which are significantly longer than the bond lengths of the large angle $HThH^+$ species (2.0 – 2.1 Å).

In order to further explore the potential energy surface of reaction 5.5, we performed relaxed potential energy scans along the ∠HThH coordinate using the

optimized $HThH^+$ structures as a starting geometry. In our theoretical study of the $Th^+ + CH_4$ reaction,[30] the DFT methods yielded similar results regardless of the basis set used. Consequently, to avoid excessive computational cost, scans were performed using the B3LYP/Seg. SDD-VQZ-MWB/6-311+G(3p) level of theory. The results of these scans are presented in Figure 5.5. Notably, neither zero-point energies nor spin-orbit effects are included in this diagram. Additionally, for the cc-pwCVQZ-PP-MDF/aug-cc-pVQZ calculations, a $^4A_1$ intermediate is found at small angles; however, at larger angles the $^4A_1$ intermediate has 1 imaginary frequency along the asymmetric Th^+-H stretch, suggesting that it is the inversion transition state to a $^4A'$ intermediate. Indeed, optimization of a geometry displaced along the imaginary frequency using the $^4A_1$ wavefunction leads to a $^4A'$ state with r(Th^+-H) = 2.1599 and 2.1601 Å. An analysis of the orbitals indicates that the symmetry of the orbitals is similar to the $^4A_1$ $[(1a_1)^2(1b_2)^1(2a_1)^1(2b_2)^1]$ found using the Seg. SDD-VQZ-MWB/6-311+G(3p) basis set. The break from C_{2v} symmetry using the larger basis sets is possibly caused by the degeneracy of the $^4A_1$ and $^4B_2$ states at linearity. Neither the $^4A_1$ nor $^4B_2$ surfaces are expected to play a prominent role in reaction 5.5.

Initially, all doublet surfaces are repulsive, so approach of Th^+ with H_2 in reaction 5.5 evolves along a quartet surface where the $^4A_2$, $^4B_1$, and $^4B_2$ surfaces are similar in energy (see also Table 5.5). Qualitatively, this can be understood on the basis of the doubly occupied 7*s* frontier orbital of Th^+ (^2D), versus its single occupation in the ^4F state. Note that the quartet surfaces for the $HThH^+$ species evolve at small angles to energies that match that calculated for Th^+ (^2D) + H_2. This disparity appears to be a result of the spin-contamination of the calculated ^2D asymptote, as none of the surfaces shown

in Figure 5.5 exhibit any appreciable spin-contamination. At larger angles, these quartet surfaces cross that of the $^2A_1$ surface that leads to the global minimum. On this surface, two covalent bonds with the H-ligands are formed via interactions of the Th^+ *6d*-electrons with the H *1s*-electrons so that the unpaired electron is found in the $2a_1$(*7s*) orbital. Loss of a H ligand from these doublet spin intermediates can potentially lead to high spin-coupled ThH^+ ($^3\Delta$, $^3\Pi$, $^3\Phi$) + H (^2S) or low spin-coupled ThH^+ ($^1\Sigma^+$) + H (^2S) products with no barrier in excess of the asymptotic energies. Overall, these surfaces show that the reaction of Th^+ (J = 3/2) with H_2 can occur via the formation of a stable dihydride intermediate with no barrier in the entrance or exit channels, presuming that the quartet and doublet surfaces couple, which seems likely give the large spin-orbit interactions in this heavy metal system. This coupling with the low-spin surface would lead to category 1 (statistical) behavior that is consistent with the mechanism indicated by the branching ratio of reactions 5.7 and 5.8, Figure 5.4.

Discussion

Basis Set Comparison

Table 5.4 shows that BDEs derived from DFT methods vary little between basis sets used for Th^+ and H; however, CCSD(T) results may differ by as much as 0.3 eV (excluding CCSD(T)/ANO-VQZ-MDF/6-311+G(3p)) between basis sets. For CCSD(T), basis sets that utilize quasi-relativistic MWB (SDD-VDZ-MWB, ANO-VQZ-MWB, and Seg. SDD-VQZ-MWB) are in better agreement with the experimental BDE than those calculated using the fully relativistic MDF ECP (ANO-VQZ-MDF and cc-pwCVXZ-PP-MDF). For DFT, BDEs calculated using the all-electron cc-pwCVXZ-PP-DK3 and cc-

pVXZ-PP-DK3 basis sets are 0 – 0.13 eV smaller than their ECP counterparts (except B3LYP/cc-pwCVQZ-PP-DK3 which is 0.01 eV larger), cc-pwCVXZ-PP-MDF and cc-pVXZ-PP-MDF, respectively (see also Table B.4). For CCSD(T) calculations, the all-electron and ECP cc-pxCVXZ-PP basis sets yield identical results, whereas the cc-pVXZ-PP-DK3 basis sets yield BDEs 0.0 – 0.03 eV smaller than their ECP counterpart.

Interestingly, the smaller basis sets appear to reproduce the experimental BDE best. This is not likely a cause of the basis set superposition error (BSSE), as calculations indicate that the BSSE is only 0.03 eV (not included in Table 5.4) for the largest basis set combination CCSD(T)/cc-pwCVQZ-PP-MDF/aug-cc-pVQZ. This is also shown by the small difference in the cc-pwCVQZ-PP and CBS values. Similarly, errors resulting from the use of the MDF ECP appear to be minimal, as the difference between CBS-cc-pwCVXZ-PP-MDF and CBS-cc-pwCVXZ-DK3 results are small, Table 5.4.

In a previous study, CCSD(T)/cc-pVQZ-PP-MDF/cc-pVTZ calculations over-predicted the BDE of singly bound ThH^+ ($^3\Delta_1$) and $ThCH_3^+$ ($^1A_1$) by 0.22 and 0.62 eV, respectively, but performed much better than the smaller basis sets for the triply bound $ThCH^+$ ($^1\Sigma^+$), underpredicting the experimental value by 0.21 eV.[30] Similarly, CBS limit extrapolations using correlation-consistent basis sets are also lower than the experimental value by 0.2 eV for several transition metal oxide cation BDEs.[91-92] For calculations involving several other ThL^+ species, it was found that high levels of theory, CCSDT(Q) and multireference configuration interaction (MRCI+Q) calculations were necessary to reproduce experimental relative energies of the ground and excited-states. Specific errors relative to the experimental difference between the ground and first excited-state (0.08 eV) were 0.06 eV for CCSD(T), 0.03 eV for CCSDT(Q), and 0.01_5 eV for MRCI+Q.[31, 77]

This was attributed to accurate recovery of correlation energy.[31] Therefore, it may be necessary to resort to very high levels of theory to reproduce experimental results, but these methods are not attempted here.

ThH^+ Electronic State

Previous theoretical work on ThH^+ by di Santo et al.[21] identified a $^3\Delta$ ground-state with a low-lying (0.01 eV) $^1\Sigma^+$ excited-state (B3LYP/SDD-VDZ-MWB/6-311+G(p)). In the present work, all levels of theory except CCSD(T) and M06 identify the $^3\Delta$ as the ground-state before accounting for spin-orbit interaction. After including spin-orbit corrections, all levels of theory except M06 indicate that the ground-level is $^3\Delta_1$. Nevertheless, the close proximity of the $^3\Delta$ and $^1\Sigma^+$ states makes unambiguous determination of the ground-state difficult; therefore, a comparison to similar species may be useful in providing additional insight into identification of the ThH^+ ground-state.

One such comparison is to HfH^+, which, like ThH^+, has either a $^1\Sigma^+$ or $^3\Delta$ ground-state,[44, 98-99] where the $^1\Sigma^+$ ($1\sigma^2 2\sigma^2$) can only be formed from the Hf^+ (^{2}D, $5d6s^2$) + H (^{2}S, $1s$) asymptote and the $^3\Delta$ ($1\sigma^2 2\sigma 1\delta$) state is formed from the Hf^+ (^{4}F, $5d^2 6s$) + H asymptote (possibly the Hf^+ (^{2}D, $5d6s^2$) + H (^{2}S, $1s$) asymptote). Because the 2σ molecular orbital (MO) is essentially the Hf^+ $6s$-orbital, the 1σ bonding orbital in the $^1\Sigma^+$ cannot be *sd*-hybridized, resulting in poor orbital overlap and a weaker BDE than the $^3\Delta$, where *sd*-hybridization of the Hf^+ bonding orbital is allowed.[44] Because the Hf^+ ground-state is ^{2}D (with a $^2D_{3/2}$ ground-level),[89] the ground-state of HfH^+ is $^1\Sigma^+$ if the stabilization resulting from an *sd*-*s* MO over a *d*-*s* MO is less than the promotion energy, E_p = 0.45 eV,[89] from the ground-level $^2D_{3/2}$ to the $^4F_{3/2}$ level. Unlike Hf^+, Th^+ has a J =

3/2 ground-level with 43% $^4F_{3/2}$ and 27% $^2D_{3/2}$ mixed character,[88] so that both the $^1\Sigma^+$ and $^3\Delta$ states can presumably evolve directly from the ground-level asymptote. Assuming that there is an advantage to forming the ThH^+ bond using a *sd*-hybridized orbital, then the likely ground-state of ThH^+ is $^3\Delta$. This simplistic analysis ignores likely second-order interactions between low-lying states of ThH^+, which the fully relativistic calculations discussed above indicate are small.

Recently there has been an effort to characterize actinide chemical bonds spectroscopically. Although ThH has been studied in an Ar matrix,[100] ThH^+ has not been studied. ThF^+, which has been studied in pulsed-field ionization zero kinetic energy (PFI-ZEKE) photoelectron spectroscopy and laser-induced fluorescence (LIF) experiments,[31, 77] may be expected to have similar characteristics as ThH^+, because both ligands have one unpaired electron and form a single covalent bond with Th^+. PFI-ZEKE experiments indicate that either the $^3\Delta_1$ or $^1\Sigma^+$ is the ground-level of ThF^+.[31, 77] Later LIF results confirmed a $^1\Sigma^+$ ground-level, with the $^3\Delta_1$ level only 316 cm^{-1} (0.04 eV) higher in energy.[31] These results are consistent with high-level quantum chemical calculations that include spin-orbit coupling, which place both the $^3\Delta$ or $^1\Sigma^+$ states as low-lying, similar to ThH^+. Bonding occurs by an interaction of the F $2p_z$-orbital with an appropriate Th^+ orbital (most likely a *sd*-hybridized orbital). The 1δ-orbital in the $^3\Delta$ state was found to be a Th^+ *6d*δ-orbital, and the filled 2σ-orbital in the $^1\Sigma^+$ state is primarily the Th^+ *7s*-orbital.[31] Heaven et al.[31] also note a slight antibonding interaction between the Th^+ *6d*π-orbitals and the F *2p*π-orbitals, an effect that cannot occur for ThH^+ because the H ligand has no occupied *p*-orbitals.

Qualitatively, the difference in the character of the π-orbitals in ThH^+ and ThF^+

suggests that the $^3\Pi$ state of ThH^+ should be lower in energy than the analogous ThF^+ $^3\Pi$ state. This is confirmed by experimental and theoretical results. Experimentally, the $^3\Pi_0$ level is found 0.42 eV above the $^1\Sigma^+$ ground-state in ThF^+ (the $^3\Pi_1$ was not observed in the range of 0 – 4000 cm^{-1}),[77] whereas theoretical calculations indicate that the $^3\Pi_0$ and $^3\Pi_1$ lie 0.61 and 0.65 eV above the ground-state, respectively.[31] In ThH^+, theoretical calculations (CCSD(T)/cc-pwCVQZ-PP-MDF/aug-cc-pVQZ) combined with empirical spin-orbit effects estimated using eq 5.9 indicate that the $^3\Pi_0$ and $^3\Pi_1$ lie 0.39 and 0.48 eV above the $^3\Delta_1$ ground-level (0.28 and 0.37 eV above the $^1\Sigma^+$), respectively.

The energy of the $^3\Pi$ levels has implications for the second-order interaction of the $^1\Sigma^+$ and $^3\Delta_1$ levels with the $^3\Pi_0$ and $^3\Pi_1$ levels, respectively. Because theoretical calculations in the present work indicate that the $^1\Sigma^+$ and $^3\Pi_0$ levels are closer in energy in ThH^+ than ThF^+, it is anticipated that the second-order interaction between these levels will be stronger than the interaction between the same levels in ThF^+. Likewise, the interaction of the $^3\Delta_1$ and $^3\Pi_1$ levels in ThH^+ will also be stronger than the corresponding levels in ThF^+. For ThF^+, theoretical calculations that explicitly treat spin-orbit interaction place the $^3\Pi_0$ and $^3\Pi_1$ levels only 0.04 eV apart compared to a 0.09 eV difference expected using eq 5.9, suggesting that the second-order interaction of the Ω = 0 levels stabilizes the $^1\Sigma^+$ state by 0.05 eV. Interestingly, the difference in energy of the $^1\Sigma^+$ (ground) and $^3\Delta_1$ states is only 0.02 eV calculated at the same level of theory (0.04 eV experimentally).[31] Thus, the second-order interaction with the $^3\Pi_0$ level is influential in making the $^1\Sigma^+$ state of ThF^+ the ground-level. Given that $^3\Pi$ state is likely closer in energy to the $^1\Sigma^+$ and $^3\Delta$ states in ThH^+ than in ThF^+, estimated spin-orbit effects from eq 5.9 suggest that the states are probably very close in energy, such that the true ThH^+

ground-state remains ambiguous. As noted above, explicit fully relativistic calculations of the spin-orbit interactions continue to confirm this close spacing, with the $^3\Delta_1$ state being the ground-state and the $^1\Sigma^+$ state 0.03 – 0.10 eV higher in energy, comparable to the 0.13 eV spacing found using the empirical spin-orbit correction.

MH^+ Thermochemistry

Because Th^+, unlike other actinides, does not populate the *5f*-orbitals in its ground-state, a good comparison can be made to transition metals with three valence electrons, Ti^+, Zr^+, and Hf^+. These have BDEs of $D_0(Ti^+\text{-H}) = 2.31 \pm 0.11$,[38] $D_0(Zr^+\text{-H}) = 2.26 \pm 0.08$,[41] and $D_0(Hf^+\text{-H}) = 2.11 \pm 0.08$ eV,[44] as measured in guided ion beam experiments analogous to the present ones. The lower Hf^+ BDE has been explained as resulting from the fully occupied *6s* orbital in the ^2D ($5d6s^2$) ground-state of Hf^+.[44] The other transition metal congeners have ^4F (d^2s) ground-states that permit ready formation of a strong $M^+(s)\text{-H}(s)$ or $M^+(sd)\text{-H}(s)$ covalent bond. The ground-level of Th^+ is a mixture of ^4F and ^2D states, which does not appear to inhibit the bond strength as $D_0(Th^+\text{-H})$ is 0.2 – 0.3 eV stronger than $D_0(Ti^+\text{-H})$ and $D_0(Zr^+\text{-H})$. This trend is similar to that reported for BDEs of the same metals with other ligands and can be attributed to lanthanide contraction.[30, 43, 101-105]

According to theory, the participation of the *d*-orbitals in group 4 MH^+ bonding increases moving down the periodic table. Previous theoretical work has indicated that *sd*-hybridization is typically not important for first row transition metals. Consequently, TiH^+ has a $^3\Phi$ ground-state[106] that can form directly from the Ti^+ ^4F ($3d^24s$) ground-state via $M^+(s)\text{-H}(s)$ bonding. *sd*-hybridization becomes more important in ZrH^+, as suggested

by the close proximity of the $^3\Delta$ and $^3\Phi$ states. Both states have been reported as the ground-state in different studies,[41, 106] and both states can be formed directly from the Zr^+ ^4F ($4d^25s$) ground-state through $M^+(sd)$-H(s) or $M^+(s)$-H(s) bonding, respectively. For the third-row transition metals, *sd*-hybridization becomes important because of the similarity in size of the *4s* and *5d* orbitals.[98] For HfH^+, the ground-state is most likely $^3\Delta$, which can be formed from the low-lying ^4F ($5d^26s$) state.[44] Likewise, the present work indicates that the bonding interaction between Th^+ and H occurs between an orbital primarily $6d\sigma$ in character and the H *1s* orbital for the likely ground-state, $^3\Delta$ (presumably because the *7s* orbital is now too large to overlap well with the *1s* orbital of H, unlike the smaller transition metal congeners).

The BDE trend can be explained more quantitatively with promotion energy (E_p) arguments where E_p is defined as the difference in energy between the M^+ ground-level and the first level with an appropriate electronic configuration (d^2s) for bonding. This definition ignores any spin decoupling effects[107] but should be qualitatively correct. Both Ti^+ and Zr^+ have $^4F_{3/2}$ (d^2s) ground-levels, so E_p = 0.0 eV. Hf^+ has a $^2D_{3/2}$ ($5d6s^2$) ground-level, and the first level with the appropriate configuration is $^4F_{3/2}$ ($5d^26s$), E_p = 0.45 eV. Likewise, ThH^+ most likely has a $^3\Delta$ ground-state, and the Th^+ J = 3/2 ground-level has primarily an appropriate configuration ($6d^27s$). This yields intrinsic BDEs (= $D_0 + E_p$) of 2.31 ± 0.11, 2.26 ± 0.08, 2.56 ± 0.08, and 2.45 ± 0.07 eV for TiH^+, ZrH^+, HfH^+, and ThH^+, respectively, which increase roughly as the metal gets heavier (within experimental uncertainty), as might be anticipated for the trend associated with the lanthanide contraction. It is also possible that the ThH^+ BDE is depressed by the $^2D_{3/2}$ ($6d7s^2$) character mixed into the J = 3/2 ground-level, such that the promotion energy is

better described as corresponding to a more pure ^{4}F level, e.g., the $^4F_{5/2}$ (65% ^{4}F, 17% ^{2}D), 0.19 eV above the ground-level,[88] leading to an intrinsic BDE of 2.64 eV. Nevertheless, because the effect of the ^{2}D character on the ThH^+ BDE is not clear, we adopt $E_p(Th^+) = 0.0$ eV.

AnH^+ Thermochemistry

In this section, we explore whether the thermochemistry of Th^+ determined here can be analyzed to provide insight into the thermochemistry of other actinide (An) systems where the thermochemistry is poorly understood. In a recent study of the reactions of An^{2+} with alkanes and alkenes using ICR, several AnH^+ species were observed in reactions at thermal temperatures.[18] For the purposes of determining lower limits to the AnH^+ BDE, the most discriminating process is reaction 5.10.

$$An^{2+} + C_3H_8 \rightarrow AnH^+ + C_3H_7^+ \qquad (5.10)$$

Reaction 5.10 was observed at thermal energies yielding UH^+, NpH^+, PuH^+, AmH^+, and CmH^+ with product branching percentages of 10, 5, 70, 90, and 10 %, respectively.[18] Thus, the ICR results suggest that a lower limit to the AnH^+ BDE can be obtained using eq 5.11:

$$D_0(An^+\text{-}H) \geq D_0(H_7C_3\text{-}H) - IE(An^+) + IE(C_3H_7) \qquad (5.11)$$

where $D_0(H_7C_3\text{-}H) = 4.20 \pm 0.02$ eV[83, 108-109] and $IE(C_3H_7) = 7.37 \pm 0.02$ eV.[83, 110] Only

$IE(U^+)$ = 10.6 eV[111] and $IE(Pu^+)$ = 11.2 eV[112] are listed in a review of atomic energy levels,[89] values that yield lower limits of $D_0(U^+\text{-H}) \geq 0.97 \pm 0.2$ eV and $D_0(Pu^+\text{-H}) \geq 0.37 \pm 0.2$ eV, where we have assumed an uncertainty of ± 0.2 eV for $IE(An^+)$. In contrast, in an evaluation of $IE(An^+)$ by Marçalo and Gibson,[9] $IE(U^+) = 11.7 \pm 0.3$ eV and $IE(Pu^+) = 11.8 \pm 0.3$ eV are given, values that indicate reaction 5.10 is exothermic no matter how weak the AnH^+ bond may be.

Other than our recent work on ThH^+,[30] the only previous experimental report of an AnH^+ BDE is that of $D_0(U^+\text{-D}) = 2.9 \pm 0.1$ eV measured in early (notably *not* guided) ion beam studies of the reactions of U^+ with CD_4 and D_2.[10] In later theoretical work, di Santo et al. report UH^+ BDEs calculated using B3LYP/SDD-VDZ-MWB/6-311+G(p) and PW91/ZORA as 2.35 eV and 2.94 eV, respectively.[21] Although the PW91/ZORA value is in good agreement with the experimental value in this case, this level of theory appears to overestimate bond strength in other molecules where experimental data is readily available.[21, 30] The difference in energy of the ThH^+ and UH^+ BDEs is potentially interesting because the measured UH^+ BDE is ~0.5 eV stronger than the ThH^+ BDE, which is opposite the results from theoretical BDEs reported by di Santo et al. that predict ThH^+ to be the stronger bond at both levels of theory investigated.

As discussed above, AnF^+ are potentially similar to the AnH^+ systems. Thermochemistry for the fluorides is more readily available with reports of $D_0(\text{Th-F}) = 6.72 \pm 0.10$ eV,[113] $D_0(\text{U-F}) = 6.72 \pm 0.10$ eV,[114] and $D_0(\text{Pu-F}) = 5.58 \pm 0.30$ eV.[115] Ionization energies for these metals are IE(Th) = 6.3067 eV, IE(U) = 6.1941 eV, and IE(Pu) = 6.026 eV.[89] Additionally, IE(ThF) = 6.3953 ± 0.0004 eV and IE(UF) = 6.34159 ± 0.00006 eV are reported in the literature.[31] Although IE(PuF) is not available in the

literature, because the ionization of AnF corresponds to the removal of a *7s*-electron for these three An, linear correlation of IE(AnF) versus IE(An) yields an estimate of IE(PuF) ≈ 6.26 eV. Alternatively, if the difference IE(AnF) – IE(An) is presumed to remain relatively constant, then IE(PuF) ≈ 6.15 eV. A conservative estimate is the average of both values, IE(PuF) = 6.2 ± 0.1_5 eV, where the uncertainty is two standard deviations of the mean. Eq 5.12 can be used to determine $D_0(Th^+\text{-}F)$ = 6.63 ± 0.10 eV, $D_0(U^+\text{-}F)$ = 6.57 ± 0.10 eV, and $D_0(Pu^+\text{-}F)$ = 5.40 ± 0.34 eV.

$$D_0(An^+\text{-}F) = D_0(An\text{-}F) - IE(AnF) + IE(An) \qquad (5.12)$$

Assuming that the AnH^+ BDE trend is similar to that of the AnF^+ trend, this analysis indicates that the ThH^+ and UH^+ BDEs should be similar, which clearly suggests that the reported UH^+ BDE is too large. Of note is the much larger AnF^+ BDEs compared to AnH^+, which may indicate bonds that are significantly more ionic than the AnH^+ bonds or contributions from donation of F(2pπ) electrons into empty An^+ (6dπ) orbitals.

The trends in these three BDEs can also be understood in terms of the promotion energy from the ground-level to a reactive level with the appropriate configuration, $E_P(An^+)$.[9] For AnL^+ with a bond order of 1, the required electron configuration could be $5f^{n-1}7s$, $5f^{n-2}6d7s$, $5f^{n-2}6d^2$, or $5f^{n-3}6d^27s$. As noted above with Th^+, the *7s*-orbital appears to be insufficient to form a strong covalent bonding interaction, such that promotion to a configuration with at least one *6d* electron is needed. Notably, the difference in BDEs between UF^+ and ThF^+ is similar to the magnitude of E_P (U^+) = 0.04 eV[89] from the ground-level $^4I_{9/2}$ ($5f^37s^2$) to $^6L_{11/2}$ ($5f^36d7s$) for U^+. Likewise, the difference between the

ThF^+ and PuF^+ BDEs is comparable to E_p = 1.08 eV[89] from the ground-level $^8F_{1/2}$ ($5f^6 7s$) to $^8K_{7/2}$ ($5f^5 6d7s$) for Pu^+ (a result that confirms that a *6d* electron is needed for bonding). Previously, Marçalo and Gibson have shown that the BDEs for AnO^{n+} (n = 0 – 2) are correlated to the promotion energy of An^{n+} to the first state with a $6d^2$ electron configuration because two valence electrons on the metal are needed to form a strong bond with O.[9] Because the typical configuration of early An^+ is $5f^{n-2}7s^2$,[89] this correlation indicates that non-*f* electrons are required for strong bonding. The diabatic (or intrinsic) BDE, $D_0(An^{n+}\text{-L})^*$, for that configuration should also be similar across the AnO^{n+} series. For n = 1, a reasonable estimate for this intrinsic BDE is $D_0(Th^+\text{-L})$ because Th^+ has a ground configuration of $6d^2 7s$. This allows for the simple model shown in eq 5.13,

$$D_0(An^+\text{-L})^* = D_0(Th^+\text{-L}) = D_0(An^+\text{-L}) + E_P\,(An^+) \qquad (5.13)$$

where $E_P(An^+)$ is the promotion energy from the ground-level to a reactive level with the appropriate configuration (again ignoring the energy associated with spin decoupling the bonding electron from other unpaired electrons on the metal).[9] Eq 5.13 allows for the estimate of $D_0(An^+\text{-L})$ from established $D_0(Th^+\text{-L})$. Consequently, we estimate the BDEs of AnF^+, AnH^+, and $AnCH_3^+$ for Ac – Cm in Table 5.6, where $D_0(Th^+\text{-}CH_3)$ was determined previously from the reaction $Th^+ + CH_4$.[30]

Conclusion

Analysis of the kinetic energy dependence of the cross sections in Figures 5.1 – 5.3 indicate that $D_0(Th^+\text{-H}) = 2.45 \pm 0.07$ eV. This value is in agreement with the

previously reported $D_0(Th^+-H) \geq 2.25 \pm 0.20$ eV measured in the reaction $Th^+ + CH_4$, as well as the PST model of the same system, which indicates a BDE of 2.45 eV.[30] Branching ratios from reactions 5.7 and 5.8 indicate that the reaction proceeds via a statistical mechanism. This is thought to occur from coupling of the mixed character surfaces of the Th^+ ground-level to several doublet surfaces, which lead to long-lived ThH_2^+ intermediates. In general, theoretical BDEs overestimate the bond strength of ThH^+ even after including spin-orbit contributions, which always improve the agreement. Furthermore, the use of the larger cc-pwCVQZ-PP and cc-pVQZ-PP basis sets (that include *i*-functions) does not improve theoretical results compared to the smaller SDD-VDZ and Seg. SDD-VQZ. This may indicate that higher levels of theory than CCSD(T) may be necessary to accurately describe these actinide BDEs. However, CCSD(T), M06, and BHLYP results are in reasonable agreement with the experimental value obtained here.

Associated Content

Relative energies and molecular parameters for ThH^+ ground and excited-states calculated at additional levels of theory. ThH^+ BDEs calculated at additional levels of theory.

Acknowledgements

This work is supported by the Heavy Element Chemistry Program, Office of Basic Energy Sciences, U. S. Department of Energy, Grant No. DE-SC0012249. We thank the Center for High Performance Computing at the University of Utah for the

generous allocation of computer time. This research used resources of the Oak Ridge Leadership Computing Facility, which is a DOE Office of Science User Facility supported under Contract DE-AC05-00OR22725. An award of computer time was provided by the Innovative and Novel Computational Impact on Theory and Experiment (INCITE) program.

References

(1). Armentrout, P. B.; Beauchamp, J. L.Reactions of U^+ and UO^+ with O_2, CO, CO_2, COS, CS_2, and D_2O. *Chem. Phys.* **1980,** *50*, 27-36.

(2). Armentrout, P. B.; Beauchamp, J. L.Collision-Induced Dissociation of UO^+ and UO_2^+. *Chem. Phys.* **1980,** *50*, 21-25.

(3). Cornehl, H. H.; Wesendrup, R.; Diefenbach, M.; Schwarz, H.A Comparative Study of Oxo-Ligand Effects in the Gas-Phase Chemistry of Atomic Lanthanide and Actinide Cations. *Chem. - Eur. J.* **1997,** *3*, 1083-1090.

(4). Gibson, J. K.; Haire, R. G.Gas-Phase Chemistry of Bare and Oxo-Ligated Protactinium Ions: A Contribution to a Systematic Understanding of Actinide Chemistry. *Inorg. Chem.* **2002,** *41*, 5897-5906.

(5). Santos, M.; Marcalo, J.; Pires, d. M. A.; Gibson, J. K.; Haire, R. G.Gas-Phase Oxidation Reactions of Neptunium and Plutonium Ions Investigated via Fourier Transform Ion Cyclotron Resonance Mass Spectrometry. *J. Phys. Chem. A* **2002,** *106*, 7190-7194.

(6). Gibson, J. K.,Role of Atomic Electronics in f-Element Bond Formation: Bond Energies of Lanthanide and Actinide Oxide Molecules. *J. Phys. Chem. A* **2003,** *107*, 7891-7899.

(7). Gibson, J. K.; Haire, R. G.; Santos, M.; Marcalo, J.; Pires, d. M. A.Oxidation Studies of Dipositive Actinide Ions, An^{2+} (An = Th, U, Np, Pu, Am) in the Gas Phase: Synthesis and Characterization of the Isolated Uranyl, Neptunyl, and Plutonyl Ions UO_2^{2+}(g), NpO_2^{2+}(g), and PuO_2^{2+}(g). *J. Phys. Chem. A* **2005,** *109*, 2768-2781.

(8). Gibson, J. K.; Haire, R. G.; Marcalo, J.; Santos, M.; Leal, J. P.; Pires de Matos, A.; Tyagi, R.; Mrozik, M. K.; Pitzer, R. M.; Bursten, B. E.FTICR/MS Studies of Gas-Phase Actinide Ion Reactions: Fundamental Chemical and Physical Properties of Atomic and Molecular Actinide Ions and Neutrals. *Eur. Phys. J. D* **2007,** *45*, 133-138.

(9). Marcalo, J.; Gibson, J. K.Gas-Phase Energetics of Actinide Oxides: An Assessment of Neutral and Cationic Monoxides and Dioxides from Thorium to Curium. *J. Phys. Chem. A* **2009,** *113*, 12599-12606.

(10). Armentrout, P. B.; Hodges, R. V.; Beauchamp, J. L.Endothermic Reactions of Uranium Ions with N_2, D_2 and CD_4. *J. Chem. Phys.* **1977,** *66*, 4683-4688.

(11). Marcalo, J.; Leal, J. P.; Pires, d. M. A.Gas Phase Actinide Ion Chemistry: Activation of Alkanes and Alkenes by Thorium Cations. *Int. J. Mass Spectrom. Ion Processes* **1996,** *157/158*, 265-274.

(12). Gibson, J. K.,Gas-Phase Transuranium Organometallic Chemistry: Reactions of Np^+, Pu^+, NpO^+, and PuO^+ with Alkenes. *J. Am. Chem. Soc.* **1998,** *120*, 2633-2640.

(13). Gibson, J. K.,Actinide Gas-Phase Chemistry: Reactions of An^+ and AnO^+ [An = Th, U, Np, Pu, Am] with Nitriles and Butylamine. *Inorg. Chem.* **1999,** *38*, 165-173.

(14). Gibson, J. K.,Gas-Phase Reactions of An^+ and AnO^{n+} [An = Th, U, Np, Pu, Am] with halogenated hydrocarbons [$C_{14}F_{24}$, C_3F_6, $C_2H_4Cl_2$, and $C_2H_4Br_2$]. *Radiochim. Acta* **1999,** *84*, 135-146.

(15). Gibson, J. K.; Haire, R. G.Berkelium and Californium Organometallic Ions. *Radiochim. Acta* **2001,** *89*, 363-369.

(16). Gibson, J. K.; Haire, R. G.; Marçalo, J.; Santos, M.; Pires de Matos, A.; Mrozik, M. K.; Pitzer, R. M.; Bursten, B. E.Gas-Phase Reactions of Hydrocarbons with An^+ and AnO^+ (An = Th, Pa, U, Np, Pu, Am, Cm): The Active Role of 5f Electrons in Organoprotactinium Chemistry. *Organometallics* **2007,** *26*, 3947-3956.

(17). di Santo, E.; Santos, M.; Michelini, M. C.; Marcalo, J.; Russo, N.; Gibson, J. K.Gas-Phase Reactions of the Bare Th^{2+} and U^{2+} Ions with Small Alkanes, CH_4, C_2H_6, and C_3H_8: Experimental and Theoretical Study of Elementary Organoactinide Chemistry. *J. Am. Chem. Soc.* **2011,** *133*, 1955-1970.

(18). Marcalo, J.; Santos, M.; Gibson, J. K.Gas-Phase Reactions of Doubly Charged Actinide Cations with Alkanes and Alkenes-Probing the Chemical Activity of 5f Electrons from Th to Cm. *Phys. Chem. Chem. Phys.* **2011,** *13*, 18322-18329.

(19). de Almeida, K. J.; Cesar, A.Methane C-H Bond Activation by Neutral Lanthanide and Thorium Atoms in the Gas Phase: A Theoretical Prediction. *Organometallics* **2006,** *25*, 3407-3416.

(20). Mazzone, G.; Michelini, M. d. C.; Russo, N.; Sicilia, E.Mechanistic Aspects of the Reaction of Th^+ and Th^{2+} with Water in the Gas Phase. *Inorg. Chem.* **2008,** *47*, 2083-2088.

(21). di Santo, E.; Michelini, M. d. C.; Russo, N.Methane C−H Bond Activation by Gas-Phase Th^+ and U^+: Reaction Mechanisms and Bonding Analysis. *Organometallics* **2009,** *28*, 3716-3726.

(22). di Santo, E.; Michelini, M. C.; Russo, N.Activation of Ethane C-H and C-C Bonds by Gas Phase Th^+ and U^+: A Theoretical Study. *J. Phys. Chem. A* **2009,** *113*, 14699-14705.

(23). Almeida, K. J. d.; Duarte, H. A.Gas-Phase Methane Activation by the Ac^+–Pu^+ Ions: Theoretical Insights into the Role of 5f Electrons/Orbitals in Early Actinide Chemistry. *Organometallics* **2009,** *28*, 3203-3211.

(24). de Almeida, K. J.; Duarte, H. A.Dehydrogenation of Methane by Gas-Phase Th, Th^+, and Th^{2+}: Theoretical Insights into Actinide Chemistry. *Organometallics* **2010,** *29*, 3735-3745.

(25). Zhou, J.; Schlegel, H. B.Ab Initio Molecular Dynamics Study of the Reaction between Th^+ and H_2O. *J Phys Chem A* **2010,** *114*, 8613-8617.

(26). Infante, I.; Kovacs, A.; La, M. G.; Shahi, A. R. M.; Gibson, J. K.; Gagliardi, L.Ionization Energies for the Actinide Mono- and Dioxides Series, from Th to Cm: Theory versus Experiment. *J. Phys. Chem. A* **2010,** *114*, 6007-6015.

(27). Kovacs, A.; Konings, R. J. M.Computed Vibrational Frequencies of Actinide Oxides $AnO^{0/+/2}$+ and $AnO_2^{0/+/2+}$ (An = Th, Pa, U, Np, Pu, Am, Cm). *J. Phys. Chem. A* **2011,** *115*, 6646-6656.

(28). Averkiev, B. B.; Mantina, M.; Valero, R.; Infante, I.; Kovacs, A.; Truhlar, D. G.; Gagliardi, L.How Accurate are Electronic Structure Methods for Actinoid Chemistry? *Theor. Chem. Acc.* **2011,** *129*, 657-666.

(29). Pereira, C. C. L.; Marsden, C. J.; Marcalo, J.; Gibson, J. K.Actinide Sulfides in the Gas Phase: Experimental and Theoretical Studies of the Thermochemistry of AnS (An = Ac, Th, Pa, U, Np, Pu, Am and Cm). *Phys. Chem. Chem. Phys.* **2011,** *13*, 12940-12958.

(30). Cox, R. M.; Armentrout, P. B.; de Jong, W. A.Activation of CH_4 by Th^+ as Studied by Guided Ion Beam Mass Spectrometry and Quantum Chemistry. *Inorg. Chem.* **2015,** *54*, 3584-3599.

(31). Heaven, M. C.; Barker, B. J.; Antonov, I. O.Spectroscopy and Structure of the Simplest Actinide Bonds. *J. Phys. Chem. A* **2014,** *118*, 10867-10881.

(32). Elkind, J. L.; Armentrout, P. B.Effect of kinetic and electronic energy on the reaction of V+ with H_2, HD, and D_2. *J. Phys. Chem.* **1985,** *89*, 5626-5636.

(33). Elkind, J. L.; Armentrout, P. B.Effect of Kinetic and Electronic Energy on the Reactions of Fe^+ with H_2, HD and D_2: State-Specific Cross Sections for $Fe^+(^6D)$ and $Fe^+(^4F)$. *J. Phys. Chem.* **1986,** *90*, 5736-5745.

(34). Elkind, J. L.; Armentrout, P. B.Effect of Kinetic and Electronic Energy on the Reactions of Mn^+ with H_2, HD and D_2 *J. Chem. Phys.* **1986,** *84*, 4862-4871.

(35). Elkind, J. L.; Armentrout, P. B.Effect of Kinetic and Electronic Energy on the Reactions of Co^+, Ni^+ and Cu^+ with H_2, HD and D_2. *J. Phys. Chem.* **1986,** *90*, 6576-6586.

(36). Elkind, J. L.; Armentrout, P. B.Transition Metal Hydride Bond Energies: First and Second Row. *Inorg. Chem.* **1986,** *25*, 1078-1080.

(37). Elkind, J. L.; Armentrout, P. B.Effect of Kinetic and Electronic Energy on the reactions of Cr^+ with H_2, HD, and D_2. *J. Chem. Phys.* **1987,** *86*, 1868-1877.

(38). Elkind, J. L.; Armentrout, P. B.Effect of Kinetic and Electronic Energy on the Reactions of Ti^+ with H_2, HD and D_2. *Int. J. Mass Spectrom. Ion Processes* **1988,** *83*, 259-284.

(39). Elkind, J. L.; Sunderlin, L. S.; Armentrout, P. B.Periodic Trends in Chemical Reactivity: Reactions of Sc^+, Y^+, La^+, and Lu^+ with H_2, D_2, and HD. *J. Phys. Chem.* **1989,** *93*, 3151-3158.

(40). Chen, Y.-M.; Elkind, J. L.; Armentrout, P. B.Reactions of Ru^+, Rh^+, Pd^+, and Ag^+ with H_2, HD, and D_2. *J. Phys. Chem.* **1995,** *99*, 10438-10445.

(41). Sievers, M. R.; Chen, Y.-M.; Elkind, J. L.; Armentrout, P. B.Reactions of Y^+, Zr^+, Nb^+, and Mo^+ with H_2, HD, and D_2. *J. Phys. Chem.* **1996,** *100*, 54-62.

(42). Zhang, X.-G.; Armentrout, P. B.Reactions of Pt^+ with H_2, D_2, and HD: Effect of Lanthanide Contraction on Reactivity and Thermochemistry. *J. Chem. Phys.* **2002,** *116*, 5565-5573.

(43). Zhang, X.-G.; Rue, C.; Shin, S.-Y.; Armentrout, P. B.Reactions of Ta^+ and W^+ with H_2, D_2, and HD: Effect of Lanthanide Contraction and Spin-Orbit Interactions on Reactivity and Thermochemistry. *J. Chem. Phys.* **2002,** *116*, 5574-5583.

(44). Hinton, C. S.; Armentrout, P. B.Guided Ion Beam and Theoretical Study of the Reactions of Hf^+ with H_2, D_2, and HD. *J. Chem. Phys.* **2010,** *133*, 124307.

(45). Hinton, C. S.; Citir, M.; Armentrout, P. B.Guided Ion Beam and Theoretical Study of the Reactions of Os^+ with H_2, D_2, and HD. *J. Chem. Phys.* **2011,** *135*, 234302.

(46). Li, F.; Hinton, C. S.; Citir, M.; Liu, F.; Armentrout, P. B.Guided Ion Beam and Theoretical Study of the Reactions of Au^+ with H_2, D_2, and HD. *J. Chem. Phys.* **2011,** *134*, 024310.

(47). Sugiyama, K.; Yoda, J.Production of YbH^+ by Chemical Reaction of Yb^+ in Excited-states with H_2 Gas. *Phys. Rev. A: At., Mol., Opt. Phys.* **1997,** *55*, R10-R13.

(48). Sunderlin, L. S.; Armentrout, P. B.Periodic Trends in Chemical Reactivity. Reactions of Sc^+, Y^+, La^+, and Lu^+ with Methane and Ethane. *J. Am. Chem. Soc.* **1989,** *111*, 3845-3855.

(49). Marcalo, J.; Santos, M.; Pires de Matos, A.; Gibson, J. K.; Haire, R. G.Gas-Phase Reactions of Doubly Charged Lanthanide Cations with Alkanes and Alkenes. Trends in Metal(2+) Reactivity. *J. Phys. Chem. A* **2008,** *112*, 12647-12656.

(50). Loh, S. K.; Hales, D. A.; Li, L.; Armentrout, P. B.Collision-Induced Dissociation of Fe_n^+ (n = 2 - 10) with Xenon: Ionic and Neutral Iron Binding Energies. *J. Chem. Phys.* **1989,** *90*, 5466-5485.

(51). Schultz, R. H.; Armentrout, P. B.Reactions of N_4^+ with Rare Gases from Thermal to 10 eV Center-of-Mass Energy: Collision-Induced Dissociation, Charge Transfer and Ligand Exchange. *Int. J. Mass Spectrom. Ion Processes* **1991,** *107*, 29-48.

(52). Teloy, E.; Gerlich, D.Integral Cross Sections for Ion-Molecule Reactions. I. The Guided Beam Technique. *Chem. Phys.* **1974,** *4*, 417-427.

(53). Gerlich, D.,Inhomogeneous RF fields: A VersatileTool for the Study of Processes with Slow Ions. *Adv. Chem. Phys.* **1992,** *82*, 1-176.

(54). Daly, N. R.,Scintillation-Type Mass Spectrometer Ion Detector. *Rev. Sci. Instrum.* **1960,** *31*, 264-267.

(55). Ervin, K. M.; Armentrout, P. B.Translational Energy Dependence of $Ar^+ + XY \rightarrow ArX^+ + Y$ (XY = H_2,D_2,HD) from Thermal to 30 eV c.m. *J. Chem. Phys.* **1985,** *83*, 166-189.

(56). Chantry, P. J.,Doppler Broadening in Beam Experiments. *J. Chem. Phys.* **1971,** *55*, 2746-2759.

(57). Haynes, C. L.; Armentrout, P. B.Thermochemistry and Structures of $CoC_3H_6^+$: Metallacycle and Metal-Alkene Isomers. *Organometallics* **1994,** *13*, 3480-3490.

(58). Kickel, B. L.; Armentrout, P. B.Reactions of Fe+, Co+, and Ni+ with Silane. Electronic State Effects, Comparison to Reactions with Methane, and M+-SiHx (x = 0-3) Bond Energies. *J. Am. Chem. Soc.* **1995,** *117*, 764-773.

(59). Kickel, B. L.; Armentrout, P. B.Guided Ion Beam Studies of the Reactions of Group 3 Metal Ions (Sc^+, Y^+, La^+, and Lu^+) with Silane. Electronic State Effects, Comparison to Reactions with Methane, and M^+-SiH_x (x = 0-3) Bond Energies. *J. Am. Chem. Soc.* **1995,** *117*, 4057-4070.

(60). Clemmer, D. E.; Chen, Y.-M.; Khan, F. A.; Armentrout, P. B.State-Specific Reactions of $Fe^+(a^6D, a^4F)$ with D_2O and Reactions of FeO^+ with D_2. *J. Phys. Chem.* **1994,** *98*, 6522-6529.

(61). Armentrout, P. B.,Kinetic Energy Dependence of Ion-Molecule Reactions: Guided Ion Beams and Threshold Measurements. *Int. J. Mass Spectrom.* **2000,** *200*, 219-241.

(62). Chesnavich, W. J.; Bowers, M. T.Theory of Translationally Driven Reactions. *J. Phys. Chem.* **1979,** *83*, 900-905.

(63). Muntean, F.; Armentrout, P. B.Guided Ion Beam Study of Collision-Induced Dissociation Dynamics: Integral and Differential Cross Sections. *J. Chem. Phys.* **2001,** *115*, 1213-1228.

(64). Frisch, M. J.; Trucks, G. W.; Schlegel, H. B.; Scuseria, G. E.; Robb, M. A.; Cheeseman, J. R.; Scalmani, G.; Barone, V.; Mennucci, B.; Petersson, G. A., et al., Gaussian 09, Revision A.1. Gaussian, Inc: Wallingford CT, 2009.

(65). Peterson, K. A.,Correlation Consistent Basis Sets for Actinides. I. The Th and U atoms. *J. Chem. Phys.* **2015,** *142*, 074105.

(66). Weigand, A.; Cao, X.; Hangele, T.; Dolg, M.Relativistic Small-Core Pseudopotentials for Actinium, Thorium, and Protactinium. *J. Phys. Chem. A* **2014,** *118*, 2519-2530.

(67). Dunning, T. H., Jr.,Gaussian Basis sets for Use in Correlated Molecular Calculations. I. The Atoms Boron Through Neon and Hydrogen. *J. Chem. Phys.* **1989,** *90*, 1007-1023.

(68). Feller, D.,The Role of Databases in Support of Computational Chemistry Calculations. *J. Comput. Chem.* **1996,** *17*, 1571-1586.

(69). Schuchardt, K. L.; Didier, B. T.; Elsethagen, T.; Sun, L.; Gurumoorthi, V.; Chase, J.; Li, J.; Windus, T. L.Basis Set Exchange: A Community Database for Computational Sciences. *J. Chem. Inf. Model.* **2007,** *47*, 1045-1052.

(70). Cao, X.; Dolg, M.; Stoll, H.Valence Basis Sets for Relativistic Energy-Consistent Small-Core Actinide Pseudopotentials. *J. Chem. Phys.* **2003,** *118*, 487-496.

(71). Douglas, M.; Kroll, N. M.Quantum Electrodynamical Corrections to the Fine Structure of Helium. *Ann. Phys. (N. Y.)* **1974,** *82*, 89-155.

(72). Hess, B. A.,Applicability of the No-Pair Equation with Free-Particle Projection Operators to Atomic and Molecular Structure Calculations. *Phys. Rev. A* **1985,** *32*, 756-763.

(73). Hess, B. A.,Relativistic Electronic-Structure Calculations Employing a Two-Component No-Pair Formalism with External-Field Projection Operators. *Phys. Rev. A: Gen. Phys.* **1986,** *33*, 3742-3748.

(74). Jansen, G.; Hess, B. A.Revision of the Douglas-Kroll Transformation. *Phys. Rev. A* **1989,** *39*, 6016-6017.

(75). de Jong, W. A.; Harrison, R. J.; Dixon, D. A.Parallel Douglas-Kroll Energy and Gradients in NWChem: Estimating Scalar Relativistic Effects using Douglas-Kroll Contracted Basis Sets. *J. Chem. Phys.* **2001,** *114*, 48-53.

(76). Barysz, M.; Sadlej, A. J.Two-Component Methods of Relativistic Quantum Chemistry: from the Douglas-Kroll Approximation to the Exact Two-Component Formalism. *J. Mol. Struct.: THEOCHEM* **2001,** *573*, 181-200.

(77). Barker, B. J.; Antonov, I. O.; Heaven, M. C.; Peterson, K. A.SpectroscopicInvestigations of ThF and ThF^+. *J. Chem. Phys.* **2012,** *136*, 104305.

(78). Karton, A.; Martin, J. M. L.Comment on: "Estimating the Hartree-Fock Limit from Finite Basis Set Calculations" [Jensen F (2005) Theor Chem Acc 113:267]. *Theor. Chem. Acc.* **2006,** *115*, 330-333.

(79). Martin, J. M. L.,Ab Initio Total Atomization Energies of Small Molecules - Towards the Basis Set Limit. *Chem. Phys. Lett.* **1996,** *259*, 669-678.

(80). Feller, D.; Peterson, K. A.; Hill, J. G.On the Effectiveness of CCSD(T) Complete Basis Set Extrapolations for Atomization Energies. *J. Chem. Phys.* **2011,** *135*, 044102.

(81). Holthausen, M. C.; Heinemann, C.; Cornehl, H. H.; Koch, W.; Schwarz, H.The Performance of Density-Functional/Hartree-Fock Hybrid Methods: Cationic Transition-Metal Methyl Complexes MCH_3^+ (M=Sc-Cu,La,Hf-Au). *J. Chem. Phys.* **1995,** *102*, 4931-4941.

(82). Foresman, J. B.; Frisch, A. E., *Exploring Chemistry with Electronic Structure Methods*. 2nd ed.; Gaussian, Inc.: Pittsburgh, PA, 1996.

(83). Johnson III, R. D., *NIST Computational Chemistry Comparison and Benchmark Database NIST Standard Reference Database Number 101 Release 16a*. August 2013.

(84). Weber, M. E.; Elkind, J. L.; Armentrout, P. B.Kinetic Energy Dependence of $Al^+ + O_2 \rightarrow AlO^+ +$ atomic O. *J. Chem. Phys.* **1986,** *84*, 1521-1529.

(85). Armentrout, P. B.,Periodic Trends in the Reactions of Atomic Ions with Molecular Hydrogen. *Int. Rev. Phys. Chem.* **1990,** *9*, 115-148.

(86). Burley, J. D.; Ervin, K. M.; Armentrout, P. B.Translational Energy Dependence of $O^+(^4S) + H_2(D_2, HD) \rightarrow OH^+(OD^+) + H(D)$ from Thermal to 30 eV c.m. *Int. J. Mass Spectrom. Ion Proc.* **1987,** *80*, 153-175.

(87). Armentrout, P. B.,Isotope Effects in the Reactions of Atomic Ions with H_2, D_2, and HD. *ACS Symp. Series* **1992,** *502*, 194-209.

(88). Blaise, J.; Wyart, J.-F. Selected Constants, Energy Levels, and Atomic Spectra of Actinides. http://web2.lac.u-psud.fr/lac/Database/Contents.html (acessed 2/9/2015)

(89). Sansonetti, J. E.; Martin, W. C.Handbook of Basic Atomic Spectroscopic Data. *J. Phys. Chem. Ref. Data* **2005,** *34*, 1559-2259.

(90). Garcia, M. A.; Morse, M. D.Resonant Two-Photon Ionization Spectroscopy of Jet-Cooled OsN: 520–418 nm. *J. Chem. Phys.* **2011,** *135*, 114304.

(91). Armentrout, P. B.,The Bond Energy of ReO^+: Guided Ion-Beam and Theoretical Studies of the Reaction of Re^+ (^7S) with O_2. *J. Chem. Phys.* **2013,** *139*, 084305.

(92). Armentrout, P. B.; Li, F.-X.Bond Energy of IrO^+: Guided Ion-Beam and Theoretical Studies of the Reaction of Ir+ (^5F) with O_2. *J. Phys. Chem. A* **2013,** *117*, 7754-7766.

(93). Armentrout, P. B.; Parke, L.; Hinton, C.; Citir, M.Activation of Methane by Os+: Guided-Ion-Beam and Theoretical Studies. *ChemPlusChem* **2013,** *78*, 1157-1173.

(94). Lefebvre-Brion, H.; Field, R. W., *The Spectra And Dynamics of Diatomic Molecules*. Elsevier: Amsterdam, 2004.

(95). *DIRAC, A Relativistic Ab Initio Electronic Structure Program, Release DIRAC14 (2014)*, written by T. Saue, L. V., H. J. Aa. Jensen, and R. Bast, with contributions from V. Bakken, K. G. Dyall, S. Dubillard, U. Ekström, E. Eliav, T. Enevoldsen, E. Faßhauer, T. Fleig, O. Fossgaard, A. S. P. Gomes, T. Helgaker, J. Henriksson, M. Iliaš, Ch. R. Jacob, S. Knecht, S. Komorovský, O. Kullie, C. V. Larsen, J. K. Lærdahl, Y. S. Lee, H. S. Nataraj, P. Norman, G. Olejniczak, J. Olsen, Y. C. Park, J. K. Pedersen, M. Pernpointner, R. di Remigio, K. Ruud, P. Sałek, B. Schimmelpfennig, J. Sikkema, A. J. Thorvaldsen, J. Thyssen, J. van Stralen, S. Villaume, O. Visser, T. Winther, and S. Yamamoto (see http://www.diracprogram.org).

(96). Dyall, K. G.,Relativistic Double-Zeta, Triple-Zeta, and Quadruple-Zeta Basis Aets for the Actinides Ac-Lr. *Theor. Chem. Acc.* **2007,** *117*, 491-500.

(97). Gaunt, J. A.,The Triplets of Helium. *Proc. R. Soc. London, Ser. A* **1929,** *1 22*, 513-532.

(98). Ohanessian, G.; Brusich, M. J.; Goddard III, W. A.Theoretical Study of Transition-metal Hydrides. 5. HfH^+ through HgH^+, BaH^+, and LaH^+. *J. Am. Chem. Soc.* **1990,** *112*, 7179-7189.

(99). Meyer, E. R.; Bohn, J. L.; Deskevich, M. P.Candidate Molecular Ions for an Electron Electric Dipole Moment Experiment. *Phys. Rev. A: At., Mol., Opt. Phys.* **2006,** *73*, 062108.

(100). Souter, P. F.; Kushto, G. P.; Andrews, L.; Neurock, M.Experimental and Theoretical Evidence for the Isolation of Thorium Hydride Molecules in Argon Matrixes. *J. Phys. Chem. A* **1997,** *101*, 1287-1291.

(101). Zhang, X.-G.; Liyanage, R.; Armentrout, P. B.The Potential Energy Surface for Activation of Methane by Pt^+: A Detailed Guided-Ion Beam Study. *J. Am. Chem. Soc.* **2001,** *123*, 5563-5575.

(102). Armentrout, M. M.; Li, F.-X.; Armentrout, P. B.Is Spin Conserved in Heavy Metal Systems? Experimental and Theoretical Studies of the Reaction of Re+ with Methane. *J. Phys. Chem. A* **2004,** *108*, 9660-9672.

(103). Armentrout, P. B.,Activation of CH_4 by Gas-Phase Mo^+ and the Thermochemistry of Mo-Ligand Complexes. *J. Phys. Chem. A* **2006,** *110*, 8327-8338.

(104). Li, F.-X.; Zhang, X.-G.; Armentrout, P. B.The Most Reactive Third-row Transition Metal: Guided Ion Beam and Theoretical Studies of the Activation of Methane by Ir^+. *Int. J. Mass Spectrom.* **2006,** *255/256*, 279-300.

(105). Zhang, X.; Schwarz, H.Bonding in Cationic MCH_2^+ (M=K–La, Hf–Rn): A Theoretical Study on Periodic Trends. *Chem. Eur. J.* **2010,** *16*, 5882 – 5888.

(106). Pettersson, L. G. M.; Bauschlicher, C. W., Jr.; Langhoff, S. R.; Partridge, H.Positive Ions of the First- and Second-row Transition Metal Hydrides. *J. Chem. Phys.* **1987,** *87*, 481-492.

(107). Carter, E. A.; Goddard, W. A., IIIRelationships Between Bond Energies in Coordinatively Unsaturated and Coordinatively Saturated Transition-Metal Complexes: a Quantitative Guide for Single, Double, and Triple bonds. *J. Phys. Chem.* **1988,** *92*, 5679-5683.

(108). Berkowitz, J.; Ellison, G. B.; Gutman, D.Three Methods to Measure RH Bond Energies. *J. Phys. Chem.* **1994,** *98*, 2744-2765.

(109). Frenkel, M. M., K.N.; Wilhoit, R.C.; Kabo, G.J.; Roganov, G.N., *Thermodynamics of Organic Compounds in the Gas State*. Thermodynamics Research Center: College Station, TX, 1994.

(110). Dyke, J.; Ellis, A.; Jonathan, N.; Morris, A.Vacuum Ultraviolet Photoelectron Spectroscopy of Transient Species. Part 18. The Cyclopropyl, Isopropyl, and n-Propyl Radicals. *J. Chem. Soc., Faraday Trans. 2* **1985,** *81*, 1573-1586.

(111). Steinhaus, D. W.; Radziemski, L. J., Jr.; Cowan, R. D. *Current Status of the Analysis of the Optical Spectra of Uranium*; Univ. California: 1971; pp 151-163.

(112). Worden, E. F.; Carlson, L. R.; Johnson, S. A.; Paisner, J. A.; Solarz, R. W.Ionization Potential of Neutral Atomic Plutonium Determined by Laser Spectroscopy. *J. Opt. Soc. Am. B* **1993,** *10*, 1998-2005.

(113). Lau, K. H.; Brittain, R. D.; Hildenbrand, D. L.High Temperature Thermodynamic Studies of Some Gaseous Thorium Fluorides. *J. Chem. Phys.* **1989,** *90*, 1158-1164.

(114). Hildenbrand, D. L.; Lau, K. H.Redetermination of the Thermochemistry of Gaseous Uranium Fluorides (UF_5, UF_2, and UF). *J. Chem. Phys.* **1991,** *94*, 1420-1425.

(115). Kent, R. A.,Mass Spectrometric Studies of Plutonium Compounds at High Temperatures. II. Enthalpy of Sublimation of Plutonium(III) Fluoride and the Dissociation Energy of Plutonium(I) Fluoride. *J. Amer. Chem. Soc.* **1968,** *90*, 5657-5659.

Table 5.1. Fitting parameters for the indicated cross section using Eq. (5.1).

Reaction	n	σ_0	E_0 (eV)	$D_0(Th^+\text{-}H)^a$
$Th^+ + H_2 \rightarrow ThH^+ + H$	1.3 ± 0.3	7.6 ± 1.3	2.18 ± 0.12	2.30 ± 0.12
$Th^+ + D_2 \rightarrow ThD^+ + D$	1.4 ± 0.1	4.6 ± 0.6	2.02 ± 0.05	2.51 ± 0.05
$Th^+ + HD \rightarrow ThH^+ + D$	1.4 ± 0.1	2.2 ± 0.2	2.15 ± 0.06	2.36 ± 0.06
$Th^+ + HD \rightarrow ThD^+ + H$	1.2 ± 0.1	1.3 ± 0.2	2.13 ± 0.19	2.35 ± 0.19

[a] Values derived from reactions forming ThD^+ include a zero-point energy correction of -0.03 eV.

Table 5.2. Comparison of theoretically computed excited-state energies (eV) to experimental values.[a]

Th^+	Experimental[b]	CCSD(T)	B3LYP	B3PW91	BHLYP	M06	PBE0
^2D ($6d7s^2$)[c]	**0.00**	**0.00** (**0.00**)	0.06 (0.12)	**0.00** (**0.00**)	**0.00** (**0.00**)	0.73	**0.00** (**0.00**)
^4F ($6d^27s$)	0.06	0.16 (0.13)	0.26 (0.13)	0.04 (0.08)	0.19 (0.19)	1.39	0.04 (0.02)
^2F ($5f7s^2$)	0.43	0.57	**0.00** (**0.00**[d])	0.15	0.32	**0.00**	0.20
^4H ($5f6d7s$)	0.67	1.17	0.45	0.29	0.74	1.24	0.36
^4F ($6d^3$)	0.81	0.98	1.04	0.73	0.93	1.81	0.72

[a] Calculated using cc-pwCVQZ-PP-MDF basis set. Values in parentheses calculated using the cc-pwCVQZ-DK3 all-electron basis set. Bolded values highlight the ground-state.
[b] Experimental energies are averaged over all spin-orbit levels and are taken from Refs. 88 and 89. Also see Supporting Information of Ref. 30.
[c] Significant spin contamination, s(s+1) ~ 1.5.
[d] Significant spin contamination, s(s+1) = 1.09.

Table 5.3. Molecular parameters and calculated relative energies (eV) for ground and excited-states of ThH^+.[a]

ThH^+	r(Th^+-H) (Å)[b]	ν (cm^{-1})[b]	CCSD(T)[c]	B3LYP	B3PW91	BHLYP	M06	PBE0
$^3\Delta_1$ ($\sigma^2\sigma\delta$)[d]	1.996	1653	**0.00** (0.05)	**0.00** (**0.00**)	**0.00** (**0.00**)	**0.00** (**0.00**)	0.10 (0.28)	**0.00** (**0.00**)
$^1\Sigma^+$ ($\sigma^2\sigma^2$)	1.946	1592	0.13 (**0.00**)	0.45 (0.27)	0.69 (0.51)	0.46 (0.28)	**0.00** (**0.00**)	0.68 (0.50)
$^3\Pi_0$ ($\sigma^2\sigma\pi$)[e]	2.001	1604	0.38 (0.35)	0.29 (0.20)	0.32 (0.23)	0.35 (0.26)	0.27 (0.36)	0.33 (0.24)
$^3\Phi_2$ ($\sigma^2\delta\pi$)[f]	2.032	1491	0.61 (0.75)	0.63 (0.72)	0.57 (0.66)	0.61 (0.70)	0.44 (0.71)	0.57 (0.66)
$^3\Sigma^-$ ($\sigma^2\delta^2$)	2.029	1547	0.96 (0.83)	1.03 (0.85)	0.98 (0.80)	1.04 (0.86)	0.97 (0.97)	0.97 (0.79)
$^3\Sigma^-$ ($\sigma^2\pi^2$)	2.014	1509	1.11(0.98)	1.21 (1.03)	1.10 (0.92)	1.17 (0.99)	0.98 (0.98)	1.09 (0.91)

[a] Structures optimized using cc-pwCVQZ-PP-MDF/aug-cc-pVQZ at the respective level of theory (except CCSD(T)) relative to the ground-level (state) with the ground-level (state) bolded. Values include spin-orbit correction to the lowest level of each state where applicable. Values in parentheses do not include spin-orbit corrections.
[b] From B3LYP/ cc-pwCVQZ-PP-MDF/aug-cc-pVQZ optimized structures. Frequencies scaled by 0.989.
[c] Single-point energy from B3LYP/ cc-pwCVQZ-PP-MDF/aug-cc-pVQZ optimized structures.
[d] Includes spin-orbit correction of -0.18 eV.
[e] Includes spin-orbit correction of -0.09 eV.
[f] Includes spin-orbit correction of -0.27 eV.

Table 5.4. Theoretical BDEs (in eV) of ThH^+.[a]

Basis Set	CCSD(T)[b,c]	B3LYP[c]	B3PW91[c]	BHLYP[c]	M06[d]	PBE0[c]
SDD-VDZ-MWB/6-311+G(3p)	2.42	2.88	2.91	2.73	2.69	2.83
Seg. SDD-VQZ-MWB/6-311+G(3p)	2.57	2.94	2.96	2.77	2.74	2.89
ANO-VQZ-MWB/6-311+G(3p)	2.57	2.92	2.95	2.75	2.72	2.87
ANO-VQZ-MDF/6-311+G(3p)	3.43	2.92	2.94	2.77	2.73	2.87
cc-pwCVQZ-PP-MDF/aug-cc-pVQZ	2.71	2.89	2.91	2.75	2.73	2.84
cc-pwCVTZ-PP-MDF/cc-pVTZ	2.64	2.89	2.91	2.75	2.71	2.85
cc-pwCVQZ-PP-MDF/cc-pVQZ	2.69	2.89	2.91	2.75	2.72	2.84
CBS-cc-pwCVXZ-MDF[e]	2.72	2.89	2.91	2.75	2.72	2.84
cc-pVTZ-DK3/cc-pVTZ[f]	2.74	2.78	2.87	2.75		2.85
cc-pVQZ-DK3/cc-pVQZ[f]	2.80	2.79	2.87	2.75		2.86
CBS-cc-pVXZ-DK3[e]	2.83	2.79	2.87	2.75		2.85
cc-pwCVTZ-DK3/cc-pVTZ[f]	2.64	2.90	2.87	2.75		2.85
cc-pwCVQZ-DK3/cc-pVQZ[f]	2.69	2.90	2.87	2.75		2.85
CBS-cc-pwCVXZ-DK3[e]	2.72	2.90	2.88	2.75		2.85

Table 5.4 Continued

[a] Calculated from structures optimized using the indicated basis sets (Th^+ basis set – ECP/H basis set) at the respective level of theory (except for CCSD(T) and all-electron calculations) relative to H + Th^+. Values include spin-orbit correction of the difference between the ^2D state averaged over all spin-orbit states and the $^4F_{3/2}$ ground-level (-0.40 eV).
[b] Single-point energy using B3LYP optimized structures.
[c] ThH^+ ($^3\Delta_1$). Include spin-orbit stabilization energy of the $^3\Delta_1$ level (0.18 eV).
[d] ThH^+ ($^1\Sigma^+$).
[e] Complete basis set limit extrapolated from correlation consistent basis sets using the extrapolation technique described in the text.
[f] Single-point energy from B3LYP/cc-pwCVQZ-PP-MDF/aug-cc-pVQZ optimized structure.

Table 5.5: Calculated molecular parameters and relative energies (eV) for ground and excited-states of $HThH^+$.[a]

state	configuration	r(Th^+-H) (Å)[b]	∠HThH (°)[b]	CCSD(T)	B3LYP	B3PW91	BHLYP	M06	PBE0
$^2A_1$	$(1a_1)^2(1b_2)^2(2a_1)^1$	1.995	102.3	0.00	0.00	0.00	0.00	0.00	0.00
				(-1.47)	(-1.62)	(-1.70)	(-1.51)	(-1.59)	(-1.72)
$^2B_1$	$(1a_1)^2(1b_2)^2(1b_1)^1$	2.021	103.5	0.35	0.29	0.25	0.29	0.11	0.26
$^2A_2$	$(1a_1)^2(1b_2)^2(1a_2)^1$	2.017	90.7	0.48	0.40	0.38	0.44	0.18	0.39
$^2B_2$	$(1a_1)^2(1b_2)^2(2b_2)^1$	2.051	95.1	1.30	0.78	0.75	1.02	0.43	0.80
$^4A_2$	$(1a_1)^2(1b_2)^1(2a_1)^1(1b_1)^1$	2.160	169.1	2.93	2.77	2.75	2.89	3.13	2.76
		2.302	*20.0*	*1.22*	*1.36*	*1.23*	*1.38*	*1.49*	*1.22*
$^4B_2$	$(1a_1)^2(1b_2)^1(2a_1)^1(3a_1)^1$	2.160	169.1	2.93	2.77	2.76	2.89	3.12	2.76
		2.334	*19.8*	*1.25*	*1.34*	*1.20*	*1.34*	*1.52*	*1.19*
$^4B_1$	$(1a_1)^2(1b_2)^1(1a_2)^1(2a_1)^1$	2.108	169.9	2.98	3.05	2.99	3.22	3.16	2.79
		2.327	*19.9*	*1.33*	*1.33*	*1.19*	*1.34*	*1.51*	*1.18*
$^4A''$[c]		2.160	180.0	2.93	2.77	2.76	2.89	3.12	2.76
$^4A_1$	$(1a_1)^2(1b_2)^1(2a_1)^1(2b_2)^1$	*2.349*	*19.8*	*2.30*	*1.79*	*1.71*	*2.03*	*1.78*	*1.74*
$^4A_2$	$(1a_1)^2(1b_2)^1(1a_2)^1(2b_2)^1$	2.093	170.1	3.52	3.69	3.48	3.83	3.54	3.46
		2.318	*20.5*	*2.95*	*2.45*	*2.26*	*2.63*	*2.34*	*2.29*

Table 5.5 Continued

[a] Single-point energies of B3LYP/cc-pwCVQZ-PP-MDF/aug-cc-pVQZ optimized structures. Values in parentheses are relative to Th^+ (^2D) + H_2. Values in italics distinguish minima found at small ∠HThH angles along the indicated diabatic potential energy surface.
[b] From B3LYP/cc-pwCVQZ-PP-MDF/aug-cc-pVQZ optimized structures.
[c] $^4A_1$ state collapses to $^4A'$ at large angles. See text.

Table 5.6. Estimation of AnL^+ bond dissociation energies (eV) from An^+ electronic parameters.[a]

An^+		$D_0(An^+-F)$		$D_0(An^+-CH_3)$		$D_0(An^+-H)$	
Ground config.[b]	Promotion Energy[b]	Experimental	Estimate	Experimental	Estimate	Experimental	Estimate
Ac^+ ($7s^2$)	0.59 (6d7s)		6.04		2.01		1.86
Th^+ ($6d^27s$)	0.00 ($6d^27s$)	6.63 ± 0.10[c]	6.63	2.60 ± 0.30[d]	2.60	2.45 ± 0.07	2.45
Pa^+ ($5f^27s^2$)	0.10 ($5f^26d7s$)		6.53	$\geq 0.29 \pm 0.30$[e]	2.50		2.35
U^+ ($5f^37s^2$)	0.04 ($5f^36d7s$)	6.57 ± 0.10[f]	6.59	$\geq 1.29 \pm 0.10$[e]	2.56	2.9 ± 0.1[g]	2.41
Np^+ ($5f^46d7s$)	0.00 ($5f^46d7s$)		6.63	$\geq 0.34 \pm 0.30$[e]	2.60		2.45
Pu^+ ($5f^67s$)	1.08 ($5f^56d7s$)	5.40 ± 0.34[h]	5.55	$\geq 0.69 \pm 0.10$[e]	1.52	$\geq 0.37 \pm 0.10$[e]	1.37
Am^+ ($5f^77s$)	1.76 ($5f^76d$)		4.87		0.84		0.69
Cm^+ ($5f^77s^2$)	0.50 ($5f^76d7s$)		6.13		2.10		1.95

Table 5.6 Continued

[a] Estimate of AnL^+ BDEs using ThL^+ BDEs as an estimate of the intrinsic AnL^+ BDE, i.e., $D_0(An^+\text{-}L) = D_0(Th^+\text{-}L) - E_P(An^+)$. See text.
[b] Promotion energy defined as the difference in energy between the ground-level and the lowest lying level with the indicated electronic configuration. Energy levels and configurations from Refs. 88 and 89.
[c] Calculated from $D_0(Th\text{-}F) = 6.72 \pm 0.10$ eV,[113] IE(Th) = 6.3067 eV,[89] and IE(ThF) = 6.3953 ± 0.0004 eV.[31]
[d] Ref. 30.
[e] Lower limits derived from results of ICR reaction $An^{2+} + C_3H_8$ from Ref. 18 using Eq. 5.11 (or analogous equation). Hydrocarbon BDEs and IEs from Ref. 83. IEs for U^+ and Pu^+ from Ref. 89. Other $IE(An^{2+})$ from Ref. 9.
[f] Calculated from $D_0(U\text{-}F) = 6.72 \pm 0.10$ eV,[114] IE(U) = 6.1941 eV,[89] and IE(UF) = 6.34159 ± 0.00006 eV.[31]
[g] Ref. 10.
[h] Calculated from $D_0(Pu\text{-}F) = 5.35 \pm 0.30$ eV[115] and IE(Pu) = 6.026 eV.[89] Ionization energy of PuF estimated as IE(PuF) = 6.26 eV. See text.

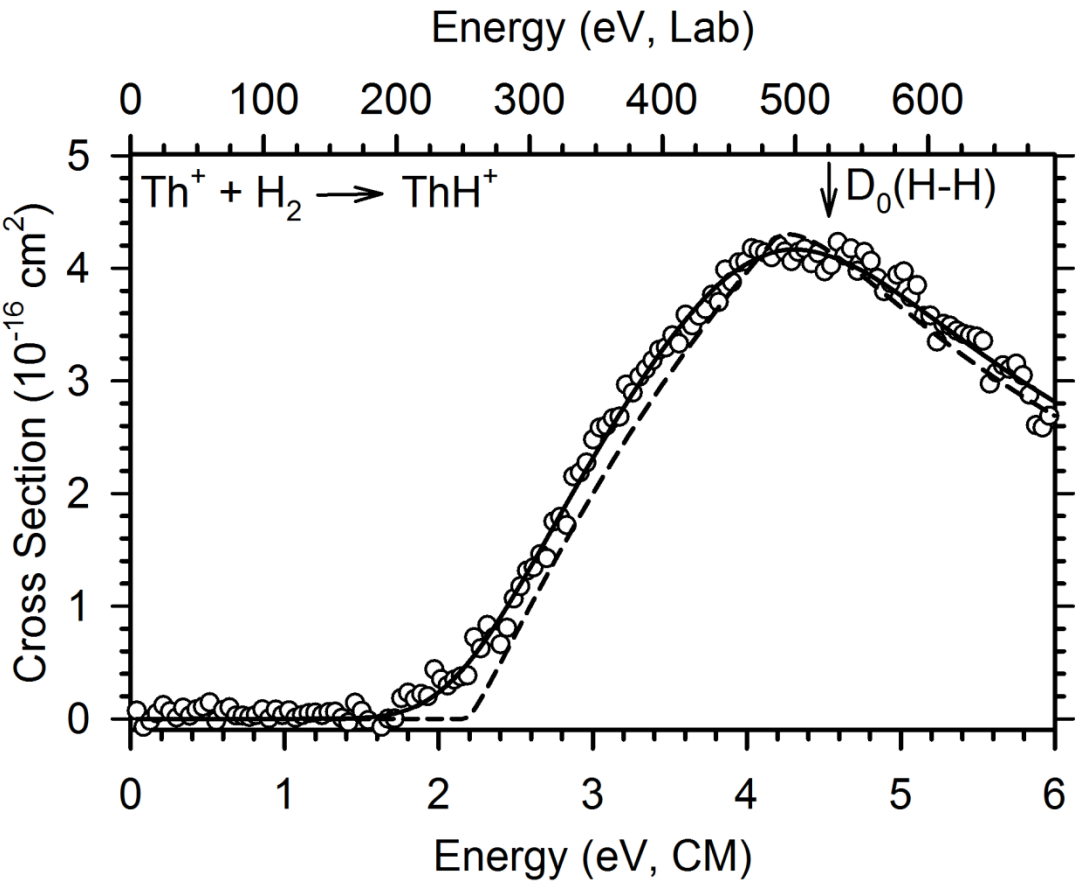

Figure 5.1. Cross sections for the reaction between Th^+ and H_2 as a function of energy in the center-of-mass (lower x-axis) and laboratory (upper x-axis) frames. The model of Eq. (5.1) with parameters from Table 5.1 is shown as a dashed line. This model convoluted over the kinetic energy and internal energy distributions of the reactants is shown as a solid line. The arrow indicates D_0(H-H) = 4.478 eV.

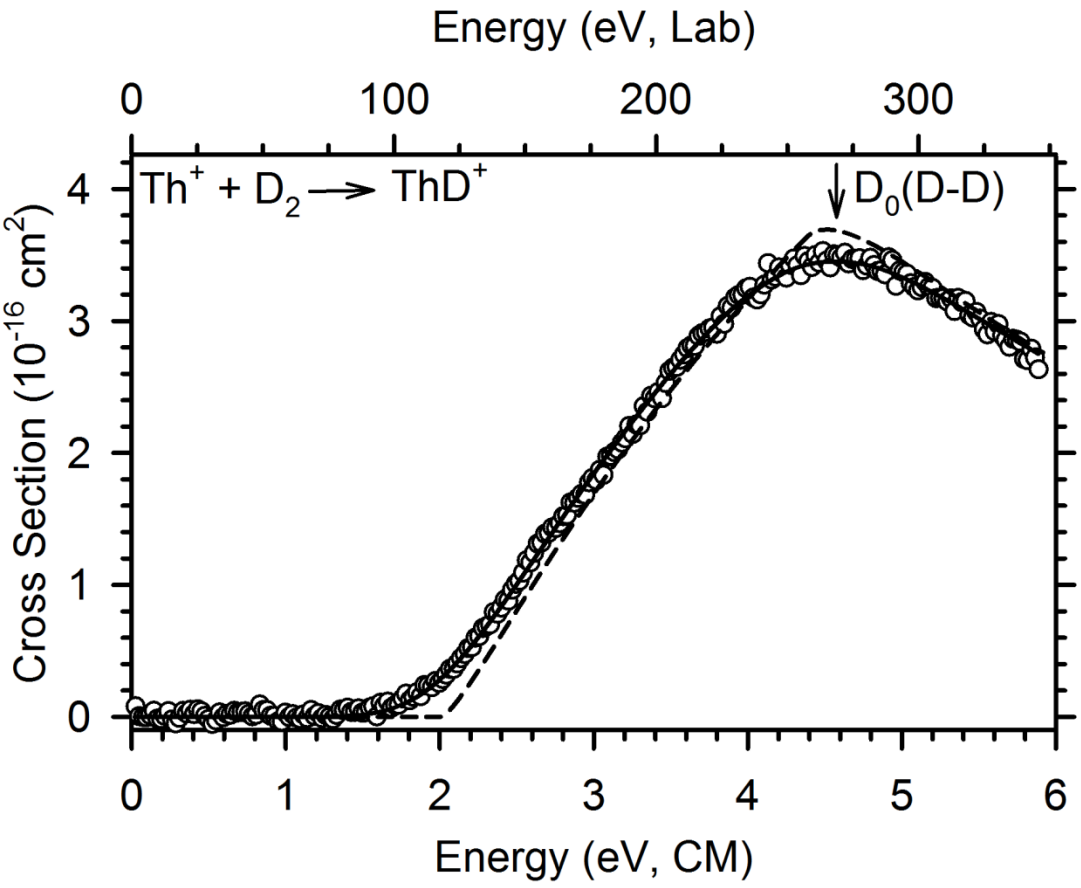

Figure 5.2. Cross sections for the reaction between Th^+ and D_2 as a function of energy in the center-of-mass (lower x-axis) and laboratory (upper x-axis) frames. The model of Eq. (5.1) with parameters from Table 5.1 is shown as a dashed line. This model convoluted over the kinetic energy and internal energy distributions of the reactants is shown as a solid line. The arrow indicates D_0(D-D) = 4.556 eV.

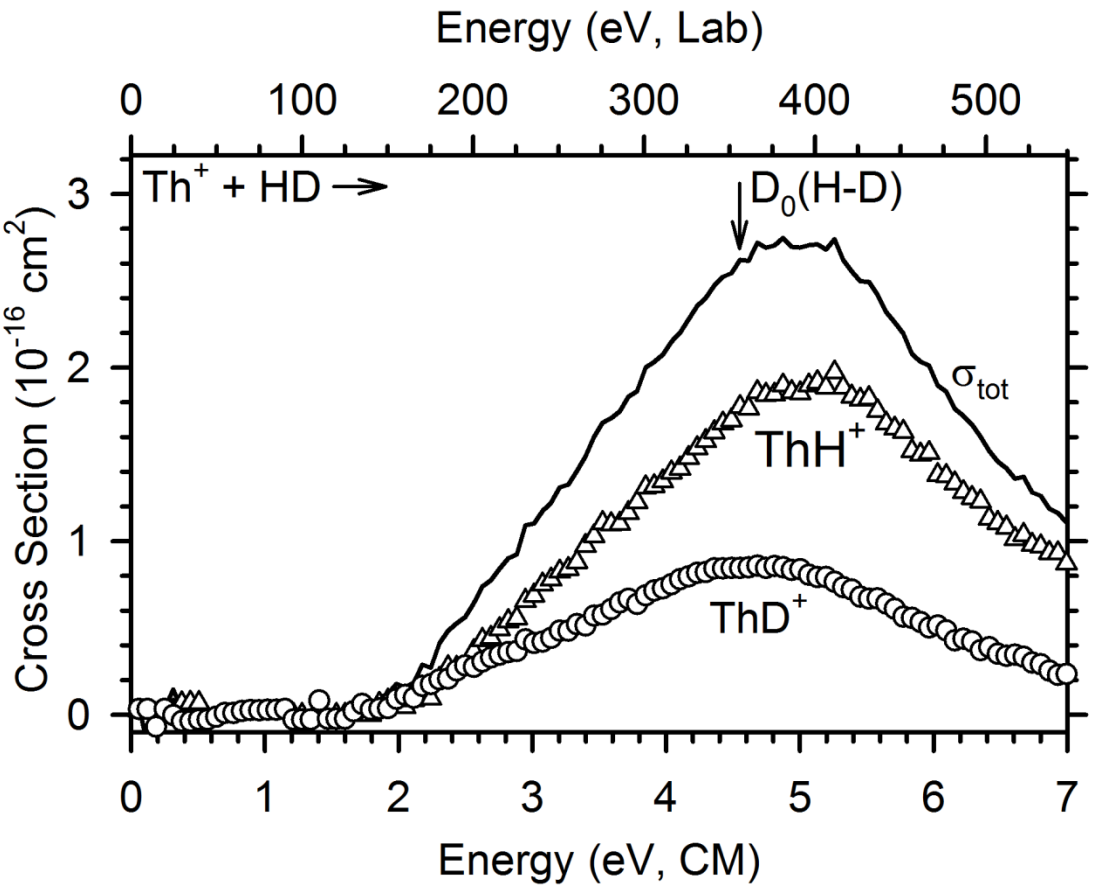

Figure 5.3. Cross sections for the reaction between Th^+ and HD as a function of energy in the center-of-mass (lower x-axis) and laboratory (upper x-axis) frames. The arrow indicates D_0(H-D) = 4.514 eV.

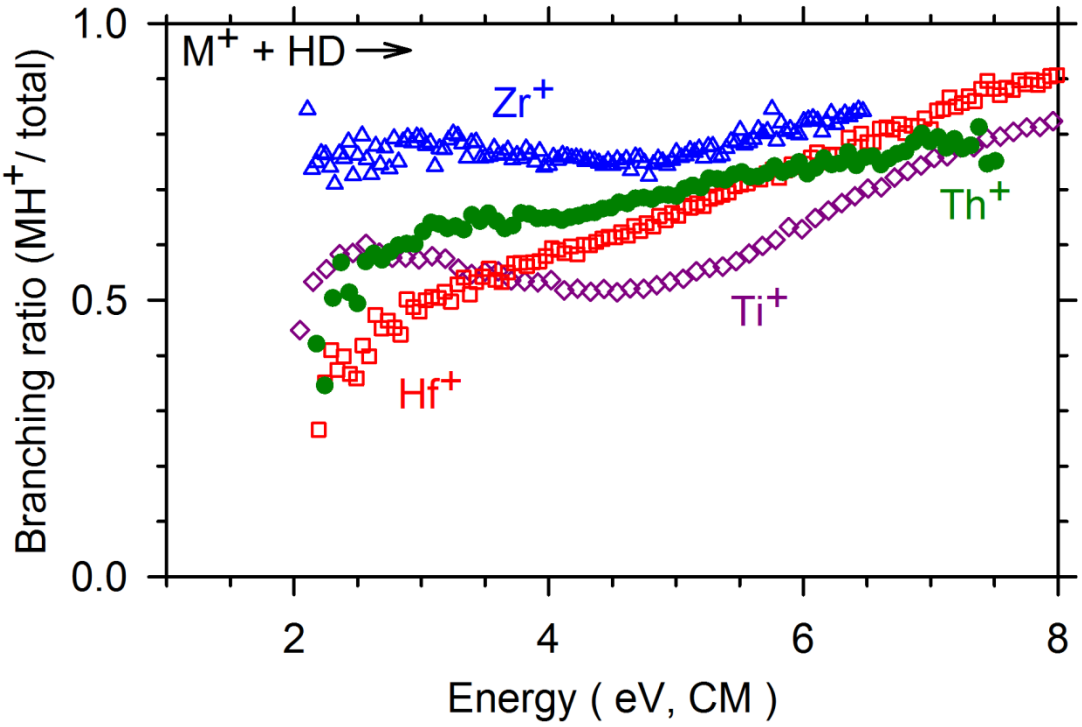

Figure 5.4. Product branching fractions ($\sigma_{MH+}/\sigma_{Total}$) for reactions of Ti^+ (open purple diamonds), Zr^+ (open blue triangles), Hf^+ (open red squares), and Th^+ (solid green circles) with HD as a function of kinetic energy in the CM frame.

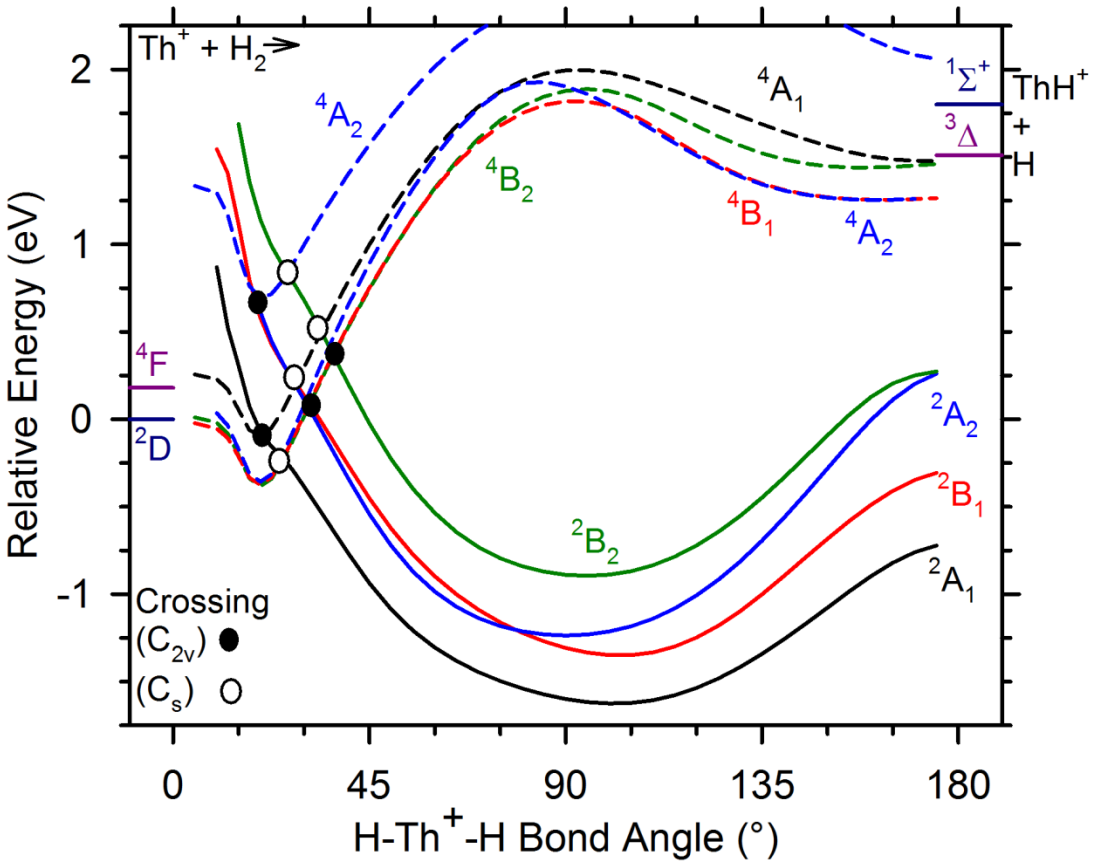

Figure 5.5. B3LYP/Seg. SDD-VQZ-MWB/6-311+(3p) relaxed potential energy surface scan calculations of the $Th^+ + H_2$ reaction in C_{2v} symmetry as a function of ∠HTh$^+$H in degrees. The energies are relative to Th^+ (^{2}D, *6d7s*^{2}) + H_2. Doublet surfaces are represented by solid lines and quartet surfaces by dashed lines.

CHAPTER 6

BOND ENERGIES OF ThO^+ AND ThC^+: A GUIDED ION BEAM AND QUANTUM CHEMICAL INVESTIGATION OF THE REACTIONS OF THORIUM CATION WITH O_2 AND CO

Richard M Cox, Murat Citir, P. B. Armentrout,

Samuel R. Battey, Kirk A. Peterson

Abstract

Kinetic energy dependent reactions of Th^+ with O_2 and CO are studied using a guided ion beam tandem mass spectrometer. The formation of ThO^+ in the reaction of Th^+ with O_2 is observed to be exothermic and barrierless with a reaction efficiency at low energies of k/k_{col} = 1.12 ± 0.22, similar to the efficiency observed in ion cyclotron resonance experiments. Formation of ThO^+ and ThC^+ in the reaction of Th^+ with CO is endothermic in both cases. The kinetic energy dependent cross sections for formation of these product ions were evaluated to determine 0 K bond dissociation energies (BDEs) of $D_0(Th^+\text{-}O)$ = 8.51 ± 0.16 eV and $D_0(Th^+\text{-}C)$ = 4.82 ± 0.29 eV. The present value of $D_0(Th^+\text{-}O)$ is within experimental uncertainty of previously reported experimental values,

whereas this is the first report of $D_0(Th^+\text{-}C)$. Both BDEs are observed to be larger than those of their transition metal congeners, TiL^+, ZrL^+, and HfL^+ (L = O and C), believed to be a result of lanthanide contraction. Additionally, the reactions were explored by quantum chemical calculations where a semiempirical model was used to estimate spin-orbit energy contributions. In general, spin-orbit effects improve the agreement of theoretical results compared to experiment. Finally, the ThO^+ BDE is compared to other actinide (An) oxide cation BDEs and a simple model utilizing An^+ promotion energies to the reactive state is used to estimate AnO^+ and AnC^+ BDEs. For AnO^+, this model yields predictions that are typically within experimental uncertainty and performs better than density functional theory calculations presented previously.

Introduction

Actinides (An) are of interest because of their use in nuclear power and because of national security concerns; however, research is hampered because of the radioactive nature of most members of the actinide series (except Th and U), which make them difficult and potentially dangerous to investigate. For this reason, it is highly desirable to employ theoretical methods to study these systems. In order to evaluate potential basis sets and theoretical methods, key fundamental experimental benchmarks are necessary. Gas-phase studies that are absent solvent effects can provide these benchmarks, and an increasing number of gas-phase studies of actinide systems have been reported.[1-17] These have been accompanied by an increasing number of theoretical reports.[14-26] Several examples of discrepancies between experimental and theoretical results exist,[14, 23-24] such that this field remains in infancy.

Of these studies, oxidation reactions are probably the best studied system. Previously, Marçalo and Gibson[13] have determined that there is a correlation between AnO^{p+} (p = 0 – 2) bond dissociation energies (BDEs) and the promotion energy (E_p) to the lowest level having a $6d^2$ configuration. (Usual ground-state configurations for An are $5f^{n-3}6d7s^2$, and $5f^{n-2}7s^2$ and for An^+ are $5f^{n-2}7s^2$ and $5f^{n-1}7s$.) Th and Th^+ are unique among the actinides because they do not populate the *5f*-orbitals in the ground-state, having $6d^27s^2$ and $6d^27s$ ground-level configurations, respectively. One interesting aspect of these configurations is that they compare directly to transition metal systems that are better understood.

Because of its $6d^2$ ground-state configuration, Th^+ is the most reactive of the actinide series and has been described as oxophilic. Because of this reactivity, it is difficult to make a direct measurement of $D_0(Th^+\text{-}O)$ with thermal methods such as ion cyclotron resonance (ICR) mass spectrometry. Currently, only a lower limit can be established as $D_0(Th^+\text{-}O) \geq D_0(H_2C\text{-}O) = 7.85$ eV by direct measurement on the basis of ICR results.[5] Indirectly, $D_0(Th^+\text{-}O)$ can be established using the thermochemical cycle in Eq. 6.1:

$$D_0(Th^+\text{-}O) = D_0(Th\text{-}O) + IE(Th) - IE(ThO) \qquad (6.1)$$

where the ionization energies IE(Th) = 6.3067 eV[27-28] and IE(ThO) = 6.60242 ± 0.0002 eV[9] are well established. Evaluations of previous thermochemical data by Pedley and Marshall[29] from high-temperature methods such as Knudsen effusion experiments provide $D_0(Th\text{-}O)$,[30-34] but such data is dependent on the free-energy functions (and

molecular parameters used) to scale energies to 0 K values. Choice of parameters can have a large impact on the reported BDE,[29, 32] a thorough discussion of which is presented below.

A unique aspect of guided ion beam tandem mass spectrometry (GIBMS) is the ability to control reactant energies over a large range of kinetic energies, which allows the study of the energy dependences of endothermic reactions to establish direct measurements of key thermodynamic information. Furthermore, no knowledge of product molecular parameters is needed. Accurate experimental determination of such BDEs is critical for establishing reliable benchmarks to which theoretical methods can be evaluated. Previously, MO^+ BDEs have successfully been measured using this technique for first,[35-38] second,[39-40] and third[41-44] row transition metals. Here we present the absolute kinetic energy dependent cross sections of the reactions of Th^+ with O_2 and CO measured using GIBMS and analyze these to determine $D_0(Th^+\text{-}O)$ and $D_0(Th^+\text{-}C)$. We also compare theoretically derived BDEs to these experimental benchmarks and discuss what implications knowledge of Th^+ thermochemical values has for the An^+ series.

Literature Thermochemistry Review

The thermochemistry of ThO^{n+} (n = 0, 1) is seemingly well established. Pedley and Marshall[29] reevaluated data primarily from Ackermann and Rau,[30-31] Hildenbrand and Murad,[32] and Murad and Hildenbrand[33] and established $D_0(Th\text{-}O) = 9.06 \pm 0.12_5$ eV. (Pedley and Marshall cite values of 9.08 ± 0.11 eV, 9.04 ± 0.03 eV and 9.09 ± 0.15 eV,[30] 9.09 ± 0.17 eV and 9.06 ± 0.17 eV,[31] 8.97 ± 0.20 eV and 9.08 ± 0.20 eV,[32] and 9.06 ± 0.11 eV.[33]) Originally, Ackermmann and Rau reported $D_0(Th\text{-}O) \leq 8.3$ eV[30] in weight

loss experiments and D_0(Th-O) = 9.0 ± 0.1 eV in Knudsen cell effusion experiments,[31] and Hildenbrand and Murad reported D_0(Th-O) = 8.79 ± 0.13 eV.[32] Because all data were extrapolated from high-temperature regimes, both Pedley and Marshall and Hildenbrand and Murad caution that significant errors can occur in the use of free-energy functions because of poorly established molecular parameters.[29, 32] In this case, errors are plausible because the parameters used by Pedley and Marshall list a $^3\Delta$ first excited-state with all spin-orbit levels at ~5000 cm^{-1} above the ground-state (presumably on the basis of work by Edvinsson[45]). In earlier work, Huber and Herzberg[46] identify the same state as $^1\Phi$. A more recent compilation[47] of experimental data identifies the state as $^3\Delta$ but with levels found at 5317, 6128, and 8600 cm^{-1} above the ground-level. This compilation agrees with theoretical work by Paulovic et al.[47] and Küchle et al.[48]

The Gas-phase Ion and Neutral Thermochemistry (GIANT) compilation[49] references Pedley and Marshall but extrapolates to 0 K differently so that D_0(Th-O) = 9.04 ± 0.11 eV. Marçalo and Gibson later adopt the value of Pedley and Marshall, but list the uncertainty as two standard deviations of the mean, D_0(Th-O) = 9.06 ± 0.25 eV.[13] Most recently, Konings et al.[50] evaluated the previously reported values of the ThO BDE and concluded D_0(Th-O) = 9.00 ± 0.10 eV (we report the uncertainty as 2 standard deviations of the mean), where the Ackermann and Rau[30] values are excluded for reasons unstated and an additional value of D_0(Th-O) = 8.89 ± 0.17 eV reported by Neubert and Zmbov[34] is used. A weighted average of the values originally reported by their respective authors (9.0 ± 0.1 eV,[31] 8.79 ± 0.13 eV,[32] and 8.89 ± 0.17 eV[34]) excluding the upper limit (≤ 8.3 eV[30]) yields D_0(Th-O) = 8.92 ± 0.14 eV, where the uncertainty is two standard deviations of the mean.

In general, reports of ThO^+ BDEs have been derived using Eq. 6.1. Data found in the GIANT compilation lead to a BDE of $D_0(Th^+\text{-}O) = 9.03 \pm 0.14$ eV,[49] but these data utilize older values of IE(Th) = 6.08 eV[51] and IE(ThO) = 6.1 ± 0.1 eV[52] (electron impact). More recent spectroscopic determinations of these values are IE(Th) = 6.3067 eV[27-28] and IE(ThO) = 6.60242 ± 0.0002 eV.[10] Using the updated IEs, a value of 8.74 ± 0.14 eV can be established from the GIANT tables D_0(Th-O) and Eq. 6.1. Marçalo and Gibson[13] report $D_0(Th^+\text{-}O) = 8.74 \pm 0.25$ eV on the basis of the Pedley and Marshall neutral BDE and the spectroscopic IEs. A value of $D_0(Th^+\text{-}O) = 8.70 \pm 0.10$ eV can be derived using Eq. 6.1 with the neutral BDE value reported by Konings et al.[50] Finally, a value of $D_0(Th^+\text{-}O) = 8.62 \pm 0.14$ eV can be derived from the weighted average of the original reports of D_0(Th-O). All values are consistent with the lower limit established in ICR studies, $D_0(Th^+\text{-}O) \geq D_0(H_2C\text{-}O) = 7.85$ eV.[5]

Unlike ThO, the thermochemistry of ThC^{p+} (p = 0, 1) is much less well established. The only report of the ThC BDE is D_{298}(Th-C) = 4.70 ± 0.18 eV determined in Knudsen cell effusion experiments.[53] An electron impact ionization energy of IE(ThC) = 7.9 ± 1.0 eV was reported in the same study and is similar to a prior value of 8.0 ± 0.1 eV.[54] Neglecting the difference between the 298 and 0 K BDEs, $D_0(Th^+\text{-}C) = 3.1 \pm 1.0$ eV can be determined using Eq. 6.1 and the lower IE value. This value is probably best expressed as a lower limit for reasons discussed below.

Experimental and Theoretical Methods

Instrument

The GIBMS used in these experiments has been described in detail previously.[55] Briefly, ions are created in a direct current discharge/flow tube source (DC/FT) described in more detail below.[56] After creation, ions are focused through a magnetic momentum analyzer where the reactant Th^+ ion beam is mass selected. These ions are decelerated to a well-defined kinetic energy and passed into a radio frequency (rf) octopole ion guide[57-58] that constrains the ions radially. The octopole passes through a static pressure reaction cell that contains the neutral reaction partner (O_2 or CO). To ensure that the probability of multiple collisions between Th^+ and the neutral gas is sufficiently small, the pressure in the reaction cell is maintained at typical pressures of 0.10 – 0.40 mTorr. Independent measurements at several pressures are performed to ensure that cross sections are independent of neutral reactant pressures. Reaction cross sections are calculated from product ion intensities relative to reactant ion intensities after correcting for background ion intensities measured when the neutral gas is no longer directed into the gas cell.[59] Uncertainties in the calculated absolute cross section are estimated to be ±20 %, with relative uncertainties of ±5%.

Laboratory ion energies (lab) are converted to the center-of-mass frame (CM) using the relationship $E_{CM} = E_{lab} \times m/(m + M)$, where m and M are the masses of the neutral reactant and ion, respectively. At very low energies, the conversion includes a correction for the truncation of the ion kinetic energy distribution, as described previously.[59] Cross sections are known to be broadened by the kinetic energy distribution of the reactant ions and the thermal (300 K) motion of the neutral reactant.[60] The absolute

zero of energy and the full width at half-maximum (fwhm) of the ion beam are determined by using the octopole guide as a retarding potential analyzer.[59] Typical fwhms of the energy distribution for these experiments were 0.4 - 0.6 eV (lab). Uncertainties in the absolute energy scale are 0.1 eV (lab). All energies reported below are in the CM frame.

Ion Source

The DC/FT source has been described in detail previously.[56] Briefly, a cathode containing the thorium powder sample (^{232}Th, 100% abundance) is held at ~2.5 kV. The resultant electric field ionizes Ar gas, which flows over the cathode in a 9:1 He/Ar mixture. The ionized Ar collides with the cathode and Th^+ ions are sputtered off and swept into the flow tube by the He/Ar flow at typical pressures of 0.3 – 0.4 Torr. In the flow tube, ions thermalize by ~10^5 collisions with carrier gas. In this work and previous work[16-17] with Th^+, there is no evidence of excited-state species. Previous experiments[61-65] utilizing the DC/FT source with transition metal ions have indicated that the internal temperature of ions generated is 300 – 1100 K. A population analysis at 300 K indicates that 99.89% of Th^+ is in its ground-level ($^4F_{3/2}$, $6d^2 7s$), whereas at 1100 K, 76 % is in the ground-level.[28, 66] Conservatively, we estimate the internal temperature to be 700 ± 400 K, where Th^+ has an average electronic energy of E_{el} = 0.02 ± 0.03 eV. This energy is incorporated into all threshold and bond dissociation energies reported here.

Data Analysis

The kinetic energy dependence of endothermic reactions is modeled using Eq. 6.2,[58, 67-68]

$$\sigma(E) = \sigma_0 \Sigma\, g_i\, (E + E_{el} + E_i - E_0)^n/E \qquad (6.2)$$

where σ_0 is an energy-independent scaling factor, E is the relative kinetic energy of the reactants, E_i is the internal energy of the neutral reactants having populations g_i ($\Sigma g_i = 1$), n is an adjustable parameter, and E_0 is the 0 K reaction threshold. Before comparison to the data, Eq. 6.2 is convoluted over the kinetic energy distributions of the reactants, and the σ_0, n, and E_0 parameters are optimized using a nonlinear least-squares method to best reproduce the experimental cross section.[59, 69] Uncertainties in E_0 are calculated from the threshold values from several independent data sets over a range of acceptable n values and combined with the absolute uncertainties in the kinetic energy scale and internal energies of reactant ions (0.02 ± 0.03 eV). At high energies, cross sections decline because of product dissociation, so Eq. 6.2 is modified to include a statistical model of the dissociation probability. This model has been discussed in detail elsewhere.[70] Briefly, the probability is controlled by two adjustable parameters: *p,* which is similar to *n,* can hold only integer values and E_d, the energy at which product cross sections begin to decline. Inclusion of this model does not significantly alter the analysis of E_0.

E_0 obtained from Eq. 6.2 is used to determine the bond dissociation energy (BDE), $D_0(Th^+\text{-}L)$, using Eq. 6.3.

$$D_0(Th^+\text{-}L) = D_0(L\text{-}R) - E_0 \quad (6.3)$$

Eq. 6.3 assumes that there are no barriers in excess of the endothermicity of the reaction. No experimental evidence was found to suggest that such a barrier is present in either system studied here, and potential energy surfaces presented below confirm that no barriers are present.

Theoretical Calculations

Most quantum chemical calculations were performed using the Gaussian 09 suite of programs.[71] For Th^+, a polarized core correlation consistent quadruple-ζ (20s17p12d11f7g4h1i)/[9s9p8d8f7g4h1i] basis set[72] is used with the Stuttgart-Cologne (MDF) small core (60 electron) relativistic effective core potential (ECP), cc-pwCVQZ-PP-MDF.[73] The cc-pwCVTZ-PP-MDF[72] and atomic natural orbital ANO-VQZ-MDF[73] basis sets are also used in combination with the MDF ECP. Additionally, Stuttgart-Dresden (SDD-VDZ-MWB), segmented quadruple-ζ (Seg. SDD-VQZ-MWB), and atomic natural orbital (ANO-VQZ-MWB) basis sets[48, 74] are used in combination with the Stuttgart-Dresden small core quasi relativistic ECP (MWB). The aug-cc-pwCVQZ,[75] cc-pwCXZ (X = T, Q),[76] and Pople[77] 6-311+G(3df) basis set are used for C and O. Extrapolation to the complete basis set limit (CBS) for the cc-pwCVXZ (X = T, Q) is performed using the Karton-Martin method,[78] Eq. 6.4, proposed for HF energies (where Y = 3 for T and Y = 4 for Q):

$$E_X = E_{CBS} + A(Y + 1)e^{-6.57\sqrt{Y}} \quad (6.4)$$

For CCSD(T) calculations, Eq. 6.5[79] is used to extrapolate the correlation energy:

$$E_X = E_{CBS} + B(Y + ½)^{-4} \quad (6.5)$$

The use of these basis sets has previously yielded reasonable results for other Th^+ systems.[16-17]

Structures were optimized using density functional theory functionals, B3LYP,[80-81] B3PW91,[82] BHandHLYP (BHLYP),[83] M06,[84] and PBE0.[85] B3LYP and B3PW91 have proven reliable in actinide theoretical calculations by us and others.[16-17, 20, 24] PBE0 and M06 have also yielded reasonable results and M06 was indicated as a promising functional in studies of the ThO_2^+ bond dissociation energy (BDE).[17, 26] BHLYP has previously performed well in actinide systems when the molecule is singly bound,[16-17] but performs poorly in systems with higher bond orders.[16, 86] Nevertheless, it is included here because it appears to perform well in energy spacing between electronic states in previous studies of Th^+.[16-17] Additionally, single-point energies using the coupled cluster method that mixes in single and double excitations and perturbative triple excitations, CCSD(T),[87-90] are performed using the B3LYP optimized structures. For electron correlation calculations using CCSD(T), the Th^+ *5s* and *5p* and the C/O *1s* electrons are frozen. All energies discussed below are corrected by the zero-point energy using the frequencies generated by their respective optimized structure after scaling by 0.989.[91] Potential energy surfaces are generated by performing relaxed potential scans along the $\angle LThO^+$ coordinate (L = C or O).

For most theoretically calculated BDEs, a semiempirical approach that corrects

for spin-orbit splitting is employed. This model is described in detail elsewhere.[16, 43-44, 92-93] Briefly, the theoretical BDE is a value averaged over all spin-orbit states of the molecule and the dissociation asymptote. To correct for the spin-orbit splitting of the asymptote, the contributions of L are considered negligible, and contributions of Th^+ are corrected by the difference in energy of the ground-level and the energy of the ground-state averaged over all spin-orbit levels. For Th^+, the ground-state is ^2D and the J = 3/2 ground-level is a mixture of the $^4F_{3/2}$ and $^2D_{3/2}$ levels. For the purpose of comparing experimental energies to theoretical energies, we have previously assigned the ground-level as $^4F_{3/2}$.[16] Experimentally, the $^4F_{3/2}$ ground-level lies 0.40 eV below the spin-orbit averaged ^2D ground-state, which lies 0.06 eV below the spin-orbit averaged ^4F state. The spin-orbit energy of ThL^+ can be corrected using a model described elsewhere;[16, 43-44, 92-93] however, for the present systems, this model is not necessary because the ThL^+ ground-states are Σ states (as discussed below) that do not exhibit first-order spin-orbit splitting. This model for spin-orbit energy corrections ignores all second-order effects from interacting states, which may lead to significant error in some cases. For the present systems, potential interacting states are separated sufficiently in energy that second-order effects are not believed to be significant.

Explicit Spin-Orbit Calculations

Explicit spin-orbit calculations, unless otherwise stated, were carried out at the CCSD(T) level of theory where only valence electrons were correlated. The calculations were carried out with the third order Douglas-Kroll-Hess (DKH3) Hamiltonian[94-95] utilizing aug-cc-pVXZ-DK basis sets[76, 96-97] on the O and C atoms and the all-electron cc-

pVXZ-DK3 basis set on Th (X = D, T, Q).[72] This combination is denoted cc-pVXZ-DK3 below. Core-valence correlation (*1s* on C and O with *5s5p5d* on Th) was also considered, and in these cases, the aug-cc-pwCVXZ-DK (O, C) and cc-pwCVXZ-DK3 (Th) basis sets were used. Geometries were optimized at the CCSD(T)/cc-pVQZ-DK3 level of theory and were consistently used as the reference geometry for all single-point calculations, except in the case of the zero-point energy (ZPE) described below.

Composite thermochemistry, as outlined in the Feller-Peterson-Dixon method (FPD),[98] was used to describe numerous contributions to the atomization energies at 298 K. The total energy breakdown is given as:

$$E_{tot} = E_{VQZ\text{-}DK} + \Delta E_{CBS} + \Delta E_{CV/CBS} + \Delta E_{SO} + \Delta E_{QED} + \Delta E_{ESC} + \Delta E_{ZPE} + \Delta H_{(0\text{-}298)} \qquad (6.6)$$

$E_{VQZ\text{-}DK}$ is the energy at the frozen-core CCSD(T)/cc-pVQZ-DK3 level of theory. The HF energies were extrapolated to the CBS limit using the Eq. 6.4 with cc-pVTZ-DK3 and cc-pVQZ-DK3 basis sets. The correlation energies were extrapolated to the CBS limit using Eq. 6.5. These two extrapolations were combined to yield the total CBS limit, with the difference in energy between $E_{VQZ\text{-}DK}$ and the CBS limit yielding ΔE_{CBS}. $\Delta E_{CV/CBS}$ is the core correlation contribution, $E_{CV} - E_{valence}$, both in the same pwCVXZ basis sets (X = T and Q), extrapolated to the CBS limit using Eq. 6.4. Harmonic frequencies at the frozen-core CCSD(T)/cc-pVDZ-DK3 level of theory were used to define the zero point vibrational energy (ZPE) of each molecule, denoted ΔE_{ZPE}. Spin-orbit (ΔE_{SO}) effects were carefully considered using the DIRAC program.[99]

SO contributions were calculated using the exact two-component (X2C)

Hamiltonian[100-101] and uncontracted VDZ basis sets. The ThC^+, ThO^+, and ThO_2^+ molecules were calculated using 2-component open-shell coupled cluster approach, CCSD(T). The $CThO^+$ ground-state $^4A''$ presented unique challenges for this method; hence this contribution was calculated at the average-of-configuration Hartree-Fock level of theory (3 electrons in 6 open-shell spinors). All SO calculations involving CCSD(T) were carried out using a virtual orbital cutoff of 12.0 au.

ΔE_{QED} is a contribution for quantum electrodynamic effects (QED), namely the Lamb shift, that are often overlooked; however, when considering molecules that contain large atoms such as actinides, this contribution can begin to become significant.[102] In this work, the local potential approach of Pyykkö has been used.[103] Thermal corrections, $\Delta H_{(0\text{-}298)}$, were calculated using standard ideal gas partition functions to correct the atomization enthalpies to 298 K.

Because of the highly multi-reference character of the $^4F_{3/2}$ ground-state of Th^+ when spin-orbit is included, all calculations were carried out relative to the excited $5f^17s^2$ ($^2F_{5/2}$) electronic state of Th^+. The Δ_{SO} term is relative to this latter atomic asymptote. The experimental excitation energy from the ground-state ($^4F_{3/2}$) to this excited-state ($^2F_{5/2}$) is well known (4490.262 cm^{-1}),[66] and this is accounted for by the term ΔE_{ESC}. These calculations, excluding the SO contributions, were carried out using the MOLPRO quantum chemistry package.[104]

Experimental Results

$Th^+ + O_2$

The cross sections as a function of kinetic energy for the reaction of thorium cation with molecular oxygen at a pressure of 0.3 mTorr are presented in Figure 6.1. The following reactions were observed:

$$Th^+ + O_2 \rightarrow \quad ThO^+ + O \tag{6.7}$$

$$ThO^+ + O_2 \rightarrow ThO_2^+ + O \tag{6.8}$$

The energy dependence of the cross section for reaction 6.7 declines with increasing energy, consistent with an exothermic, barrierless reaction. At low energies, the reaction efficiency is $k/k_{col} = 1.21 \pm 0.24$, where the collision limit, k_{col}, is defined as the Langevin-Gioumousis-Stevenson (LGS) rate.[105] This is consistent with the results of two separate FT-ICR studies where the reaction efficiency was observed as $k/k_{col} = 1.12 \pm 0.22$[3] and $k/k_{col} = 0.86 \pm 0.43$.[5] The cross section declines with an energy dependence of $E^{-0.40 \pm 0.1}$, consistent with the energy dependence ($E^{-1/2}$) of the LGS cross section (σ_{LGS}) until approximately 0.6 eV, where the cross section levels until 2 eV. At 2 eV, the cross section begins to decline more rapidly until dropping off even faster beginning near 6 eV. The rapid decline starting near 6 eV can be attributed to there being sufficient energy present to dissociate the ThO^+ product, a process that can begin at $D_0(O\text{-}O) = 5.117$ eV.[106]

The energy dependence of reaction 6.7 from 0.6 – 2 eV is unusual because the cross section deviates from σ_{LGS} and has a shallower energy dependence. This cannot be

a transition to the hard sphere collision limit, which we estimate as 16 $Å^2$, calculated using the atomic radii reported by Waber and Cromer[107] (Th = 1.186 Å and O = 0.450 Å) and r(O-O) = 1.208 Å reported by Huber and Herzberg.[108] (Note that the atomic radius is used as an estimate of the Th^+ ionic radius, but the expected error will be minimal.) A similar energy has been observed previously in the reactions of Zr^+ and Nb^+ with O_2.[40] A possible explanation, explored and previously presented in detail,[40] is that these reactions couple with the $M^{2+} + O_2^-$ ($V_1 \propto r^{-1}$) asymptote, thus creating a Coulombic interaction that is more attractive than the ion–induced dipole interaction ($V_4 \propto r^{-4}$). In the Zr^+ and Nb^+ cases, the $M^{2+} + O_2^-$ asymptotes are too high in energy to influence the reaction dynamics.[40] By contrast, the deviation from σ_{LGS} occurs at higher energies for Th^+ and IE(Th^+) = 11.65 ± 0.35 eV[13] is significantly smaller than IE(Zr^+) = 13.1 eV and IE(Nb^+) = 14.0 eV.[28] Thus, the Coulombic interaction may be significant in the Th^+ case. Calculations of the V_1 and V_4 surfaces following the procedure in Ref. 40 are explained in detail in the Supporting Information. The results indicate that near 0.5 eV the bond distance at the $V_1 = V_4$ crossing point exceeds the V_4 maximum so that the reaction may crossover and proceed along the more attractive V_1 potential.

The ThO_2^+ cross section in Figure 6.1 is dependent on the O_2 neutral reactant gas pressure, indicating that ThO_2^+ forms in a sequential process, reaction 6.8. The cross section for reaction 6.8 has an energy dependence of $E^{-1.1 \pm 0.2}$, consistent with that expected for product formation in sequential reactions occurring at the LGS rate. The observation of reaction 6.8 is interesting because direct measures of the reaction $ThO^+ + O_2$ yield no products in FT-ICR experiments at thermal energies.[3, 12] Consistent with these ICR observations, GIBMS studies of the $ThO^+ + O_2$ reaction in our lab yield an

energy dependence inconsistent with a simple exothermic reaction. Because of unusual reaction dynamics, a more complete analysis of this reaction is beyond the scope of the present text and will be published elsewhere.[109] Ultimately, the explanation for this dichotomy is that reaction 6.8 is observed because the ThO^+ products from reaction 6.7 are not thermalized.

$Th^+ + CO$

The cross sections of the reaction of Th^+ with CO as a function of kinetic energy are presented in Figure 6.2. Both reactions 6.9 and 6.10 are observed.

$$Th^+ + CO \rightarrow ThO^+ + C \quad (6.9)$$

$$\rightarrow ThC^+ + O \quad (6.10)$$

Reaction 6.9 has an apparent threshold of 2.5 eV, with a cross section that increases with increasing energy until it peaks near 8 eV. Reaction 6.10 has an apparent threshold near 7.5 eV that corresponds with the initial decline of the ThO^+ cross section. The ThC^+ cross section peaks near $D_0(C\text{-}O) = 11.109 \pm 0.005$ eV.[106] Although not apparent on the logarithmic scale on Figure 6.2, the total $Th^+ + CO$ reaction cross section peaks near $D_0(C\text{-}O)$, where sufficient energy is available to allow both ThO^+ and ThC^+ product to dissociate, equivalent to atomizing CO according to reaction 6.11.

$$Th^+ + CO \rightarrow Th^+ + O + C \quad (6.11)$$

Thermochemical and Theoretical Results

ThO^+

The barrierless cross section for reaction 6.7 indicates that $D_0(Th^+\text{-}O) \geq D_0(O\text{-}O) = 5.117 \pm 0.001$ eV, consistent with previous ICR results[3, 5] and reported literature values.[13, 50] Modelling the ThO^+ cross section of reaction 6.9 reproduces the experimental cross section over the entire energy range, Figure 6.2. The measured threshold is $E_0 = 2.60 \pm 0.16$ eV, with other modelling parameters used in Eq. 6.2 listed in Table 6.1. This yields $D_0(Th^+\text{-}O) = 8.51 \pm 0.16$ eV from Eq. 6.3. The present value is lower than (but within experimental uncertainty of) the BDE adopted by Marçalo and Gibson, 8.74 ± 0.25 eV,[13] and is within combined experimental uncertainties of the value derived from Konings et al., 8.70 ± 0.10 eV.[50] Interestingly, when combined with IE(Th) and IE(ThO) in Eq. 6.1, the present value leads to $D_0(Th\text{-}O) = 8.81 \pm 0.16$ eV. This agrees very well with $D_0(Th\text{-}O) = 8.79 \pm 0.13$ eV, originally reported by Hildenbrand and Murad,[32] and with $D_0(Th\text{-}O) = 8.89 \pm 0.17$ eV, originally reported by Neubert and Zmbov.[34] Thus, the present work suggests that the lower values of $D_0(Th\text{-}O)$ in the literature are probably more accurate.

The ground and excited-states of ThO^+ calculated with the cc-pwCVQZ-PP-MDF basis sets are listed in Table 6.2. Values obtained using additional basis sets are listed in Table C.1 in the Supporting Information section. The calculated ground-state of ThO^+ is $^2\Sigma^+$ with a $(1\sigma)^2(2\sigma)^2(1\pi)^4(3\sigma)^1$ molecular orbital occupation. The 1σ-orbital is the O *2s*-orbital, the 2σ-bonding orbital is formed as two O $2p_z$-electrons are donated into an empty Th^+ $6d_{z2}$-orbital, and the 1π-bonding orbitals are formed as the remaining O *2p*-electrons pair with the two Th^+ $6d\pi$-electrons. Note that this configuration corresponds to

a triple bond, consistent with the very strong bond. The radical electron is found in the 3σ-orbital, which is largely composed of the Th^+ *7s*-orbital, indicating that the $^2\Sigma^+$ state forms from the atomic asymptote, Th^+ (^{4}F, $6d^27s$) + O (^{3}P), the ground-level configuration. Previous theoretical reports also find a $^2\Sigma^+$ ground-state with the singly occupied σ-orbital having 93% *7s*-character.[22, 26] A low-lying $^2\Delta$ state is also found 0.35 – 0.58 eV higher in energy than the ground-state where the lone electron moves to a *6dδ*-orbital (1δ). A relaxed potential scan of the diabatic potential energy surface for dissociation of ThO^+ ($^2\Delta$), Figure C.2, suggests that this state correlates with the Th^+ (^{4}F, $6d^3$) + O (^{3}P) asymptote. A third doublet state ($^2\Pi$) where an electron from the $1\pi_b$ bonding orbital is moved to the Th^+ *7s*-orbital, a $(1\sigma)^2(2\sigma)^2(1\pi)^3(3\sigma)^2$, is also found 0.73 – 1.22 eV higher in energy. This state is most likely formed from Th^+ (^{2}D, $6d7s^2$) + O (^{3}P). Because the J = 3/2 level has $^4F_{3/2}$ and $^2D_{3/2}$ mixed character, the $^2\Pi$ state presumably can form directly from the Th^+ ground-level. Additional states were also found but were at least 4 eV higher in energy, Table 6.2.

Experiments performed using pulsed field ionization-zero kinetic energy (PFI-ZEKE) photoelectron spectroscopy have determined a $^2\Sigma^+$ ground-state for ThO^+.[9] Low-lying levels of $^2\Delta_{3/2}$, $^2\Delta_{5/2}$, and $^2\Pi_{1/2}$ at 0.36, 0.72, and 0.92 eV higher in energy than the ground-state, respectively, were also found. For reference to the theoretical values, which are an average energy of all spin-orbit levels, the experimental average of the $^2\Delta$ levels weighted over the spin-orbit degeneracies is 0.58 eV. Table 6.2 indicates that the present calculations are in very good agreement with the experimental electronic state energies.

Bond lengths and vibrational frequencies calculated using B3LYP/cc-pwCVQZ-PP-MDF/aug-cc-pwCVQZ are listed in Table 6.2. Molecular parameters calculated using

additional levels of theory are listed in Tables C2 and C3 in the Supporting Information section. In general, the B3LYP/cc-pwCVQZ-PP-MDF/aug-cc-pwCVQZ values agree very well with the experimental values. This is particularly true for the $^2\Sigma^+$ ground-state, where theory is in very good agreement with the experimental bond length, 1.808 Å,[9] and the calculated frequency differs from experiment by only 5 cm^{-1}.

Theoretical BDEs calculated in this work are presented in Table 6.3. After inclusion of spin-orbit effects, theoretical BDEs are 8.61 – 8.76 eV, 8.55 – 8.89 eV, 8.70 – 8.80 eV, and 8.89 – 8.94 eV for the SDD-VDZ-MWB, Seg. SDD-VQZ-MWB, and cc-pwCVQZ-PP-MDF/aug-cc-pwCVQZ basis sets and CBS limit, respectively. Likewise the FPD composite thermochemistry approach yields a BDE of 8.81 eV. BDEs calculated with additional basis sets and methods are listed in Table C.4 in the Supporting Information. In general, B3LYP and CCSD(T) values (except CCSD(T)/CBS) are in good agreement with the experimental BDE reported here. Previous work by Pereira et al.[14] has calculated theoretical BDEs for ThO^+ using the Seg. SDD-VQZ-MWB basis set for Th^+ and a *10s6p* basis contracted to *5s3p* by Dunning for O in conjunction with B3LYP and MPW1PW91 DFT functionals. They find $D_0(Th^+\text{-}O)$ of 9.02 and 9.29 eV for B3LYP and MPW91PW91, respectively, with no consideration for spin-orbit energy. Applying the spin-orbit correction used here yields values of 8.62 and 8.89 eV, respectively, where the B3LYP value is also in very good agreement with the present experimental work.

ThC^+

Modelling of the cross section from reaction 6.10 indicates that $E_0 = 6.29 \pm 0.29$ eV, leading to $D_0(Th^+\text{-}C) = 4.82 \pm 0.29$ eV. To the best of our knowledge, no determination of this BDE has been reported in the literature, although the value, $D_0(Th^+\text{-}C) = 3.1 \pm 1.0$ eV, can be calculated from Eq. 6.1 using data from Knudsen cell experiments. For reasons discussed below, this latter value is almost certainly too low because the IE(ThC) = 7.9 ± 1.0 eV is inaccurate. A better estimate of IE(ThC) can be established as 6.19 ± 0.34 eV using our value of $D_0(Th^+\text{-}C)$ along with $D_0(Th\text{-}C) = 4.70 \pm 0.18$ eV[53] with Eq. 6.1 (neglecting the difference between the 0 K and 298 K BDE).

Theoretical calculations establish $^2\Sigma^+$ ($1\sigma^2 1\pi^4 2\sigma$) as the ground-state of ThC^+ where the 1σ is primarily the C *2s*-orbital, the 1π orbitals are an interaction of the C 2*pπ* and Th^+ 6*dπ*-orbitals, and the 2σ is a bonding interaction between C 2*pσ* and a *sd*-hybridized Th^+ orbitals. Thus, ThC^+ has a bond order of 2.5, explaining its weaker bond compared to ThO^+. A $^4\Pi$ excited-state is found 0.52 – 0.94 eV higher in energy where one π-electron is moved to the 3σ-orbital (Th^+ *7s*). A second excited-state ($^2\Pi$) is found 0.55 – 0.86 eV higher than the ground-state where one π-electron is moved to the 2σ-orbital. Other states found were at least 0.96 eV higher in energy than the ground-state and are listed in Table 6.2. Energies calculated using additional basis sets are listed in Table C.1 in the Supporting Information. B3LYP bond lengths for ThC^+ ground and excited-states are listed in Table 6.2 and additional levels of theory are listed in Table C.2. The calculated bond length is $r(Th^+\text{-}C) = 1.903$ Å, which is shorter than that calculated for $ThCH_2^+$, $r(Th^+\text{-}C) = 2.05$ Å (B3LYP/SDD-VDZ-MWB), but similar to that for $ThCH^+$, 1.92 Å (B3LYP/SDD-VDZ-MWB).[16] These calculations also show that

$ThCH^+$ has a triple bond, whereas $ThCH_2^+$ has a double bond, compared to the bond order for ThC^+ found here of 2.5. In our previous work, we also determined bond strengths of $D_0(Th^+\text{-}CH_2) \geq 4.54 \pm 0.09$ eV and $D_0(Th^+\text{-}CH) = 6.19 \pm 0.16$ eV. On the basis of the bond orders, one expects that $D_0(Th^+\text{-}CH)$ should lie between these values, which is consistent with our 4.82 ± 0.29 eV BDE but inconsistent with the much lower 3.1 ± 1.0 eV.

Theoretical BDEs for ThC^+ are listed in Table 6.3. When including spin-orbit energy corrections, the BDEs are 4.84 – 5.21 eV (SDD-VDZ-MWB), 4.72 – 5.33 eV (Seg. SDD-VDZ-MWB), 4.81 – 5.20 eV (cc-pwCVQZ-PP-MDF), 4.99 – 5.38 eV (CBS-MDF), and 5.00 eV (FPD). BDEs calculated with additional basis sets and methods are listed in Table C.4 in the Supporting Information. In general, all levels of theory are in reasonable agreement with the experimental BDE. In particular, CCSD(T) (except CCSD(T)/CBS) values are within experimental uncertainty and B3LYP values are in excellent agreement with the experimental value. These values are similar to those calculated for $ThCH_2^+$, 4.44 – 5.04 eV (Seg. SDD-VQZ-MWB), and much smaller than those reported for $ThCH^+$, 5.57 – 6.21 eV (Seg. SDD-VQZ-MWB). This is again consistent with a bond order in between that of $ThCH_2^+$ (2) and $ThCH^+$ (3).

In order to calculate IE(ThC), additional calculations were performed for ThC using the B3LYP/cc-pwCVQZ-PP-MDF/aug-cc-pwCVQZ approach. Additional single-point energies were calculated using CCSD(T)/cc-pwCVQZ-PP-MDF/aug-cc-pwCVQZ with the B3LYP optimized structures. Results are listed in Table C.4 in the Supporting Information section. We find that the ThC ground-state is $^3\Sigma^+$ ($1\sigma^2 1\pi^4 2\sigma 3\sigma$), where orbital compositions are similar to those of ThC^+ discussed above. Thus, the electron

removed upon ionization of ThC is from the nonbonding 3σ (largely Th 7*s*) orbital, so that it is likely that IE (ThC) ≈ IE(Th) and that $D_0(Th^+\text{-}C) \approx D_0(Th\text{-}C)$. Calculated ionization energies of ThC are 6.40 (B3LYP) and 6.33 (CCSD(T)) eV within experimental uncertainty of the 6.19 ± 0.34 eV value determined here and well below the electron impact values previously reported.

Potential Energy Surfaces

$Th^+ + O_2$

Relaxed potential energy scans of the electronic surfaces for reaction 6.7, $Th^+ + O_2$, were calculated at the B3LYP/SDD-VDZ-MWB/6-311+G(3df) level and are presented in Figure 6.3. Notably, these surfaces (as well as those for $Th^+ + CO$) do not include consideration of spin-orbit effects. Initially, the reaction originates on a $^2A'$ surface where the minimum at very small angles ° can be understood as a linear Th^+-O-O intermediate that lies 3 eV below the reactants. $^2A''$ and $^4A'$ surfaces lie slightly higher in energy. This $^2A'$ ($^2\Sigma^+$) intermediate has $r(Th^+\text{-}O)$ = 1.9 Å, 0.1 Å longer than the 1.8 Å bond length in ThO^+ ($^2\Sigma^+$). The r(O-O) bond length of 1.3 Å is elongated from 1.2 Å in unbound O_2. The stability of these intermediates appears to come from a covalent interaction of the Th^+ *6d*-electrons with the O_2 π* antibonding orbitals. At slightly larger angles, there is a slight barrier relative to the intermediate along both doublet surfaces as Th^+ begins to insert into the O-O bond. At ~35°, there is an apparent crossing with the $^2A_1$, $^2A_2$, and $^2B_1$ surfaces that lead to potential wells near an angle of 45°. These are all still adducts of Th^+ with O_2, which pass over barriers as the ∠OThO angle increases, until dropping slightly as a linear thorium dioxide cation is approached. This leads to several

excited-states of linear ThO_2^+. The $^2A_1$ surface crosses that for the $^2B_2$ surface (avoided in C_S symmetry) that leads to a linear global minimum that is at least 3 eV lower in energy than all other surfaces and 8.5 eV below ground-state reactants. This $^2B_2$ surface leads to the linear $^2\Sigma_u^+$ ground-state of ThO_2^+, which has been previously characterized.[22] This intermediate should readily dissociate to the ThO^+ ($^2\Sigma^+$) + O (^3P) product asymptote, 4.8 eV higher in energy than ThO_2^+ ($^2\Sigma_u^+$). Clearly, these surfaces show that reaction 6.7 can occur with no barrier above the reactants, consistent with experiment. Further, the attractive nature of the surfaces is consistent with the efficiency of the reaction observed.

A number of quartet surfaces were also explored and are shown in Figure 6.3. These could also lead to the ThO^+ ($^2\Sigma^+$) + O (^3P) products with no barriers but are clearly higher-energy pathways.

If spin-orbit effects are considered, the main change to the surface is the ground-level of the reactants (and the principally occupied level) becomes Th^+ ($^4F_{3/2}$) + O_2 ($^3\Sigma_g^-$), which lies 0.40 eV lower than the ^2D state shown in Figure 6.3. These reactants can combine to form doublet, quartet, and sextet surfaces (where the latter should be repulsive as they include no covalent interactions). Thus, evolution from reactants to products along the doublet (or quartet) surfaces remains barrierless and efficient.

<u>Th^+ + CO</u>

Surfaces from relaxed potential surface scans calculated using B3LYP/SDD-VDZ-MWB/6-311+G(3df) for reactions 6.9 and 6.10, Th^+ + CO, are presented in Figure 6.4. At small angles, the lowest-energy reaction pathway evolves along the $^4A''$ surface where the initial intermediate is linear Th^+-C-O lying 1.4 eV below the reactants. A $^2A''$

state is also observed 1.2 eV below the reactants. Notably, at small angles near the reactant asymptote, s(s+1) values of this doublet are typically ~1.76, suggesting that there is considerable spin-contamination for this doublet surface. At slightly larger angles, a barrier to Th^+ insertion into the C-O bond is observed. In this vicinity, a second $^4A''$ surface becomes the lowest-energy surface and leads to an intermediate at 115°. This intermediate has r(Th^+-O) = 1.82 Å, similar to the bond length of ThO^+, and r(Th^+-C) = 2.34 Å, which is significantly longer than the bond length of ThC^+. Thus, this intermediate can be viewed as an adduct between ThO^+ ($^2\Sigma^+$) and C (^3P), where the quartet spin indicates no covalent coupling between the two. This intermediate can readily dissociate to the ThO^+ ($^2\Sigma^+$) + C (^3P) asymptote 2.1 eV higher in energy than the reactant asymptote with no barrier above the product asymptote. Additionally, no barrier beyond the endothermicity of reaction 6.9 exists such that the global minimum can readily dissociate to the ThC^+ ($^2\Sigma^+$) + O (^3P) product asymptote that is ~6 eV higher in energy than the reactants. Overall, the potential energy surface (PES) in Figure 6.4 is very similar to the analogous Hf^+ + CO reaction PES.[42] Like Th^+ + CO, Hf^+ has low-lying $^4A''$ and $^2A''$ surfaces that approach linear at small angles, and a $^4A''$ intermediate is found near 115°.

If spin-orbit effects are considered, the Th^+ ($^4F_{3/2}$) reacts with CO ($^1\Sigma^+$) along a quartet spin surface; however, because the J = 3/2 ground-level is actually a mixture of $^4F_{3/2}$ and $^2D_{3/2}$, both doublet and quartet surfaces should be accessible in the reaction. Furthermore, this presumably permits switching between surfaces of different spin with some facility.

Discussion

Comparison of Theoretical Methods

Previously ThH^+ and $ThCH_3^+$ BDEs calculated utilizing CCSD(T)/cc-pVQZ-PP-MDF/cc-pVTZ yielded results that overestimated the experimental values by 0.2 – 0.6 eV, whereas the calculated BDE for $ThCH^+$ reproduced the experimental value reasonably well.[16] Here, CCSD(T)/cc-pwCVQZ-PP-MDF/aug-cc-pwCVQZ calculations overestimate the experimental BDE of ThO^+ and ThC^+ by 0.52 and 0.26 eV, respectively. Meanwhile, CCSD(T)/Seg. SDD-VQZ-MWB calculations reproduce the experimental value for both ThO^+ and ThC^+ within experimental uncertainty, and CCSD(T)/SDD-VDZ-MWB calculations reproduce the experimental ThC^+ BDE within uncertainty and overestimate the ThO^+ BDE by 0.25 eV. MADs for CCSD(T)/ cc-pwCVQZ-PP-MDF, CCSD(T)/Seg. SDD-VQZ-MWB, and CCSD(T)/SDD-VDZ-MWB are 0.39, 0.07, and 0.17, respectively, indicating that at least for calculating BDEs there is no advantage in using the larger cc-pwCVQZ-PP-MDF basis set compared to the smaller Seg. SDD-VQZ-MWB basis set for these systems. Similarly, MADs for CCSD(T)/cc-pwCVQZ-PP-MDF, CCSD(T)/Seg. SDD-VQZ-MWB, and CCSD(T)/SDD-VDZ-MWB are 0.28, 0.27, and 0.37, respectively, when comparing ThH^+, $ThCH^+$, $ThCH_3^+$ and $ThCH_4^+$ theoretical BDEs to experimental values. (Only a lower limit can be established for $ThCH_2^+$.)[16]

For DFT methods, there is little difference between calculations using the cc-pwCVQZ-PP-MDF and Seg. SDD-VQZ-MWB basis sets for all methods. In general, these calculations overestimate the experimental BDE, with the exception of BHLYP calculations. BHLYP has previously been shown to perform poorly for multiply bound species.[86] Calculations utilizing the SDD basis set also tend to overestimate the

experimental BDE, but with the exception of BHLYP calculations, perform better compared to the other basis sets. MADs listed in Table 6.4 indicate that there is little advantage to using the larger KAP and Seg. SDD basis sets in DFT calculations for these systems.

In general, B3PW91, and PBE0 methods yield similar BDEs to each other regardless of the basis set used and tend to overestimate the experimental BDE with MADs of 0.34, and 0.32 eV, respectively (cc-pwCVQZ-PP-MDF). However, B3LYP calculations perform reasonably well with MADs of 0.10, 0.17, and 0.06 eV for the cc-pwCVQZ-PP-MDF, Seg. SDD-VQZ-MWB, and SDD-VDZ-MWB basis sets, respectively. CCSD(T) calculations, with the exception of CCSD(T)/CBS (MAD = 0.40 eV), also reproduce the experimental value well with MADs of 0.07, 0.17, and 0.14 eV for the Seg. SDD-VQZ-MWB, SDD-VDZ-MWB, and cc-pwCVQZ-PP-MDF basis sets, respectively. In all calculations, the inclusion of spin-orbit effects improves accuracy compared to the experimental values.

In the present work, BHLYP/cc-pwCVQZ-PP-MDF calculations successfully predict order and magnitude of the ThO^+ excited-states. B3LYP/cc-pwCVQZ-PP-MDF and CCSD(T)/cc-pwCVQZ-PP-MDF perform similarly, whereas the other methods predict the correct ordering but underestimate the energy gaps between excited-states. In previous work,[16-17] BHLYP calculations reproduced the experimental order of Th^+ ground- and excited-states with a high degree of accuracy in the energy spacing, while all other methods, including B3LYP and CCSD(T), either ordered the states incorrectly or spaced the states too closely. Although BHLYP performs poorly in predicting the absolute BDEs for higher bond order species, it appears to perform reasonably well at

predicting relative energies of excited-states.

Comparison to Transition Metal Oxide and Carbide Cations

One interesting aspect of Th^+ is that its ground-level does not populate the *5f*-orbitals in the ground-state, unlike the other members of the actinide series. Its ground-state configuration, a mixture of ^4F ($6d^27s$) and ^2D ($6d7s^2$), can be directly compared with those for the group 4 transition metal cations, Ti^+ (^4F, $3d^24s$), Zr^+ (^4F, $4d^25s$), and Hf^+ (^2D, $5d6s^2$), which also have three valence electrons. Such a comparison has profitably been included in our analysis of the $Th^+ + CH_4$[16] and $Th^+ + H_2$[17] systems, and others have noted the similarities in the electronic structures of Th^+ and Hf^+ species.[9, 15] Here, we also include a comparison to the lanthanide Ce^+ (^4H, $4f5d^2$), which also has three valence electrons. With the exception of CeO^+, all thermochemical values in this discussion are measured in guided ion beam experiments.[38, 40, 42] A brief description of the thermochemical values used to evaluate $D_0(Ce^+\text{-}O)$ can be found in the Supporting Information section.

MO^+ BDEs for the group 4 transition metals and Ce are $D_0(Ti^+\text{-}O) = 6.88 \pm 0.07$,[38] $D_0(Zr^+\text{-}O) = 7.76 \pm 0.11$ eV,[40] $D_0(Ce^+\text{-}O) = 8.82 \pm 0.21$ eV,[110] and $D_0(Hf^+\text{-}O) = 6.91 \pm 0.11$ eV[42] compared to $D_0(Th^+\text{-}O) = 8.51 \pm 0.16$ eV. For TiO^+ - CeO^+, the BDEs increase moving down the periodic table consistent with the trend expected for the lanthanide contraction.[86, 111-113] The lower-than-expected BDE for Hf^+ can be explained as a result of the Hf^+ ground-state (^2D, $5d6s^2$) and its doubly occupied *6s* orbital. Because formation of an M^+-O triple bond requires the metal cation to have two unpaired electrons that can adopt π-symmetry,[114] Hf^+ must be promoted to a higher state, thereby

reducing the BDE. The first level with the correct symmetry ($^4F_{3/2}$, $5d^26s$) is 0.45 eV higher in energy than the ground-level. Similarly, it might have been expected that $D_0(Th^+\text{-}O) > D_0(Ce^+\text{-}O)$; however, this discrepancy can potentially be explained by the considerable ^2D ($6d7s^2$) character mixed into the J = 3/2 ground-level.[66]

Additionally, the binding between CeO^+ and the group 4 MO^+ including ThO^+ molecules is slightly different. In all cases, the bonding interaction occurs as the O $2p\sigma$-electrons are donated into the M^+ $d\sigma$-orbital and the M^+ $d\pi$-electrons π-bond with the O $2p\pi$-electrons, forming a strong triple bond. For these M^+, there is one remaining electron that is found in a nominally nonbonding orbital. For Ce^+, the nonbonding electron originates from the *4f*-orbital. Because the *4f* orbitals do not extend far enough spatially to participate in bonding,[6] this electron can be understood as a true nonbonding orbital electron. Indeed, theoretical studies indicate that CeO^+ has a $^2\Phi$ ground-state.[115] For the transition metal cations and Th^+, the unpaired electron originates from the *nd* or (*n+1*)*s* orbital and can be placed in either the 1δ or 3σ orbital to form $^2\Delta$ or $^2\Sigma^+$ states, respectively. Of the two orbitals, the δ-orbital does not have the correct symmetry to interact with the bonding orbitals, but the σ-orbital can potentially interact with the 2σ and 4σ* orbitals and can be pushed up in energy through configuration interaction.[114] Because the δ-orbital is a true nonbonding orbital (whereas the 3σ may not be), the comparison of CeO^+ BDE is more applicable to the MO^+ $^2\Delta$ diabatic BDE; however, the $^2\Delta$ state appears to be formed by the M^+ (^4F, nd^3) + O (^3P, $2p^4$) asymptote for at least Th^+ (see Figure C.2 in the Supporting Information), whereas the $^2\Sigma^+$ can be formed from the sd^2 ground-state M^+ (or first excited-state for Hf^+). Assuming a (slightly) repulsive interaction of the 3σ-orbital, then the $^2\Delta$ BDE is expected to be stronger, but the $^2\Delta$ state

is the ground-state if and only if the stabilization energy ($^2\Delta$ BDE - $^2\Sigma^+$ BDE) exceeds the promotion energy from the ground-level to the first level with nd^3 configuration. Only TiO^+ appears to meets this criterion,[42, 116-117] but the diabatic (intrinsic) BDE along the M^+ (^4F, nd^3) + O (^3P, $2p^4$) asymptote can be calculated from existing experimental data using Eq. 6.12:

$$D_0(M^+\text{-}O)^* = D_0(M^+\text{-}O) + E_p(nd^3) - E_p(^2\Delta_{3/2}) \quad (6.12)$$

For Th^+, $E_p(6d^3)$ = 0.87 eV and the promotion energy from the $^2\Sigma^+$ ground-state to the $^2\Delta_{3/2}$ level for ThO^+ is $E_p(^2\Delta_{3/2})$ = 0.36 eV, so that $D_0(Th^+\text{-}O)^*$ = 9.02 ± 0.16 eV. Unfortunately, there is insufficient experimental data ($E_p(^2\Delta_{3/2})$ is unknown) to extend the analysis to ZrO^+ and HfO^+, but $E_p(^2\Delta_{3/2})$ = 0.0 eV for TiO^+ and $E_p(6d^3)$ = 0.11 eV[28, 116] for Ti^+ so that $D_0(Ti^+\text{-}O)^*$ = 6.99 ± 0.07 eV. This yields $D_0(Ti^+\text{-}O)^* < D_0(Ce^+\text{-}O) < D_0(Th^+\text{-}O)^*$ consistent with the expected trend associated with lanthanide contraction.[86, 111-113]

Additionally, the above analysis indicating that the $^2\Delta$ state is more strongly bound than the $^2\Sigma^+$ suggests that configuration interaction between the σ-orbitals does indeed push the 3σ nonbonding orbital up in energy. This indicates that while the 3σ orbital is mostly nonbonding in character, it does possess slight antibonding character as well. The character of the 3σ-orbital may be important when comparing the ThO^+ BDE to AnO^+ BDEs discussed in more depth below.

The periodic trends for MC^+ for the group 4 transition metal cations and ThC^+ parallel the trends for MO^+ with $D_0(Ti^+\text{-}C)$ = 4.05 ± 0.24 eV,[38] $D_0(Zr^+\text{-}C)$ = 4.72 ± 0.11

eV,[40] $D_0(Hf^+-C) = 3.19 \pm 0.03$ eV[42] and $D_0(Th^+-C) = 4.82 \pm 0.29$ eV, where all values are from guided ion beam experiments. $D_0(Ce^+-C)$ can be calculated using Eq. 6.1 from $D_0(Ce-C) = 4.57 \pm 0.12$ eV,[118] IE(CeC) = 6.0 ± 0.8 eV,[118] and IE(Ce) = 5.5387 eV[28] as $D_0(Ce^+-C) = 4.11 \pm 0.81$ eV; however, the large uncertainty makes comparison to the other metal cations inexact. Comparison with the oxide values suggests that the true CeC^+ BDE is close to the upper limit in this range.

With the exception of HfC^+, all BDEs increase moving down the periodic table, consistent with the trend expected for the lanthanide contraction.[86, 111-113] Like HfO^+, the lower-than-expected BDE for HfC^+ can be explained as a result of the Hf^+ ground-state configuration (^{2}D, $5d6s^2$) that is not conducive to bonding.[42] This is largely supported by quantum chemical calculations that indicate that HfC^+ has a $^2\Sigma^+$ ($1\sigma^2 1\pi^4 2\sigma$) ground-state that cannot be formed directly from the ground-state Hf^+ (^{2}D, $6d7s^2$) + C (^{3}P, $2s^2 2p^2$) asymptote.

Comparison to Actinide Oxide and Carbide Cations

Another interesting aspect of the present results is the potential insight into the thermochemistry of other actinides that are more dangerous to work with experimentally. Ostensibly, all An^+ (except Ac^+) should be able to form the requisite σ and π bonds in AnO^+ from their respective ground-state configurations, because population of the *f*-orbitals allows an empty *6d*-orbital for donation from the O *2pσ*-electrons, and the *5f*-orbitals (unlike the *4f*-orbitals in the Ln) may be large enough to participate in bonding.[12-13] However, experimental work indicates that An^+ reactivity and AnO^+ BDEs are correlated to the promotion energy of the An^+ from its ground-level to the first level with

a $6d^2$ configuration, $E_p(6d^2)$.[13] Thus, an AnO^+ intrinsic BDE can be defined using Eq. 6.13.[6]

$$D_0(An^+\text{-}O)^* = D_0(An^+\text{-}O) + E_p(6d^2) \quad (6.13)$$

Because $E_p(6d^2)$ = 0.00 eV for Th^+, $D_0(An^+\text{-}O)^*$ should equal $D_0(Th^+\text{-}O)$, which allows for the determination of AnO^+ BDEs across the actinide series. This has previously been done by Gibson[6] with previously accepted thermochemical values; however, the ThO^+ BDE determined here is lower than the previously reported value, so AnO^+ BDEs are redetermined here using the present value with Eq. 6.13 and presented in Table 6.4. Uncertainties are derived from the uncertainty in the present value of $D_0(Th^+\text{-}O)$ and, when applicable, the uncertainty in the estimated $E_p(6d^2)$.

For comparison of the estimates in Table 6.4 to experimental values, we adopt the values determined by Marçalo and Gibson[13] using Eq. 6.1 with previous thermochemical values; however, we also note some potential problems in these reported values. 1) The experimental IE(PaO) = 5.9 ± 0.2 eV[13] determined in electron impact experiments is probably too low, as evidenced by theoretical studies that systematically place IE(PaO) = 6.2 – 6.5 eV.[14, 26] In particular, one study using CCSD(T) (that calculates IE(AnO) for all other AnO studied at -0.16 – 0.06 eV within experimental values) indicates that IE(PaO) = 6.31;[26] therefore, $D_0(Pa^+\text{-}O)$ is probably lower than reported by Marçalo and Gibson by 0.3 – 0.6 eV. 2) In the FT-ICR studies of the reaction of $Am^+ + CO_2$, the AmO^+ product was observed but only at the detection limit (k/k_{col} = 0.001).[7] Unless this reaction inefficiency is the result of spin-restrictions or a thermal barrier, a small population of

reactants at the nominal temperature (300 K) would be expected to have sufficient energy to react if $D_0(Am^+\text{-}O) \approx D_0(OC\text{-}O) = 5.453 \pm 0.002$ eV so that $D_0(Am^+\text{-}O)$ may actually be lower than that reported. 3) Negative results in the reaction of $Cm^+ + OCS$[14] studied using FT-ICR may indicate that $D_0(Cm^+\text{-}O) \leq D_0(SC\text{-}O) = 6.86 \pm 0.03$ eV, which is 0.08 eV lower than the mean value reported by Marçalo and Gibson. We note that the FT-ICR experiment result is within experimental uncertainty of the reported value and that the FT-ICR results may be influenced by the formation of CmS^+, which is thermodynamically more favored.

In general, the empirical model deviates from the experimental BDE by ~0.3 eV. The largest deviation from the experimental value is the predicted AmO^+ BDE that underestimates the reported bond energy by 0.8 eV, but this may be due to reason 2 in the previous paragraph or an error in the estimated promotion energy. Additionally, the reactive configuration of Th^+ (n = 3) $5f^{n-3}6d^27s$ differs from the typical reactive configuration of An^+, $5f^{n-2}6d^2$, with the exception of Pa^+ (n = 4) that is also $5f^{n-3}6d^27s$. As mentioned above, the *7s*-orbital that is the primary contributor to the σ nonbonding orbital may have some antibonding character resulting from configuration interaction; therefore, a better comparison would use the ThO^+ ($^2\Delta$) BDE = 9.02 ± 0.16 eV in Eq. 6.11. These results are also included in Table 6.4. In general, using the Th^+ ($^2\Delta$) BDE decreases the MAD from the experimental literature value from 0.37 to 0.26, which is comparable to the MADs of several methods from theoretical calculations, Table 6.3, and within experimental uncertainty in most cases. This is of particular note because previously reported theoretical BDEs calculated using DFT functionals underestimated several AnO^+ (Np, Pu, Am, and Cm) BDEs in some cases by a considerable amount for

reasons that are currently unclear.[14]

Presumably the model presented in Eq. 6.13 is useful for estimating any AnL^+ BDE that correlates with any promotion energy, such as is likely true for all AnL^+ if *f*-electrons do not participate in bonding. However, because C has fewer valence electrons available for bonding than O, the binding model may be different than O, which requires 2 electrons that can adopt π-symmetry. This indicates that the applicable E_p for AnC^+ may be the energy required to promote to the first configuration with two non-*f* electrons that can adopt σ or π symmetry, $E_p(6d^2)$ or $E_p(6d7s)$. Therefore, estimates of all AnC^+ BDEs are also calculated using Eq. 6.13 with $D_0(An^+\text{-}C)^* = D_0(Th^+\text{-}C) = 4.82 \pm 0.29$ eV and $E_p(6d^2)$ or $E_p(6d7s)$, respectively, with results listed in Table 6.4. Uncertainties are derived from the uncertainty in $D_0(Th^+\text{-}C)$ and, when applicable, the uncertainty in the estimated promotion energy.

Unlike AnO^+ BDEs, the AnC^+ BDEs are unknown, with the exception of ThC^+ reported here, but $D_0(U^+\text{-}C) = 4.8 \pm 0.5$ eV can be derived from $D_0(U\text{-}C) = 4.72 \pm 0.16$ eV[119] and $IE(UC) = 6.1 \pm 0.5$ eV,[120] and $IE(U) = 6.1914$ eV[28] utilizing Eq. 6.1. Here, the Eq. 6.13 estimate using $E_p(6d^2)$ underestimates the experimental UC^+ BDE but lies within the combined uncertainties. The estimate utilizing $E_p(6d7s)$ reproduces the experimental BDE with high fidelity, but additional information is necessary to determine which model, $E_p(6d^2)$ or $E_p(6d7s)$, yields better results overall.

Conclusion

Analysis of the kinetic energy dependence of the cross section from reaction 6.9, Figure 6.2, indicates that $D_0(Th^+\text{-}O) = 8.51 \pm 0.16$ eV. This value indicates that the BDE

is ~0.2 eV lower than previously accepted literature values, but closely matches the $D_0(Th^+\text{-}O)$ = 8.49 ± 0.13 and 8.59 ± 0.17 eV derived from Eq. 6.1 using the values originally reported by Hildenbrand and Murad[32] and Neubert and Zmbov,[34] respectively, and the updated IEs.[9, 28] This discrepancy likely arises from the choice of parameters used to extrapolate data from high temperatures to 0 K for D_0(Th-O). As noted by Murad and Hildenbrand, the choice of parameters can be a significant source of error.[29, 32] $D_0(Th^+\text{-}O)$ is larger than its transition metal cation congeners, Ti^+, Zr^+, and Hf^+, consistent with the result expected because of lanthanide contraction; however, $D_0(Th^+\text{-}O)$ is weaker than its lanthanide counterpart, $D_0(Ce^+\text{-}O)$, which can be explained in part by the mixed character of the Th^+ J = 3/2 ground-level and by the apparent, slightly antibonding character of the 3σ (largely *7s*) orbital (a result of configuration interaction) compared to the *4f* nonbonding orbital in CeO^+.

Analysis of the cross section in reaction 6.10, Figure 6.2, provides the first experimental report of $D_0(Th^+\text{-}C)$ = 4.82 ± 0.29 eV. IE(ThC) = 6.19 ± 0.34 eV can also be calculated using Eq. 6.1 and the neutral ThC BDE reported by Gupta and Gingerich.[53] This value agrees well with theoretical calculations and is a significant improvement on the previous value reported on the basis of appearance energies in Knudsen effusion cell studies.[53] Like ThO^+, $D_0(Th^+\text{-}C)$ is larger than its transition metal cation congeners, consistent with that expected because of lanthanide contraction.

Finally, ThL^+ BDEs are used to estimate AnL^+ BDEs using the simple model in Eq. 6.13. Subsequent evaluation using the Marçalo and Gibson[13] evaluation of experimental AnO^+ BDEs indicates that this model generally provides estimates within experimental uncertainty of literature values. Because current DFT calculations tend to

underestimate AnO^+ BDEs (in some cases severely),[14] Eq. 6.13 may prove to be a simple and useful tool to estimate AnL^+ BDEs where experimental work would otherwise be difficult.

Associated Content

Analysis of the coupling between V_4 and V_1 potential energy surfaces. Brief evaluation of CeO^+ literature values. ThL^+ (L=C,O) BDEs and molecular parameters of the ground and excited-states evaluated at additional levels of theory. Quantum chemical calculations of ThC.

Acknowledgements

This work is supported by the Heavy Element Chemistry Program, Office of Basic Energy Sciences, U. S. Department of Energy, through Grants No. DE-SC0012249 (PBA) and DE-FG02-12ER16329 (KAP). PBA and RMC also thank the Center for High Performance Computing at the University of Utah for the generous allocation of computer time. Dr. Bert de Jong is thanked for his helpful advice on spin-orbit calculations.

References

(1) Armentrout, P. B.; Beauchamp, J. L., *Chem. Phys.* **1980,** *50*, 21-25.

(2) Armentrout, P. B.; Beauchamp, J. L., *Chem. Phys.* **1980,** *50*, 27-36.

(3) Cornehl, H. H.; Wesendrup, R.; Diefenbach, M.; Schwarz, H., *Chem. - Eur. J.* **1997,** *3*, 1083-1090.

(4) Gibson, J. K.; Haire, R. G., *Inorg. Chem.* **2002,** *41*, 5897-5906.

(5) Santos, M.; Marcalo, J.; Pires, d. M. A.; Gibson, J. K.; Haire, R. G., *J. Phys. Chem. A* **2002,** *106*, 7190-7194.

(6) Gibson, J. K., *J. Phys. Chem. A* **2003,** *107*, 7891-7899.

(7) Santos, M.; Marcalo, J.; Leal, J. P.; Pires de Matos, A.; Gibson, J. K.; Haire, R. G., *Int. J. Mass Spectrom.* **2003,** *228*, 457-465.

(8) Gibson, J. K.; Haire, R. G.; Santos, M.; Marcalo, J.; Pires, d. M. A., *J. Phys. Chem. A* **2005,** *109*, 2768-2781.

(9) Goncharov, V.; Heaven, M. C., *J. Chem. Phys.* **2006,** *124*, 064312.

(10) Heaven, M. C., *Phys. Chem. Chem. Phys.* **2006,** *8*, 4497-4509.

(11) Gibson, J. K.; Haire, R. G.; Marcalo, J.; Santos, M.; Leal, J. P.; Pires de Matos, A.; Tyagi, R.; Mrozik, M. K.; Pitzer, R. M.; Bursten, B. E., *Eur. Phys. J. D* **2007,** *45*, 133-138.

(12) Gibson, J. K.; Haire, R. G.; Marçalo, J.; Santos, M.; Pires de Matos, A.; Mrozik, M. K.; Pitzer, R. M.; Bursten, B. E., *Organometallics* **2007,** *26*, 3947-3956.

(13) Marcalo, J.; Gibson, J. K., *J. Phys. Chem. A* **2009,** *113*, 12599-12606.

(14) Pereira, C. C. L.; Marsden, C. J.; Marcalo, J.; Gibson, J. K., *Phys. Chem. Chem. Phys.* **2011,** *13*, 12940-12958.

(15) Heaven, M. C.; Barker, B. J.; Antonov, I. O., *J. Phys. Chem. A* **2014,** *118*, 10867-10881.

(16) Cox, R. M.; Armentrout, P. B.; de Jong, W. A., *Inorg. Chem.* **2015,** *54*, 3584-3599.

(17) Cox, R. M.; Armentrout, P. B.; de Jong, W. A., *manuscript in preparation*.

(18) Mazzone, G.; Michelini, M. d. C.; Russo, N.; Sicilia, E., *Inorg. Chem.* **2008,** *47*, 2083-2088.

(19) Almeida, K. J. d.; Duarte, H. A., *Organometallics* **2009,** *28*, 3203-3211.

(20) di Santo, E.; Michelini, M. d. C.; Russo, N., *Organometallics* **2009,** *28*, 3716-3726.

(21) di Santo, E.; Michelini, M. C.; Russo, N., *J. Phys. Chem. A* **2009,** *113*, 14699-14705.

(22) Infante, I.; Kovacs, A.; La, M. G.; Shahi, A. R. M.; Gibson, J. K.; Gagliardi, L., *J. Phys. Chem. A* **2010,** *114*, 6007-6015.

(23) Zhou, J.; Schlegel, H. B., *J Phys Chem A* **2010,** *114*, 8613-8617.

(24) de Almeida, K. J.; Duarte, H. A., *Organometallics* **2010,** *29*, 3735-3745.

(25) Kovacs, A.; Konings, R. J. M., *J. Phys. Chem. A* **2011,** *115*, 6646-6656.

(26) Averkiev, B. B.; Mantina, M.; Valero, R.; Infante, I.; Kovacs, A.; Truhlar, D. G.; Gagliardi, L., *Theor. Chem. Acc.* **2011,** *129*, 657-666.

(27) Kohler, S.; Deissenberger, R.; Eberhardt, K.; Erdmann, N.; Herrmann, G.; Huber, G.; Kratz, J. V.; Nunnemann, M.; Passler, G.; Rao, P. M.; Riegel, J.; Trautmann, N.; Wendt, K., *Spectrochim. Acta, Part B* **1997,** *52B*, 717-726.

(28) Sansonetti, J. E.; Martin, W. C., *J. Phys. Chem. Ref. Data* **2005,** *34*, 1559-2259.

(29) Pedley, J. B.; Marshall, E. M., *J. Phys. Chem. Ref. Data* **1983,** *12*, 967-1031.

(30) Ackermann, R. J.; Rauh, E. G.; Thorn, R. J.; Cannon, M. C., *J. Phys. Chem.* **1963,** *67*, 762-769.

(31) Ackermann, R. J.; Rauh, E. G., *High Temp. Sci.* **1973,** *5*, 463-473.

(32) Hildenbrand, D. L.; Murad, E., *J. Chem. Phys.* **1974,** *61*, 1232-1237.

(33) Murad, E.; Hildenbrand, D. L., *J. Chem. Phys.* **1975,** *63*, 1133-1139.

(34) Neubert, A.; Zmbov, K. F., *High Temp. Sci.* **1974,** *6*, 303-308.

(35) Loh, S. K.; Lian, L.; Armentrout, P. B., *J. Chem. Phys.* **1989,** *91*, 6148-6163.

(36) Loh, S. K.; Fisher, E. R.; Lian, L.; Schultz, R. H.; Armentrout, P. B., *J. Phys. Chem.* **1989,** *93*, 3159-3167.

(37) Fisher, E. R.; Elkind, J. L.; Clemmer, D. E.; Georgiadis, R.; Loh, S. K.; Aristov, N.; Sunderlin, L. S.; Armentrout, P. B., *J. Chem. Phys.* **1990,** *93*, 2676-2691.

(38) Clemmer, D. E.; Elkind, J. L.; Aristov, N.; Armentrout, P. B., *J. Chem. Phys.* **1991,** *95*, 3387-3393.

(39) Chen, Y.-M.; Armentrout, P. B., *J. Chem. Phys.* **1995,** *103*, 618-625.

(40) Sievers, M. R.; Chen, Y.-M.; Armentrout, P. B., *J. Chem. Phys.* **1996,** *105*, 6322-6333.

(41) Zhang, X.-G.; Armentrout, P. B., *J. Phys. Chem. A* **2003,** *107*, 8904-8914.

(42) Hinton, C. S.; Li, F.; Armentrout, P. B., *Int. J. Mass Spectrom.* **2009,** *280*, 226-234.

(43) Armentrout, P. B., *J. Chem. Phys.* **2013,** *139*, 084305.

(44) Armentrout, P. B.; Li, F.-X., *J. Phys. Chem. A* **2013,** *117*, 7754-7766.

(45) Edvinsson, G. Dissertation, Stockholm, 1971.

(46) Hurber, K. P.; Herzberg, G., In *NIST Chemistry WebBook, NIST Standard Reference 69*, Linstrom, P. J.; Mallard, W. G., Eds. National Institute of Standards and Technology: Gaithersburg, MD.

(47) Paulovic, J.; Nakajima, T.; Hirao, K.; Lindh, R.; Malmqvist, P. A., *J. Chem. Phys.* **2003,** *119*, 798-805.

(48) Kuechle, W.; Dolg, M.; Stoll, H.; Preuss, H., *J. Chem. Phys.* **1994,** *100*, 7535-7542.

(49) Lias, S. G.; Bartmess, J. E.; Liebman, J. F.; Holmes, J. L.; Levin, R. D.; Mallard, W. G., *J. Phys. Chem. Ref. Data, Suppl.* **1988,** *17*, 1-861

(50) Konings, R. J. M.; Benes, O.; Kovacs, A.; Manara, D.; Sedmidubsky, D.; Gorokhov, L.; Iorish, V. S.; Yungman, V.; Shenyavskaya, E.; Osina, E., *J. Phys. Chem. Ref. Data* **2014,** *43*, 01310101-01310195.

(51) Sugar, J., *J. Chem. Phys.* **1974,** *60*, 4103.

(52) Rauh, E. G.; Ackermann, R. J., *J. Chem. Phys.* **1974,** *60*, 1396-1400.

(53) Gupta, S. K.; Gingerich, K. A., *J. Chem. Phys.* **1980,** *72*, 2795-2800.

(54) Kohl, F. J.; Stearns, C. A., *High Temp. Sci.* **1974,** *6*, 284-302.

(55) Loh, S. K.; Hales, D. A.; Li, L.; Armentrout, P. B., *J. Chem. Phys.* **1989,** *90*, 5466-5485.

(56) Schultz, R. H.; Armentrout, P. B., *Int. J. Mass Spectrom. Ion Processes* **1991,** *107*, 29-48.

(57) Teloy, E.; Gerlich, D., *Chem. Phys.* **1974,** *4*, 417-427.

(58) Armentrout, P. B., *Int. J. Mass Spectrom.* **2000,** *200*, 219-241.

(59) Ervin, K. M.; Armentrout, P. B., *J. Chem. Phys.* **1985,** *83*, 166-189.

(60) Chantry, P. J., *J. Chem. Phys.* **1971,** *55*, 2746-2759.

(61) Haynes, C. L.; Armentrout, P. B., *Organometallics* **1994,** *13*, 3480-3490.

(62) Clemmer, D. E.; Chen, Y.-M.; Khan, F. A.; Armentrout, P. B., *J. Phys. Chem.* **1994,** *98*, 6522-6529.

(63) Kickel, B. L.; Armentrout, P. B., *J. Am. Chem. Soc.* **1995,** *117*, 764-773.

(64) Kickel, B. L.; Armentrout, P. B., *J. Am. Chem. Soc.* **1995,** *117*, 4057-4070.

(65) Sievers, M. R.; Chen, Y.-M.; Elkind, J. L.; Armentrout, P. B., *J. Phys. Chem.* **1996,** *100*, 54-62.

(66) Blaise, J.; Wyart, J.-F. Selected Constants, Energy Levels, and Atomic Spectra of Actinides. http://web2.lac.u-psud.fr/lac/Database/Contents.html (acessed 2/9/2015)

(67) Chesnavich, W. J.; Bowers, M. T., *J. Phys. Chem.* **1979,** *83*, 900-905.

(68) Muntean, F.; Armentrout, P. B., *J. Chem. Phys.* **2001,** *115*, 1213-1228.

(69) Aristov, N.; Armentrout, P. B., *J. Am. Chem. Soc.* **1986,** *108*, 1806-1819.

(70) Weber, M. E.; Elkind, J. L.; Armentrout, P. B., *J. Chem. Phys.* **1986,** *84*, 1521-1529.

(71) Frisch, M. J.; Trucks, G. W.; Schlegel, H. B.; Scuseria, G. E.; Robb, M. A.; Cheeseman, J. R.; Scalmani, G.; Barone, V.; Mennucci, B.; Petersson, G. A.; Nakatsuji, H.; Caricato, M.; Li, X.; Hratchian, H. P.; Izmaylov, A. F.; Bloino, J.; Zheng, G.; Sonnenberg, J. L.; Hada, M.; Ehara, M.; Toyota, K.; Fukuda, R.; Hasegawa, J.; Ishida, M.; Nakajima, T.; Honda, Y.; Kitao, O.; Nakai, H.; Vreven, T.; Montgomery, J. A., Jr.; Peralta, J. E.; Ogliaro, F.; Bearpark, M.; Heyd, J. J.; Brothers, E.; Kudin, K. N.; Staroverov, V. N.; Kobayashi, R.; Normand, J.; Raghavachari, K.; Rendell, A.; Burant, J. C.; Iyengar, S. S.; Tomasi, J.; Cossi, M.; Rega, N.; Millam, N. J.; Klene, M.; Knox, J. E.; Cross, J. B.; Bakken, V.; Adamo, C.; Jaramillo, J.; Gomperts, R.; Stratmann, R. E.; Yazyev, O.; Austin, A. J.; Cammi, R.; Pomelli, C.; Ochterski, J. W.; Martin, R. L.; Morokuma, K.; Zakrzewski, V. G.; Voth, G. A.; Salvador, P.; Dannenberg, J. J.; Dapprich, S.; Daniels, A. D.; Farkas, Ö.; Foresman, J. B.; Ortiz, J. V.; Cioslowski, J.; Fox, D. J., Gaussian 09, Revision A.1. Gaussian, Inc: Wallingford CT, 2009.

(72) Peterson, K. A., *J. Chem. Phys.* **2015,** *142*, 074105.

(73) Weigand, A.; Cao, X.; Hangele, T.; Dolg, M., *J. Phys. Chem. A* **2014,** *118*, 2519-2530.

(74) Cao, X.; Dolg, M.; Stoll, H., *J. Chem. Phys.* **2003,** *118*, 487-496.

(75) Woon, D. E.; Dunning, T. H., Jr., *J. Chem. Phys.* **1995,** *103*, 4572-4585.

(76) Dunning, T. H., Jr., *J. Chem. Phys.* **1989,** *90*, 1007-1023.

(77) Krishnan, R.; Binkley, J. S.; Seeger, R.; Pople, J. A., *J. Chem. Phys.* **1980,** *72*, 650-654.

(78) Karton, A.; Martin, J. M. L., *Theor. Chem. Acc.* **2006,** *115*, 330-333.

(79) Martin, J. M. L., *Chem. Phys. Lett.* **1996,** *259*, 669-678.

(80) Becke, A. D., *J. Chem. Phys.* **1993,** *98*, 5648-5652.

(81) Lee, C.; Yang, W.; Parr, R. G., *Phys. Rev. B: Condens. Matter* **1988,** *37*, 785-789.

(82) Perdew, J. P.; Burke, K.; Wang, Y., *Phys. Rev. B: Condens. Matter* **1996,** *54*, 16533-16539.

(83) Becke, A. D., *J. Chem. Phys.* **1993,** *98*, 1372-1377.

(84) Zhao, Y.; Truhlar, D. G., *Theor. Chem. Acc.* **2008,** *120*, 215-241.

(85) Adamo, C.; Barone, V., *J. Chem. Phys.* **1999,** *110*, 6158-6170.

(86) Zhang, X.; Schwarz, H., *Chem. Eur. J.* **2010,** *16*, 5882 – 5888.

(87) Purvis, G. D., III; Bartlett, R. J., *J. Chem. Phys.* **1982,** *76*, 1910-1918.

(88) Pople, J. A.; Head-Gordon, M.; Raghavachari, K., *J. Chem. Phys.* **1987,** *87*, 5968-5975.

(89) Scuseria, G. E.; Janssen, C. L.; Schaefer, H. F., III, *J. Chem. Phys.* **1988,** *89*, 7382-7387.

(90) Scuseria, G. E.; Schaefer, H. F., III, *J. Chem. Phys.* **1989,** *90*, 3700-3703.

(91) Foresman, J. B.; Frisch, A. E., *Exploring Chemistry with Electronic Structure Methods*. 2nd ed.; Gaussian, Inc.: Pittsburgh, PA, 1996.

(92) Garcia, M. A.; Morse, M. D., *J. Chem. Phys.* **2011,** *135*, 114304.

(93) Armentrout, P. B.; Parke, L.; Hinton, C.; Citir, M., *ChemPlusChem* **2013,** *78*, 1157-1173.

(94) Douglas, M.; Kroll, N. M., *Ann. Phys. (N. Y.)* **1974,** *82*, 89-155.

(95) Reiher, M.; Wolf, A., *J. Chem. Phys.* **2004,** *121*, 10945-10956.

(96) Kendall, R. A.; Dunning, T. H., Jr.; Harrison, R. J., *J. Chem. Phys.* **1992,** *96*, 6796-6806.

(97) de Jong, W. A.; Harrison, R. J.; Dixon, D. A., *J. Chem. Phys.* **2001,** *114*, 48-53.

(98) Feller, D.; Peterson, K. A.; Dixon, D. A., *J. Chem. Phys.* **2008,** *129*, 204105.

(99) *DIRAC, a relativistic ab initio electronic structure program, Release DIRAC14 (2014)*, written by T. Saue, L. V., H. J. Aa. Jensen, and R. Bast, with contributions from V. Bakken, K. G. Dyall, S. Dubillard, U. Ekström, E. Eliav, T. Enevoldsen, E. Faßhauer, T. Fleig, O. Fossgaard, A. S. P. Gomes, T. Helgaker, J. Henriksson, M. Iliaš, Ch. R. Jacob, S. Knecht, S. Komorovský, O. Kullie, C. V. Larsen, J. K. Lærdahl, Y. S. Lee, H. S. Nataraj, P. Norman, G. Olejniczak, J. Olsen, Y. C. Park, J. K. Pedersen, M. Pernpointner, R. di Remigio, K. Ruud, P. Sałek, B. Schimmelpfennig, J. Sikkema, A. J. Thorvaldsen, J. Thyssen, J. van Stralen, S. Villaume, O. Visser, T. Winther, and S. Yamamoto (see http://www.diracprogram.org).

(100) Park, Y.-C.; Lim, I. S.; Lee, Y. S., *Bull. Kor. Chem. Soc.* **2012,** *33*, 803.

(101) Visscher, L.; Lee, T. J.; Dyall, K. G., *J. Chem. Phys.* **1996,** *105*, 8769-8776.

(102) Dyall, K. G.; Bauschlicher, C. W.; Schwenke, D. W.; Pyykko, P., *Chem. Phys. Lett.* **2001,** *348*, 497-500.

(103) Pyykko, P.; Zhao, L.-B., *J. Phys. B: At., Mol. Opt. Phys.* **2003,** *36*, 1469-1478.

(104) *MOLPRO, version 2012.1, a package of ab initio programs*, written by H. -J. Werner, P. J. K., G. Knizia, F. R. Manby, M. Schutz, P. Celani, T. Korona, R. Lindh, A. Mitrushenkov, G. Rauhut, K. R. Shamasundar, T. B. Adler, R. D. Amos, A. Bernhardsson, A. Berning, D. L. Cooper, M. J. O. Deegan, A. J. Dobbyn, F. Eckert, E. Goll, C. Hampel, A. Hesselmann, G. Hertzer, T. Hrenar, G. Jansen, C. Koppl, Y. Liu, A. W. Lloyd, R. A. Mata, A. J. May, S. J. McNicholas, W. Meyer, M. E. Mura, A. Nicklass, D. P. O'Neill, P. Palmieri, D. Peng, K. Pflüger, R. Pitzer, M. Reiher, T. Shiozaki, H. Stoll, A. J. Stone, R. Tarroni, T. Thorsteinsson, M. Wang (see see http://www.molpro.net).

(105) Gioumousis, G.; Stevenson, D. P., *J. Chem. Phys.* **1958,** *29*, 294-299.

(106) NIST Computational Chemistry Comparison and Benchmark Database NIST Standard Reference Database Number 101 Release 16a. Johnson III, R. D.Ed. http://cccbdb.nist.gov (acessed 8/20/2014)

(107) Waber, J. T.; Cromer, D. T., *The Journal of Chemical Physics* **1965,** *42*, 4116-4123.

(108) Huber, K. P.; Herzberg, G., *Molecular Spectra and Molecular Structure. IV. Constants of Diatomic Molecules*. Van Nostrand Reinhold Co.: 1979.

(109) Cox, R. M; Armentrout, P. B., *To be published*.

(110) *This Work see Supporting Information*.

(111) Zhang, X.-G.; Liyanage, R.; Armentrout, P. B., *J. Am. Chem. Soc.* **2001,** *123*, 5563-5575.

(112) Zhang, X.-G.; Armentrout, P. B., *J. Chem. Phys.* **2002,** *116*, 5565-5573.

(113) Li, F.-X.; Zhang, X.-G.; Armentrout, P. B., *Int. J. Mass Spectrom.* **2006,** *255/256*, 279-300.

(114) Schroder, D.; Schwarz, H.; Shaik, S., *Struct. Bonding (Berlin)* **2000,** *97*, 91-123.

(115) Wu, Z. J.; Guan, W.; Meng, J.; Su, Z. M., *J. Cluster Sci.* **2007,** *18*, 444-458.

(116) Nakao, Y.; Hirao, K.; Taketsugu, T., *J. Chem. Phys.* **2001,** *114*, 7935-7940.

(117) Van Zee, R. J.; Li, S.; Weltner, W., Jr., *Chem. Phys. Lett.* **1994,** *217*, 381-386.

(118) Kingcade, J. E., Jr.; Cocke, D. L.; Gingerich, K. A., *High Temp. Sci.* **1983,** *16*, 89-109.

(119) Gupta, S. K.; Gingerich, K. A., *J. Chem. Phys.* **1979,** *71*, 3072-3080.

(120) Gingerich, K. A., *J. Chem. Phys.* **1969,** *50*, 2255-2256.

Table 6.1. Fitting parameters from Eq. 6.2 for the indicated reaction cross section.

Reaction	n	σ_0	E_0 (eV)	$D_0(Th^+\text{-}L)$
$Th^+ + CO \rightarrow ThO^+ + C$	1.4 ± 0.2	3.5 ± 1.0	2.60 ± 0.16	8.51 ± 0.16
$Th^+ + CO \rightarrow ThC^+ + O$	1.6 ± 0.2	0.8 ± 0.3	6.29 ± 0.29	4.82 ± 0.29

Table 6.2. Molecular parameters and relative energies (in eV) of low-lying states of ThO^+ and ThC^+.[a]

ThL^+	State	r(Th^+-L)[b]	ν[b]	Expt.[c]	CCSD(T)[d]	B3LYP	B3PW91	BHLYP	M06	PBE0
ThO^+	$^2\Sigma^+$ ($1\sigma^2 2\sigma^2 1\pi^4 3\sigma$)	1.808	950	0.00	0.00	0.00	0.00	0.00	0.00	0.00
		(1.807)	(955)							
	$^2\Delta$ ($1\sigma^2 2\sigma^2 1\pi^4 1\delta$)	1.825	902	0.58[f]	0.58	0.51	0.41	0.48	0.36	0.41
			(918[e])							
	$^2\Pi$ ($1\sigma^2 2\sigma^2 1\pi^3 3\sigma^2$)	1.834	884	0.92[g]	1.21	0.96	0.84	1.01	0.73	0.86
			(904)							
	$^4\Delta$ ($1\sigma^2 1\pi^4 2\sigma 1\delta 3\sigma$)	2.003	672		4.48	4.25	4.24	3.95	4.56	4.21
	$^4\Pi$ ($1\sigma^2 2\sigma 1\pi^4 3\sigma 2\pi$)	2.007	666		4.91	4.39	4.42	4.20	4.57	4.41
	$^4\Sigma^+$ ($1\sigma^2 2\sigma 1\pi^4 3\sigma 4\sigma$)	2.006	669		5.07	4.49	4.52	4.33	4.70	4.52
	$^4\Sigma^-$ ($1\sigma^2 2\sigma 1\pi^4 1\delta^2$)	2.017	653		5.35	5.20	5.13	4.87	5.36	5.09

Table 6.2 (continued)

ThL^+	State	$r(Th^+-L)^b$	ν^b	Experimental[c]	CCSD(T)[d]	B3LYP	B3PW91	BHLYP	M06	PBE0
ThC^+	$^2\Sigma^+$ ($1\sigma^2 1\pi^4 2\sigma$)	1.902	903		0.00	0.00	0.00	0.00	0.00	0.00
	$^4\Pi$ ($1\sigma^2 1\pi^3 2\sigma 3\sigma$)	2.049	766		0.80	0.61	0.69	0.52	0.94	0.70
	$^2\Pi$ ($1\sigma^2 1\pi^3 2\sigma^2$)	2.023	668		0.82	0.64	0.77	0.55	0.85	0.77
	$^4\Phi$ ($1\sigma^2 1\pi^3 2\sigma 1\delta$)	2.068	737		1.32	1.07	1.09	0.95	1.22	1.09
	$^4\Sigma^-$ ($1\sigma^2 1\pi^2 2\sigma^2 1\delta$)	2.124	696		1.55	1.31	1.46	1.27	1.50	1.50
	$^2\Delta$ ($1\sigma^2 1\pi^4 1\delta$)	1.962	828		1.79	1.68	1.76	1.68	1.67	1.79
	$^2\Pi$ ($1\sigma^2 1\pi^4 2\pi$)	1.970	814		2.41	2.08	2.12	2.17	2.02	2.18

[a] Structure optimized at respective level of theory (except CCSD(T)) using cc-pwCVQZ-PP-MDF/aug-cc-pwCVQZ basis sets.
[b] Bond lengths (in Å) or frequencies (in cm^{-1}) from B3LYP/cc-pwCVQZ-PP-MDF/aug-cc-pwCVQZ optimized structures. Frequencies scaled by 0.989. Value in parentheses are experimental values from Ref. 9.
[c] Ref. 9.
[d] Single-point energies calculated using B3LYP/KAP/6-311+G(3df) optimized structures.
[e] Frequency of the $^2\Delta_{3/2}$ level. Frequency of the $^2\Delta_{5/2}$ level is 915 cm^{-1}.
[f] Average energy of the $^2\Delta$ state weighted over all spin-orbit degeneracies.
[g] Energy of the $^2\Pi_{1/2}$ level.

Table 6.3. Comparison of theoretical $D_0(Th^+-R)$ to experimental values (in eV).[a]

	Experimental			Theoretical			
ThL^+	Literature	This Work	Basis Set	CCSD(T)[b]	B3LYP	B3PW91	PBE0
ThO^+	8.74 ± 0.25[c]	8.51 ± 0.16	SDD	8.76	8.61	8.73	
	8.70 ± 0.10[d]		Seg. SDD	8.55	8.75	8.88	8.82
	≥ 7.85[e]		cc-pwCVQZ-PP-MDF[f]	8.70	8.70	8.80	8.75
			CBS-MDF[g]	8.94	8.89	8.99	8.94
			FPD[h]	8.81			
ThC^+	$\geq 3.12 \pm 0.21$[i]	4.82 ± 0.29	SDD	4.90	4.84	5.21	
			Seg. SDD	4.72	4.92	5.30	5.33
			cc-pwCVQZ-PP-MDF	4.92	4.81	5.16	5.20
			CBS-MDF	5.18	4.99	5.34	5.38
			FPD	5.00			
MAD[j]			SDD	0.17	0.06	0.31	
			Seg. SDD	0.07	0.17	0.43	0.41
			cc-pwCVQZ-PP-MDF	0.14	0.10	0.41	0.31
			CBS-MDF	0.40	0.28	0.50	0.50
			FPD	0.24			

Table 6.3 Continued

[a] From structures optimized at the respective level of theory (except CCSD(T)) with the indicated basis set. Energies include estimated spin-orbit correction of -0.40 eV. See text and Ref. 16.
[b] Energies from single-point calculations using B3LYP optimized structures with the indicated basis set for Th^+.
[c] Ref. 13.
[d] Calculated from D_0(Th-O) from Ref. 50 utilizing IE(ThO) from Ref. 9 and IE(Th) from Ref. 28. See text.
[e] Ref. 5.
[f] cc-pwCVQZ-PP-MDF/aug-cc-pwcVQZ basis sets.
[g] Complete basis set limit extrapolated from pwCVXZ-PP-MDF/cc-pwCVXZ (X = T, Q) basis sets using Eq. 6.4 and 6.5, see text.
[h] Feller-Peterson-Dixon model for composite thermochemistry. See text and Eq. 6.6. Parameters found in Table C.5. in the Supporting Information.
[i] Ref. 53.
[j] Mean absolute deviation from experimental value.

Table 6.4. Estimates of $D_0(An^+-L)$ (in eV) from Eq. 6.11 using An^+ electronic parameters.[a]

An^+ (config.)	Reactive config.	E_p[b]	Experimental[c]	$D_0(An^+-O)$	$D_0(An^+-O)$*[d]	Experimental	$D_0(An^+-C)$
Ac^+ ($7s^2$)	$6d^2$	1.64		6.87 ± 0.16	7.38 ± 0.16		3.18 ± 0.29
	$6d7s$	0.59		7.92 ± 0.16	8.43 ± 0.16		4.23 ± 0.29
Th^+ ($6d^27s$)	$6d^27s$	0.00	8.51 ± 0.16[e]	8.51 ± 0.16	9.02 ± 0.16	4.82 ± 0.29[e]	4.82 ± 0.29
Pa^+ ($5f^27s^2$)	$5f6d^27s$	0.59	8.29 ± 0.52	7.92 ± 0.16	8.43 ± 0.16		4.23 ± 0.29
	$5f^26d7s$	0.10		8.41 ± 0.16	8.92 ± 0.16		4.72 ± 0.29
U^+($5f^37s^2$)	$5f^36d^2$	0.57	8.02 ± 0.13	7.94 ± 0.16	8.45 ± 0.16	4.8 ± 0.5[f]	4.25 ± 0.29
	$5f^36d7s$	0.04		8.47 ± 0.16	8.98 ± 0.16		4.78 ± 0.29
Np^+ ($5f^46d7s$)	$5f^46d^2$	0.90 ± 0.40[g]	7.88 ± 0.10	7.61 ± 0.43	8.12 ± 0.43		3.92 ± 0.49
	$5f^46d7s$	0.00		8.51 ± 0.16	9.02 ± 0.16		4.82 ± 0.29
Pu^+ ($5f^67s$)	$5f^56d^2$	2.14	6.75 ± 0.20	6.37 ± 0.16	6.88 ± 0.16		2.68 ± 0.29
	$5f^56d7s$	1.08		7.43 ± 0.16	7.94 ± 0.16		3.74 ± 0.29
Am^+ ($5f^77s$)	$5f^66d^2$	3.60 ± 0.20[g]	5.80 ± 0.29	4.91 ± 0.26	5.42 ± 0.26		1.22 ± 0.35
	$5f^66d7s$	2.50 ± 0.10[g]		6.01 ± 0.19	6.52 ± 0.19		2.32 ± 0.31
Cm^+ ($5f^77s^2$)	$5f^76d^2$	1.84	6.94 ± 0.39	6.67 ± 0.16	7.18 ± 0.16		2.98 ± 0.29
	$5f^76d7s$	0.50		8.01 ± 0.16	8.52 ± 0.16		4.32 ± 0.29
MAD[h]	$5f^46d^2$			0.38	0.26		0.56
	$5f^{n-2}6d7s$			0.53	1.04		0.03

Table 6.4 Continued

[a] Model BDEs calculated using Eq. 6.11 for the specified E_p. See text. Uncertainty estimated from uncertainty in $D_0(An^+\text{-}L)^*$ and estimated E_p when applicable.
[b] Unless noted otherwise, from Ref. 28.
[c] Unless noted otherwise, from Ref. 13.
[d] Model BDE calculated using Eq. 6.11 with ThO^+ ($^2\Delta_1$) BDE. See text.
[e] This work.
[f] Calculated with Eq. 6.1 with values from Refs. 28, 116, and 117.
[g] Estimated E_p from Ref. 13.
[h] Mean absolute deviation of designated model BDE from the experimental mean. Value excludes ThL^+

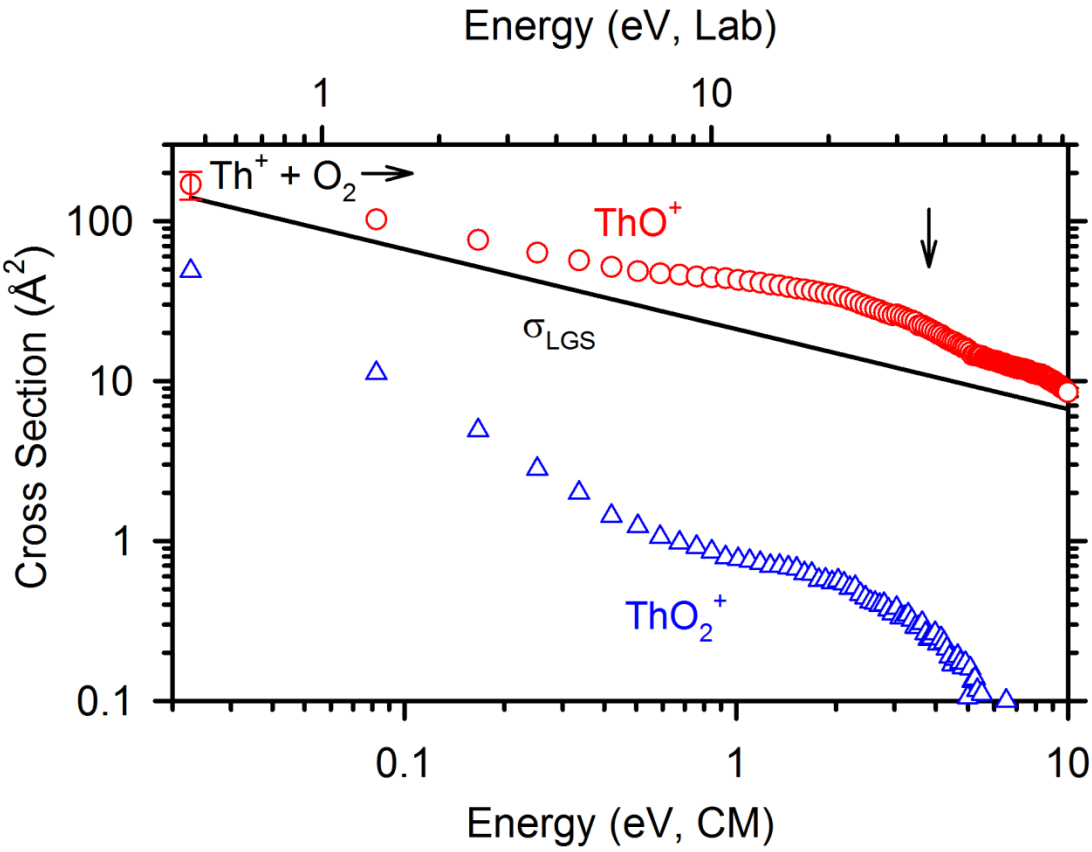

Figure 6.1. The absolute cross section of the reaction of $Th^+ + O_2$ as a function of kinetic energy in the laboratory (upper x-axis) and center-of-mass (lower x-axis) frames. The solid line represents the Langevin-Gioumousis-Stevenson collision limit. The arrow shows D_0(O-O) = 5.117 ± 0.001 eV.

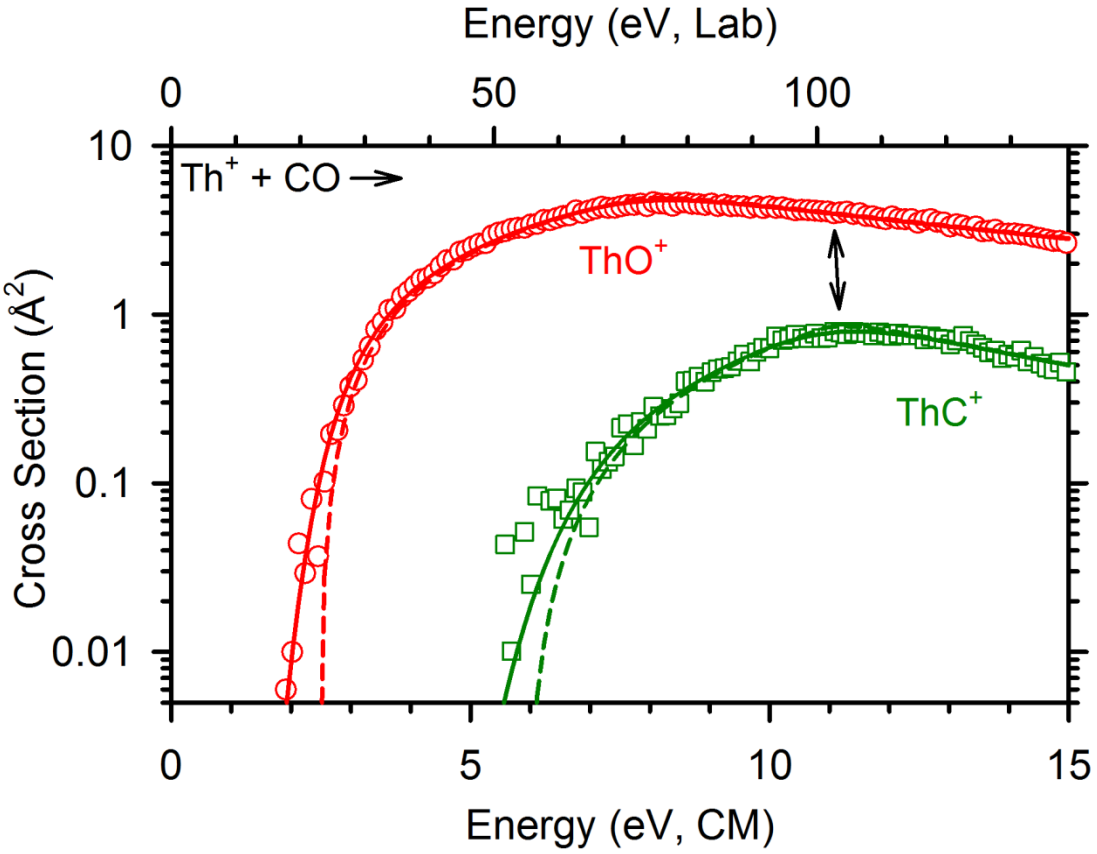

Figure 6.2. The absolute cross section of the reaction of Th^+ + CO as a function of kinetic energy in the laboratory (upper x-axis) and center-of-mass (lower x-axis) frames with model cross sections, Eq. 6.2, convoluted over the reactant internal energies (solid lines) and unconvoluted (dashed lines). The arrow shows D_0(C-O) = 11.109 ± 0.005 eV.

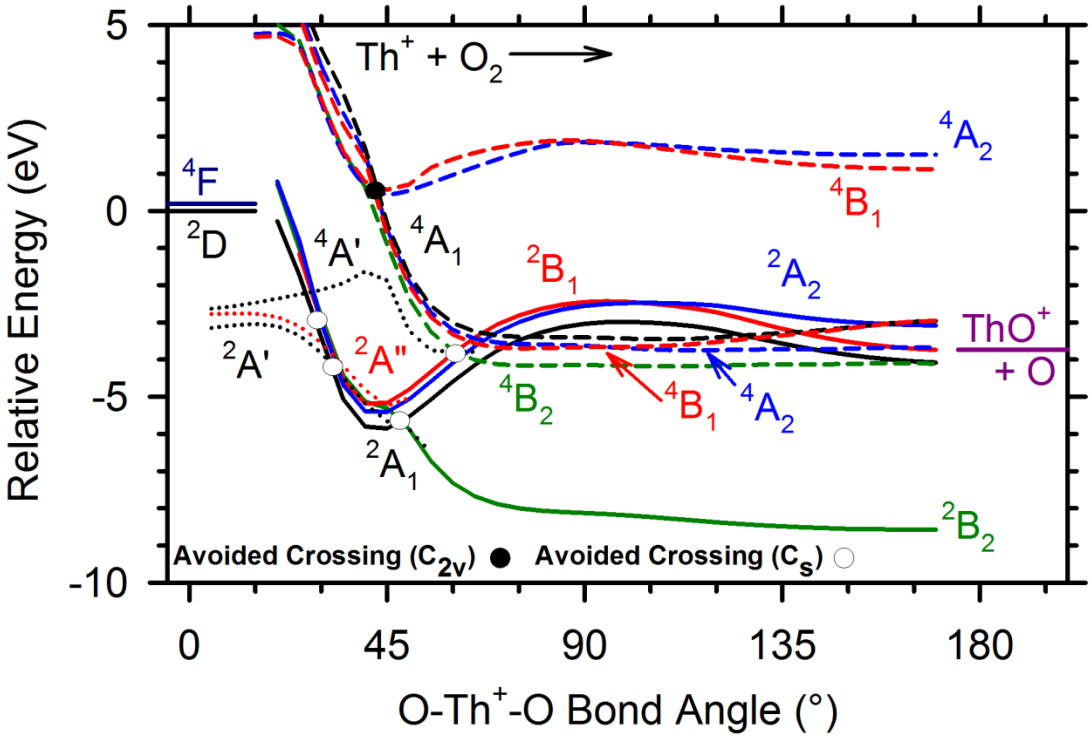

Figure 6.3. B3LYP/SDD-VDZ-MWB/6-311+G(3df) relaxed energy calculations of the potential energy surface of the $Th^+ + O_2$ reaction as a function of ∠OTh^+O in degrees. The energies are relative to Th^+ (^2D, $6d7s^2$) + O_2. Doublet surfaces are represented by solid lines and quartet surfaces by dashed lines. Surfaces with C_s symmetry are represented by dotted lines.

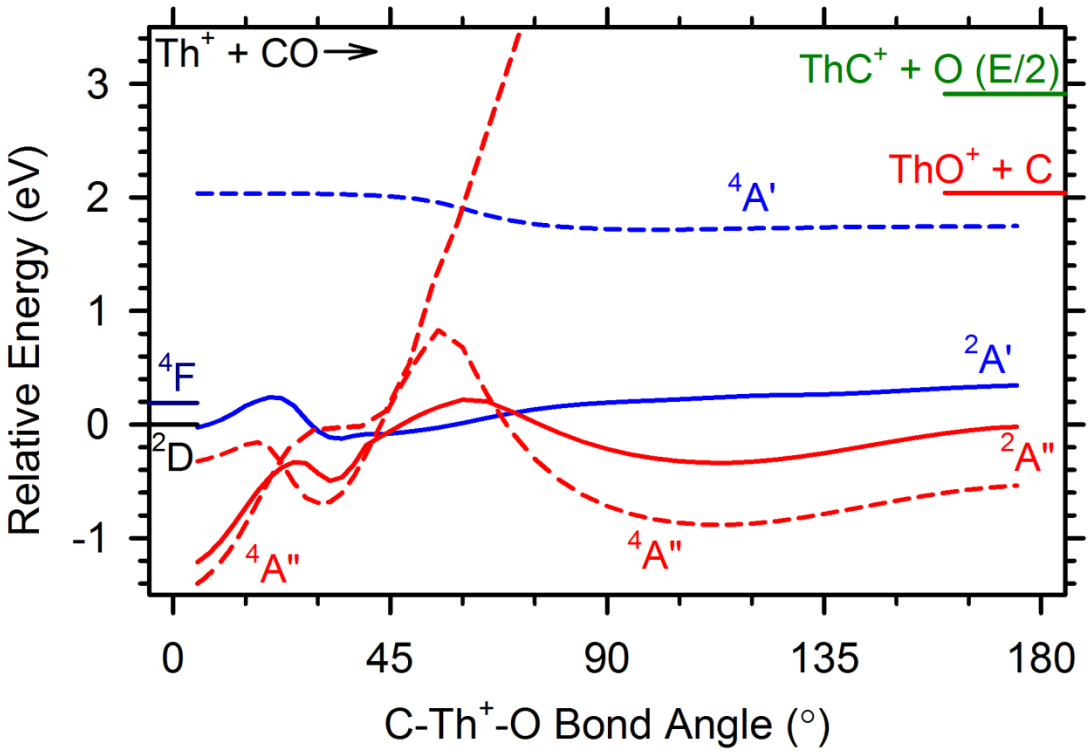

Figure 6.4. B3LYP/SDD-VDZ-MWB/6-311+G(3df) relaxed potential energy surface calculations of the Th^+ + CO reaction in C_s symmetry as a function of ∠CTh^+O in degrees. Energies are relative to Th^+ (^2D, $6d7s^2$) + CO. Doublet surfaces are represented by solid lines and quartet surfaces by dashed lines.

APPENDIX A

SUPPORTING INFORMATION FOR CHAPTER 4

Assignment of Th^+ levels

In Th^+, the $^2D_{3/2}$ and $^2D_{5/2}$ ($6d7s^2$) levels mix extensively with the $^4F_{3/2}$ and $^4F_{5/2}$ ($6d^27s$) levels[1] such that the choice of levels representative of each state for comparison to theoretical calculations is difficult. Three levels at 0, 1860, and 4113 cm^{-1} are identified with ~ 30 % ^2D character (Table A.1).[1] The level at 4113 cm^{-1} has $^2D_{5/2}$ as its primary component. Of the two remaining levels, the level at 1860 cm^{-1} has more $^2D_{3/2}$ (36%) character than the ground-level (27%). Because it has more $^2D(6d7s^2)$ character, the level at 1860 cm^{-1} is assigned as ^2D, and the ground-level is assigned as ^4F. The ^4F spin-orbit levels are chosen as identified in Table A.1 so that after averaging the ^2D and ^4F states over all spin-orbit levels, the ^2D state lies 517.97 cm^{-1} below the ^4F state. As a reference, the $^4F_{3/2}$ lies 3729.96 cm^{-1} (0.46 eV) below the ^4F energy averaged over all spin-orbit levels, and the $^2D_{3/2}$ lies 1352.05 cm^{-1} (0.17 eV) below the averaged ^2D energy. All other spin-orbit components of each state are relatively unambiguous, Table A.1.

Alternatively, the ground-level could have been chosen as the J = 3/2 spin-orbit component of the ^2D state instead of the level at 1860 cm^{-1}. Then, the ^2D state would lie 1527.65 cm^{-1} below the ^4F state, the $^2D_{3/2}$ level would lie 2468.02 cm^{-1} (0.31 eV) below

the average ^{2}D energy, and the $^4F_{5/2}$ level would be the lowest level in the ^{4}F state and would lie 2473.77 cm^{-1} (0.31 eV) below the average ^{4}F energy. Further discussion below indicates the choice in the preceding paragraph (and listed in Table A.1) is the better assignment.

Calculating ζ_{6d} (Th)

The ground-state for the neutral Th atom is a ^{3}F ($6d^27s^2$) configuration.[1,2] Given $E^{SO} = (1/2)\zeta\ (c,L,S)[J(J+1) - L(L+1) - S(S+1)] = (1/2)\zeta$ for a ^{3}F term,[3] the $^3F_2$ level should be stabilized by $2\zeta_{6d}$ from the unperturbed ground-state. The $^3F_4$ level then is destabilized by $(3/2)\zeta_{6d}$. Assuming that second-order perturbations from other states are minimal, then the difference between the ground-level $^3F_2$ (0.000 cm^{-1}) and the $^3F_4$ (4961.659 cm^{-1}) level is $(7/2)\zeta_{6d}$, such that ζ_{6d} (Th) = 1417.617 cm^{-1} (0.176 eV). This is similar to the theoretically derived value of ζ_{6d}(Th) = 0.2 eV.[4]

In contrast to the neutral Th atom, the Th^+ cation has significant mixing in its ground-state such that it is difficult to obtain ζ_{6d} from spectral data. Because the charge on a cation contracts the orbitals, it is expected that ζ_{6d} for Th^+ should be larger than that of the neutral Th. The ζ_{5d} and ζ_{4d} parameters for Hf^+ and Zr^+ increase by a ratio of 1.030 and 1.027, respectively, over their neutral counterparts. As a congener, it is expected that Th^+ will increase by a similar factor. Therefore, ζ_{6d} for Th is multiplied by the average of the ratios for Hf^+ and Zr^+, 1.028, to obtain ζ_{6d} = 1457.740 cm^{-1} (0.181 eV) for Th^+.

For a ^{4}F (s^1d^2) configuration, $E^{SO} = (1/2)\zeta\ (c,L,S)[J(J+1) - L(L+1) - S(S+1)] = (1/3)\zeta_{6d}$,[3] so that the estimated difference between the $^4F_{7/2}$ and $^4F_{9/2}$ levels of Th^+, which are nearly pure ^{4}F in character (Table A.1),[1] is 3/2 ζ_{6d} = 2186.610 cm^{-1}. This prediction

agrees nicely with the experimental difference between the $^4F_{7/2}$ (4146.476 cm^{-1}) and $^4F_{9/2}$ (6213.490 cm^{-1}) of 2066.914 cm^{-1}. (Note this also predicts that the $^4F_{5/2}$ and $^4F_{3/2}$ levels should lie near 2000 and 0 cm^{-1}, helping to validate the assignments made above.) Furthermore, the difference between the $^2\Delta_{3/2}$ (2933.7 cm^{-1}) and $^2\Delta_{5/2}$ (5814.4 cm^{-1}) levels of ThO^+ observed using PFI-ZEKE is 2880.7 cm^{-1}.[5] Given that for a molecule $E^{SO} = A\Lambda M_S$ for a given level specified by $\Omega = \Lambda + M_S$,[3] each level deviates from the unperturbed state by A = ζ_{6d}(Th) = 1457.740 cm^{-1} such that the estimated difference is 2 ζ_{6d} (Th) = 2915.5 cm^{-1} between the $^2\Delta_{3/2}$ and $^2\Delta_{5/2}$ levels. This prediction compares well to the experimental work[5] and better than the theoretically derived value for ζ_{6d}(Th) (0.2 eV),[4] which would result in a difference of 3226.2 cm^{-1} between the two levels.

Phase Space Theory Competitive Model

The energy dependences of the cross sections in Figures 4.1 and A.1 indicate that the $ThCH_2^+ + H_2$, $ThH^+ + CH_3$, and $ThCH_3^+ + H$ products share a common intermediate, $HThCH_3^+$. As discussed in the text, because $ThCH_2^+ + H_2$ is thermodynamically more favorable than the latter products, competition is expected to shift the thresholds for formation of ThH^+ and $ThCH_3^+$ to higher energies. A simple estimation of this shift is to compare the $D_0(Th^+\text{-}H)$ measured here to the $D_0(Th^+\text{-}H)$ measured in the reaction $Th^+ + H_2$, which has no competitive shift in threshold. Doing so indicates that the threshold for $ThH^+ + CH_3$ is shifted 0.21 ± 0.19 eV higher in energy. Because $ThCH_3^+ + H$ has a similar threshold as $ThH^+ + CH_3$, the kinetic shift should be comparable; therefore, correcting the $D_0(ThCH_3^+)$ by 0.21 ± 0.19 eV should give a good estimate of the true BDE.

To assess the validity of this estimated shift, we performed phase space theory (PST) calculations in which angular momentum is explicitly conserved using molecular parameters (vibrational and rotational constants) calculated here for all three product channels and the return to reactants. In these calculations, the absolute magnitude of the cross sections is set by the LGS collision limit, such that the main adjustable parameter is the reaction threshold, E_0. The results of this calculation are found in Figure A.2. The comparison of the PST model to experiment is consistent with a reaction occurring with an efficiency of at least 50%, which could be an electronic surface effect. Also the shape of the PST cross sections for $ThCH_2^+$ and ThH^+ products are nicely reproduced over the entire energy range, and the shape of the combined $ThCH_3^+$ and $ThCH^+$ cross section is nicely reproduced in the threshold region. (Deviations at higher energy probably result from dissociation of $ThCH_3^+$ to $ThCH_2^+$ + H, a decomposition that is not included in the model.) The relative magnitudes of the ThH^+ + CH_3, and $ThCH_3^+$ + H cross sections are also reproduced, which is consistent with their very different angular momentum constraints mentioned in the text. The PST threshold for the $ThCH_2^+$ cross section is $E_0(ThCH_2^+)$ = 0.15 eV consistent with the threshold determined using Eq. 4.1, Table 4.1. Similarly, the PST thresholds of $E_0(ThH^+)$ = 2.05 eV and $E_0(ThCH_3^+)$ = 1.78 eV are shifted by 0.33 eV from the values listed in Table 4.1, consistent with a shift of 0.21 ± 0.19 eV estimated above. Notably, the difference in threshold energies between these channels remains the same in both analyses.

References

(1) Blaise, J.; Wyart, J.-F. Selected Constants, Energy Levels, and Atomic Spectra of Actinides. http://web2.lac.u-psud.fr/lac/Database/Contents.html.

(2) Sansonetti, J. E.; Martin, W. C. *J. Phys. Chem. Ref. Data* **2005**, *34*, 1559-2259.

(3) Lefebvre-Brion, H.; Field, R. W. *The Spectra And Dynamics of Diatomic Molecules*; Elsevier: Amsterdam, 2004.

(4) Jones, M. D.; Albers, R. C. *Phys. Rev. B: Condens. Matter Mater. Phys.* **2009**, *79*, 045107.

(5) Goncharov, V.; Heaven, M. C. *J. Chem. Phys.* **2006**, *124*, 064312.

(6) *NIST Computational Chemistry Comparison and Benchmark Database NIST Standard Reference Database Number 101 Release 16a*; Johnson III, R. D., Ed., August 2013.

(7) Zhang, X.-G.; Liyanage, R.; Armentrout, P. B. *J. Am. Chem. Soc.* **2001**, *123*, 5563-5575.

(8) Cox, R.; Armentrout, P. B. *manuscript in preparation*.

(9) Marçalo, J.; Leal, J. P.; Pires de Matos, A. *Int. J. Mass Spectrom. Ion Processes* **1996**, *157/158*, 265-274.

(10) Gibson, J. K.; Haire, R. G.; Marçalo, J.; Santos, M.; Pires de Matos, A.; Mrozik, M. K.; Pitzer, R. M.; Bursten, B. E. *Organomet.* **2007**, *26*, 3947-3956.

Table A.1. Low-lying spin-orbit levels of Th^+ with major electronic state components of each level [a]

Assigned Term	J	% 1st Component	% 2nd Component	Energy (cm^{-1})	Population (300 K)	Population (1100 K)	Avg. Weighted Energy (cm^{-1})[b]
^2D ($6d7s^2$)	3/2	52 ($6d^27s$) ^4F	36 ($6d7s^2$) ^2D	1859.938	0.0001	0.0668	0.000
	5/2	36 ($6d7s^2$) ^2D	30 ($6d^27s$) ^4F	4113.359	0.0000	0.0053	
^4F ($6d^27s$)	3/2	43 ($6d^27s$) ^4F	27 ($6d7s^2$) ^2D	0.000	0.9989	0.7604	517.986
	5/2	65($6d^27s$) ^4F	17 ($6d7s^2$) ^2D	1521.896	0.0010	0.1558	
	7/2	96 ($6d^27s$) ^4F		4146.576	0.0000	0.0067	
	9/2	89 ($6d^27s$) ^4F		6213.490	0.0000	0.0006	
^2F ($5f7s^2$)	5/2	89 ($5f7s^2$) ^2F		4490.262	0.0000	0.0032	3500.344
	7/2	85 ($5f7s^2$) ^2F		8378.859	0.0000	0.0000	
^2P ($6d^27s$)	1/2	36 ($6d^27s$) ^2P	36 ($6d^3$) ^2P	7828.560	0.0000	0.0000	4616.586
^4P ($6d^27s$)	1/2	70 ($6d^27s$) ^4P	13 ($6d^27s$) ^2P	6244.294	0.0000	0.0001	5032.024
	3/2	89 ($6d^27s$) ^4P	3 ($6d^3$) ^4F	8018.192	0.0000	0.0000	
	5/2	71 ($6d^27s$) ^4P	13 ($6d^27s$) ^2F	9061.103	0.0000	0.0000	
^4H ($5f6d7s$)	7/2	78 ($5f6d7s$) ^4H	17 ($5f6d7s$) ^2G	6168.356	0.0000	0.0005	5396.474
	9/2	37 ($5f6d7s$) ^4H	27 ($5f6d7s$) ^2G	6700.186	0.0000	0.0003	
	11/2	81 ($5f6d7s$) ^4H	13 ($5f6d7s$) ^2H	10189.067	0.0000	0.0000	
	13/2	96 ($5f6d7s$) $^4H_2$		13406.430	0.0000	0.0000	
^2G ($5f6d7s$)	7/2	50 ($5f6d7s$) ^2G	17 ($5f6d7s$) ^4F	9202.265	0.0000	0.0000	6010.155
	9/2	44 ($5f6d7s$) ^2G	31 ($5f6d7s$) ^4H	9238.020	0.0000	0.0000	

Assigned Term	J	% 1st Component	% 2nd Component	Energy (cm^{-1})	Population (300 K)	Population (1100 K)	Avg. Weighted Energy (cm^{-1})
^4F (*5f6d7s*)	3/2	74 (*5f6d7s*) ^4F	20 (*5f6d7s*) ^2D	6691.387	0.0000	0.0006	6552.301
	5/2	54 (*5f6d7s*) ^4F	25 (*5f6d7s*) ^2D	7331.485	0.0000	0.0004	
	7/2	60 (*5f6d7s*) ^4F	11 (*5f6d7s*) ^4G	9720.297	0.0000	0.0000	
	9/2	53 (*5f6d7s*) ^4F	30 (*5f6d7s*) ^4G	12488.287	0.0000	0.0000	
^2G ($6d^27s$)	7/2	54 ($6d^27s$) ^2G	27 ($6d^3$) ^2G	9711.962	0.0000	0.0000	6870.633
	9/2	41 (*5f6d7s*) ^2G	30 ($6d^3$) ^2G	10379.122	0.0000	0.0000	
^2D ($6d7s^2$)	3/2	41 ($6d^3$) ^4F	16 ($6d7s^2$)	7001.420	0.0000	0.0000	7538.900
	5/2	44 ($6d^27s$) ^2G	20 ($6d7s^2$)	13250.509	0.0000	0.0000	
^2F ($6d^27s$)	5/2	62 ($6d^27s$) ^2F	11 ($6d7s^2$) ^2D	8605.841	0.0000	0.0000	7659.383
	7/2	40 ($6d^3$) ^4F	34 ($6d^27s$) ^2F	12570.493	0.0000	0.0000	
^4F ($6d^3$)	3/2	43 ($6d^3$) ^4F	21 ($6d^27s$) ^2P	8460.352	0.0000	0.0000	7844.342
	5/2	84 ($6d^3$) ^4F	6 ($6d7s^2$) ^2D	9400.964	0.0000	0.0000	
	7/2	46 ($6d^3$) ^4F	33 ($6d7s^2$) ^2F	10855.320	0.0000	0.0000	
	9/2	60 ($6d^3$) ^4F	33 ($6d7s^2$) ^2G	13248.710	0.0000	0.0000	
^4G (*5f6d7s*)	5/2	83 (*5f6d7s*) ^4G	6 ($6d^27p$) ^4G	9585.404	0.0000	0.0000	9713.952
	7/2	54 (*5f6d7s*) ^4G	8(*5f6d7s*) ^2G	11116.584	0.0000	0.0000	
	9/2	57 (*5f6d7s*) ^4G	20 (*5f6d7s*) ^4F	13468.967	0.0000	0.0000	
	11/2	91 (*5f6d7s*) ^4G	4 ($6d^27p$) ^4G	15349.879	0.0000	0.0000	

[a] Refs. 1 and 2.

[b] Average energy of all spin-orbit levels weighted by the level degeneracy and relative to the ^2D ground-state.

Table A.2. Thermochemical Data at 0 K

Species[a]	$\Delta_f H_0°$ (kJ/mol)	Species[b]	$\Delta_f H_0°$ (kJ/mol)
H	216.035 ± 0.006	D	219.807 ± 0.004
CH	592.5 ± 0.6	CD	592.2 ± 1.7
CH_2	390.7 ± 1.6	CD_2	385.0 ± 2.5
CH_3	150.0 ± 0.3	CD_3	141.4 ± 0.04
CH_4	-66.6 ± 0.3	CD_4	-80.3 ± 0.4

[a] Ref. 6.
[b] See Ref. 7 and references therein.

Table A.3. Comparison of theoretically computed excited-state energies (eV) to spin-orbit averaged experimental values.

State	Experimental[a]	Basis Set	CCSD(T)	B3LYP	B3PW91	BHLYP
^{2}D ($6d7s^2$)	0.00	SDD[b]	**0.00**	0.12	0.02	**0.00**
		ANO[c]	**0.00**	0.17	**0.00**	**0.00**
		Seg. SDD[d]	**0.00**	0.20	0.004	**0.00**
		KAP[e]	**0.00**			
^{4}F ($6d^27s$)	0.06	SDD[b]	0.30	0.31	0.05	0.19
		ANO[c]	0.17	0.34	0.01	0.17
		Seg. SDD[d]	0.19	0.38	0.02	0.18
		KAP[e]	0.12			
^{2}F ($5f^27s$)	0.43	SDD[b]	1.47	**0.00**	0.10	0.27
		ANO[c]	0.63	**0.00**	0.03	0.22
		Seg. SDD[d]	0.58	**0.00**	**0.00**	0.19
^{4}H ($5f6d7s$)	0.67	SDD[b]	2.19	0.49	**0.00**	0.69
		ANO[c]	1.31	0.44	0.16	0.62
		Seg. SDD[d]	1.26	0.46	0.15	0.60
^{4}F ($6d^3$)	0.81	SDD[b]	1.34	1.07	0.72	0.91
		ANO[c]	1.06	1.07	0.64	0.86
		Seg. SDD[d]	1.08	1.12	0.66	0.88

Table A.3 Continued

[a] Spin-orbit averaged values from Refs. 1 and 2. The choice of levels used for each state is explained in the Supporting Information.
[b] Calculated using SDD basis set with ECP.
[c] Calculated using (14s13p10d8f6g)/[6s6p5d4f3g] atomic natural orbital basis set with SDD ECP.
[d] Calculated using (14s13p10d8f6g)/[10s9p5d4f3g] segmented basis set with SDD ECP.
[e] Calculated using (20s17p12d11f5g3h1i)/[7s7p6d5f5g3h1i] basis with Stuttgart-Cologne ECP and NWChem.

Table A.4. Electronic state, zero-point energy, and relative energy of all optimized structures.[a]

Species	State	s(s+1)	E (E_h)	ZPE (E_h)	E_{rel} (eV)
H	^2S	0.75	-0.502257		
H_2	$^1\Sigma^+$	0.00	-1.179572	0.010065	
CH	$^2\Pi$	0.75	-38.495898	0.006450	
CH_2	$^3B_1$	2.01	-39.167949	0.017157	
CH_3	$^2A''$	0.75	-39.857665	0.029666	
CH_4	$^1A_1$	0.00	-40.533963	0.044558	
Th^+	^2F	0.75	-407.331466		0.00
	^2D	1.50	-407.326882		0.12
	^4F	3.75	-407.319847		0.32
	^4G	3.75	-407.313189		0.50
	^4F	3.75	-407.292002		1.07
ThH^+	$^3\Delta$	2.00	-407.947040	0.003825	0.00
	$^3\Pi$	2.00	-407.939906	0.003712	0.19
	$^1\Sigma^+$	0.00	-407.936791	0.003840	0.28
	$^3\Phi$	2.01	-407.920405	0.003446	0.71
	$^3\Sigma^-$	2.01	-407.909205	0.003494	1.02
$ThCH^+$	$^1\Sigma$	0.00	-446.053389	0.012287	0.00
	$^3\Sigma$	2.00	-445.940256	0.011512	3.06
$HThC^+$	$^3A'$	2.01	-445.964430	0.006301	2.26
	$^1\Sigma$	0.00	-445.945406	0.005238	2.75
	$^3\Pi$	2.01	-445.938823	0.004886	2.92
	$^1A'$	0.00	-445.938813	0.006558	2.96
$ThCH_2^+$	$^2A'$	0.75	-446.691022	0.021034	0.00
	$^2A_1$	0.75	-446.687995	0.019956	0.05
	$^2A''$	0.75	-446.668039	0.0209228	0.62
	$^4A''$	3.75	-446.642738	0.020473	1.30
$HThCH^+$	^2A	0.75	-446.639667	0.016258	1.27
	$^2\Sigma^+$	0.76	-446.574250	0.021462	3.19

Species	State	s(s+1)	E (E_h)	ZPE (E_h)	E_{rel} (eV)
$HThCH^+$		3.76	-446.537257	0.014732	4.01
	$^4A'$	3.75	-446.532716	0.011683	4.05
H_2ThC^+	^4A	3.75	-446.544338	0.011362	3.73
	^2A	1.75	-446.523767	0.011281	4.29
$ThCH_3^+$	^3E	2.00	-447.307161	0.032081	0.00
	$^1A_1$	0.00	-447.304280	0.031604	0.07
$HThCH_2^+$	$^1A'$	0.00	-447.301371	0.026605	0.01
	$^3A'$	2.01	-447.210107	0.038357	2.81
H_2ThCH^+	^3A	2.01	-447.218553	0.020842	2.11
	^1A	0.00	-447.188040	0.021513	2.95
1, $Th^+(CH_4)$[b]	^2A	1.35	-447.877592	0.045006	-0.44
	$^2A'$	1.35	-447.877580	0.045516	-0.43
	$^4A''$	3.75	-447.870913	0.044795	-0.27
TS1/2[b]	^2A	0.79	-447.855920	0.036859	-0.08
	^4A	3.76	-447.812311	0.035497	1.07
2, $HThCH_3^+$[b]	$^2A'$	0.75	-447.921819	0.036934	-1.87
	$^2A''$	0.75	-447.906628	0.036874	-1.45
	$^4A'$	3.76	-447.825921	0.036047	0.72
TS2/3[b]	^2A	0.75	-447.876331	0.035358	-0.67
	^4A	3.76	-447.804724	0.033565	1.23
3, $(H_2)ThCH_2^+$[b]	^2A	0.75	-447.879288	0.036581	-0.72
	^4A	3.75	-447.831208	0.033885	0.52
TS2/4[b]	^2A	0.76	-447.867974	0.030655	-0.57
4, $H_2ThCH_2^+$[b]	$^2A'$	0.75	-447.875672	0.030812	-0.78
TS4/3[b]	^2A	0.77	-447.838417	0.029124	0.19

[a] Optimized at B3LYP/SDD/6-311++G(d,p) level of theory.
[b] Labels refer to species found in Figures 4.5 and S3. Energies are referenced to $Th^+(^2D) + CH_4$ without spin-orbit corrections.

Table A.5. Comparison of experimental and theoretical bond dissociation energies (eV)[a]

	Experimental			Theoretical			
Bond	This Work	Literature	Basis Set	CCSD(T) [b]	B3LYP	B3PW91	BHLYP
Th^+-H ($^3\Delta_1$)[c,d]	≥2.25 ± 0.20	2.46 ± 0.07[e]	SDD[f]	2.64 (**2.42**)	**3.10 (2.88)**	**3.13 (2.91)**	**2.95 (2.73)**
			ANO[g]	2.79 (**2.57**)	**3.14 (2.92)**	**3.17 (2.95)**	**2.97 (2.75)**
			Seg. SDD[h]	2.80 (**2.58**)	**2.98 (2.76)**	**2.97 (2.75)**	**2.75 (2.53)**
			KAP[i]	2.91 (**2.69**)			
Th^+-H ($^1\Sigma^+$)[c]			SDD[f]	**2.82** (**2.42**)	2.81 (2.41)	2.60 (2.20)	2.66 (2.26)
			ANO[g]	**2.88** (2.48)	2.84 (2.44)	2.64 (2.24)	2.68 (2.28)
			Seg. SDD[h]	**2.87** (2.47)	2.86 (2.46)	2.66 (2.26)	2.71 (2.31)
			KAP[i]	**2.95** (2.55)			
Th^+-CH ($^1\Sigma^+$)[c]	6.19 ± 0.16		SDD[f]	5.64 (5.24)	6.12 (5.72)	6.60 (6.20)	5.53 (5.13)
			ANO[g]	6.22 (5.82)	6.19 (5.79)	6.61 (6.21)	5.57 (5.17)
			Seg. SDD[h]	6.04 (5.64)	6.20 (5.80)	6.61 (6.21)	5.57 (5.17)
			KAP[i]	6.38 (5.98)			
Th^+-CH_2 ($^2A'$)[c]	≥4.54 ± 0.09	≥4.74 ± 0.02[j]	SDD[f]	4.82 (4.42)	5.23 (4.83)	5.34 (4.94)	4.73 (4.33)
			ANO[g]	5.32 (4.92)	5.31 (4.91)	5.42 (5.02)	4.80 (4.40)
			Seg. SDD[h]	5.14 (4.74)	5.32 (4.92)	5.44 (5.04)	4.82 (4.44)
			KAP[i]	5.34 (4.94)			

Bond	This Work	Literature	Basis Set	CCSD(T) [b]	B3LYP	B3PW91	BHLYP
Th^+-CH_3 (^3E)[c,d]	2.60 ± 0.30		SDD[f]	2.97 (2.75)	**3.27 (3.05)**	**3.45 (3.23)**	**2.99 (2.77)**
			ANO[g]	3.35 (3.13)	**3.33 (3.11)**	**3.52 (3.30)**	**2.97 (2.75)**
			Seg. SDD[h]	3.17 (2.95)	**3.35 (3.13)**	**3.54 (3.32)**	**2.98 (2.76)**
			KAP[i]	3.44 (**3.22**)			
Th^+-CH_3 ($^1A_1$)[c]			SDD[f]	**3.47 (3.07)**	3.20 (2.80)	3.15 (2.75)	2.88 (2.48)
			ANO[g]	**3.57 (3.17)**	3.26 (2.86)	3.22 (2.82)	2.93 (2.53)
			Seg. SDD[h]	**3.39 (2.99)**	3.29 (2.89)	3.25 (2.85)	2.96 (2.56)
			KAP[i]	**3.62** (**3.22**)			
Th^+-CH_4	0.47 ± 0.05		SDD[f]	0.28 (0.48)	0.47 (0.52)	0.55 (0.57)	0.25 (0.41)
(^2A/($^4A''$))[k]			ANO[g]	0.56 (0.60)	0.57 (0.51)	0.65 (0.57)	0.34 (0.43)
			Seg. SDD[h]	0.36 (0.49)	0.56 (0.51)	0.64 (0.57)	0.33 (0.43)
			KAP[i]	0.41 (0.51)			
MAD[l]			SDD[f]	0.49 (0.37)	0.35 (0.35)	0.50 (0.30)	0.44 (0.39)
			ANO[g]	0.38 (0.30)	0.38 (0.35)	0.56 (0.33)	0.41 (0.38)
			Seg. SDD[h]	0.37 (0.27)	0.34 (0.32)	0.51 (0.28)	0.36 (0.32)
			KAP[i]	0.44 (0.28)			

Table A.5 Continued

[a] All values are relative to Th^+ (^2D, $6d7s^2$). Values in parentheses are relative to Th^+ ($^4F_{3/2}$,$6d^27s$) and include estimated spin-orbit corrections. Optimized at the indicated level of theory using the respective basis set for Th^+ and a 6-311++G(3df,3p) for C and H See text. For ThH^+ and $ThCH_3^+$, the calculated ground-state is in bold.

[b] CCSD(T) single-point calculations using B3LYP/Seg. SDD/6-311++G(3df,3p) optimized structures.

[c] Spin-orbit correction of -0.40 eV, the empirical difference between the ^2D averaged over all spin-orbit states and the $^4F_{3/2}$.

[d] Spin-orbit correction of 0.18 eV for stabilization of $^3\Delta_1$ state. See text.

[e] Ref. 8.

[f] Optimized at the indicated level of theory using an SDD basis set with ECP (60 e^-) for Th^+ and a 6-311++G(3df,3p) for C and H.

[g] Optimized at the indicated level of theory using (14s13p10d8f6g)/[6s6p5d4f3g] atomic natural orbital set with SDD ECP for Th^+ and a 6-311++G(3df,3p) for C and H.

[h] Optimized at the indicated level of theory using (14s13p10d8f6g)/[10s9p5d4f3g] segmented basis set with SDD ECP for Th^+ and a 6-311++G(3df,3p) for C and H.

[i] Calculated using (20s17p12d11f5g3h1i)/[7s7p6d5f5g3h1i] basis with Stuttgart-Cologne ECP.

[j] Result based on FT-ICR results reported in Refs. 9 and 10. Utilizes updated $D_0(H_2C\text{-}H_2) = 4.74 \pm 0.02$ eV. See Table A.2 and Ref. 6.

[k] Value in parentheses corresponds to the $^4A''$ ground-state after including spin-orbit effects. See text and Figure 4.4.

[l] Mean absolute deviation of ground-state theoretical BDEs from the experimental value. Calculation excludes $ThCH_2^+$. Values in parentheses correspond to MADs after inclusion of spin-orbit estimates.

Table A.6. Geometrical parameters of structures in Figures 5 and S3 optimized using B3LYP/SDD/6-311++G(d,p).[a]

Species	State	r(Th^+-H)	r(Th^+-C)	r(C-H)	∠HThC	∠HCH
1, $Th^+(CH_4)$[b,c]	^2A		2.78	1.11, 1.10 (2), 1.09		112.9, 112.3 (2), 106.4
			[2.67]	[1.11 (3), 1.09]		[112.7, 112.2, 112.1, 106.4]
	$^4A''$		2.89	1.10 (2), 1.09 (2)		112.8, 112.6 (2), 106.2
			[2.71]	[1.11, 1.10 (2), 1.08]		[112.3 (3), 106.2]
TS1/2[b,c]	^2A		2.29	1.37, 1.17, 1.11, 1.09		131.2, 106.1, 104.7, 100.0
			[2.28]	[1.40, 1.13 (2), 1.09]		[117.9, 117.1, 107.6, 106.8]
	^4A	2.01	2.86	1.09 (3)	70.4	119.0, 118.6 (2)
2, $HThCH_3^+$[b]	$^2A'$	1.99	2.31	1.10 (3)	97.6	108.4, 107.6 (2)
	$^4A'$	2.04	2.68	1.09 (3)	165.6	117.2, 117.1 (2)
TS2/3[b]	^2A	2.16, 2.12	2.11	1.12, 1.09	93.6, 72.7, 47.5	110.9
	^4A	2.22, 2.16	2.43	1.09 (2)	112.5, 61.8, 31.1	112.3
3, $(H_2)ThCH_2^+$[b]	^2A	2.43, 2.37	2.07	1.12, 1.09	91.2, 83.6, 64.8	111.4
	^4A	2.40 (2)	2.32	1.10, 1.09	124.6, 104.9 (2)	110.7
TS2/4[b]	^2A	2.02, 2.01	2.23	1.10, 1.09	131.3, 100.7,[d] 99.9, 58.3	110.8
4, $H_2ThCH_2^+$[b]	$^2A'$	2.01 (2)	2.32	1.10 (2)	124.7, 102.5,[d] 99.2 (2)	110.5
TS4/3[b]	^2A	2.04 (2)	2.18	1.10, 1.09	135.2, 112.9, 38.9[d]	110.8
$ThCH_2^+$[c]	$^2A'$		2.03	1.13, 1.09	89.7[e]	111.7
			[2.02]	[1.13, 1.09]	[86.8][e]	[111.2]
	$^4A''$		2.34	1.10 (2)	125.2[e]	109.6

Table A.6 Continued

[a] Bond lengths in Å and bond angles in degrees. Values in parentheses are degeneracies.
[b] Labels refer to species found in Figures 4.5 and A.3.
[c] Values in brackets optimized using PBE0/KAP/cc-pVTZ.
[d] Angle is ∠HThH.
[e] Angle is ∠ThCH.

Table A.7. Spin-orbit corrected single-point energies (in kJ/mol) relative to the Th^+ ($^4F_{3/2}$) + CH_4 reactants.[a]

Species	State	CCSD(T)	B3LYP	B3PW91	BHLYP
$Th^+ + CH_4$	$^2D_{3/2}$ + $^1A_{1g}$	22.2, 22.2, 22.2	22.2, 22.2, 22.2	22.2, 22.2, 22.2	22.2, 22.2, 22.2
	$^4F_{3/2}$ + $^1A_{1g}$	0.0, 0.0, 0.0	0.0, 0.0, 0.0	0.0, 0.0, 0.0	0.0, 0.0, 0.0
$Th^+(CH_4)$ (1)	^2A	-3.9, -31.4, -13.0	-22.9, -32.5, -31.5	-31.1, -40.5, -39.5	-2.3, -10.6, -9.3
	$^4A''$	-46.5, -58.0, -47.5	-49.9, -48.8, -49.4	-55.4, -54.9, -55.4	-39.7, -41.5, -41.8
TS1/2	^2A	65.7, 26.4, 44.8	30.8, 22.9, 21.5	13.5, 5.3, 3.6	73.8, 66.5, 65.0
	^4A	156.7, 128.0, 139.8	140.5, 111.7, 110.8	126.9, 98.4, 97.4	130.3, 124.7, 123.8
$HThCH_3^+$ (2)	$^2A'$	-102.8, -141.2, -123.2	-141.7, -148.4, -150.1	-154.2, -161.6, -163.7	-116.6, -123.0, -125.1
	$^4A'$	151.9, 117.3, 135.8	104.1, 100.6, 99.7	91.9, 88.7, 87.5	127.3, 121.0, 119.8
TS2/3	^2A	12.6, -35.6, -16.9	-27.1, -35.3, -36.7	-52.1, -60.8, -62.6	22.8, 14.7, 13.0
	^4A	200.9, 160.5, 178.7	156.3, 149.2, 148.1	129.7, 122.5, 121.1	189.6, 183.3, 181.9
TS2/4	^2A	40.6, -6.0, 12.4	-15.9, -23.7, -25.4	-30.2, -38.7, -40.8	21.5, 13.8, 11.6
$H_2ThCH_2^+$ (4)	$^2A'$	18.7, -25.5, -7.4	-35.7, -44.1, -45.8	-45.0, -54.1, -56.2	-12.5, -20.9, -23.1
TS4/3	^2A	131.2, 80.2, 99.4	57.3, 49.2, 48.0	35.7, 27.5, 25.8	109.5, 101.3, 99.6
$(H_2)ThCH_2^+$ (3)	^2A	1.8, -45.4, -26.8	-31.4, -39.3, -40.4	-50.1, -58.4, -59.8	12.2, 4.6, 3.1
	^4A	129.0, 89.3, 107.1	87.8, 97.2, 79.8	70.2, 62.4, 60.4	112.0, 105.5, 103.6
$ThCH_2^+ + H_2$	$^2A'$ + $^1\Sigma_g^+$	15.9, -30.2, -13.0	-16.4, -23.7, -25.3	-28.9, -36.6, -38.6	24.8, 18.4, 16.4
	$^4A''$ + $^1\Sigma_g^+$	139.8, 104.4, 117.2	102.9, 97.2, 92.0	90.0, 84.2, 77.8	123.7, 118.7, 112.6

Table A.7 Continued

[a] Structures optimized and vibrational frequencies calculated using B3LYP/SDD/6-311++G(d,p). Single-point energies calculated at the respective level of theory with SDD, ANO, and Seg. SDD/6-311++G(3df,3p) and are zero-point corrected (scaled by 0.989). Energies for all intermediates (except 1), transition states, and products are corrected by the difference in energy of the average ^{2}D state and $^{4}F_{3/2}$ level Th^{+} (38.4 kJ/mol) except for **1** where the well depth remains constant relative to its asymptote, see text. Note that the spin-orbit corrected reactant asymptotes are fixed at their empirical energy difference.

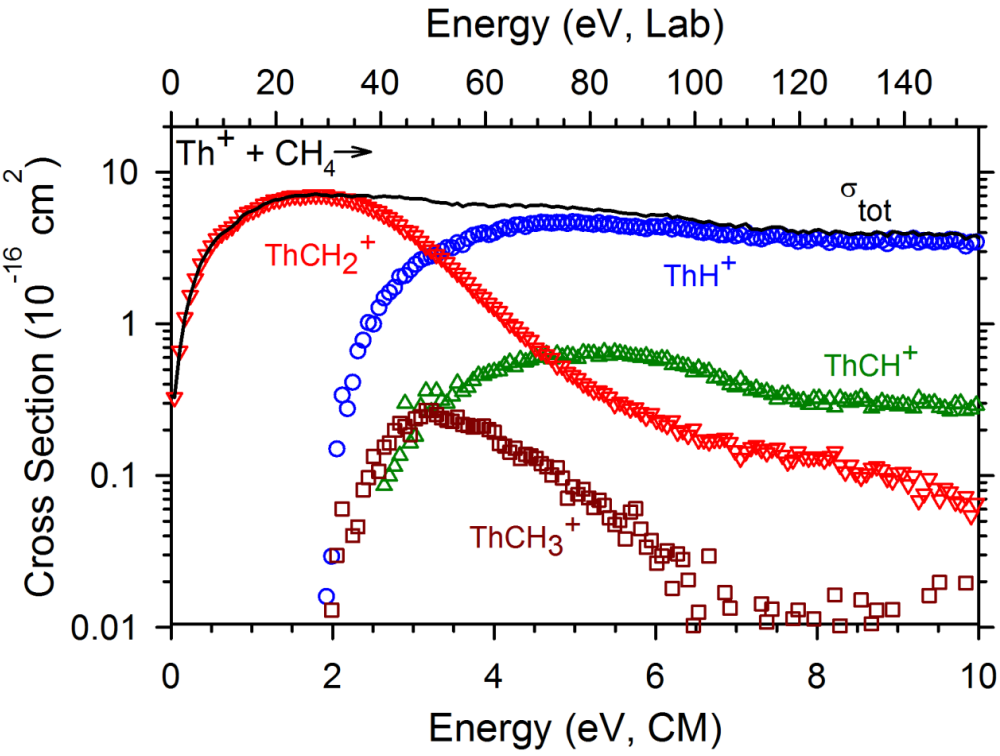

Figure A.1. Cross sections for the reactions between Th^+ and CH_4 as a function of energy in the CM (lower x-axis) and Lab (upper x-axis) frames.

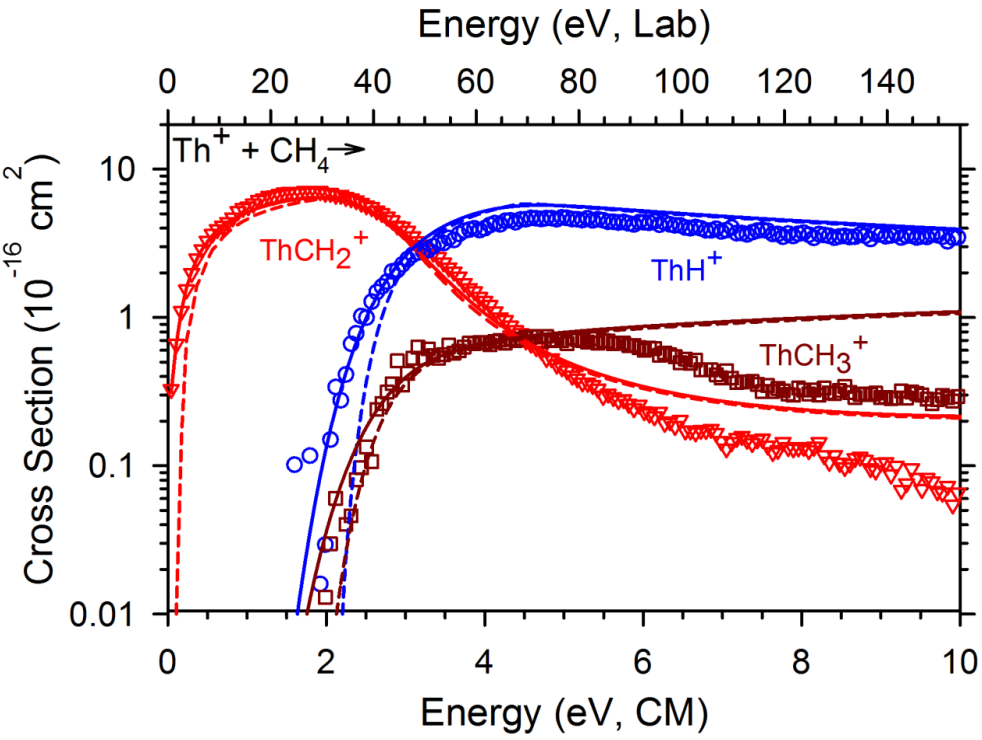

Figure A.2. Phase space theory model of the cross sections of the reaction of Th^+ + CH_4 using molecular parameters obtained from B3LYP/SDD/6-311++G(d,p) calculations. Full and dashed lines are the models with and without experimental energy broadening, respectively.

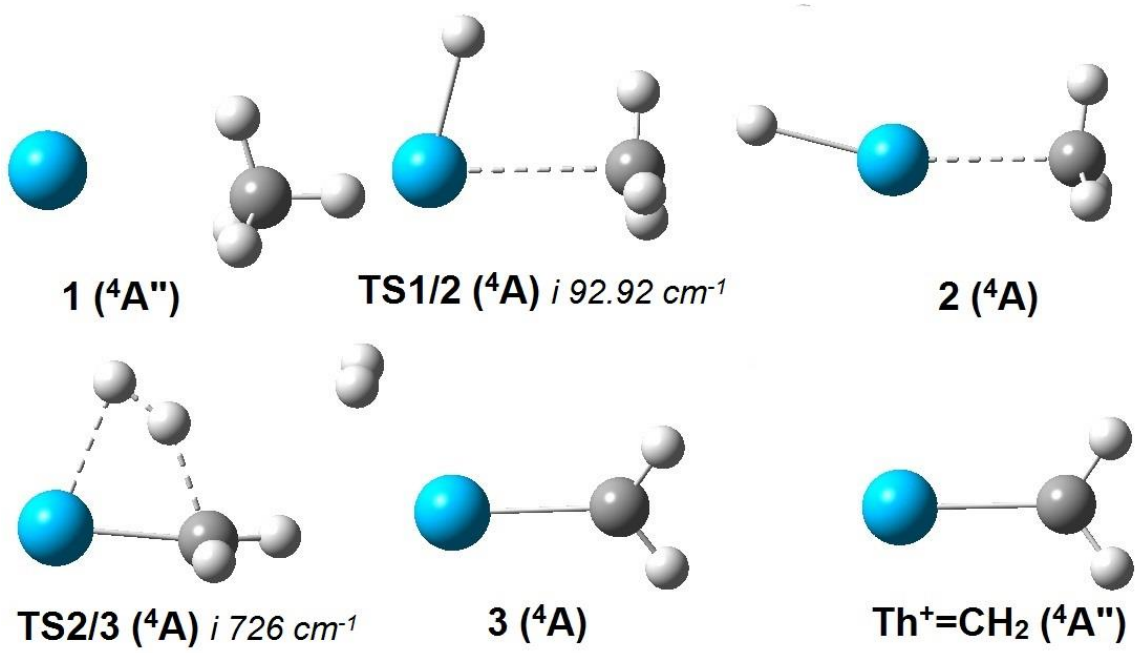

Figure A.3. Geometrical structures of each quartet spin intermediate and transition state in Figure 4.4. All structures optimized using the B3LYP/SDD/6-311++G(d,p) approach.

APPENDIX B

SUPPORTING INFORMATION FOR CHAPTER 5

Table B.1. Calculated ground and excited-states of ThH^+ (in eV).[a]

ThH^+	Basis Set	CCSD(T)[b]	B3LYP	B3PW91	BHLYP	M06	PBE0
$^3\Delta_1$ ($\sigma^2\sigma\delta$)[c]	SDD VDZ-MWB/6-311+G(3p)	**0.00** (0.18)	**0.00** (**0.00**)	**0.00** (**0.00**)	**0.00** (**0.00**)	0.09 (0.27)	**0.00** (**0.00**)
	Seg. SDD-VQZ-MWB/6-311+G(3p)	**0.00** (0.07)	**0.00** (**0.00**)	**0.00** (**0.00**)	**0.00** (**0.00**)	0.04 (0.22)	**0.00** (**0.00**)
	ANO-VQZ-MWB/6-311+G(3p)	**0.00** (0.07)	**0.00** (**0.00**)	**0.00** (**0.00**)	**0.00** (**0.00**)	0.04 (0.22)	**0.00** (**0.00**)
	ANO-VQZ-MDF/6-311+G(3p)	**0.00** (0.06)	**0.00** (**0.00**)	**0.00** (**0.00**)	**0.00** (**0.00**)	0.07 (0.25)	**0.00** (**0.00**)
	cc-pVQZ-PP-MDF/cc-pVQZ	**0.00** (0.05)	**0.00** (**0.00**)	**0.00** (**0.00**)	**0.00** (**0.00**)	0.09 (0.27)	**0.00** (**0.00**)
	cc-pwCVQZ-PP-MDF/cc-pVQZ	**0.00** (0.05)	**0.00** (**0.00**)	**0.00** (**0.00**)	**0.00** (**0.00**)	0.09 (0.27)	**0.00** (**0.00**)
	cc-pwCVQZ-PP-MDF/aug-cc-pVQZ	**0.00** (0.07)	**0.00** (**0.00**)	**0.00** (**0.00**)	**0.00** (**0.00**)	0.10 (0.27)	**0.00** (**0.00**)
$^1\Sigma^+$ ($\sigma^2\sigma^2$)	SDD-VDZ-MWB/6-311+G(3p)	**0.00** (**0.00**)	0.46 (0.28)	0.69 (0.51)	0.46 (0.28)	**0.00** (**0.00**)	0.67 (0.49)
	Seg. SDD-VQZ-MWB/6-311+G(3p)	0.11 (**0.00**)	0.48 (0.30)	0.70 (0.52)	0.46 (0.28)	**0.00** (**0.00**)	0.69 (0.51)
	ANO-VQZ-MWB/6-311+G(3p)	0.11 (**0.00**)	0.48 (0.30)	0.71 (0.53)	0.47 (0.29)	**0.00** (**0.00**)	0.69 (0.51)
	ANO-VQZ-MDF/6-311+G(3p)	0.12 (**0.00**)	0.47 (0.29)	0.70 (0.52)	0.47 (0.29)	**0.00** (**0.00**)	0.69 (0.51)
	cc-pVQZ-PP-MDF/cc-pVQZ	0.13 (**0.00**)	0.45 (0.27)	0.69 (0.51)	0.46 (0.28)	**0.00** (**0.00**)	0.68 (0.50)
	cc-pwCVQZ-PP-MDF/cc-pVQZ	0.13 (**0.00**)	0.45 (0.27)	0.69 (0.51)	0.46 (0.28)	**0.00** (**0.00**)	0.68 (0.50)
	cc-pwCVQZ-PP-MDF/aug-cc-pVQZ	0.11 (**0.00**)	0.45 (0.27)	0.69 (0.51)	0.46 (0.28)	**0.00** (**0.00**)	0.68 (0.50)

Table B.1 (continued)

ThH^+	Basis Set	CCSD(T)[b]	B3LYP	B3PW91	BHLYP	M06	PBE0
$^3\Pi_0$ ($\sigma^2\sigma\pi$)[d]	SDD-VDZ-MWB/6-311+G(3p)	0.43 (0.52)	0.28 (0.19)	0.31 (0.22)	0.34 (0.25)	0.21 (0.30)	0.33 (0.24)
	Seg. SDD-VQZ-MWB/6-311+G(3p)	0.40 (0.38)	0.27 (0.18)	0.30 (0.21)	0.32 (0.23)	0.20 (0.29)	0.31 (0.22)
	ANO-VQZ-MWB/6-311+G(3p)	0.40 (0.38)	0.27 (0.18)	0.30 (0.21)	0.32 (0.23)	0.20 (0.29)	0.32 (0.23)
	ANO-VQZ-MDF/6-311+G(3p)	0.40 (0.37)	0.28 (0.19)	0.32 (0.23)	0.34 (0.25)	0.24 (0.33)	0.33 (0.24)
	cc-pVQZ-PP-MDF/cc-pVQZ	0.40 (0.36)	0.29 (0.20)	0.32 (0.23)	0.35 (0.26)	0.26 (0.35)	0.33 (0.24)
	cc-pwCVQZ-PP-MDF/cc-pVQZ	0.39 (0.35)	0.29 (0.20)	0.32 (0.23)	0.35 (0.26)	0.28 (0.35)	0.33 (0.25)
	cc-pwCVQZ-PP-MDF/aug-cc-pVQZ	0.39 (0.37)	0.29 (0.20)	0.32 (0.23)	0.35 (0.26)	0.27 (0.35)	0.34 (0.25)
$^3\Phi_2$ ($\sigma^2\delta\pi$)[e]	SDD-VDZ-MWB/6-311+G(3p)	0.77 (1.04)	0.62 (0.71)	0.56 (0.65)	0.60 (0.69)	0.42 (0.69)	0.55 (0.64)
	Seg. SDD-VQZ-MWB/6-311+G(3p)	0.68 (0.84)	0.61 (0.70)	0.54 (0.63)	0.58 (0.67)	0.38 (0.65)	0.54 (0.63)
	ANO-VQZ-MWB/6-311+G(3p)	0.67 (0.83)	0.60 (0.69)	0.53 (0.62)	0.58 (0.67)	0.37 (0.64)	0.53 (0.62)
	ANO-VQZ-MDF/6-311+G(3p)	0.65 (0.80)	0.60 (0.69)	0.54 (0.63)	0.58 (0.67)	0.38 (0.65)	0.53 (0.62)
	cc-pVQZ-PP-MDF/cc-pVQZ	0.63 (0.77)	0.63 (0.72)	0.57 (0.66)	0.61 (0.70)	0.44 (0.71)	0.57 (0.66)
	cc-pwCVQZ-PP-MDF/cc-pVQZ	0.63 (0.77)	0.66 (0.75)	0.57 (0.66)	0.61 (0.70)	0.49 (0.76)	0.57 (0.66)
	cc-pwCVQZ-PP-MDF/aug-cc-pVQZ	0.62 (0.76)	0.63 (0.72)	0.57 (0.66)	0.61 (0.70)	0.44 (0.71)	0.57 (0.66)

Table B.1 (continued)

ThH^+	Basis Set	CCSD(T)[b]	B3LYP	B3PW91	BHLYP	M06	PBE0
$^3\Sigma^-$ ($\sigma^2\delta^2$)	SDD-VDZ-MWB/6-311+G(3p)	1.10 (1.10)	1.01 (0.83)	0.97 (0.79)	1.02 (0.84)	0.89 (0.89)	0.96 (0.78)
	Seg. SDD-VQZ-MWB/6-311+G(3p)	1.01 (0.90)	1.02 (0.84)	0.96 (0.78)	1.02 (0.84)	0.92 (0.92)	0.95 (0.77)
	ANO-VQZ-MWB/6-311+G(3p)	0.93 (0.82)	1.01 (0.83)	0.94 (0.76)	1.01 (0.83)	0.92 (0.92)	0.93 (0.75)
	ANO-VQZ-MDF/6-311+G(3p)	0.98 (0.86)	1.00 (0.82)	0.95 (0.77)	1.00 (0.82)	0.91 (0.91)	0.94 (0.76)
	cc-pVQZ-PP-MDF/cc-pVQZ	0.96 (0.83)	1.03 (0.85)	0.98 (0.80)	1.04 (0.86)	0.97 (0.97)	0.97 (0.79)
	cc-pwCVQZ-PP-MDF/cc-pVQZ	0.97 (0.83)	1.03 (0.85)	0.98 (0.80)	1.04 (0.86)	0.96 (0.96)	0.97 (0.79)
	cc-pwCVQZ-PP-MDF/aug-cc-pVQZ	0.91 (0.80)	1.03 (0.85)	0.98 (0.80)	1.03 (0.85)	0.96 (0.96)	0.97 (0.79)
$^3\Sigma^-$ ($\sigma^2\pi^2$)	SDD-VDZ-MWB/6-311+G(3p)	1.28 (1.28)	1.22 (1.02)	1.09 (0.91)	1.17 (0.99)	0.95 (0.95)	1.08 (0.90)
	Seg. SDD-VQZ-MWB/6-311+G(3p)	1.19 (1.08)	1.21 (1.03)	1.08 (0.90)	1.15 (0.97)	0.95 (0.95)	1.07 (0.89)
	ANO-VQZ-MWB/6-311+G(3p)	1.17 (1.06)	1.19 (1.01)	1.07 (0.89)	1.14 (0.96)	0.95 (0.95)	1.06 (0.88)
	ANO-VQZ-MDF/6-311+G(3p)	1.15 (1.03)	1.18 (1.00)	1.06 (0.88)	1.14 (0.96)	0.92 (0.92)	1.06 (0.88)
	cc-pVQZ-PP-MDF/cc-pVQZ	1.12 (0.99)	1.21 (1.03)	1.10 (0.92)	1.17 (0.99)	0.98 (0.98)	1.09 (0.91)
	cc-pwCVQZ-PP-MDF/cc-pVQZ	1.12 (0.99)	1.21 (1.03)	1.10 (0.92)	1.17 (0.99)	0.97 (0.97)	1.09 (0.91)
	cc-pwCVQZ-PP-MDF/aug-cc-pVQZ	1.13 (1.02)	1.21 (1.03)	1.10 (0.92)	1.17 (0.99)	0.98 (0.98)	1.09 (0.91)

Table B.1 Continued

[a] Structures optimized using indicated basis sets (Th^+-ECP/H) at the respective level of theory (except CCSD(T)) relative to the ground-level (state) with the ground-level (state) bolded. Values include spin-orbit correction to the lowest level of each state,s where applicable. Values in parentheses do not include spin-orbit corrections.
[b] Structures optimized using B3LYP with the indicated basis sets.
[c] Spin-orbit correction of -0.18 eV.
[d] Spin-orbit correction of -0.09 eV.
[e] Spin-orbit correction of -0.27 eV.

Table B.2. Calculated bond distances, r(Th^+-H) for ThH^+ ground and excited-states (in Å).[a]

ThH^+	Basis Set	B3LYP	B3PW91	BHLYP	M06	PBE0
$^3\Delta$ ($\sigma^2\sigma\delta$)	SDD-VDZ-MWB/6-311+G(3p)	1.991	1.983	1.981	1.986	1.981
	Seg. SDD-VQZ-MWB/6-311+G(3p)	1.989	1.982	1.979	1.984	1.979
	ANO-VQZ-MWB/6-311+G(3p)	1.989	1.981	1.978	1.985	1.979
	ANO-VQZ-MDF/6-311+G(3p)	1.994	1.988	1.985	1.990	1.985
	cc-pVQZ-PP-MDF/cc-pVQZ	1.996	1.989	1.987	1.994	1.987
	cc-pwCVQZ-PP-MDF/cc-pVQZ	1.996	1.990	1.988	1.993	1.987
	cc-pwCVQZ-PP-MDF/aug-cc-pVQZ	1.996	1.990	1.988	1.992	1.987
$^1\Sigma^+$ ($\sigma^2\sigma^2$)	SDD-VDZ-MWB/6-311+G(3p)	1.933	1.948	1.938	1.915	1.943
	Seg. SDD-VQZ-MWB/6-311+G(3p)	1.925	1.946	1.933	1.911	1.942
	ANO-VQZ-MWB/6-311+G(3p)	1.927	1.947	1.934	1.913	1.943
	ANO-VQZ-MDF/6-311+G(3p)	1.949	1.954	1.942	1.919	1.949
	cc-pVQZ-PP-MDF/cc-pVQZ	1.945	1.954	1.945	1.922	1.950
	cc-pwCVQZ-PP-MDF/cc-pVQZ	1.946	1.955	1.945	1.922	1.951
	cc-pwCVQZ-PP-MDF/aug-cc-pVQZ	1.946	1.955	1.945	1.921	1.951
$^3\Pi$ ($\sigma^2\sigma\pi$)	SDD-VDZ-MWB/6-311+G(3p)	1.997	1.987	1.981	1.989	1.983
	Seg. SDD-VQZ-MWB/6-311+G(3p)	1.996	1.988	1.982	1.983	1.984
	ANO-VQZ-MWB/6-311+G(3p)	1.995	1.986	1.980	1.983	1.982
	ANO-VQZ-MDF/6-311+G(3p)	1.999	1.991	1.986	1.981	1.987
	cc-pVQZ-PP-MDF/cc-pVQZ	2.000	1.992	1.988	1.984	1.989
	cc-pwCVQZ-PP-MDF/cc-pVQZ	2.001	1.993	1.988	1.984	1.990
	cc-pwCVQZ-PP-MDF/aug-cc-pVQZ	2.001	1.993	1.988	1.982	1.990

Table B.2 (continued)

ThH^+	Basis Set	B3LYP	B3PW91	BHLYP	M06	PBE0
$^3\Phi$ ($\sigma^2\delta\pi$)	SDD-VDZ-MWB/6-311+G(3p)	2.027	2.013	2.009	2.015	2.007
	Seg. SDD-VQZ-MWB/6-311+G(3p)	2.029	2.015	2.011	2.017	2.010
	ANO-VQZ-MWB/6-311+G(3p)	2.026	2.012	2.009	2.016	2.007
	ANO-VQZ-MDF/6-311+G(3p)	2.030	2.016	2.014	2.018	2.011
	cc-pVQZ-PP-MDF/cc-pVQZ	2.031	2.018	2.015	2.022	2.013
	cc-pwCVQZ-PP-MDF/cc-pVQZ	2.033	2.019	2.016	2.021	2.012
	cc-pwCVQZ-PP-MDF/aug-cc-pVQZ	2.032	2.018	2.016	2.019	2.013
$^3\Sigma^-$ ($\sigma^2\delta^2$)	SDD-VDZ-MWB/6-311+G(3p)	2.029	2.014	2.015	2.019	2.012
	Seg. SDD-VQZ-MWB/6-311+G(3p)	2.024	2.015	2.014	2.012	2.012
	ANO-VQZ-MWB/6-311+G(3p)	2.022	2.016	2.013	2.012	2.013
	ANO-VQZ-MDF/6-311+G(3p)	2.027	2.018	2.018	2.016	2.016
	cc-pVQZ-PP-MDF/cc-pVQZ	2.028	2.019	2.019	2.021	2.017
	cc-pwCVQZ-PP-MDF/cc-pVQZ	2.029	2.020	2.020	2.020	2.018
	cc-pwCVQZ-PP-MDF/aug-cc-pVQZ	2.029	2.020	2.020	2.018	2.018
$^3\Sigma^-$ ($\sigma^2\pi^2$)	SDD-VDZ-MWB/6-311+G(3p)	2.009	1.994	1.995	1.987	1.990
	Seg. SDD-VQZ-MWB/6-311+G(3p)	2.003	1.991	1.996	1.988	1.988
	ANO-VQZ-MWB/6-311+G(3p)	2.000	1.989	1.994	1.987	1.986
	ANO-VQZ-MDF/6-311+G(3p)	2.013	1.996	2.001	1.991	1.993
	cc-pVQZ-PP-MDF/cc-pVQZ	2.013	1.996	2.001	1.993	1.993
	cc-pwCVQZ-PP-MDF/cc-pVQZ	2.014	1.997	2.002	1.992	1.994
	cc-pwCVQZ-PP-MDF/aug-cc-pVQZ	2.014	1.997	2.002	1.990	1.994

[a] Structures optimized using indicated basis sets with the respective level of theory.

Table B.3. Vibrational Frequencies of ThH^+ ground and excited-states (in cm^{-1}).[a]

ThH^+	B3LYP	B3PW91	BHLYP	M06	PBE0
$^3\Delta$ ($\sigma^2\sigma\delta$)	1671	1697	1722	1624	1708
$^1\Sigma^+$ ($\sigma^2\sigma^2$)	1609	1760	1792	1886	1760
$^3\Pi$ ($\sigma^2\sigma\pi$)	1622	1651	1680	1646	1661
$^3\Phi$ ($\sigma^2\delta\pi$)	1508	1549	1606	1471	1560
$^3\Sigma^-$ ($\sigma^2\delta^2$)	1564	1595	1634	1537	1608
$^3\Sigma^-$ ($\sigma^2\pi^2$)	1525	1605	1613	1566	1615

[a] Calculated at the indicated level of theory with cc-pwCVQZ-PP-MDF/aug-cc-pVQZ basis sets. Frequencies unscaled.

Table B.4. Theoretical BDEs for ThH^+ (in eV).[a]

$D_0(Th^+-H)$	Basis Set	CCSD(T)[b]	B3LYP	B3PW91	BHLYP	M06	PBE0
$^3\Delta_1$[c]	SDD-VDZ-MWB/6-311+G(3p)	**2.42**	**2.88**	**2.91**	**2.73**	2.60	**2.83**
		(2.64)	(**3.10**)	(**3.13**)	(**2.93**)	(2.82)	(**3.05**)
	SDD-VDZ-MWB/aug-cc-pVQZ	2.69	**2.90**	**2.92**	**2.74**	2.61	**2.85**
		(**2.91**)	(**3.12**)	(**3.14**)	(**2.96**)	(2.83)	(**3.07**)
	Seg. SDD-VQZ-MWB/6-311+G(3p)	**2.57**	**2.94**	**2.96**	**2.77**	2.70	**2.89**
		(2.79)	(**3.16**)	(**3.18**)	(**2.99**)	(2.92)	(**3.11**)
	Seg. SDD-VQZ-MWB/aug-cc-pVQZ	**2.64**[d]	**2.96**	**2.99**	**2.79**	2.72	**2.91**
		(2.88)	(**3.18**)	(**3.21**)	(**3.01**)	(2.94)	(**3.13**)
	ANO-VQZ-MWB/6-311+G(3p)	**2.57**	**2.92**	**2.95**	**2.75**	2.68	**2.87**
		(2.79)	(**3.14**)	(**3.17**)	(**2.97**)	(2.90)	(**3.19**)
	ANO-VQZ-MDF/6-311+G(3p)	**3.43**[e]	**2.92**	**2.94**	**2.77**	2.66	**2.87**
		(3.65)	(**3.14**)	(**3.16**)	(**2.99**)	(2.88)	(**3.09**)
	cc-pVTZ-PP-MDF/aug-cc-pVQZ	**2.68**[f]	**2.90**	**2.92**	**2.76**	2.64	**2.85**
		(2.90)	(**3.12**)	(**3.14**)	(**2.98**)	(2.86)	(**3.07**)
	cc-pVQZ-PP-MDF/6-311+G(3p)	**2.74**	**2.89**	**2.91**	**2.75**	2.62	**2.84**
		(2.96)	(**3.11**)	(**3.13**)	(**2.97**)	(2.84)	(**3.06**)

Table B.4. (continued)

$D_0(Th^+-H)$	Basis Set	CCSD(T)[b]	B3LYP	B3PW91	BHLYP	M06	PBE0
$^3\Delta_1$[c]	cc-pVQZ-PP-MDF/aug-cc-pVQZ	**2.71**	**2.88**	**2.90**	**2.74**	2.61	**2.83**
		(2.93)	(**3.10**)	(**3.12**)	(**2.96**)	(2.83)	(**3.05**)
	cc-pVTZ-PP-MDF/cc-pVTZ	**2.74**	**2.89**	**2.91**	**2.75**	2.65	**2.85**
		(2.96)	(**3.11**)	(**3.13**)	(**2.99**)	(2.87)	(**3.07**)
	cc-pVQZ-PP-MDF/cc-pVQZ	**2.81**	**2.89**	**2.91**	**2.75**	2.62	**2.84**
		(3.03)	(**3.11**)	(**3.13**)	(**2.99**)	(2.84)	(**3.06**)
	CBS-pVXZ-PP-MDF[g]	**2.86**	**2.89**	**2.91**	**2.75**	2.62	**2.84**
		(3.08)	(**3.11**)	(**3.13**)	(**2.99**)	(2.84)	(**3.06**)
	cc-pwCVTZ-PP-MDF/aug-cc-pVQZ	2.73	**2.90**	**2.92**	**2.76**	2.64	**2.85**
		(2.95)	(**3.12**)	(**3.14**)	(**2.98**)	(2.86)	(**3.07**)
	cc-pwCVQZ-PP-MDF/6-311+G(3p)	**2.64**	**2.89**	**2.91**	**2.75**	2.62	**2.84**
		(2.86)	(**3.11**)	(**3.13**)	(**2.97**)	(2.84)	(**3.06**)
	cc-pwCVQZ-PP-MDF/aug-cc-pVQZ	**2.71**	**2.89**	**2.91**	**2.75**	2.63	**2.84**
		(2.93)	(**3.11**)	(**3.13**)	(**2.97**)	(2.85)	(**3.06**)
	cc-pwCVTZ-PP-MDF/cc-pVTZ	**2.64**	**2.89**	**2.91**	**2.75**	2.63	**2.85**
		(2.86)	(**3.11**)	(**3.13**)	(**2.97**)	(2.85)	(**3.07**)

Table B.4. (continued)

$D_0(Th^+-H)$	Basis Set	CCSD(T)[b]	B3LYP	B3PW91	BHLYP	M06	PBE0
$^3\Delta_1$[c]	cc-pwCVQZ-PP-MDF/cc-pVQZ	**2.69**	**2.89**	**2.91**	**2.75**	2.62	**2.84**
		(2.91)	(**3.11**)	(**3.13**)	(**2.97**)	(2.84)	(**3.06**)
	CBS-pwCVXZ-PP-MDF[g]	**2.72**	**2.89**	**2.91**	**2.75**	2.62	**2.84**
		(2.94)	(**3.11**)	(**3.13**)	(**2.97**)	(2.84)	(**3.06**)
	cc-pVTZ-PP-DK3/cc-pVTZ[h]	**2.74**	**2.78**	**2.87**	**2.75**		**2.85**
		(2.96)	(**3.00**)	(**3.09**)	(**2.97**)		(**3.07**)
	cc-pVQZ-PP-DK3/cc-pVQZ[h]	**2.80**	**2.79**	**2.87**	**2.75**		**2.86**
		(3.02)	(**3.01**)	(**3.09**)	(**2.97**)		(**3.08**)
	CBS-cc-pVXZ-PP-DK3[g]	**2.83**	**2.79**	**2.87**	**2.75**		**2.85**
		(3.05)	(**3.01**)	(**3.09**)	(**2.97**)		(**3.07**)
	cc-pwCVTZ-PP-DK3/cc-pVTZ[h]	**2.64**	**2.78**	**2.87**	**2.75**		**2.85**
		(2.86)	(**3.00**)	(**3.09**)	(**2.97**)		(**3.07**)
	cc-pwCVQZ-PP-DK3/cc-pVQZ[h]	**2.69**	**2.78**	**2.87**	**2.75**		**2.85**
		(2.91)	(**3.00**)	(**3.09**)	(**2.97**)		(**3.07**)
	CBS-cc-pwCVXZ-PP-DK3[g]	**2.72**	**2.78**	**2.88**	**2.75**		**2.85**
		(2.94)	(**3.00**)	(**3.10**)	(**2.97**)		(**3.07**)

Table B.4. (continued)

$D_0(Th^+-H)$	Basis Set	CCSD(T)[b]	B3LYP	B3PW91	BHLYP	M06	PBE0
$^1\Sigma^+$	SDD-VDZ-MWB/6-311+G(3p)	**2.42**	2.43	2.21	2.27	**2.69**	2.16
		(**2.82**)	(2.83)	(2.61)	(2.67)	(**3.09**)	(2.56)
	SDD-VDZ-MWB/aug-cc-pVQZ	**2.71**	2.44	2.66	2.58	**2.70**	2.61
		(**3.11**)	(2.84)	(3.06)	(2.98)	(**3.10**)	(3.01)
	Seg. SDD-VQZ-MWB/6-311+G(3p)	2.47	2.46	2.26	2.31	**2.74**	2.20
		(**2.87**)	(2.86)	(2.66)	(2.71)	(**3.14**)	(2.60)
	Seg. SDD-VQZ-MWB/aug-cc-pVQZ	2.67	2.50	2.29	2.34	**2.77**	2.23
		(3.07)	(2.90)	(2.69)	(2.74)	(**3.17**)	(2.63)
	ANO-VQZ-MWB/6-311+G(3p)	2.46	2.44	2.24	2.28	**2.72**	2.18
		(2.86)	(2.84)	(2.64)	(2.68)	(**3.02**)	(2.58)
	ANO-VQZ-MDF/6-311+G(3p)	3.31[e]	2.45	2.25	2.30	**2.73**	2.18
		(3.71)	(2.85)	(2.65)	(2.70)	(**3.03**)	(2.58)
	cc-pVTZ-PP-MDF/aug-cc-pVQZ	2.62	2.45	2.23	2.30	**2.73**	2.17
		(3.02)	(2.85)	(2.63)	(2.70)	(**3.13**)	(2.57)
	cc-pVQZ-PP-MDF /6-311+G(3p)	2.60	2.44	2.22	2.29	**2.72**	2.16
		(**3.00**)	(2.84)	(2.62)	(2.69)	(**3.12**)	(2.56)

Table B.4. (continued)

$D_0(Th^+-H)$	Basis Set	CCSD(T)[c]	B3LYP	B3PW91	BHLYP	M06	PBE0
$^1\Sigma^+$	cc-pVQZ-PP-MDF /aug-cc-pVQZ	2.59	2.44	2.21	2.28	**2.71**	2.16
		(**2.99**)	(2.84)	(2.61)	(2.68)	(**3.11**)	(2.56)
	cc-pVTZ-PP-MDF/cc-pVTZ	2.67	2.44	2.22	2.29	**2.72**	2.17
		(3.07)	(2.84)	(2.62)	(2.69)	(**3.12**)	(2.57)
	cc-pVQZ-PP-MDF/cc-pVQZ	2.68	2.44	2.22	2.29	**2.72**	2.16
		(3.08)	(2.84)	(2.62)	(2.69)	(**3.12**)	(2.56)
	CBS-cc-pVXV-PP-MDF[g]	2.69	2.44	2.22	2.29	**2.71**	2.16
		(3.09)	(2.84)	(2.62)	(2.69)	(**3.11**)	(2.56)
	cc-pwCVTZ-PP-MDF/aug-cc-pVQZ	2.62	2.46	2.23	2.31	**2.74**	2.18
		(**3.02**)	(2.86)	(2.63)	(2.71)	(**3.14**)	(2.68)
	cc-pwCVQZ-PP-MDF/6-311+G(3p)	2.50	2.44	2.22	2.29	**2.72**	2.16
		(**2.90**)	(2.84)	(2.62)	(2.69)	(**3.12**)	(2.66)
	cc-pwCVQZ-PP-MDF/aug-cc-pVQZ	2.62	2.45	2.23	2.30	**2.73**	2.17
		(**3.02**)	(2.85)	(2.63)	(2.70)	(**3.13**)	(2.67)
	cc-pwCVTZ-PP-MDF/cc-pVTZ	2.52	2.44	2.22	2.29	**2.71**	2.17
		(**2.92**)	(2.84)	(2.62)	(2.69)	(**3.11**)	(2.67)

Table B.4. (continued)

$D_0(Th^+-H)$	Basis Set	CCSD(T)[b]	B3LYP	B3PW91	BHLYP	M06	PBE0
$^1\Sigma^+$	cc-pwCVQZ-PP-MDF/cc-pVQZ	2.56	2.44	2.22	2.29	**2.72**	2.17
		(**2.96**)	(2.84)	(2.62)	(2.69)	(**3.12**)	(2.67)
	CBS-cc-pwCVXZ-PP-MDF[g]	2.59	2.44	2.22	2.29	**2.72**	2.16
		(**2.99**)	(2.84)	(2.62)	(2.69)	(**3.12**)	(2.66)
	cc-pVTZ-PP-DK3/cc-pVTZ[h]	2.61	2.31	2.15	2.28		2.15
		(**3.01**)	(2.71)	(2.55)	(2.68)		(2.55)
	cc-pVQZ-PP-DK3/cc-pVQZ[h]	2.64	2.31	2.15	2.28		2.15
		(**3.04**)	(2.71)	(2.56)	(2.68)		(3.55)
	CBS-cc-pVXZ-PP-DK3[g]	2.66	2.31	2.15	2.27		2.14
		(**3.06**)	(2.71)	(2.55)	(2.67)		(2.54)
	cc-pwCVTZ-PP-DK3/cc-pVTZ[h]	2.50	2.30	2.16	2.28		2.15
		(**2.90**)	(2.70)	(2.56)	(2.68)		(2.55)
	cc-pwCVQZ-PP-DK3/cc-pVQZ[h]	2.54	2.31	2.16	2.28		2.15
		(**2.94**)	(2.71)	(2.56)	(2.68)		(2.55)
	CBS-cc-pwCVQZ-PP-DK3[g]	2.56	2.31	2.15	2.27		2.14
		(**2.96**)	(2.71)	(2.55)	(2.67)		(2.54)

Table B.4 Continued

[a] Calculated from structures optimized using the indicated basis sets (Th^+-ECP/H) at the respective level of theory (except CCSD(T) and all-electron DK3 calculations). Values include spin-orbit correction of the difference between the ^2D state averaged over all spin-orbit states and the $^4F_{3/2}$ ground-level (-0.40 eV). Values in parentheses do not include spin-orbit corrections, i.e., are relative to Th^+ (^2D) + H(^2S). Ground-state in bold.
[b] Single-point energy from B3LYP optimized structure.
[c] Include spin-orbit stabilization energy of $^3\Delta_1$ (0.18 eV).
[d] Value includes a BSSE correction of -0.11 eV.
[e] Results poorly understood. See text.
[f] Value includes a BSSE correction of -0.78 eV.
[g] Complete basis set limit extrapolated from indicated basis sets.
[h] Single-point energy from B3LYP/cc-pwCVQZ-PP-MDF/aug-cc-pVQZ optimized structure.
.

APPENDIX C

SUPPORTING INFORMATION FOR CHAPTER 6

Coupling of $Th^{2+} + O_2^-$

A quantitative analysis of the coupling of the $Th^{2+} + O_2^-$ with the $Th^+ + O_2$ reaction is shown in Figure C.1 according to the procedure set forth by Sievers et al.[1] The solid line represents the ion-induced dipole potential including the centrifugal potential, Eq. C.1:

$$V_4(r) = -\alpha e^2/8\pi\varepsilon_0 r^4 + (b_{max}/r)^2 E \qquad (C.1)$$

where $\alpha = 1.57$ Å^3 is the polarizability volume of O_2,[2] e is the charge of an electron, ε_0 is the permittivity of free space, r is the $Th^+ - O_2$ bond distance, E is the relative kinetic energy of the reactants, and b_{max} is the maximum impact parameter leading to a reaction. b_{max} is equivalent to $(\sigma_{LGS}/\pi)^{1/2}$ where the Langevin-Gioumousis-Stevenson cross section, σ_{LGS},[3] is defined according to Eq. C.2:

$$\sigma_{LGS} = \pi e(\alpha/2\pi\varepsilon_0 E)^{1/2} \qquad (C.2)$$

The dashed line represents the Coulombic potential and centrifugal potential being displaced by the asymptotic energy E(CT), Eq. C.3:

$$V_1(r) = -2e^2/4\pi\varepsilon_0 r + (b_{max}/r)^2 E + E(\mathrm{CT}) \qquad (C.3)$$

where E(CT) is defined according to Eq. C.4:

$$E(\mathrm{CT}) = \mathrm{IE}(\mathrm{Th}^+) + \mathrm{EA}(\mathrm{O_2}) \qquad (C.4)$$

The ionization energy of Th^+, IE(Th^+) = 11.65 ± 0.35 eV,[4] from Marcalo and Gibson's evaluation of actinide thermochemical values is adopted. The electron affinity of O_2, EA(O_2) = 0.448 eV, is taken from Ervin et al.[5]

Figure C.1a represents the calculation of the V_4 and V_1 surfaces for r = 0 – 15 Å at E = 0.03 eV. Figure C.1b shows the region near the crossing for E = 0.03 eV, where the surface crossing is inside r_{max} so that the reaction is limited by the V_4 potential. At E = 0.50 eV, the crossing between the V_4 and V_1 surfaces is near r_{max} so that the V_1 potential may begin to be influential. At the collision energy where the experimental reaction cross section begins to deviate from σ_{LGS}, E = 0.60 eV, the crossing occurs at bond distance greater than the r_{max} of V_4 so that at larger impact parameters, the $Th^+ + O_2$ reaction can occur by coupling with the $Th^{2+} + O_2$ surface, which is overall more attractive than the V_4 surface.

CeO^+ Thermochemistry

Existing reports of $D_0(Ce^+\text{-}O)$ have been derived from Eq. C.5.

$$D_0(Ce^+\text{-}O) = D_0(Ce\text{-}O) + IE(Ce) - IE(CeO) \qquad (C.5)$$

Of these values, IE(Ce) = 5.5387 eV[6] is the most reliably established. In their review of metal oxide bond dissociation energies (BDEs), Pedley and Marshall report $D_0(Ce\text{-}O)$ = 8.30 ± 0.13 eV[7] derived from 8.31 ± 0.13 eV,[8] 8.31 ± 0.16 eV,[9] 8.28 ± 0.13 eV, and 8.30 ± 0.13 eV.[10] This is similar to the value determined by Konings et al., $D_0(Ce\text{-}O)$ = 8.23 ± 0.08 eV,[11] who in addition to the above work cite an additional obscure source. The weighted average of the reported ionization energies of CeO is IE = 5.0 ± 0.1 eV, derived from values of 5.2 ± 0.5 eV,[12] 5.2 ± 0.2 eV,[10] 6.0 ± 0.5 eV,[13] 5.3 ± 0.5 eV,[14] and 4.9 ± 0.1 eV[15] all from electron impact experiments. Using Eq. 1, we determine a value of $D_0(Ce^+\text{-}O)$ = 8.82 ± 0.21 eV using the Pedley and Marshall neutral BDE and $D_0(Ce^+\text{-}O)$ = 8.75 ± 0.19 eV from the Konings et al. value. We adopt the more conservative Pedley and Marshall value, which is similar to the value Gibson cites, $D_0(Ce^+\text{-}O)$ = 8.80 ± 0.16 eV.[16] These values are also consistent with the experimental lower limits of $D_0(Ce^+\text{-}O) \geq D_0(OC\text{-}O)$ = 5.45 eV[17] determined in ion cyclotron experiments and $D_0(Ce^+\text{-}O) \geq D_0(N\text{-}O)$ = 6.50 eV[18] determined in flow tube mass spectrometry experiments.

References

(1) Sievers, M. R.; Chen, Y.-M.; Armentrout, P. B. *J. Chem. Phys.* **1996**, *105*, 6322-6333.

(2) Rothe, E. W.; Bernstein, R. B. *J. Chem. Phys.* **1959**, *31*, 1619-1627.

(3) Gioumousis, G.; Stevenson, D. P. *J. Chem. Phys.* **1958**, *29*, 294-299.

(4) Marcalo, J.; Santos, M.; Pires de Matos, A.; Gibson, J. K.; Haire, R. G. *J. Phys. Chem. A* **2008**, *112*, 12647-12656.

(5) Ervin, K. M.; Anusiewicz, I.; Skurski, P.; Simons, J.; Lineberger, W. C. *J. Phys. Chem. A* **2003**, *107*, 8521-8529.

(6) Sansonetti, J. E.; Martin, W. C. *J. Phys. Chem. Ref. Data* **2005**, *34*, 1559-2259.

(7) Pedley, J. B.; Marshall, E. M. *J. Phys. Chem. Ref. Data* **1983**, *12*, 967-1031.

(8) Walsh, P. N.; Dever, D. F.; White, D. *J. Phys. Chem.* **1961**, *65*, 1410-1413.

(9) Coppens, P.; Smoes, S.; Drowart, J. *Trans. Faraday Soc.* **1967**, *63*, 2140-2148.

(10) Ackermann, R. J.; Rauh, E. G. *J. Chem. Thermodyn.* **1971**, *3*, 609-624.

(11) Konings, R. J. M.; Benes, O.; Kovacs, A.; Manara, D.; Sedmidubsky, D.; Gorokhov, L.; Iorish, V. S.; Yungman, V.; Shenyavskaya, E.; Osina, E. *J. Phys. Chem. Ref. Data* **2014**, *43*, 01310101-01310195.

(12) Staley, H. G.; Norman, J. H. *Int. J. Mass Spectrom. Ion Phys.* **1969**, *2*, 35-43.

(13) Gingerich, K. A.; Pupp, C. *J. Chem. Phys.* **1971**, *54*, 3713-3716.

(14) Piacente, V.; Bardi, G.; Malaspina, L.; Desideri, A. *J. Chem. Phys.* **1973**, *59*, 31-36.

(15) Ackermann, R. J.; Rauh, E. G.; Thorn, R. J. *J. Chem. Phys.* **1976**, *65*, 1027-1031.

(16) Gibson, J. K. *J. Phys. Chem. A* **2003**, *107*, 7891-7899.

(17) Cornehl, H. H.; Wesendrup, R.; Diefenbach, M.; Schwarz, H. *Chem. - Eur. J.* **1997**, *3*, 1083-1090.

(18) Blagojevic, V.; Flaim, E.; Jarvis, M. J. Y.; Koyanagi, G. K.; Bohme, D. K. *Int. J. Mass Spectrom.* **2006**, *249/250*, 385-391.

Table C.1. Calculated ground and excited-states of ThO^+ and ThC^+ (in eV).[a]

ThO^+ [b]	Basis Set	CCSD(T)[c]	B3LYP	B3PW91	BHLYP	M06	PBE0
$^2\Sigma^+$ ($1\sigma^2 2\sigma^2 1\pi^4 3\sigma$)	SDD-VDZ-MWB/6-311+G(3df)	**0.00**	**0.00**	**0.00**	**0.00**	**0.00**	**0.00**
	Seg. SDD-VQZ-MWB/6-311+G(3df)	**0.00**	**0.00**	**0.00**	**0.00**	**0.00**	**0.00**
	ANO-VQZ-MWB/6-311+G(3df)	**0.00**	**0.00**	**0.00**	**0.00**	**0.00**	**0.00**
	ANO-VQZ-MDF/6-311+G(3df)	**0.00**	**0.00**	**0.00**	**0.00**	**0.00**	**0.00**
	cc-pVQZ-PP-MDF/6-311+G(3df)	**0.00**	**0.00**	**0.00**	**0.00**	**0.00**	**0.00**
	cc-pwCVQZ-PP-MDF/aug-cc-pwCVQZ	**0.00**	**0.00**	**0.00**	**0.00**	**0.00**	**0.00**
	cc-pwCVTZ-PP-MDF/cc-pwCVTZ	**0.00**	**0.00**	**0.00**	**0.00**	**0.00**	**0.00**
	cc-pwCVQZ-PP-MDF/cc-pwCVQZ	**0.00**	**0.00**	**0.00**	**0.00**	**0.00**	**0.00**
$^2\Delta$ ($1\sigma^2 2\sigma^2 1\pi^4 1\delta$)	SDD-VDZ-MWB/6-311+G(3df)	0.76	0.51	0.41	0.47	0.33	
	Seg. SDD-VQZ-MWB/6-311+G(3df)[e]	0.66	0.50	0.40	0.48	0.32	0.41
	ANO-VQZ-MWB/6-311+G(3df)	0.64	0.49	0.39	0.46	0.31	0.39
	ANO-VQZ-MDF/6-311+G(3df)	0.62	0.49	0.39	0.46	0.31	0.39
	cc-pVQZ-PP-MDF/6-311+G(3df)	0.58	0.51	0.41	0.48	0.35	0.41
	cc-pwCVQZ-PP-MDF/aug-cc-pwCVQZ	0.58	0.51	0.41	0.48	0.36	0.41
	cc-pwCVTZ-PP-MDF/cc-pwCVTZ	0.59	0.50	0.40	0.47	0.35	0.41
	cc-pwCVQZ-PP-MDF/cc-pwCVQZ	0.58	0.51	0.41	0.47	0.35	0.41

Table C.1. (continued)

ThO^{+} [b]	Basis Set	CCSD(T)[c]	B3LYP	B3PW91	BHLYP	M06	PBE0
$^2\Pi$ ($1\sigma^2 2\sigma^2 1\pi^3 3\sigma^2$)	SDD-VDZ-MWB/6-311+G(3df)	1.66	0.96	0.83	1.00	0.69	
	Seg. SDD-VQZ-MWB/6-311+G(3df)[e]	1.33	0.94	0.81	0.98	0.67	0.84
	ANO-VQZ-MWB/6-311+G(3df)	1.31	0.93	0.80	0.97	0.66	0.83
	ANO-VQZ-MDF/6-311+G(3df)						
	cc-pVQZ-PP-MDF/6-311+G(3df)	1.22	1.00	0.88	1.05	0.73	0.90
	cc-pwCVQZ-PP-MDF/aug-cc-pwCVQZ	1.21	0.96	0.84	1.01	0.73	0.86
	cc-pwCVTZ-PP-MDF/cc-pwCVTZ	1.27	0.96	0.83	1.00	0.71	0.86
	cc-pwCVQZ-PP-MDF/cc-pwCVQZ	1.22	0.96	0.84	1.01	0.72	0.86
$^4\Delta$ ($1\sigma^2 1\pi^4 2\sigma 1\delta 3\sigma$)	SDD-VDZ-MWB/6-311+G(3df)	4.29	4.29	4.30	3.99	4.56	
	Seg. SDD-VQZ-MWB/6-311+G(3df)[e]	4.49	4.33	4.33	4.06	4.60	4.31
	ANO-VQZ-MWB/6-311+G(3df)	4.45	4.32	4.32	4.05	4.59	4.30
	ANO-VQZ-MDF/6-311+G(3df)	4.39	4.27	4.27	3.99	4.56	4.25
	cc-pVQZ-PP-MDF/6-311+G(3df)	4.46	4.27	4.29	3.98	4.57	4.24
	cc-pwCVQZ-PP-MDF/aug-cc-pwCVQZ	4.48	4.25	4.24	3.95	4.56	4.21
	cc-pwCVTZ-PP-MDF/cc-pwCVTZ	4.42	4.26	4.25	3.97	4.56	4.23
	cc-pwCVQZ-PP-MDF/cc-pwCVQZ	4.47	4.25	4.24	3.95	4.55	4.21

Table C.1. (continued)

ThO^{+} [b]	Basis Set	CCSD(T)[c]	B3LYP	B3PW91	BHLYP	M06	PBE0
$^4\Pi$ ($1\sigma^2 2\sigma 1\pi^4 3\sigma 2\pi$)	SDD-VDZ-MWB/6-311+G(3df)	4.99	4.41	4.45	4.21	4.55	
	Seg. SDD-VQZ-MWB/6-311+G(3df)[e]	4.94	4.43	4.47	4.25	4.59	4.46
	ANO-VQZ-MWB/6-311+G(3df)	4.91	4.43	4.46	4.24	4.58	4.46
	ANO-VQZ-MDF/6-311+G(3df)	4.88	4.41	4.44	4.22	4.57	4.44
	cc-pVQZ-PP-MDF/6-311+G(3df)	4.90	4.41	4.44	4.22	4.58	4.43
	cc-pwCVQZ-PP-MDF/aug-cc-pwCVQZ	4.91	4.39	4.42	4.20	4.57	4.41
	cc-pwCVTZ-PP-MDF/cc-pwCVTZ	4.90	4.40	4.43	4.21	4.57	4.43
	cc-pwCVQZ-PP-MDF/cc-pwCVQZ	4.91	4.39	4.42	4.20	4.56	4.41
$^4\Sigma^{+}$ ($1\sigma^2 2\sigma 1\pi^4 3\sigma 4\sigma$)	SDD-VDZ-MWB/6-311+G(3df)	5.37	4.50	4.54	4.33	4.68	
	Seg. SDD-VQZ-MWB/6-311+G(3df)[e]	5.09	4.51	4.55	4.36	4.72	4.55
	ANO-VQZ-MWB/6-311+G(3df)	5.08	4.51	4.55	4.36	4.71	4.55
	ANO-VQZ-MDF/6-311+G(3df)	5.07	4.50	4.54	4.35	4.70	4.54
	cc-pVQZ-PP-MDF/6-311+G(3df)	5.06	4.50	4.54	4.35	4.71	4.54
	cc-pwCVQZ-PP-MDF/aug-cc-pwCVQZ	5.07	4.49	4.52	4.33	4.70	4.52
	cc-pwCVTZ-PP-MDF/cc-pwCVTZ	5.07	4.49	4.53	4.34	4.70	4.53
	cc-pwCVQZ-PP-MDF/cc-pwCVQZ	5.07	4.49	4.52	4.33	4.70	4.52

Table C.1. (continued)

ThO^{+} [b]	Basis Set	CCSD(T)[c]	B3LYP	B3PW91	BHLYP	M06	PBE0
$^4\Sigma^-$ ($1\sigma^2 2\sigma 1\pi^4 1\delta^2$)	SDD-VDZ-MWB/6-311+G(3df)	5.34	5.22	5.16	4.89	5.35	
	Seg. SDD-VQZ-MWB/6-311+G(3df)[e]	5.42	5.25	5.20	4.96	5.34	5.17
	ANO-VQZ-MWB/6-311+G(3df)	5.38	5.23	5.18	4.93	5.32	5.14
	ANO-VQZ-MDF/6-311+G(3df)	5.28	5.19	5.12	4.87	5.28	5.09
	cc-pVQZ-PP-MDF/6-311+G(3df)	5.33	5.22	5.15	4.90	5.38	5.12
	cc-pwCVQZ-PP-MDF/aug-cc-pwCVQZ	5.35	5.20	5.13	4.87	5.36	5.09
	cc-pwCVTZ-PP-MDF/cc-pwCVTZ	5.31	5.20	5.13	4.88	5.36	5.10
	cc-pwCVQZ-PP-MDF/cc-pwCVQZ	5.34	5.20	5.13	4.87	5.35	5.09
ThC^{+} [b]	Basis Set	CCSD(T)[c]	B3LYP	B3PW91	BHLYP	M06	PBE0
$^2\Sigma^+$ ($1\sigma^2 1\pi^4 3\sigma$)	SDD-VDZ-MWB/6-311+G(3df)	**0.00**	**0.00**	**0.00**	**0.00**	**0.00**	**0.00**
	Seg. SDD-VQZ-MWB/6-311+G(3df)[e]	**0.00**	**0.00**	**0.00**	**0.00**	**0.00**	**0.00**
	ANO-VQZ-MWB/6-311+G(3df)	**0.00**	**0.00**	**0.00**	**0.00**	**0.00**	**0.00**
	ANO-VQZ-MDF/6-311+G(3df)	**0.00**	**0.00**	**0.00**	**0.00**	**0.00**	**0.00**
	cc-pVQZ-PP-MDF/6-311+G(3df)	**0.00**	**0.00**	**0.00**	**0.00**	**0.00**	**0.00**
	cc-pwCVQZ-PP-MDF/aug-cc-pwCVQZ	**0.00**	**0.00**	**0.00**	**0.00**	**0.00**	**0.00**
	cc-pwCVTZ-PP-MDF/cc-pwCVTZ	**0.00**	**0.00**	**0.00**	**0.00**	**0.00**	**0.00**
	cc-pwCVQZ-PP-MDF/cc-pwCVQZ	**0.00**	**0.00**	**0.00**	**0.00**	**0.00**	**0.00**

Table C.1. (continued)

ThC^{+} [b]	Basis Set	CCSD(T)[c]	B3LYP	B3PW91	BHLYP	M06	PBE0
$^4\Pi$ ($1\sigma^2 1\pi^3 2\sigma 3\sigma$)	SDD-VDZ-MWB/6-311+G(3df)	0.49	0.67	0.75	0.58	0.99	
	Seg. SDD-VQZ-MWB/6-311+G(3df)[e]	0.73	0.66	0.75	0.57	0.99	0.75
	ANO-VQZ-MWB/6-311+G(3df)	0.73	0.67	0.76	0.59	1.07	0.76
	ANO-VQZ-MDF/6-311+G(3df)	0.71	0.63	0.71	0.54	0.97	0.72
	cc-pVQZ-PP-MDF/6-311+G(3df)	0.78	0.62	0.69	0.53	0.94	0.70
	cc-pwCVQZ-PP-MDF/aug-cc-pwCVQZ	0.80	0.61	0.69	0.52	0.94	0.70
	cc-pwCVTZ-PP-MDF/cc-pwCVTZ	0.74	0.62	0.69	0.53	0.93	0.70
	cc-pwCVQZ-PP-MDF/cc-pwCVQZ	0.79	0.62	0.69	0.52	0.94	0.70
$^2\Pi$ ($1\sigma^2 1\pi^3 2\sigma^2$)	SDD-VDZ-MWB/6-311+G(3df)	0.54	0.68	0.82	06.0	0.87	
	Seg. SDD-VQZ-MWB/6-311+G(3df)[e]	0.76	0.68	0.82	0.60	0.87	0.82
	ANO-VQZ-MWB/6-311+G(3df)	0.77	0.69	0.83	0.61	0.87	0.83
	ANO-VQZ-MDF/6-311+G(3df)	0.75	0.66	0.79	0.57	0.87	0.79
	cc-pVQZ-PP-MDF/6-311+G(3df)	0.80	0.64	0.77	0.55	0.86	0.78
	cc-pwCVQZ-PP-MDF/aug-cc-pwCVQZ	0.82	0.64	0.77	0.55	0.85	0.77
	cc-pwCVQZ-PP-MDF/cc-pwCVQZ	0.77	0.65	0.77	0.55	0.85	0.78
	cc-pwCVTZ-PP-MDF/cc-pwCVTZ			0.77	0.55	0.85	0.77

Table C.1. (continued)

ThC^{+} [b]	Basis Set	CCSD(T)[c]	B3LYP	B3PW91	BHLYP	M06	PBE0
$^4\Phi$ ($1\sigma^2 1\pi^3 2\sigma 1\delta$)	SDD-VDZ-MWB/6-311+G(3df)		1.12	1.15	1.01	1.26	
	Seg. SDD-VQZ-MWB/6-311+G(3df)[e]	1.33	1.11	1.14	1.00	1.25	1.15
	ANO-VQZ-MWB/6-311+G(3df)	1.32	1.12	1.14	1.00	1.26	1.15
	ANO-VQZ-MDF/6-311+G(3df)	1.28	1.08	1.10	0.96	1.24	1.11
	cc-pVQZ-PP-MDF/6-311+G(3df)	1.30	1.07	1.09	0.96	1.22	1.10
	cc-pwCVQZ-PP-MDF/aug-cc-pwCVQZ	1.32	1.07	1.09	0.95	1.22	1.09
	cc-pwCVTZ-PP-MDF/cc-pwCVTZ	1.28	1.07	1.09	0.95	1.21	1.10
	cc-pwCVQZ-PP-MDF/cc-pwCVQZ	1.32	1.07	1.09	0.95	1.22	1.10
$^4\Sigma^-$ ($1\sigma^2 1\pi^2 2\sigma^2 1\delta$)	SDD-VDZ-MWB/6-311+G(3df)	1.04	1.35	1.51	1.31	1.55	
	Seg. SDD-VQZ-MWB/6-311+G(3df)[e]	1.45	1.35	1.51	1.31	1.58	1.55
	ANO-VQZ-MWB/6-311+G(3df)	1.46	1.36	1.53	1.32	1.59	1.56
	ANO-VQZ-MDF/6-311+G(3df)	1.45	1.33	1.49	1.29	1.55	1.52
	cc-pVQZ-PP-MDF/6-311+G(3df)	1.52	1.31	1.47	1.27	1.50	1.50
	cc-pwCVQZ-PP-MDF/aug-cc-pwCVQZ	1.55	1.31	1.46	1.27	1.50	1.50
	cc-pwCVTZ-PP-MDF/cc-pwCVTZ	1.47	1.31	1.47	1.27	1.49	1.50
	cc-pwCVQZ-PP-MDF/cc-pwCVQZ	1.54	1.31	1.46	1.27	1.50	1.50

Table C.1. (continued)

ThC^{+} [b]	Basis Set	CCSD(T)[c]	B3LYP	B3PW91	BHLYP	M06	PBE0
$^2\Delta$ ($1\sigma^2 1\pi^4 1\delta$)	SDD-VDZ-MWB/6-311+G(3df)	1.48	1.74	1.82	1.75	1.73	
	Seg. SDD-VQZ-MWB/6-311+G(3df)[e]	1.84	1.73	1.80	1.73	1.69	1.84
	ANO-VQZ-MWB/6-311+G(3df)	1.83	1.73	1.81	1.73	1.70	1.84
	ANO-VQZ-MDF/6-311+G(3df)	1.79	1.69	1.77	1.69	1.68	1.79
	cc-pVQZ-PP-MDF/6-311+G(3df)	1.78	1.69	1.76	1.68	1.67	1.79
	cc-pwCVQZ-PP-MDF/aug-cc-pwCVQZ	1.79	1.68	1.76	1.68	1.67	1.79
	cc-pwCVTZ-PP-MDF/cc-pwCVTZ	1.79	1.69	1.76	1.68	1.67	1.79
	cc-pwCVQZ-PP-MDF/cc-pwCVQZ	1.79	1.68	1.76	1.68	1.67	1.79
$^2\Pi$ ($1\sigma^2 1\pi^4 2\pi$)	SDD-VDZ-MWB/6-311+G(3df)	2.22	2.13	2.18	2.25	2.07	
	Seg. SDD-VQZ-MWB/6-311+G(3df)[e]	2.49	2.09	2.14	2.20	2.02	2.20
	ANO-VQZ-MWB/6-311+G(3df)	2.50	2.10	2.15	2.21	2.02	2.21
	ANO-VQZ-MDF/6-311+G(3df)	2.47	2.08	2.13	2.18	2.02	2.19
	cc-pVQZ-PP-MDF/6-311+G(3df)	2.42	2.07	2.12	2.17	2.00	2.18
	cc-pwCVQZ-PP-MDF/aug-cc-pwCVQZ	2.41	2.08	2.12	2.17	2.02	2.18
	cc-pwCVTZ-PP-MDF/cc-pwCVTZ	2.44	2.08	2.12	2.17	2.01	2.18
	cc-pwCVQZ-PP-MDF/cc-pwCVQZ	2.41	2.08	2.12	2.17	2.02	2.18

Table C.1 Continued

[a] Structures optimized using indicated basis sets (Th^+-ECP/C,O) at the respective level of theory (except CCSD(T)) relative to the ground state with the ground state bolded.
[b] Orbitals are ordered as 1σ, 2σ, 1π, 1δ, and 3σ and described in the main text.
[c] Structures optimized using B3LYP with the indicated basis sets.

Table C.2. Calculated bond distances, r(Th^+-L) for ThL^+ (L= C,O) ground and excited-states (in Å).

ThO^+	Basis Set	B3LYP	B3PW91	BHLYP	M06	PBE0
$^2\Sigma^+$ ($1\sigma^2 2\sigma^2 1\pi^4 3\sigma$)	SDD-VDZ-MWB/6-311+G(3df)	1.807	1.797	1.793	1.783	
	Seg. SDD-VQZ-MWB/6-311+G(3df)[e]	1.799	1.790	1.784	1.786	1.774
	ANO-VQZ-MWB/6-311+G(3df)	1.800	1.791	1.785	1.786	1.775
	ANO-VQZ-MDF/6-311+G(3df)	1.808	1.799	1.793	1.783	1.794
	cc-pVQZ-PP-MDF/6-311+G(3df)	1.807	1.798	1.792	1.783	1.794
	cc-pwCVQZ-PP-MDF/aug-cc-pwCVQZ	1.808	1.798	1.793	1.782	1.794
	cc-pwCVTZ-PP-MDF/cc-pwCVTZ	1.808	1.799	1.793	1.785	1.794
	cc-pwCVQZ-PP-MDF/cc-pwCVQZ	1.808	1.798	1.793	1.782	1.794
$^2\Delta$ ($1\sigma^2 2\sigma^2 1\pi^4 1\delta$)	SDD-VDZ-MWB/6-311+G(3df)	1.825	1.815	1.809	1.805	
	Seg. SDD-VQZ-MWB/6-311+G(3df)[e]	1.819	1.808	1.802	1.797	1.803
	ANO-VQZ-MWB/6-311+G(3df)	1.819	1.808	1.802	1.797	1.803
	ANO-VQZ-MDF/6-311+G(3df)	1.826	1.816	1.802	1.797	1.803
	cc-pVQZ-PP-MDF/6-311+G(3df)	1.825	1.814	1.808	1.803	1.809
	cc-pwCVQZ-PP-MDF/aug-cc-pwCVQZ	1.825	1.815	1.808	1.801	1.810
	cc-pwCVTZ-PP-MDF/cc-pwCVTZ	1.826	1.815	1.809	1.805	1.810
	cc-pwCVQZ-PP-MDF/cc-pwCVQZ	1.825	1.815	1.808	1.802	1.810

Table C.2. (continued)

ThO^+	Basis Set	B3LYP	B3PW91	BHLYP	M06	PBE0
$^2\Pi$ ($1\sigma^2 2\sigma^2 1\pi^3 3\sigma^2$)	SDD-VDZ-MWB/6-311+G(3df)	1.833	1.822	1.818	1.810	
	Seg. SDD-VQZ-MWB/6-311+G(3df)[e]	1.826	1.816	1.811	1.802	1.811
	ANO-VQZ-MWB/6-311+G(3df)	1.827	1.816	1.811	1.802	1.811
	ANO-VQZ-MDF/6-311+G(3df)					
	cc-pVQZ-PP-MDF/6-311+G(3df)	1.834	1.824	1.818	1.810	1.819
	cc-pwCVQZ-PP-MDF/aug-cc-pwCVQZ	1.834	1.823	1.818	1.808	1.818
	cc-pwCVTZ-PP-MDF/cc-pwCVTZ	1.834	1.824	1.818	1.812	1.819
	cc-pwCVQZ-PP-MDF/cc-pwCVQZ	1.834	1.823	1.818	1.808	1.818
$^4\Delta$ ($1\sigma^2 1\pi^4 2\sigma 1\delta 3\sigma$)	SDD-VDZ-MWB/6-311+G(3df)	2.008	1.991	2.002	2.012	
	Seg. SDD-VQZ-MWB/6-311+G(3df)[e]	2.001	1.983	1.993	2.002	1.977
	ANO-VQZ-MWB/6-311+G(3df)	2.001	1.984	1.994	2.002	1.978
	ANO-VQZ-MDF/6-311+G(3df)	2.005	1.988	1.997	2.007	1.981
	cc-pVQZ-PP-MDF/6-311+G(3df)	2.003	1.984	1.993	2.003	1.978
	cc-pwCVQZ-PP-MDF/aug-cc-pwCVQZ	2.003	1.985	1.995	2.001	1.979
	cc-pwCVTZ-PP-MDF/cc-pwCVTZ	2.002	1.984	1.994	2.004	1.978
	cc-pwCVQZ-PP-MDF/cc-pwCVQZ	2.003	1.985	1.995	2.002	1.979

Table C.2. (continued)

ThO^+	Basis Set	B3LYP	B3PW91	BHLYP	M06	PBE0
$^4\Pi$ ($1\sigma^2 2\sigma 1\pi^4 3\sigma 2\pi$)	SDD-VDZ-MWB/6-311+G(3df)	2.011	1.992	2.010	2.025	
	Seg. SDD-VQZ-MWB/6-311+G(3df)[e]	2.004	1.986	2.004	2.000	1.981
	ANO-VQZ-MWB/6-311+G(3df)	2.005	1.986	2.004	2.000	1.982
	ANO-VQZ-MDF/6-311+G(3df)	2.008	1.990	2.007	2.004	1.986
	cc-pVQZ-PP-MDF/6-311+G(3df)	2.005	1.987	2.005	2.000	1.983
	cc-pwCVQZ-PP-MDF/aug-cc-pwCVQZ	2.007	1.988	2.006	2.000	1.984
	cc-pwCVTZ-PP-MDF/cc-pwCVTZ	2.006	1.988	2.005	2.002	1.983
	cc-pwCVQZ-PP-MDF/cc-pwCVQZ	2.007	1.988	2.006	2.001	1.984
$^4\Sigma^+$ ($1\sigma^2 2\sigma 1\pi^4 3\sigma 4\sigma$)	SDD-VDZ-MWB/6-311+G(3df)	2.026	2.007	2.020	2.012	
	Seg. SDD-VQZ-MWB/6-311+G(3df)[e]	2.003	1.984	2.002	1.999	1.980
	ANO-VQZ-MWB/6-311+G(3df)	2.004	1.985	2.002	1.999	1.980
	ANO-VQZ-MDF/6-311+G(3df)	2.007	1.989	2.005	2.003	1.984
	cc-pVQZ-PP-MDF/6-311+G(3df)	2.005	1.986	2.003	1.999	1.982
	cc-pwCVQZ-PP-MDF/aug-cc-pwCVQZ	2.006	1.987	2.004	1.999	1.983
	cc-pwCVTZ-PP-MDF/cc-pwCVTZ	2.006	1.987	2.003	2.001	1.982
	cc-pwCVQZ-PP-MDF/cc-pwCVQZ	2.006	1.987	2.004	2.000	1.983

Table C.2. (continued)

ThO^+	Basis Set	B3LYP	B3PW91	BHLYP	M06	PBE0
$^4\Sigma^-$ ($1\sigma^2 2\sigma 1\pi^4 1\delta^2$)	SDD-VDZ-MWB/6-311+G(3df)	2.011	1.992	2.010	2.009	
	Seg. SDD-VQZ-MWB/6-311+G(3df)[e]	2.021	2.000	2.012	2.019	1.994
	ANO-VQZ-MWB/6-311+G(3df)	2.020	1.999	2.012	2.019	1.993
	ANO-VQZ-MDF/6-311+G(3df)	2.020	2.003	2.014	2.020	1.996
	cc-pVQZ-PP-MDF/6-311+G(3df)	2.016	1.997	2.010	2.014	1.991
	cc-pwCVQZ-PP-MDF/aug-cc-pwCVQZ	2.017	1.998	2.011	2.011	1.993
	cc-pwCVTZ-PP-MDF/cc-pwCVTZ	2.017	1.999	2.010	2.015	1.992
	cc-pwCVQZ-PP-MDF/cc-pwCVQZ	2.017	1.998	2.011	2.012	1.993
ThC^+	Basis Set	B3LYP	B3PW91	BHLYP	M06	PBE0
$^2\Sigma^+$ ($1\sigma^2 1\pi^4 3\sigma$)	SDD-VDZ-MWB/6-311+G(3df)	1.894	1.885	1.88	1.871	
	Seg. SDD-VQZ-MWB/6-311+G(3df)[e]	1.892	1.883	1.885	1.867	1.880
	ANO-VQZ-MWB/6-311+G(3df)	1.893	1.883	1.886	1.867	1.880
	ANO-VQZ-MDF/6-311+G(3df)	1.903	1.894	1.886	1.878	1.896
	cc-pVQZ-PP-MDF/6-311+G(3df)	1.903	1.893	1.895	1.877	1.890
	cc-pwCVQZ-PP-MDF/aug-cc-pwCVQZ	1.902	1.893	1.895	1.875	1.890
	cc-pwCVTZ-PP-MDF/cc-pwCVTZ	1.903	1.896	1.894	1.878	1.890
	cc-pwCVQZ-PP-MDF/cc-pwCVQZ	1.902	1.893	1.895	1.876	1.890

Table C.2. (continued)

ThC^+	Basis Set	B3LYP	B3PW91	BHLYP	M06	PBE0
$^4\Pi$ ($1\sigma^2 1\pi^3 2\sigma 3\sigma$)	SDD-VDZ-MWB/6-311+G(3df)	2.043	2.032	2.035	2.019	
	Seg. SDD-VQZ-MWB/6-311+G(3df)[e]	2.040	2.029	2.031	2.014	2.026
	ANO-VQZ-MWB/6-311+G(3df)	2.040	2.030	2.031	2.024	2.026
	ANO-VQZ-MDF/6-311+G(3df)	2.048	2.038	2.039	2.023	2.034
	cc-pVQZ-PP-MDF/6-311+G(3df)	2.049	2.038	2.040	2.024	2.035
	cc-pwCVQZ-PP-MDF/aug-cc-pwCVQZ	2.049	2.038	2.040	2.023	2.035
	cc-pwCVTZ-PP-MDF/cc-pwCVTZ	2.050	2.039	2.041	2.026	2.035
	cc-pwCVQZ-PP-MDF/cc-pwCVQZ	2.049	2.038	2.040	2.023	2.035
$^2\Pi$ ($1\sigma^2 1\pi^3 2\sigma^2$)	SDD-VDZ-MWB/6-311+G(3df)	2.007	2.003	2.014	1.923	
	Seg. SDD-VQZ-MWB/6-311+G(3df)[e]	2.007	2.001	2.012	1.918	1.998
	ANO-VQZ-MWB/6-311+G(3df)	2.005	1.999	2.012	1.919	1.997
	ANO-VQZ-MDF/6-311+G(3df)	2.021	2.015	2.023	1.930	2.012
	cc-pVQZ-PP-MDF/6-311+G(3df)	2.023	2.017	2.024	1.933	2.013
	cc-pwCVQZ-PP-MDF/aug-cc-pwCVQZ	2.023	2.017	2.024	1.932	2.014
	cc-pwCVTZ-PP-MDF/cc-pwCVTZ	2.024	2.018	2.025	1.933	2.014
	cc-pwCVQZ-PP-MDF/cc-pwCVQZ		2.017	2.024	1.933	2.014

Table C.2. (continued)

ThC^+	Basis Set	B3LYP	B3PW91	BHLYP	M06	PBE0
$^4\Phi$ ($1\sigma^2 1\pi^3 2\sigma 1\delta$)	SDD-VDZ-MWB/6-311+G(3df)	2.063	2.050	2.050	2.044	
	Seg. SDD-VQZ-MWB/6-311+G(3df)[e]	2.061	2.048	2.048	2.043	2.043
	ANO-VQZ-MWB/6-311+G(3df)	2.061	2.048	2.048	2.043	2.042
	ANO-VQZ-MDF/6-311+G(3df)	2.068	2.056	2.056	2.050	2.050
	cc-pVQZ-PP-MDF/6-311+G(3df)	2.068	2.056	2.056	2.050	2.050
	cc-pwCVQZ-PP-MDF/aug-cc-pwCVQZ	2.068	2.055	2.055	2.047	2.050
	cc-pwCVTZ-PP-MDF/cc-pwCVTZ	2.069	2.056	2.056	2.051	2.051
	cc-pwCVQZ-PP-MDF/cc-pwCVQZ	2.068	2.055	2.055	2.048	2.050
$^4\Sigma^-$ ($1\sigma^2 1\pi^2 2\sigma^2 1\delta$)	SDD-VDZ-MWB/6-311+G(3df)	2.119	2.113	2.104	2.088	
	Seg. SDD-VQZ-MWB/6-311+G(3df)[e]	2.115	2.109	2.099	2.082	2.102
	ANO-VQZ-MWB/6-311+G(3df)	2.116	2.109	2.099	2.082	2.103
	ANO-VQZ-MDF/6-311+G(3df)	2.123	2.117	2.107	2.093	2.110
	cc-pVQZ-PP-MDF/6-311+G(3df)	2.124	2.118	2.108	2.096	2.112
	cc-pwCVQZ-PP-MDF/aug-cc-pwCVQZ	2.124	2.118	2.108	2.095	2.112
	cc-pwCVTZ-PP-MDF/cc-pwCVTZ	2.125	2.119	2.109	2.097	2.113
	cc-pwCVQZ-PP-MDF/cc-pwCVQZ	2.124	2.118	2.108	2.097	2.112

Table C.2. (continued)

ThC^+	Basis Set	B3LYP	B3PW91	BHLYP	M06	PBE0
$^2\Delta$ ($1\sigma^2 1\pi^4 1\delta$)	SDD-VDZ-MWB/6-311+G(3df)	1.956	1.941	1.950	1.935	
	Seg. SDD-VQZ-MWB/6-311+G(3df)[e]	1.955	1.940	1.948	1.933	1.935
	ANO-VQZ-MWB/6-311+G(3df)	1.954	1.940	1.948	1.933	1.935
	ANO-VQZ-MDF/6-311+G(3df)	1.962	1.947	1.955	1.941	1.943
	cc-pVQZ-PP-MDF/6-311+G(3df)	1.962	1.947	1.955	1.940	1.942
	cc-pwCVQZ-PP-MDF/aug-cc-pwCVQZ	1.962	1.946	1.955	1.937	1.942
	cc-pwCVTZ-PP-MDF/cc-pwCVTZ	1.962	1.947	1.955	1.940	1.943
	cc-pwCVQZ-PP-MDF/cc-pwCVQZ	1.962	1.946	1.955	1.937	1.942
$^2\Pi$ ($1\sigma^2 1\pi^4 2\pi$)	SDD-VDZ-MWB/6-311+G(3df)	1.964	1.948	1.960	1.943	
	Seg. SDD-VQZ-MWB/6-311+G(3df)[e]	1.962	1.947	1.957	1.940	1.943
	ANO-VQZ-MWB/6-311+G(3df)	1.962	1.947	1.958	1.940	1.943
	ANO-VQZ-MDF/6-311+G(3df)	1.970	1.954	1.965	1.948	1.950
	cc-pVQZ-PP-MDF/6-311+G(3df)	1.970	1.954	1.965	1.947	1.950
	cc-pwCVQZ-PP-MDF/aug-cc-pwCVQZ	1.970	1.954	1.965	1.945	1.950
	cc-pwCVTZ-PP-MDF/cc-pwCVTZ	1.970	1.954	1.965	1.948	1.950
	cc-pwCVQZ-PP-MDF/cc-pwCVQZ	1.970	1.954	1.965	1.945	1.950

[a] Structures optimized using indicated basis set with the respective level of theory.

Table C.3. Vibrational Frequencies of ThL^+ ground and excited-states (in cm^{-1}).[a]

ThO^+	B3LYP	B3PW91	BHLYP	M06	PBE0
$^2\Sigma^+$ ($1\sigma^2 2\sigma^2 1\pi^4 3\sigma$)	960	979	1003	1023	990
$^2\Delta$ ($\sigma^2\sigma^2\pi^4\delta$)	912	934	959	952	946
$^2\Pi$ ($\sigma^2\sigma^2\pi^3\sigma^2$)	894	915	939	936	927
$^4\Delta$ ($\sigma^2\pi^4\sigma\delta\sigma$)	680	692	696	649	696
$^4\Pi$ ($\sigma^2\sigma\pi^4\sigma\pi$)	673	685	681	638	688
$^4\Sigma^+$ ($\sigma^2\sigma\pi^4\sigma\sigma$)	676	687	682	648	690
$^4\Sigma^-$ ($\sigma^2\sigma\pi^4\delta^2$)	661	673	673	627	677
ThC^+	B3LYP	B3PW91	BHLYP	M06	PBE0
$^2\Sigma^+$ ($\sigma^2\pi^4\sigma$)	913	934	937	961	944
$^4\Pi$ ($\sigma^2\pi^3\sigma\sigma$)	774	786	802	804	796
$^2\Pi$ ($\sigma^2\pi^3\sigma^2$)	675	701	755	763	716
$^4\Phi$ ($\sigma^2\pi^3\sigma\delta$)	746	761	776	767	770
$^4\Sigma^-$ ($\sigma^2\pi^2\sigma^2\delta$)	704	710	733	716	719
$^2\Delta$ ($\sigma^2\pi^4\delta$)	837	865	867	849	875
$^2\Pi$ ($\sigma^2\pi^4\pi$)	823	852	851	836	862

[a] Calculated from optimized structures at indicated level of theory with cc-pwCVQZ-PP-MDF/aug-pwCVQZ basis sets. Frequencies unscaled.

Table C.4. Theoretical BDEs for ThO^+ and ThC^+ in eV.[a]

ThL^+	Basis Set	CCSD(T)[b]	B3LYP	B3PW91	BHLYP	M06	PBE0
ThO^+	SDD-VDZ-MWB/6-311+G(3df)	8.76	8.61	8.73	7.72	8.69	
	Seg. SDD-VQZ-MWB/6-311+G(3df)[e]	8.55	8.75	8.88	7.89	8.89	8.82
	ANO-VQZ-MWB/6-311+G(3df)	8.80	8.73	8.85	7.86	8.86	8.79
	ANO-VQZ-MDF/6-311+G(3df)	9.33	8.76	8.87	7.90	8.89	8.81
	cc-pVQZ-PP-MDF/6-311+G(3df)	9.03	8.72	8.84	7.88	8.86	8.78
	cc-pwCVQZ-PP-MDF/aug-cc-pwCVQZ	8.70	8.70	8.80	7.85	8.81	8.75
	cc-pwCVTZ-PP-MDF/cc-pwCVTZ	8.47	8.74	8.83	7.87	8.84	8.79
	cc-pwCVQZ-PP-MDF/cc-pwCVQZ	8.65	8.71	8.81	7.86	8.79	8.77
	CBS[c]	8.94	8.89	8.99	8.04	8.95	8.94
	FPD[d]	8.80					

Table C.4. (continued)

ThL^+	Basis Set	CCSD(T)[b]	B3LYP	B3PW91	BHLYP	M06	PBE0
ThC^+	SDD-VDZ-MWB/6-311+G(3df)	4.90	4.84	5.21	4.19	5.25	
	Seg. SDD-VQZ-MWB/6-311+G(3df)[e]	4.72	4.92	5.30	4.27	5.37	5.33
	ANO-VQZ-MWB/6-311+G(3df)	4.89	4.91	5.29	4.26	5.36	5.31
	ANO-VQZ-MDF/6-311+G(3df)	5.55	4.89	5.26	4.25	5.36	5.29
	cc-pVQZ-PP-MDF/6-311+G(3df)	5.08	4.81	5.17	4.18	5.24	5.20
	cc-pwCVQZ-PP-MDF/aug-cc-pwCVQZ	4.92	4.81	5.16	4.17	5.25	5.20
	cc-pwCVTZ-PP-MDF/cc-pwCVTZ	4.68	4.81	5.17	4.18	5.24	5.21
	cc-pwCVQZ-PP-MDF/cc-pwCVQZ	4.88	4.81	5.16	4.18	5.23	5.20
	CBS[c]	5.18	4.99	5.34	4.35	5.41	5.38
	FPD[d]	5.00					

Table C.4 Continued

[a] From structures optimized using the indicated basis sets at the respective level of theory (except CCSD(T)). BDEs are corrected by -0.40 eV, the difference in energy between the ^2D ground-state averaged over all spin-orbit states and the $^4F_{3/2}$ ground-level and are relative to Th^+ ($^4F_{3/2}$) + L.
[b] Single-point energies from B3LYP optimized structures.
[c] Complete basis set limit for the cc-pwCVXZ-PP-MDF/cc-pwCVXZ (X = T, Q) basis sets extrapolated as described in the main text.
[d] Feller-Peterson-Dixon method for composite thermochemistry. See description in main text. Parameters in Table C.5.

Table C.5. Calculated DK3-CCSD(T) atomization energies (in eV). See Eq.6.6 in main text for details.

Molecule	$E_{VQZ\text{-}DK}$	ΔE_{CBS}	ΔE_{CV}	ΔE_{QED}	ΔE_{so}	ΔE_{ESC}	$\Delta E_{(ZPE)}$	ΣD_0	$\Delta H_{(0\text{-}298)}$
ThC^+ ($^2\Sigma^+$)	6.16	0.08	-0.38	0.03	-0.29		-0.05	5.00	0.04
ThO^+ ($^2\Sigma^+$)	9.82	0.07	-0.28	0.01	-0.21	-0.56	-0.06	8.80	0.04
ThO_2^+ ($^2\Sigma_u^+$)	14.47	0.14	-0.25	0.03	-0.17		-0.08	13.61	0.06
$CThO^+$ ($^4A''$)	12.79	0.10	-0.29	0.03	-0.17		-0.10	11.80	0.08

Table C.6. Calculated ground and excited-states of ThC (in eV).

ThC	Configuration	r(Th-C)[a]	ν[a]	CCSD(T)[b]	B3LYP[a]
$^3\Sigma^+$	$1\sigma^2 1\pi^4 2\sigma 3\sigma$	1.937	880	0.00	0.00
$^1\Sigma^+$	$1\sigma^2 1\pi^4 2\sigma^2$	1.878	945	0.30	0.67
$^3\Pi$	$1\sigma^2 1\pi^3 2\sigma^2 3\sigma$	2.077	613	0.67	0.60
$^3\Delta$	$1\sigma^2 1\pi^4 2\sigma 1\delta$	1.959	814	1.18	1.07

[a] Parameters from B3LYP/cc-pwCVQZ-PP-MDF/aug-cc-pwCVQZ optimized structures. Bond lengths in Å and vibrational frequencies in cm^{-1} (unscaled).
[b] Single-point energies from B3LYP optimized structures

.

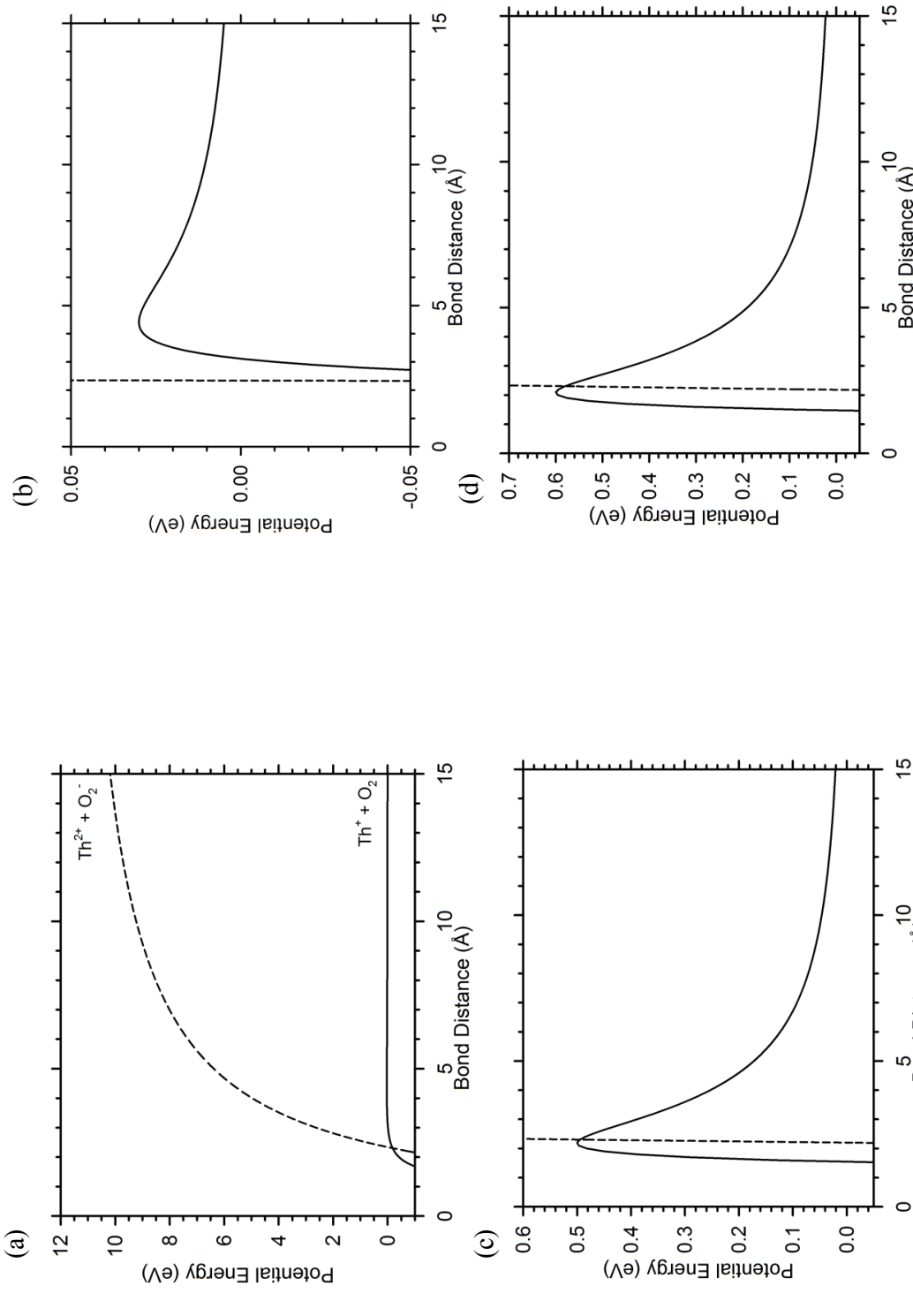

Figure C.1. Potential energy surfaces for an ion-induced dipole with centrifugal potential, V_4, (solid line) and a Coulombic potential with centrifugal potential and asymptotic potential of 12 eV, V_1, (dashed line). (a) shows potential energy curves for E = 0.03 eV over an extended energy range. (b), (c), and (d) show the region near the crossing between the two surfaces for E = 0.03, 0.50, and 0.60 eV, respectively.

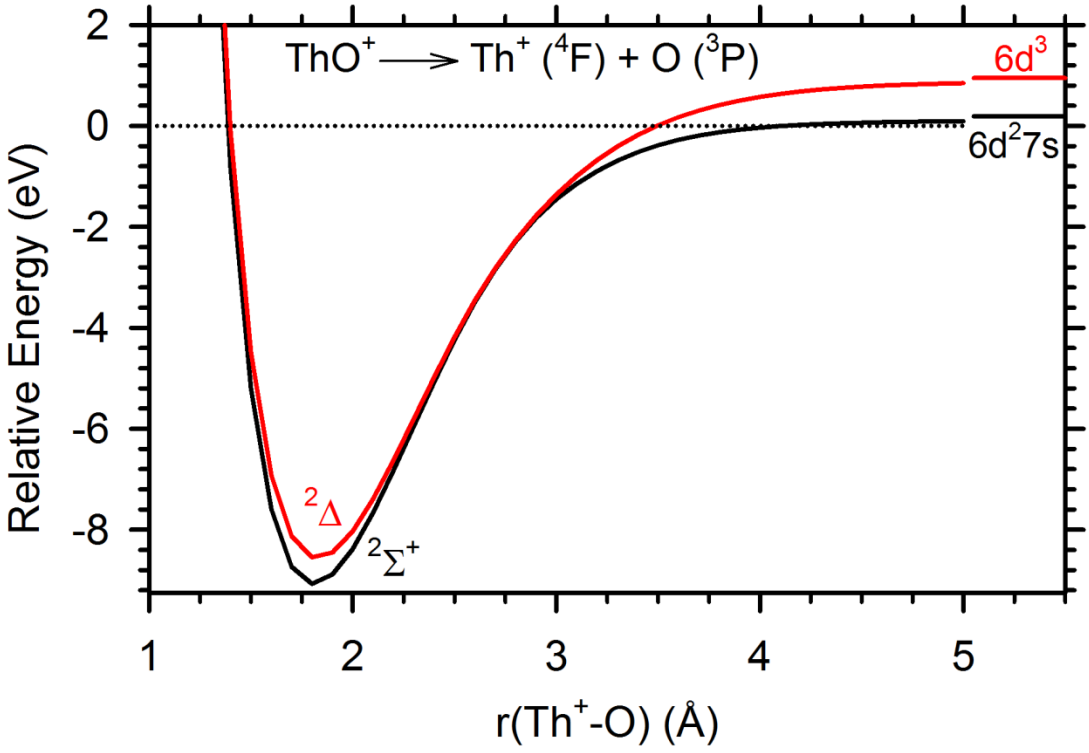

Figure C.2. B3LYP/SDD/6-311+G(3df) relaxed energy calculations of the potential energy surface of the diabatic bond dissociation energy of ThO^+ low-lying states as a function of r(Th^+-O). Energies relative to Th^+ (^{2}D, $6d7s^2$) + O (^{3}P).